

Stellar dynamics and extreme-mass ratio inspirals

Pau Amaro-Seoane

**Max Planck Institute for Gravitational Physics
(Albert Einstein Institute)
Potsdam-Golm, Germany**

Pau.Amaro-Seoane@aei.mpg.de

Nowadays it is well-established that in the centre of the Milky Way a massive black hole (MBH) with a mass of about four million solar masses is lurking. While there is an emerging consensus about the origin and growth of supermassive black holes (with masses larger than a billion solar masses), MBHs with smaller masses such as the one in our galactic centre remain an understudied enigma. The key to understanding these holes, how some of them grow by orders of magnitude in mass is to understand the dynamics of the stars in the galactic neighborhood. Stars and the central MBH chiefly interact through the gradual inspiral of the stars into the MBH due to the emission of gravitational radiation. Also stars produce gases which will be subsequently accreted by the MBH by collisions and disruptions brought about by the strong central tidal field. Such processes can contribute significantly to the mass of the MBH and progress in understanding them requires theoretical work in preparation for future gravitational radiation millihertz missions and X-ray observatories. In particular, a unique probe of these regions is the gravitational radiation that is emitted by some compact stars very close to the black holes and which will could be surveyed by a millihertz gravitational wave interferometer scrutinizing the range of masses fundamental to the understanding of the origin and growth of supermassive black holes. By extracting the information carried by the gravitational radiation, we can determine the mass and spin of the central MBH with unprecedented precision and we can determine how the holes “eat” stars that happen to be near them.

Contents

1	Massive black holes and their possible progenitors	9
1.1	Active galactic nuclei	10
1.1.1	AGN taxonomy	14
1.1.2	The unified model	15
1.1.3	A rough estimate of the mass of the central object	16
1.2	Massive black holes and their possible progenitors	17
1.3	Tidal disruptions	17
1.4	EMRIs	19
1.5	Limitations	20
2	GWs as a probe to stellar dynamics and the cosmic growth of SMBHs	23
2.1	GWs and stellar dynamics	23
2.2	The mystery of the growth of MBHs	24
2.3	A magnifying glass	25
2.4	A problem of ~ 10 orders of magnitude	27
2.4.1	Galactic or Cosmological dynamics	27
2.4.2	Cluster dynamics	27
2.4.3	Relativistic stellar dynamics	28
2.5	Actual data	28
3	A taxonomy of orbits in galactic nuclei	33
3.1	Spherical potentials	33
3.2	Non-spherical potentials	34
4	Two-body relaxation in galactic nuclei	39
4.1	Introduction	39

CONTENTS

4.2	Two-body relaxation	40
4.2.1	The relaxation time	40
4.2.2	Collision time	42
4.2.3	The crossing time	42
4.3	Dynamical friction	43
4.4	The diffusion and loss-cone angles	45
5	“Standard” mass segregation	49
5.1	Introduction	49
5.2	Single-mass clusters	50
5.3	Mass segregation in two mass-component clusters	52
5.4	Clusters with a broader mass spectrum with no MBH	61
5.5	Core-collapse evolution	63
5.6	Clusters with a broader mass spectrum with a MBH	65
6	Introduction to EMRIs	71
6.1	A hidden stellar population in galactic nuclei	71
6.2	Fundamentals of EMRIs	73
6.3	Orbital evolution due to emission of gravitational waves	78
6.4	Decoupling from dynamics into the relativistic regime	81
7	Beyond the standard model of two-body relaxation	87
7.1	The standard picture	87
7.2	Coherent or resonant relaxation	87
7.3	Strong mass segregation	91
7.4	Tidal separation of binaries	95
7.5	The role of the MBH spin	99
7.6	A barrier for captures	99
7.7	Extended stars EMRIs	101
7.8	The butterfly effect	101
7.9	Role of the gas	104
8	Integration of dense stellar systems and EMRIs	107
8.1	Introduction	107
8.2	Fokker-Planck	110
8.3	Moment models	113
8.4	Solving conducting, self-gravitating gas spheres	119
8.5	The local approximation	123
8.6	Hénon Monte-Carlo codes	126

8.7	Applications of Monte-Carlo and Fokker-Planck simulations to the EMRI problem . . .	128
8.8	Future of statistical stellar-dynamical simulations for EMRIs	131
8.9	Direct-summation N -body codes	133
8.10	List of public available codes and URLs	135
9	A note on the use of the Ancient Greek word <i>barathron</i> to refer to a black hole	137
10	Bibliography	141

Foreword to the first version of the review

The volume where capture orbits are produced is so small in comparison to other typical length-scales of interest in astrodynamics that it has been usually seen as unimportant and irrelevant to the global dynamical evolution of the system. The only exception has been the tidal disruption of stars by massive black holes. Only when it turned out that the slow, adiabatic inspiral of compact objects on to massive black holes will provide us with valuable information did astrophysicists start to address the question in more detail. Since the problem of EMRIs (Extreme-Mass Ratio Inspiral) started to draw our attention, there has been a notable progress in answering fundamental questions of stellar dynamics. The discoveries have been many and some of them remain puzzling. The field is developing very quickly and we are making important breakthroughs even before a millihertz mission flies.

When I was approached and asked to write this review, I was glad to accept it without realising the dimensions of the task. I was told that it should be *similar to a plenary talk for a wide audience*. I have a personal problem with instructions like this. I remember that when I was nine or ten years old, our Spanish teacher Maribel asked us to summarise a story we had read together in class. I asked her to please define “summarise”, because I could easily produce a summary of one, two or fifteen pages, depending on what she was actually expecting from us. She was confused and I never got a clear answer. She replied that “A summary is a summary and that’s it”. In this occasion I am afraid that I have run into the same snag and I have gone for the many-pages approach, to be sure that any newcomer will have a good overview of the subject, with relevant references, in a single document. If the document is too long, please address your complains to her, because she is the only responsible.

However, I would like to note that I have *not* focused on gathering as much information as possible from different sources. I think it is more interesting for the reader, though harder for the writer, to have a consistent document. This can be done by introducing the subject step by step, rather than working out a compendium of citations of the related literature. For instance, I present results that I have not previously published that will, I hope, enlighten the reader.

In this first version of the review I focus on the the problem of EMRIs from an “orthodox” standpoint, i.e. specially on phenomena based on standard two-body relaxation and the segregation of mass, which are fundamental to understand the basis of the problem. **I plan on extending the review to include tidal disruptions of stars in the next version of the review.**

Recently there has been a marked upsurge in the number of articles published concerning resonant relaxation and relativistic corrections. As I write these lines there are a number of articles about to be submitted with important implications to the calculations of captures. I thus expect to make a major revision of this article soon and expand it to tidal disruptions of stars in dense stellar systems. Also, from the point of view of millihertz GW missions, as the reader probably has already read, the “European Space Agency will go alone on next generation space mission”¹. This will certainly have an impact on the sensitivity curve of the future ESA millihertz interferometer, for which there exists a preliminary study (“eLISA/NGO”, see the Science Case in Amaro-Seoane et al., 2012a). Nevertheless, it is likely

¹http://blogs.nature.com/news/thegreatbeyond/2011/03/european_space_agency_to_go_it.html

to change again, so that I resolved to refer to a generic “LISA-like” instrument, which has been our notion for the last few decades. Indeed, the sensitivity curves of the full LISA and the new envisioned eLISA are not dramatically different. Thus, I will be referring to the mission throughout the whole text as, simply, “LISA”, and I will be using its sensitivity curve in all examples.

P. Amaro Seoane, Berlin, May 23, 2012

Chapter 1

Massive black holes and their possible progenitors

Massive objects avoiding light to escape from it is a concept that goes back to the 18th century, when John Michell (1724 – 1793), an English natural philosopher and geologist overtook Laplace with the idea that a very massive object could be able to stop light escaping from it thanks to its overwhelming gravity. Such an object would be *black*, that is, invisible, precisely because of the lack of light (Michell, 1784; Schaffer, 1979). I.e. a *dark star*. He wrote:

“If the semi-diameter of a sphere of the same density as the sun is in the proportion of five hundred to one, and by supposing light to be attracted by the same force in proportion to its mass with other bodies, all light emitted from such a body would be made to return towards it, by its own proper gravity.”

That dark star would hence not be directly observable, but one could use the kinematics of a companion star if in a binary. He even derived the corresponding radius, which approximately is the Schwarzschild radius.

Even though we will sift through this concept oftentimes in the work to be presented along the next chapters, it appears to be necessary to give an initial, short overview of the subject.

A “black hole”¹ embraces the observation of phenomena which are associated with matter accretion on to it, for we are not able to directly observe it. Emission of electromagnetic radiation, accretion discs and emerging jets are some, among others, evidences we have for the existence of such massive dark objects, lurking at the centre of galaxies.

On the other hand, spectroscopic and photometric studies of the stellar and gas dynamics in the inner regions of local spheroidal galaxies and prominent bulges give us the certainty that nearly all galaxies should harbour a central massive dark object, with a tight relationship between its mass and the mass or the velocity dispersion of the host galaxy spheroidal component (as we will see ahead). Nonetheless, even though we should mention that we

¹This term was first employed by John Archibald Wheeler (b. 1911)

do not dispose of any direct evidence that such massive dark objects are black holes, alternative explanations are sorely constrained (see, for instance, Kormendy 2003 and also Amaro-Seoane et al. 2010 for an exercise on constraining the properties of scalar fields with the observations in the galactic centre, although the authors conclude that at least one would need a mixed configuration with a black hole at the centre).

Super-massive black holes are ensconced at the centre of *active galaxies*. What we understand with *active* is a galaxy in which we can find an important amount of emitted energy which cannot be attributed to its “normal” components. AGNs, as they are usually denominated, have the powerhouse for their observed phenomena in a compact region in the centre.

We will embark in the next chapters of this review on a study of the dynamics of stellar systems harbouring a central massive object in order to extract the dominant physical processes and their parameter dependences like dynamical friction and mass friction, as an interlude to the astrophysics of extreme-mass ratio inspirals. This first chapter is devoted to a general description of the scenario with which we shall deal with. Firstly, we give a short bird’s-eye view of active galactic nuclei in order to clearly exhibit the boundaries of our problem and then, secondly, we will give an extending to the present time summary on the possible nature of the central dark object and its possible origin and formation.

1.1 Active galactic nuclei

The expression “active galactic nucleus” of a galaxy (AGN henceforth) is referred to the *energetic phenomena occurring at the central regions of galaxies which cannot be explained in terms of stars, dust or interstellar gas*. The released energy is emitted across most of the electromagnetic spectrum, UV, X-rays, as infrared, radio waves and gamma rays. Such objects have big luminosities (10^4 times that of a typical galaxy) coming from tiny volumes ($\ll 1 \text{ pc}^3$); in the case of a typical Seyfert galaxy the luminosity is about $\sim 10^{11} L_{\odot}$ ($L_{\odot} = 3.83 \cdot 10^{33} \text{ erg/s}$ is the luminosity of the sun), whilst for a typical quasar it is brighter by a factor 100 or even more; actually they can emit as much as some thousand galaxies like our Milky-Way. They are thus the most powerful objects in the universe. There is a connexion between young galaxies and the creation of active nuclei, because this luminosity can strongly vary with the red-shift.

Anticipating something on which we will elaborate a bit ahead, nowadays one explains the generation of energy resorting to matter accreting on to a super-massive black hole in the range of mass $\mathcal{M}_{\bullet} \sim 10^6-10^9 M_{\odot}$ (where \mathcal{M}_{\bullet} is the black hole mass). In this process, angular momentum flattens the structure of the in-falling material to a so-called *accretion disc*.

For some alternative and interesting schemes to MBHs, see Ginzburg and Ozernoy (1964) for spinars, Arons et al. (1975) for clusters of stellar mass BHs or neutron stars and Terlevich (1989) for *warmers*: massive stars with strong mass-loss spend a significant amount of their He-burning phase to the left of the ZAMS on the HR diagram. The ionisation spectrum of a young cluster of massive stars will be strongly

influenced by extremely hot and luminous stars.

It is frequent to observe jets, which may be arising from the accretion disc (see figure 1.1), although we do not dispose of direct observations that corroborate this. Accretion is a very efficient channel of turning matter into energy. Whilst nuclear fusion reaches only a few percent, accretion can breeze in almost 50% of the mass-energy of a star into energy.

Being a bit more punctilious, we should say that hallmarks for AGNs are the frequency of their electro-magnetic emission frequencies, observed from $\lesssim 100$ MHz (as low frequency radio sources) to $\gtrsim 100$ MeV (which corresponds to $\sim 2 \cdot 10^{22}$ Hz gamma ray sources). Giant jets give the upper size of manifest activity $\lesssim 6$ Mpc $\sim 2 \cdot 10^{25}$ cm², and the lower limit is given by the covered distance by light in the shortest X-ray variability times, which is $\sim 2 \cdot 10^{12}$ cm.

As regards the size, we can envisage this as a radial distance from the very centre of the AGN where, ostensibly, a SMBH is harboured and the different observed features of the nucleus (see figure 1.1). From the centre outwards, we have first a UV ionising source amidst the optical continuum region. This, in turn, is enclosed by the emission line clouds (NLR, BLR³) and the compact radio sources and these betwixt another emitting region etc.

The radiated power at a certain frequency per *dex*⁴ frequency ranges from $\sim 10^{39}$ erg/s (radio power of the MW) to $\sim 10^{48}$ erg/s, the emitted UV power of the most powerful, high-redshifted quasars. Such broad frequencies and radius ranges for emission makes us to duly

note that they are far out of thermal equilibrium. This manifests in two ways: first, smaller regions are hotter; second, components of utterly different temperature can exist together, even though components differ in one or two orders of magnitude in size.

We have to somehow specify what we mean with the term AGN. For this scope we should name the observable phenomena which are used to detect them; on the other hand, nevertheless, AGNs can be noticed in many ways, but this does not mean that all of them partake the same features. In fact, an AGN “picks up” some of these defining qualities to be such an object.

Very small angular size If we have optical images of the host galaxy, the nucleus happens to be a very bright point with a flux that can touch or even surpass the rest one of the host galaxy. In figure 1.2 we can see an example of this, Messier 63, taken in infrared light.

Radio astronomical observations were the first proof for the existence of non-stellar activity in external galaxies. Early observations revealed that many bright radio sources have the shape of two lobes with a galaxy situated at half the distance (see figure 1.3). Even though radio astronomical techniques are powerful, they might be misleading, since the radio band never accounts for more than $\sim 1\%$ of the bolometric luminosity; to boot, less biased surveys bore witness that the most AGNs emit a much smaller portion of their total power in the radio.

High luminosity This can run in the case of an AGN from about 1% of a typical galaxy up to $\sim 10^4$ times as great. Of course these limits are not completely fixed, for there can be “hid-

²If we do not take into account the ionising radiation on intergalactic medium

³See subsection 1.1.1

⁴A “unit” in the logarithmic axis

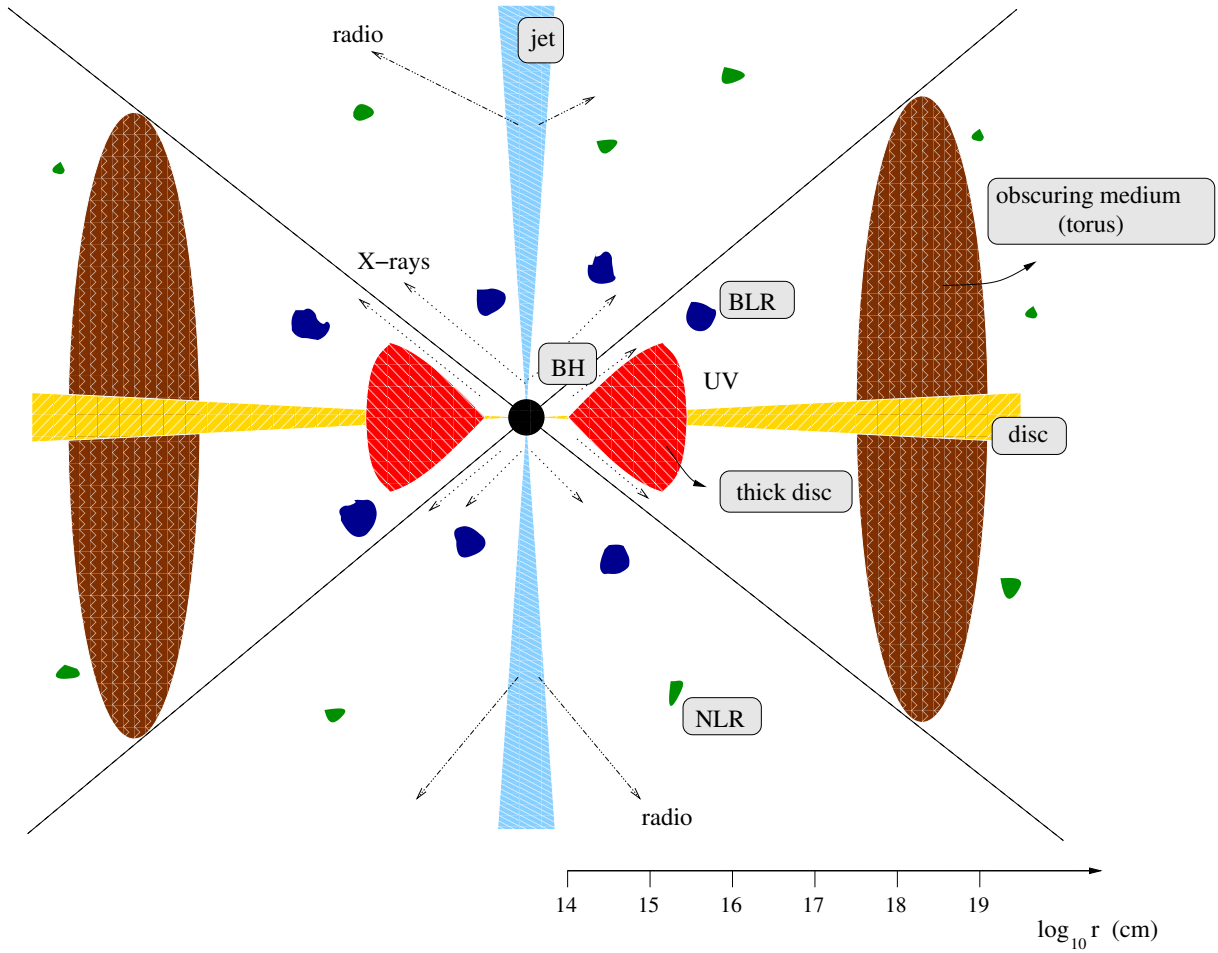


Figure 1.1: Unified model of an AGN. A relativistic jet is only to be found in radio-loud sources. In the vicinity of the central BH we may find a flared-up disc due to X-rays.



Figure 1.2: Messier 63, “Spitzer’s Sunflower”. Image taken in infrared light by NASA’s Spitzer Space Telescope.

den” a huge population with lower, non observable luminosities; another possible reason for the incapacity of observation is relativistic beaming, or obscuration, due to thick dust extinction, which can misguide our measurements. Compared with the galaxy spectra, an AGN continuum spectra looks stunningly different. The energy flux per logarithmic bandwidth produces a spectrum far broader compared with that of a galaxy. In comparison with a galaxy, AGNs give out in the radio band a fraction of bolometric luminosity that is about an order of magnitude greater, and the corresponding in the x-ray band is between three and four larger.

Variability is often said to be a distinctive characteristic of AGNs; this is relative for, even though the most of them can be seen to vary in the optical band, the typical amplitude over time-scales is frequently 10%. There is no a fixed time-scale on which AGNs vary, and therefore it is hard to measure their amplitude of

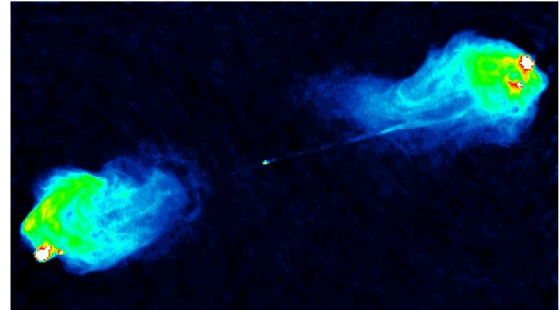


Figure 1.3: Cygnus A at 6 cm wavelength (Perley et al., 1984). The total extent of this source is ~ 120 kpc.

variability. We can find a subgroup of these objects that can be observed to vary even from night to night, and cumulative changes of factors of hundred have happened over year time-scales. In figure 1.4 we can see an example of this rapid variation (Pian et al., 1997).

Polarisation Like in the case of galaxies, even though stars are in itself unpolarised, the light we observe is by and large polarised by about 0.5% because of interstellar dust transmission polarisation. As for the AGNs, they are also polarised, linearly and with a fractional polarisation of between 0.5 – 2%. We find a minority that is much more polarised, frequently $\sim 10\%$. We have a strong variation on both the magnitude and the direction of the polarisation for those objects that are strongly polarised and have strongly variable total flux. Nonetheless, variability does have bounds, for circular polarisation has never been detected.

Emission lines This draws our attention, for it is easy and productive to study them. On the contrary to most of galaxies, these are very prominent for this kind of objects. The observed

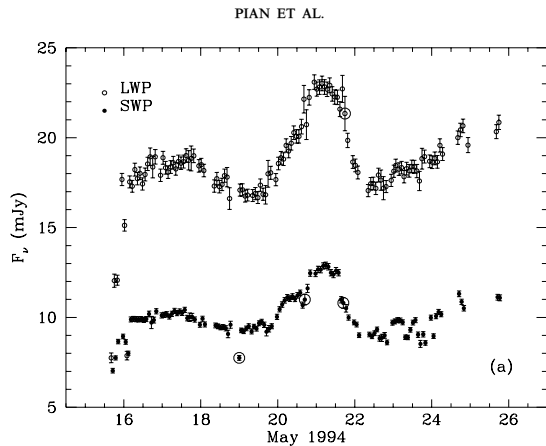


Figure 1.4: Two ultraviolet light curves for PKS 2155-304. The open circles show the continuum flux at 2800 Å; the filled ones at 1400 Å. We can see that within one day changes of several tens of percent occurred.

emission lines are stereotypic from one AGN to the other; almost at all times we observe Ly α , the Balmer lines, the C_{IV} 1549 doublet etc. Oftentimes is seen the FeK α x-ray line near 6.4 KeV.

1.1.1 AGN taxonomy

To key out the sub-variety of AGNs we are talking about we have several terms. Whether or not the distinctions is beneficial is something we could call into question, but we have to know it if we want to follow “the conversation”. A deep description of all AGNs nomenclatures with their typical characteristics is beyond the scope of this work. Here we just want to give a general idea of the vast variety of AGNs and main features. We have different ways of categorisation, depending on by which criteria we want to classify. Some of the terms are self-explanatory; like, for instance *radio loud* or *radio quiet*. OVV

is the acronym for *Optically Violently Variable*, for in the optic band we have very rapid and large amplitude variability, as the name itself reveals. Others are coined terms; *Quasar* is simply the pronounced form of “QSR” (*Quasi-Stellar Radio source*), but after a time the meaning changed and evolved to “generic AGN”; nowadays it has nothing to do with the radio luminosity. In fact, for instance, very low luminosity AGNs are called *micro-quasars*. Some terms bring up the name of the first people that identified the class: Carl Seyfert remarked the first *Seyfert galaxies*, and they were split up later into two types, depending on the existence or not of broad wings in the emission lines. In an equal manner, Fanaroff and Riley pointed out a distinction in luminosity and morphology among the radio galaxies, and so they were named *FR galaxies* after them. We find also far-out histories in the nomenclature of AGNs: The type *BL Lac Objects* were initially identified as variable stars in the Lacerta constellation and, thus, they were named “BL Lac”. The term *Blazar* springs up from the fact that the power output of the classes OVV and BL Lac “blazes” dramatically and was thought to unify them, because they are very similar.

In table 1.1 (taken from Krolik 1999) an object is said to be point-like if an optical point source can be seen. By broad-band we mean that there is a comparable luminosity in the infrared, optical and x-ray bands. The existence in the optical and ultraviolet spectra of lines several thousand (hundred) km/s in width is meant with broad-lines (narrow-lines). By radio we understand that for the object the fraction of luminosity emitted in the radio is relatively large, perhaps $\sim 10^{-3}$ of the bolometric. The members of a class should vary by

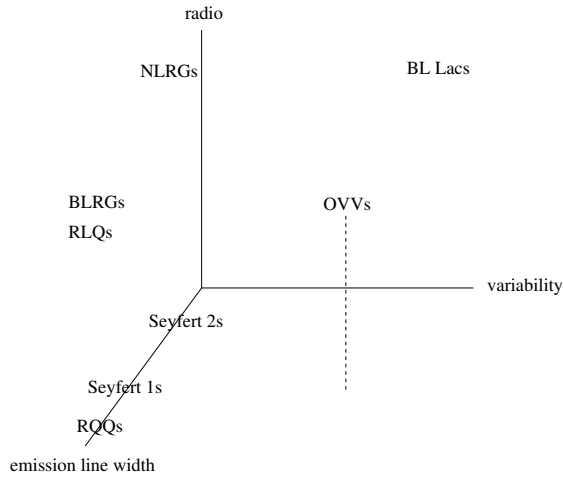


Figure 1.5: Classification of AGNs in a three-dimensional parameter space.

an order of magnitude or more in the optical band over a human time life for the variable entrance and for polarisation the optical light should be at least a few percent linearly polarised. In the table we have added the subdivision *LINERs*, which stands for “Low-Ionisation Nuclear Emission Region”, but this category is on the verge of activity; it is not clear whether or not these galaxies are really active.

This classification allows us to arrange the types in a three-dimensional parameter space, since we find that we have the groups radio-loud against radio-quiet, strong variable against all the others and narrow emission lines against broad emission lines. We can display a three-parameter space in which we locate each of the types of AGNs, as we see in figure 1.5 (after the figure of Krolik 1999).

1.1.2 The unified model

After a study of a few decades, as we commented at the beginning of this chapter, a unification scheme for AGNs has appeared in the community. According to it, a well-mannered AGN should have the following identifying characteristics (see Fig 1.1),

Super-massive black hole – in the range of $10^{6-10} M_{\odot}$

Accretion disc and corona – heated by magnetic and/ or viscous processes with optical radiation though soft X-ray energy

Broad line region – with high velocity gas

Narrow line region – corresponding to lower velocity gas

Obscuring medium – which can adopt a torus form or another geometry. This has the characteristic, as its names pinpoints, of hiding the broad-line region from some directions owing to its material (dust). It is located at about 10 – 100 pc between the smaller inner region from which the broad emission lines come from and the more external zone where the narrow emission lines emerge

Relativistic jet – emerging at distances of about $\sim 100 R_{\text{Schw}}$ (Schwarzschild radius) of the BH. The extension of these objects can be out to tens of hundreds of parsecs or even Mpc

Excluding intrinsic variances in BH’s differentia, like M_{\bullet} , ionisation parameter, size, density, luminosity etc, the unification model properties (except for, maybe, relativistic jets) stay staunch to all AGNs. In conformity with it, many of the main observational characteristics that we have described before are due

Type	Point-like	Broad-band	BL	NL	Radio	Variable	Polarised
Radio-loud quasars	yes	yes	yes	yes	yes	some	some
Radio-quiet quasars	yes	yes	yes	yes	weak	weak	weak
Broad line radio galaxies (FR2 only)	yes	yes	yes	yes	yes	weak	weak
Narrow line radio galaxies (FR1 and FR2)	no	no	no	yes	yes	no	no
OVV quasars	yes	yes	yes	yes	yes	yes	yes
BL Lac objects	yes	yes	no	no	yes	yes	yes
Seyferts type 1	yes	yes	yes	yes	weak	some	weak
Seyferts type 2	no	yes	no	yes	weak	no	some
LINERs	no	no	no	yes	no	no	no

Table 1.1: The AGN taxonomy. BL stands for broad lines and NL for narrow lines

to orientation and are not intrinsic differences. The galaxy appears as a Seyfert 2 or NLRG at the regions where the obscuring medium stops the direct view of the central parts. Facing the AGN, as we look into the inner regions and it appears as Seyfert 1s or, in radio-loud, BLRGs to radio-loud quasars and at inferior luminosities, BL Lacs.

1.1.3 A rough estimate of the mass of the central object

A direct consequence of the paradigm of SMBHs at the centre of ancient galaxies to explain the energy emitted by quasars is that relic SMBHs should inhabit at least a fraction of present-day galaxies (Rees, 1990). This conclusion was first made quantitative by Soltan (1982), revisited in more detail and by Yu and Tremaine (2002).

In a system of luminosity L with a lifetime T_{lum} , if ϵ is the conversion of matter to energy (accretion) efficiency, one should expect that in the system, an amount of material $LT_{\text{lum}}/\epsilon c^2$ has been gathered at some place, where c is the light velocity. We are referring to the central

super-massive black hole, harboured by the host galaxy. We will give a description of such an object in the next section and pore over it in the next chapters.

If we are capable of determining T_{lum} and ϵ , we will have a rough idea of what \mathcal{M} is. Usually, for ϵ one can prove that $\epsilon \sim 1/10$ is a suitable value (McCray, 1979). Assuming that the lobes are powered by the central engine, we have that, for Cyg A, with a lobe separation of 80 kpc, $T_{\text{lum}} \sim 4 \cdot 10^7$ yr and, so, $\mathcal{M}_{\bullet} \sim 10^8 M_{\odot}$. If we do not have at our disposal double radio sources, we can follow a different argument: if the lifetime of the galaxy is $\sim 10^{10}$ yr and 1% of galaxies are active and they all go through activity phases, $T_{\text{lum}} \sim 10^8$ yr; this means that, for the more luminous sources ($L \geq 10^{47}$ erg/s), $\mathcal{M}_{\bullet} \sim 10^{10} M_{\odot}$. On the other hand, if we had used the luminosity per unit volume from quasars from observations, we would have found out that, since this gives the energy output per unit volume over the age of the universe, the mass density of “recycled” material is consistent with an average dead mass of $10^8 M_{\odot}$. A number of independent deductions leads to a similar result (Frank et al., 2002).

1.2 Massive black holes and their possible progenitors

The quest for the source of the luminosities of $L \approx 10^{12} L_{\odot}$ produced on such small scales, jets and other properties of quasars and other types of active galactic nuclei led in the 60's and 70's to a thorough research that hint to the inkling of “super-massive central objects” harboured at their centres. These were suggested to be the main source of such characteristics (Lynden-Bell, 1967; Lynden-Bell and Rees, 1971; Hills, 1975). Lynden-Bell (1969) showed that the release of gravitational binding energy by stellar accretion on to a MBH could be the primary powerhouse of an AGN (Lynden-Bell, 1969).

In the last decade, observational evidences have been accumulating that strongly suggest that massive BHs are indeed present at the centre of most galaxies, with a significant spheroidal component. Mostly thanks to the *HST*, the kinematics in present-day universe of gas or stars has been measured in the central parts of tens of nearby galaxies. In almost all cases⁵, proper modelling of the measured motions requires the presence of a central compact dark object with a mass of a few 10^6 to $10^9 M_{\odot}$ (Ferrarese et al., 2001; Gebhardt et al., 2002; Pinkney et al., 2003; Kormendy, 2003, and references therein). Note, however, that the conclusion that such an object is indeed a BH rather than a cluster of smaller dark objects (like neutron stars, brown dwarfs etc) has only been reached for two galaxies. The first one is the Milky Way itself at the centre of which the case for a $3\text{--}4 \times 10^6 M_{\odot}$ MBH has been clinched, mostly through ground-based IR observations of the fast orbital motions of a

few stars (Ghez et al. 2005a; Schödel et al. 2003 and see Genzel et al. 2010 for a review). The second case is NGC4258, which passes a central Keplerian gaseous disc with H_2O MASER strong sources allowing high resolution VLBI observations down to 0.16 pc of the centre (Miyoshi et al., 1995; Herrnstein et al., 1999; Moran et al., 1999).

In any case, it is nowadays largely accepted that the central dark object required to explain kinematics data in local active and non-active galaxies is an MBH. The large number of galaxies surveyed has allowed to study the demographics of the MBHs and, in particular, look for correlations with properties of the host galaxy. The most remarkable ones are the fact that the MBH has a mass which is roughly about 0.1% of the stellar mass of the spheroidal component of the galaxy and that the mass of the BH, M_{\bullet} , correlates even more tightly with the velocity of this component. These facts certainly strike a close link between the formation of the galaxy and the massive object harboured at its centre.

1.3 Tidal disruptions

The centre-most part of a galaxy, its *nucleus* consists of a cluster of a few 10^7 to a few 10^8 stars surrounding the DCO, assumed from now onward to be a MBH, with a size of a few pc. The nucleus is naturally expected to play a major role in the interaction between the DCO and the host galaxy, as we mentioned before. In the nucleus, stellar densities in excess of 10^6 pc^{-3} and relative velocities of order a few 100 to a few 1000 km s^{-1} are reached. In these exceptional conditions and unlike anywhere else

⁵With, notably, the possible exception of M33 (Gebhardt et al., 2001; Merritt et al., 2001)

in the bulk of the galaxy, collisional effects⁶ come into play. These include 2-body relaxation, i.e. mutual gravitational deflections, and genuine contact collisions between stars.

This means that, if a star happens to pass very close to the MBH, some part of it or all of it may be teared apart because of the so-called tidal gravity of the central object. The difference of gravitational forces on points diametrically separated of the star alter its shape, from its initial approximately spherical architecture to an ellipsoidal one and, in the end, the star is disrupted. This radius can be easily calculated as follows. The star gets disrupted whenever the work exerted over it by the tidal force exceeds its own binding energy, (all energies are per unit mass):

$$E_{\text{bind}} = \alpha \frac{Gm_{\star}}{r_{\star}} \quad (1.1)$$

$$\alpha = \frac{3}{5-n}$$

where n is the polytropic index (Chandrasekhar, 1942).

$$(F_1 - F_2) 2r_{\star} = \alpha \frac{Gm_{\star}}{r_{\star}} \quad (1.2)$$

$$F_1 = \frac{GM_{\bullet}}{(r_t - r_{\star})^2},$$

$$F_2 = \frac{GM_{\bullet}}{(r_t + r_{\star})^2}. \quad (1.3)$$

⁶“Collisional” does not mean necessarily that the stars physically collide. This a stellar dynamics term to express that the number of stars per pc^3 is such that we have to take into account exchange of energy and angular momentum between stars.

Considering $r_{\star} \ll r_t$, we can approximate the expressions:

$$\frac{1}{(r_t - r_{\star})^2} \approx \frac{1}{r_t^2} + \frac{2r_{\star}}{r_t^3}$$

$$\frac{1}{(r_t + r_{\star})^2} \approx \frac{1}{r_t^2} - \frac{2r_{\star}}{r_t^3}; \quad (1.4)$$

then,

$$r_t = \left[\frac{2}{3}(5-n) \frac{\mathcal{M}_{\bullet}}{m_{\star}} \right]^{1/3} r_{\star}. \quad (1.5)$$

For solar-type stars it is (considering a $n = 3$ polytrope)

$$r_t \simeq 1.4 \times 10^{11} \left(\frac{\mathcal{M}_{\bullet}}{M_{\odot}} \right)^{1/3} \text{ cm}. \quad (1.6)$$

In figure 1.7 we give an intuitive image of a tidal disruption of an extended star, where distortions due to gravitational-lens have not been taken into consideration. In figure 1.8, on the left we show a Chandra x-ray image of J1242-11 with a scale of 40 arcsec on a side. This figure pinpoints one of the most extreme variability events ever detected in a galaxy. One plausible explanation for the extreme brightness of the ROSAT source could be accretion of stars on to a super-massive black hole. On the right we have its optical companion piece, obtained with the 1.5 m Danish telescope at ESO/La Silla. The right circle indicates the position of the Chandra source in the centre of the brighter galaxy.

These processes may contribute significantly to the mass of the MBH (Murphy et al., 1991; Freitag and Benz, 2002). Tidal disruptions trigger phases of bright accretion that may reveal the presence of a MBH in an otherwise quiescent, possibly very distant, galaxy (Hills, 1975; Gezari et al., 2003).

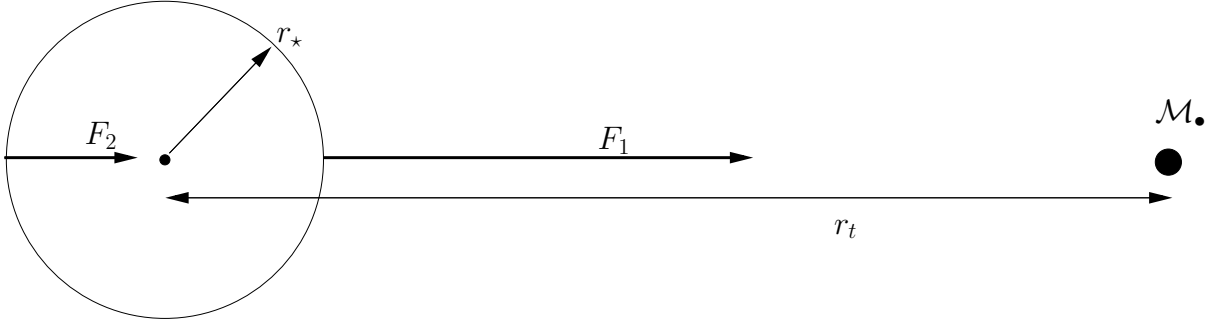


Figure 1.6: Decomposition of the tidal forces over a star

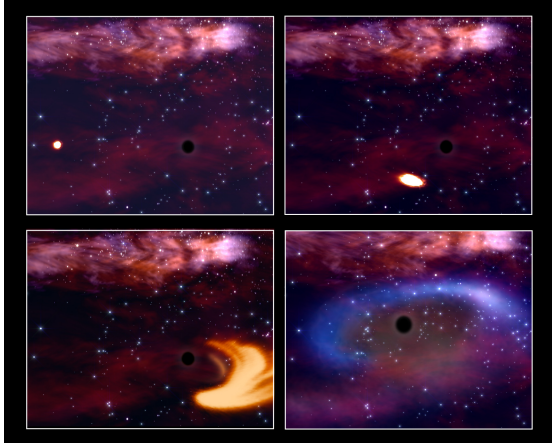


Figure 1.7: Schematic representation of the tidal disruption process. In the first panel on the left, an extended star approaches the central MBH. As soon as the star feels the overwhelming tidal forces acting on it, the initial spherical architecture becomes spheroidal and the star starts to be torn apart. On the third panel the star is totally ripped and about 50% of it accreted on to the MBH. Credits: ESA and Stefanie Komossa (Max Planck Institute for Extraterrestrial Physics). Illustration credit M. Weiss

1.4 EMRIs

On the other hand, stars can be swallowed whole if they are kicked directly through the horizon of the MBH (so-called *direct plunges*) or gradually inspiral due to the emission of GWs. The latter process, known as an “*Extreme Mass Ratio Inspiral*” (EMRI) is one of the main objects of interest for eLISA (Evolved Laser Interferometer Space Antenna Amaro-Seoane et al., 2012a). A compact object, a star so dense that it will not be disrupted by the tidal forces of the MBH, (say, a neutron star, a white dwarf or a small stellar black hole), is able to approach very closely to the central MBH. When the compact object comes very close to the MBH, a large amount of orbital energy is radiated away, causing the semi-major axis shrink. This phenomenon will be repeated thousand of times as the object inspirals until is swallowed by the central MBH.

The “doomed” object spends many orbits around the MBH before it is swallowed. When doing so, it radiates energy which can be conceptualised as a snapshot containing detailed information about space-time and *all the physical parameters* which characterise the binary,

the MBH and the small stellar black hole: their masses, spins, inclination and their sky position. The emitted GWs encode a map of the space-time. If we can record and decode it, then we will be able to test the theory that massive dark objects are indeed Kerr black holes as the theory of general relativity predicts, and not exotic objects such as boson stars. This would be the ultimate test of general relativity.

The detection of such an EMRI will allow us to do very exciting science: EMRIs will give us measurements of the masses and spins of BHs to an accuracy which is beyond that of any other astrophysical technique. Such information will tell us about cosmic evolution, about the history and growth of MBHs in the nearby universe, with an accuracy which has no precedent.

1.5 Limitations

So far, galactic nuclei have been modelled as isolated spherical clusters (i.e. Murphy et al. (1991); Freitag and Benz (2002)). However, non-spherical structures such as triaxial bulges, bars or stellar discs are common on scales of 100-1000 pc, and also the nucleus itself may be non-spherical. E.g. it could be rotating, as a result of a merger with another nucleus (Milosavljević and Merrit, 2001) or due to dissipative interactions between the stars and a dense accretion disc (Rauch, 1995). The influence of non-sphericity at small and intermediate scales on the structure and evolution of the nucleus has been little explored but it could boost the estimates of capture and disruption rates by orders of magnitudes (Merritt and Poon 2004a; Poon and Merritt 2004a, Amaro-Seoane, Brem,

Malkov, Vilkoviskij and Spurzem 2012, in preparation).

The theoretical study of the structure and evolution of a stellar cluster (galactic nucleus or globular cluster) harbouring a central MBH started a few decades years ago. However, due to the complex nature of the problem which includes many physical processes and span a huge range of time and length scales, as we will see in the next chapters, our understanding of such systems is still incomplete. As in many fields of astrophysics, analytical computations can only been applied to highly idealised situations and only a very limited variety of numerical methods have been developed so far that can tackle this problem. In the next chapters we will address the most relevant astrophysical phenomena for EMRIs and in the last chapter we give a description of a few different approaches to study these scenarios with numerical schemes.

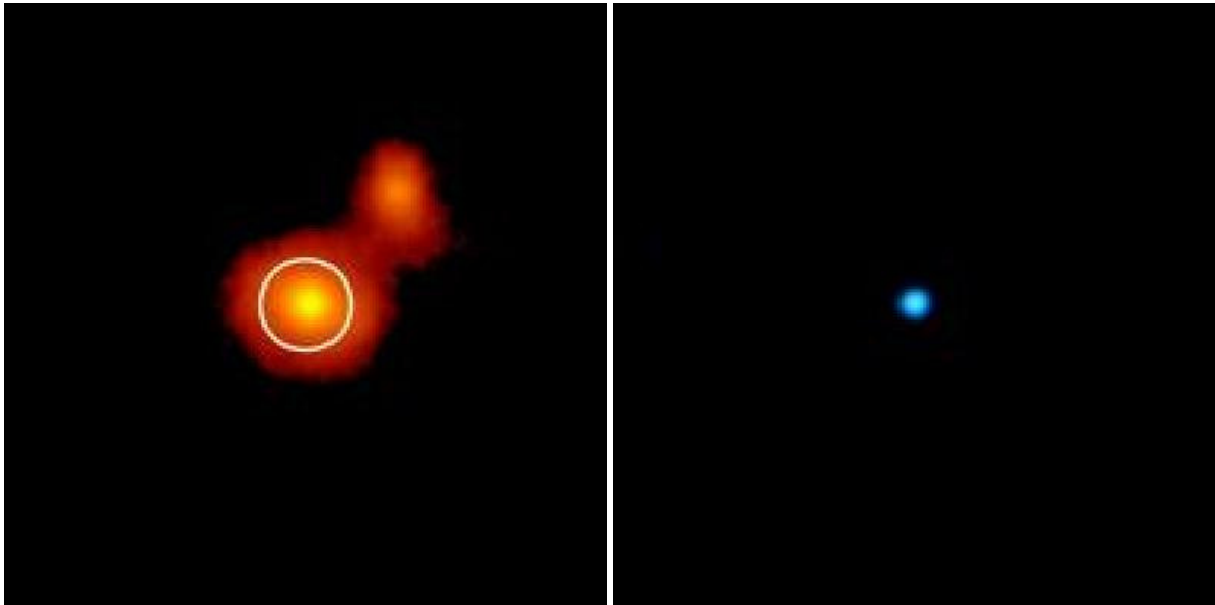


Figure 1.8: Optical and x-ray images of RX J1242-11. Credits: (left) ESO/MPE/S.Komossa and (right) NASA/CXC/MPE, (Komossa et al., 2004).

Chapter 2

GWs as a probe to stellar dynamics and the cosmic growth of SMBHs

2.1 GWs and stellar dynamics

The challenge of detection and characterization of gravitational waves is strongly coupled with the dynamics of dense stellar systems. This is specially true in the case of the capture of a compact object by a MBH.

In order to estimate how many events one can expect and what we can assess about the distribution of parameters of the system, we need to have a very detailed comprehension of the physics. In this regard, the potential detection of GWs is an incentive to dive into a singular realm otherwise irrelevant for the global dynamics of the system.

A harbinger in this respect has been the tidal disruption of stars as a way to feed the central MBH. About 50% of the torn star remains bound to the MBH and is accreted on to it, producing an electromagnetic flare which tops out in the UV/X-rays, emitting a luminosity close to Eddington. This has been scrutinized attentively as possible way of identifying and characterizing an otherwise quiescent, possibly very distant, galaxy (Renzini et al., 1995; Komossa, 2002; Gezari et al., 2009). Nonethe-

less, the complications of accretion are particularly intricate, tight on many different timescales to the microphysics of gaseous processes. Even on local, galactic accreting objects the complications of accretion are convoluted. It is thus extremely difficult to understand how to extract out of the flare very detailed information about extragalactic MBH. The question of feeding a MBH is a statistical one. We do not care about individual events to understand the growth in mass of the hole, but about the statistics of the rates on cosmological timescales. Obviously, if we tried to understand the individual processes, we would fail.

The question of what happens to a compact object as it approaches the central MBH never raised before we had the incentive of direct detection of gravitational radiation. When we started to address this problem, we realised that there were many questions of stellar dynamics that either did not have an answer or that had not even been addressed at all. We have now more questions than answers.

We will discuss about the relaxation processes we know play a major role in the dy-

namics of this particular regime. This involves two-body as well as many bodies coherent or non-coherent relaxation. The list of processes is most likely incomplete, for there can still be additional, even more complicated processes unknown to us.

Astrophysical objects such as a binary of black holes, generate perturbations in space and time that spread like ripples on a pond. Such ripples, known as “gravitational waves” or “gravitational radiation”, travel at the speed of light, outward from their source. These gravitational waves are predicted by general relativity, first proposed by Einstein. Whilst the strength of gravitational waves diminishes with distance, they neither stop nor slow.

Measurement of these gravitational waves will give astrophysicists a totally new and different way of studying the Universe: instead of analysing the propagation and transformation of particles such as photons, we will have direct information from the fabric of spacetime itself. The information carried by the gravitational radiation will tell us in exquisite detail about the history, behaviour and structure of the universe: from the Big Bang to black holes. Nonetheless, gravitational radiation has yet to be detected.

2.2 The mystery of the growth of MBHs

As we have mentioned before, one of the most exciting results of modern astronomy is the discovery, mostly through high-resolution observations of the kinematics of stars and gas, that most, if not all, nearby bright galaxies harbor a dark, massive, compact object at their centres. (Ferrarese and Ford, 2005; Kormendy, 2004). The

most spectacular case is our own galaxy, the Milky Way. By tracking and interpreting the stellar dynamics at the centre of our galaxy, we have the most well-established evidence for the existence of a massive black hole (MBH). The close examination of the Keplerian orbits of the so-called “S-stars” (also called S0-stars, where the letter S stands simply for source) has revealed the nature of the central dark object located at the Galactic Center. By following one of them, S2 (S02), the mass of SgrA* was estimated to be about $3.7 \times 10^6 M_{\odot}$ within a volume with radius no larger than 6.25 light-hours (Schödel et al., 2003; Ghez et al., 2003). More recent data based on 16 years of observations set the mass of the central MBH to $\sim 4 \times 10^6 M_{\odot}$ (Eisenhauer et al., 2005; Ghez et al., 2005b, 2008; Gillessen et al., 2009). Observations of other galaxies indicate that the masses of MBH can reach a few billion solar masses (M_{\odot}).

Many correlations linking the MBH’s mass and overall properties of its host spheroid (bulge or elliptical galaxy) have been discovered. The tightest are with the spheroid mass (Häring and Rix, 2004), its velocity dispersion ($M - \sigma$ relation, Tremaine et al. (2002)) and degree of concentration (Erwin et al., 2004). Consequently, understanding the origin and evolution of these MBHs necessitates their study in the context of their surrounding stellar systems. Claims of detection of “intermediate-mass” black holes (IMBHs, with masses ranging between $100 - 10^4 M_{\odot}$) at the center of globular clusters (Gebhardt et al., 2002; Gerssen et al., 2002) raise the possibility that these correlations extend to much smaller systems, but the strongest –if not totally conclusive– observational evidences for the existence of IMBHs are ultra-luminous X-ray sources (Miller and Colbert, 2004; Kong et al.,

2009).

The study of the innermost kinematics in galactic nuclei are difficult, specially for low-mass MBH (ranging between 10^5 and $10^7 M_\odot$) and moreso for the even less-massive IMBHs. Nowadays using adaptive optics we could optimistically hope to get a handful of measurements of stellar velocities of such targets about ~ 5 kpc away in some ten years. Nevertheless, we need a bright reference star to guide us; the requirement of an astrometric reference system is fundamental.

Therefore, in order to follow the same scheme of detection of inner stellar kinematics and of the masses of MBHs in distant galaxies, we need the Very Large Telescope interferometer and one of the next-generation instruments, either the VSI or GRAVITY (Gillessen et al., 2006; Eisenhauer et al., 2008). Only then can we improve our astrometric accuracy by the necessary factor of ~ 10 . This could allow us to follow the motion of stars orbiting a central MBH in a galaxy with the resolution we need to extract the mass of the black hole from the kinematics of the stars.

Although there is an emerging consensus about the growth of large-mass MBHs thanks to Softan's argument, MBHs with masses up to $10^7 M_\odot$, such as our own MBH in the Galactic Centre (with a mass of $\sim 4 \times 10^6 M_\odot$), are enigmatic. There are many different arguments to explain their masses: accretion of multiple stars from arbitrary directions Hills (1975), mergers of compact objects such as stellar-mass black holes and neutron stars Quinlan and Shapiro (1990) or IMBHs falling on to the MBH (Portegies Zwart et al., 2006), or by more peculiar means such as accretion of dark matter Ostriker (2000) or collapse of supermassive stars

(Hara, 1978; Shapiro and Teukolsky, 1979; Rees, 1984; Amaro-Seoane, 2004a; Begelman, 2010). Low-mass MBHs and, thus, the early growth of *all* MBHs, remain a conundrum.

2.3 A magnifying glass

The evolved Laser Interferometer Space Antenna / New Gravitational Wave Observatory (eLISA/NGO, see Amaro-Seoane et al., 2012a,b, and also the official AEI URL¹), based on the the former NASA-ESA configuration (LISA, see e.g. Danzmann, 2000), is a conceived space-borne observatory for detecting low frequency gravitational waves (GW). The “full version of ” LISA, which will be our reference point throughout the review, consists of three spacecrafts arranged in an equilateral triangle 1 million kilometers on a side, all in a heliocentric orbit. LISA is designed to cover the low-frequency broadband of gravitational radiation, from about 0.1 to 100 millihertz. In this band of frequencies, the Universe is populated in strong sources of GWs such as binaries of supermassive black holes merging in galaxies, massive black holes “swallowing” entirely small compact objects like stellar black holes, neutron stars and white dwarfs. The information is encoded in the gravity waves: the history of galaxies and black holes, the physics of dense matter and stellar remnants like stellar black holes, as well as general relativity and the behaviour of space and time itself. Chinese mission study options (“ALIA” from now onwards, see Bender et al., 2005; Crowder and Cornish, 2005; Gong et al., 2011) will also be able to catch these systems with good signal-to-noise ratios, although the mass-ratio for the capture of COs by MBHs will not be as extreme.

¹<http://elisa-ngo.org/>

ALIA focuses rather on intermediate-mass ratio inspirals.

In any case, a key property of GW astrophysics is the fact that GWs interact only very weakly with matter. The observations we will make with LISA will not suffer any of the usual problems in astrophysics absorption, scattering, or obscuration. This is what makes LISA-like missions such as eLISA/NGO or ALIA unique. It is not “merely” a test of general relativity; these missions would be able to corroborate with underlying theory the nature of the central dark objects which we observe now in most galaxies. In this regard, a LISA-like mission would be the most powerful “telescope” ever in the history of astronomy. We will get direct information from the heart of the densest stellar systems in the Universe: galactic nuclei, nuclear stellar clusters and globular clusters. The LISA mission technology will be tested with the LISA Pathfinder² mission, a 100% European effort (from the European Space Agency), scheduled for launch in 2014 from Kourou, French Guiana. The Pathfinder will contain one shortened arm of the full-LISA interferometer. The main goal of the mission is to check that the technology required by a LISA-like mission is feasible. Moreover, LISA Pathfinder will be the first in-flight test of gravitational wave detection metrology.

For the full success of a mission such as LISA, it is important that we *understand* the systems that we expect to observe. A deep theoretical comprehension of the sources which will populate LISA’s field of view is important to achieve its main goals.

Whilst main-sequence stars are tidally disrupted when approaching the central MBH, compact objects (stellar black holes, neutron stars,

and white dwarfs) slowly spiral into the MBH and are swallowed whole after some $\sim 10^5$ orbits in the LISA band. At the closest approach to the MBH, the system emits a burst of GWs which contains information about spacetime and the masses and spins of the system. We can envisage each such burst as a snapshot of the system. This is what makes EMRIs so appealing: a set of $\sim 10^5$ bursts of GWs radiated by *one* system will tell us with the utmost accuracy about the system itself, it will test general relativity, it will tell us about the distribution of dark objects in galactic nuclei and globular clusters and, thus, we will have a new understanding of the physics of the process. New phenomena, unknown and unanticipated, are likely to be discovered.

If the central MBH has a mass larger than $10^7 M_\odot$, then the signal of an inspiraling stellar black hole, even in its last stable orbit (LSO) will have a frequency too low for detection. On the other hand, if it is less massive than $10^4 M_\odot$, the signal will also be quite weak unless the source is very close. This is why one usually assumes that the mass range of MBHs of interest in the search of EMRIs for LISA is between $[10^7, 10^4] M_\odot$. Nonetheless, if the MBH is rotating rapidly, then even if it has a mass larger than $10^7 M_\odot$, the LSO will be closer to the MBH and thus, even at a higher frequency, the system should be detectable. This would push the total mass to a few $\sim 10^7 M_\odot$.

For a binary of a MBH and a stellar black hole to be in the LISA band, it has to have a frequency of between roughly 1 and 10^{-5} Hz. The emission of GWs is more efficient as they approach the LSO, so that LISA will detect the sources when they are close to the LSO line. The total mass required to observe systems with

²<http://sci.esa.int/lisapf>

frequencies between 0.1 Hz and 10^{-4} is of $10^4 - 10^7 M_\odot$. For masses larger than $10^7 M_\odot$ the frequencies close to the LSO will be too low, so that their detection will be very difficult. On the other hand, for a total mass of less than $10^3 M_\odot$ we could in principal detect them at an early stage, but then the amplitude of the GW would be rather low.

On the top of this, the measurement of the emitted GWs will give us very detailed information about the spin of the central MBH. With current techniques, we can only hope to measure MBH spin through X-ray observations of Fe K α profiles, but the numerous uncertainties of this technique may disguise the real value. Moreover, such observations can only rarely be made.

This means that LISA will scrutinize exactly the range of masses fundamental to the understanding of the origin and growth of super-massive black holes. By extracting the information encoded in the GWs of this scenario, we can determine the mass of the central MBH with a ridiculous relative precision of $\sim 10^{-4}$. Additionally, the mass of the compact object which falls into the MBH and the eccentricity of the orbit will be recovered from the gravitational radiation with a fractional accuracy of also $\sim 10^{-4}$. All this means that LISA will not be “just” the ultimate test of general relativity, but an exquisite probe of the spins and range of masses of interest for theoretical and observational astrophysics and cosmology.

2.4 A problem of ~ 10 orders of magnitude

For the particular problem of how does a compact object end up being an extreme-mass ratio

inspiral, we have to study very different astrophysical regimes, spanning over many orders of magnitude.

2.4.1 Galactic or Cosmological dynamics

In figure 2.1 we depict the three different realms of stellar dynamics of relevance for the problem of EMRIs. At the largest scale you have the galaxy, with a size of a few kiloparsecs. Just as a point of reference, the gravitational radius of a MBH of $10^6 M_\odot \sim 5 \cdot 10^{-8}$ pc. The relaxation time, t_{rlx} which we will introduce with more detail ahead, is a timescale which can be envisaged as the required time for the stars to exchange energy E and angular momentum J among them, it is the time which the stars need to “see” each other individually and not only the average, background stellar potential of the whole stellar system. For the galaxy t_{rlx} is larger than the Hubble time, which means that, on average, it has not influence on the galaxy at all. A test star will only feel the mean potential of the rest of the stars and it will never exchange either E or J with any other star. The system is “collisionless”, in the meaning that two-body interactions can be neglected. This defines the realm of stellar galactic dynamics, the one investigated in Cosmological simulations using e.g. N -body integrators. Since we do not have to take into account the strong interactions between stars, one can easily simulate ten billion particles with these integrators.

2.4.2 Cluster dynamics

If we zoom in by typically a factor of 10^3 , we enter the (mostly Newtonian) stellar dynamics of galactic nuclei. There, $t_{\text{rlx}} \sim 10^8 - 10^{10}$ yrs.

In this realm stars do feel the graininess of the stellar potential. The closer we get to the central MBH, the higher σ will be, if the system is in centrifugal equilibrium; the stars have to orbit around the MBH faster. In particular, S2 (or S02), one of the S-stars (S0-stars) for which we have enough data to reconstruct the orbit to a very high level of confidence -as we saw in the previous chapter- has been observed to move with a velocity of $15 \cdot 10^3 \text{ km s}^{-1}$. Typically, t_{rlx} is (in occasions *much*) shorter than the age of the system, of a few $\sim 10^8 - 10^{10}$ yrs. For these kind of systems one has to take into account relaxation, exchange of E and J between stars. The system is “collisional”. When we have to take into account this in the numerical simulations, the result is that we cannot simulate with N -body integrators more than some thousands of stars on a computer. To get to more realistic particle numbers one has to resort to beowulf supercomputers, special-purpose hardware or the graphic processor units. We will discuss about this ahead.

2.4.3 Relativistic stellar dynamics

Last, in the right panel, we have the relativistic regime of stellar dynamics when we enlarge the previous by a factor of ten millions. There the role of relativistic effects is of paramount importance for the evolution of the system. In this zone, generally, *there are no stars*. Even at the densities which characterise a galactic nucleus, the probability of having a star in such a tiny volume is extremely small. What’s more, even if we had a significantly larger volume, or a much higher density for the galactic nucleus, so that we had a few stars close to the MBH, these would be quickly merger with the MBH due to the emission of GWs, which is what de-

fines an EMRI. But they do it in a *too* fast way. These systems can be collisional or collisionless, depending on how many stars we have at a given time. If they are there, they will exchange E and J with eachother. Nevertheless, relaxation is not well-defined in this regime.

The key point here is how to replenish that area, so that there are other stars replacing those which merge quickly with the central MBH. On average, there are *zero* stars. As a matter of fact, and in general, for the general study of the stellar dynamics of galactic nuclei, the role of this last realm is negligible. One does not have to bother for the effects of GR; most, if not all, stars are on a Newtonian regime. The impact on the dynamics of galactic nuclei is zero. It is as a matter of fact somehow impressive that this last region dominated by the effects of GR has an effect whatsoever worth studying it. But, as we will see ahead, the encoded information that one can recover out of the detection of an EMRI about its surrounding dynamical system is dramatic. If we want to address this problem, we are, therefore, “forced” to cope with a problem of some seven orders of magnitude in particular, when understanding the role of the dynamics of galactic nuclei in relativistic dynamics and of ten orders of magnitude in the big picture.

2.5 Actual data

In figure 2.2 we show data constrained by actual measurements. One of the very first questions one has to address when trying to understand the stellar dynamics around a MBH is *how many stars are there and how do they distribute around it*. Unfortunately there are very few observations for this because we are

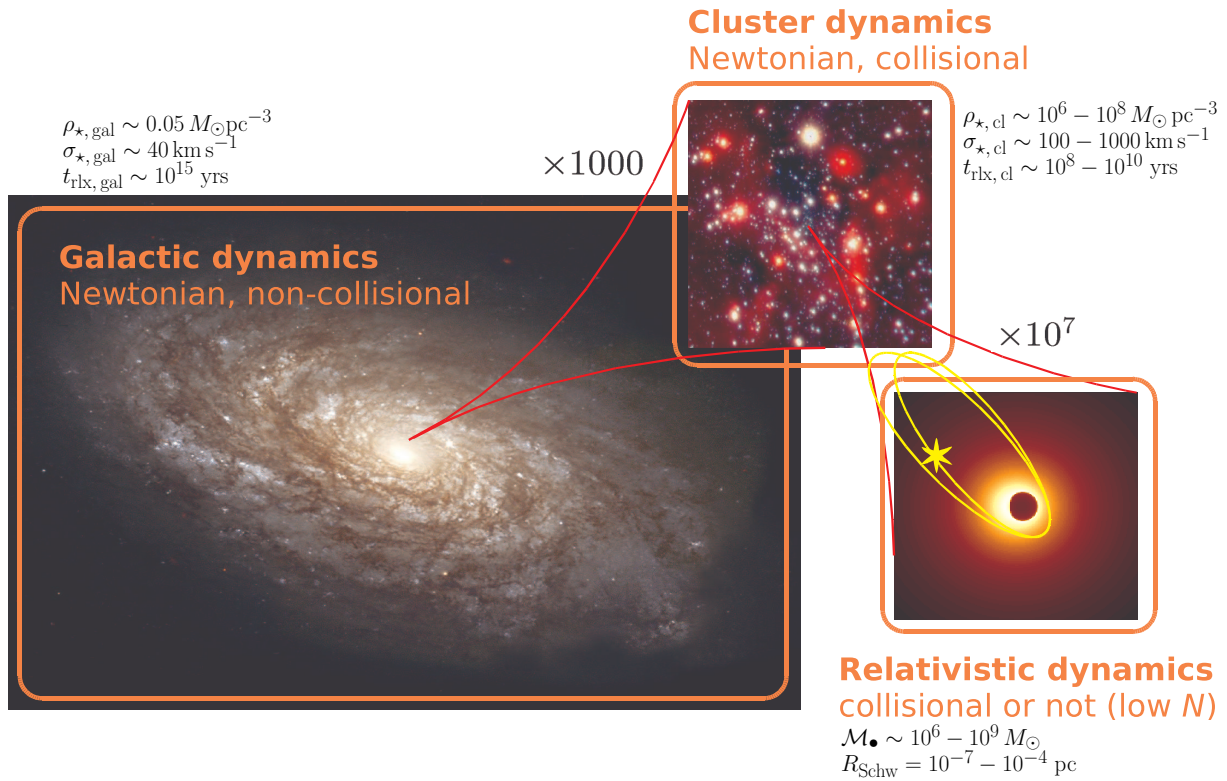


Figure 2.1: On the left and with the largest scale the galaxy has an average density of stars of about $0.05 M_{\odot} \text{pc}^{-3}$. The velocity dispersion is $\sim 40 \text{ km s}^{-1}$. From these quantities one can infer that the relaxation time in the vicinity of our Sun is $t_{\text{rlx}} \sim 10^{15} \text{ yrs}$. The upper panel shows the galactic nucleus that such a galaxy has. A typical size for it is $\sim 1 \text{ pc}$, the stellar density ranges between $10^6 - 10^8 M_{\odot} \text{pc}^{-3}$ and the velocity dispersion is of $\sigma \sim 100 - 1000 \text{ km s}^{-1}$. In this region, $t_{\text{rlx}} \sim 10^8 - 10^{10} \text{ yrs}$. In the last panel, we have that the dynamics of the system is dominated by General Relativity. The mass of the central object, an MBH, ranges between 10^6 and $10^9 M_{\odot}$ and its size is given by the Schwarzschild radius, $R_{\text{Schw}} = 10^{-7} - 10^{-4} \text{ pc}$

interested in nuclei that harbour lower-mass MBHs, so that they have a small radius of influence r_{inf} and, thus, they are observationally very difficult to resolve. Currently there are only a very few galaxies that are both in the range of GW frequencies interesting for us and that have a resolved r_{inf} . For these we have information of how bound stars are distributed around the central MBH that can become EMRIs. Obviously the Milky Way (MW) is one of these galaxies. In the figure the stellar density profile of the MW is displayed. We see that it goes up to at least $10^8 M_{\odot}/\text{pc}^3$ in the inner regions. This number has been calculated by assuming a population of stars; one has to deproject the observation, because we are only seeing a few of the total amount of stars, the brightest ones. One assumes that the observed stars are tracing an underlying population invisible for us. This requires a considerable amount of modelling to obtain the final results. These are uncertain by, maximum, a factor of ten. In the same figure we have another nucleus, M32, which should be harbouring an MBH with a mass similar to the one located in the GC. The density profile happens to be similar to the one corresponding to the GC. Whether this is a coincidence or something deeper is not clear. In any case, and to *first order of approximation*, we can state that once we know the mass of the MBH, we know the way stars distribute around it. Later it will be obvious to the lector what is the relevance of this point.

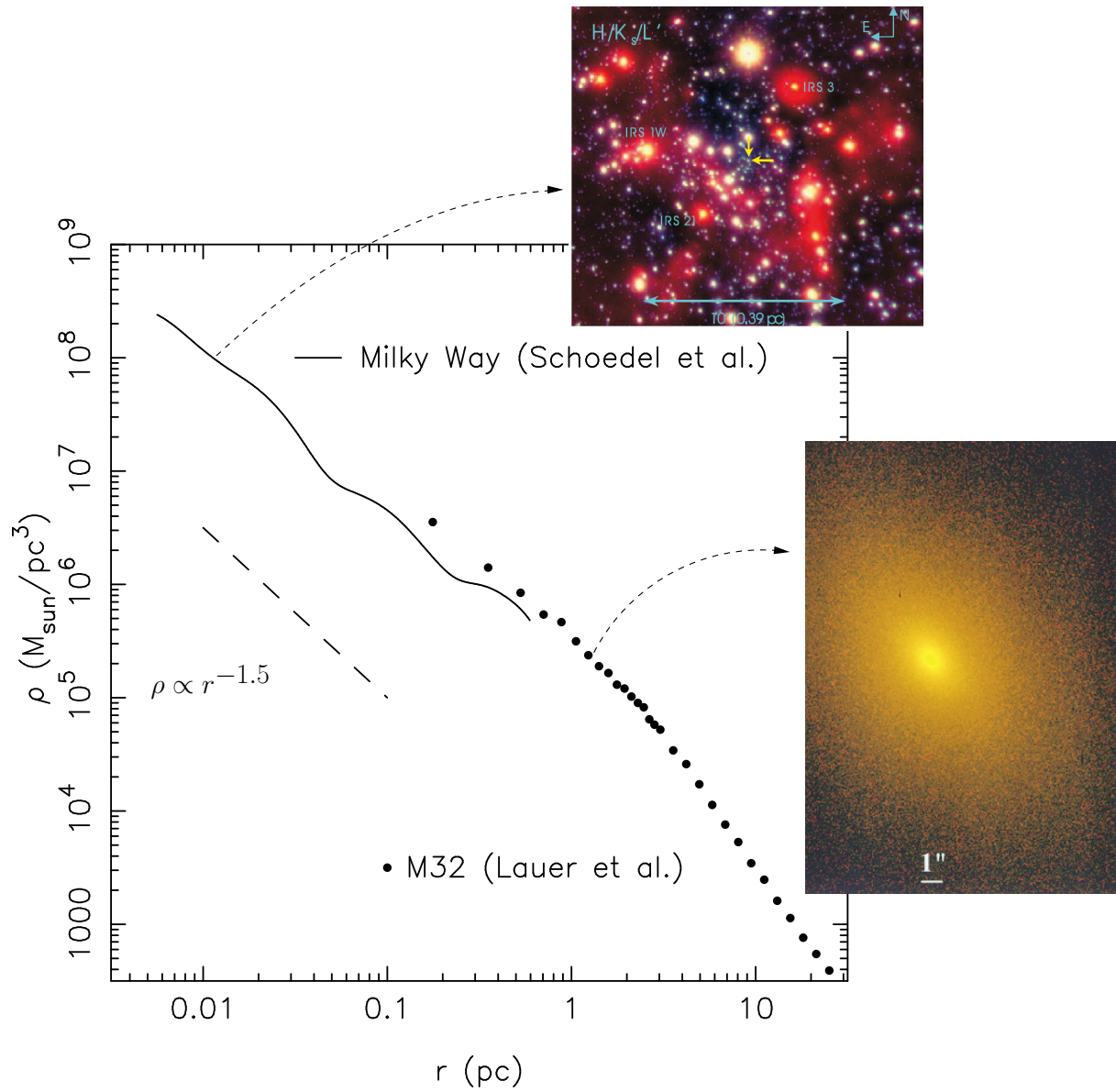


Figure 2.2: Density profile for the GC of the MW and for M32, both with MBHs of masses $3 \times 10^6 M_{\odot}$ and influence radii ~ 3 pc. The dashed curve on the very left corresponds to a slope of $\rho \propto r^{-3/2}$ (adapted from Merritt, 2006; Schödel et al., 2002; Lauer et al., 1998)

Chapter 3

A taxonomy of orbits in galactic nuclei

Before we address the physics and event rate estimates of EMRIs, it is crucial that we have a good comprehension of the kind of orbits that we might expect in the environments natural to COs. An important factor in understanding how a star can become an EMRI is the shape and evolution of its orbit. In this chapter we will address these two aspects. We will firstly *not* take into account the role of relaxation. The stellar potential in which our test star m_\bullet is moving is completely smooth. The star exchanges E and J with the rest of stars on a timescale which is so long that we can neglect it. For any purposes, the test star will not feel any individual star, but a background potential.

3.1 Spherical potentials

Consider now figure3.1; there we have two orbits which differ in their eccentricity. The rosettes are characterised by its E and J . Since the test stars do not suffer any individual gravitational tug from the stellar system (at least not on a noticeable timescale), the orbital elements are

kept. The periapsis¹ is fixed because J is conserved, so that the test star will never come arbitrarily close to the central MBH. In order to get anything interesting, one needs a perturbation of the system.

A different situation, however, is when the orbit of the test star is *within* the R_{infl} of the MBH. In this case the orbits look more and more like Keplerian ellipses, unless one gets *very* close to the central MBH, so that we get relativistic precession. In figure3.2 we have an ellipse which precesses. This is neither the relativistic precession nor an advance, but a pure Newtonian perihelion (periapsis) retard, counterclockwise. The timescale for it is

$$\begin{aligned} T_{\text{New, PS}} &\approx \frac{\mathcal{M}_\bullet}{M_\star(a)} P_{\text{orb}} \\ &\approx \frac{R_{\text{infl}}}{a} P_{\text{orb}} \end{aligned} \quad (3.1)$$

In this last equation, $M_\star(a)$ is the amount of stellar mass encompassed within the orbit. The

¹In the related literature there exist other terms to refer to the distance of maximum or minimum approach to a black hole; namely *peribarthron* and *apobarthron*, respectively. There seems to be a confusion and wrong use of the later. We discuss this in the last chapter of this review.

Newtonian periapsis retard is the result of the fact that we do not have a perfect Keplerian orbit because we do not have a point mass, but an *extended* mass distribution. As an exercise, we can compare last equation to the relativistic periapsis *advance* (in order of magnitude),

$$T_{\text{Rel, PS}} \approx \frac{R_{\text{peri}}}{R_{\text{Schw}}} P_{\text{orb}} \quad (3.2)$$

This equation is only relevant for orbits whose periapsis is very small, whilst the later one is only important for relatively extended orbits (because $M_{\star}(a)$ is larger)

3.2 Non-spherical potentials

The most general case is the triaxial potential, in which we still have symmetry but neither spherical nor axial-symmetric, it is a general ellipsoidal configuration. The J has no component conserved. This, obviously, allows orbits to in principle get “as close as they want” to the centre. Not *all* orbits will, but there are specific families of orbits which, if one waits long enough, will get arbitrarily close to the centre. This is evidently very relevant for our study. These orbits are referred to as *centrophilic* orbits for clear reasons. Models of triaxial galaxies have found that there is a significant fraction of such orbits even very close to the central MBH. At distances as short as $r < R_{\text{infl}}$, within the sphere of influence, some models have as many as 20% of stars that are on centrophilic orbits. One should nevertheless bear in mind that these are *models*, not corroborated by direct observations of galaxies. They depend on a number of set-up parameters which will result on strong fluctuations of the final result: the true number could be according to these

models between 0 – 20%. Therefore we unfortunately do not know what the real implications of significance of the modeling is for observed nuclei, since it is not well-constrained. Of course, one can resort to (non-collisional) N -body simulations to study the merger of two galaxies to see in the resulting product how many of these orbits one can get.

As for the implications in the detection rates of EMRIs, this could have a huge impact in the event rate but the problem should probably be revisited due to the enormous difficulties that forces us to make broad simplifications. For instance, we should explore the behaviour of the potential *very* close to the MBH because, by definition, at some point the potential is completely dominated by the MBH and, thus, spherically symmetric. The only realistic hope here are those stars that typically are on orbits with semi-major axis much larger than the radii of interests for us, so that even if they spend most of the time very far away from the MBH, they are set on a centrophilic orbit due to the triaxiality of the system, but it is unclear whether these can contribute significantly to the local density around the MBH. As an example of the kind of orbits one can get in a triaxial galactic nucleus, in figure 3.5 we give some representative examples of *centrophobic* orbits from Poon and Merritt (2001) (cases b, c, d, e), and see also the more recent work of Merritt and Vasiliev (2011). This means that the stars do never reach the centre. The non conservation of J can set stars on either centrophilic orbits or, also, on centrophobic orbits. These can be envisaged as a generalisation of rosette orbits. Nevertheless, since we are interested in EMRIs, we will focus on centrophilic orbits and leave the further description of centrophobic orbits

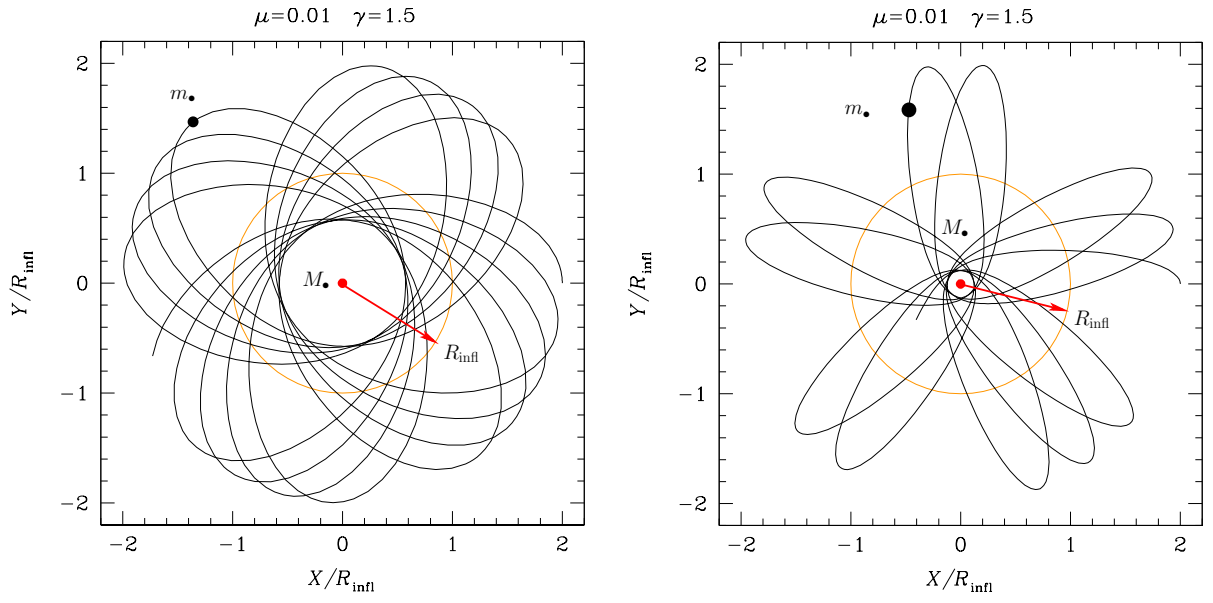


Figure 3.1: Projection in the X–Y plane of the evolution of two test star orbits in a stellar system without relaxation. The central, orange point represents the position of the MBH, the black dots on the orbits the position of the test stars and the red arrow delimits the influence radius R_{infl} of the MBH. The right panel represents a case with a larger eccentricity. The orbits extend further than the R_{infl}

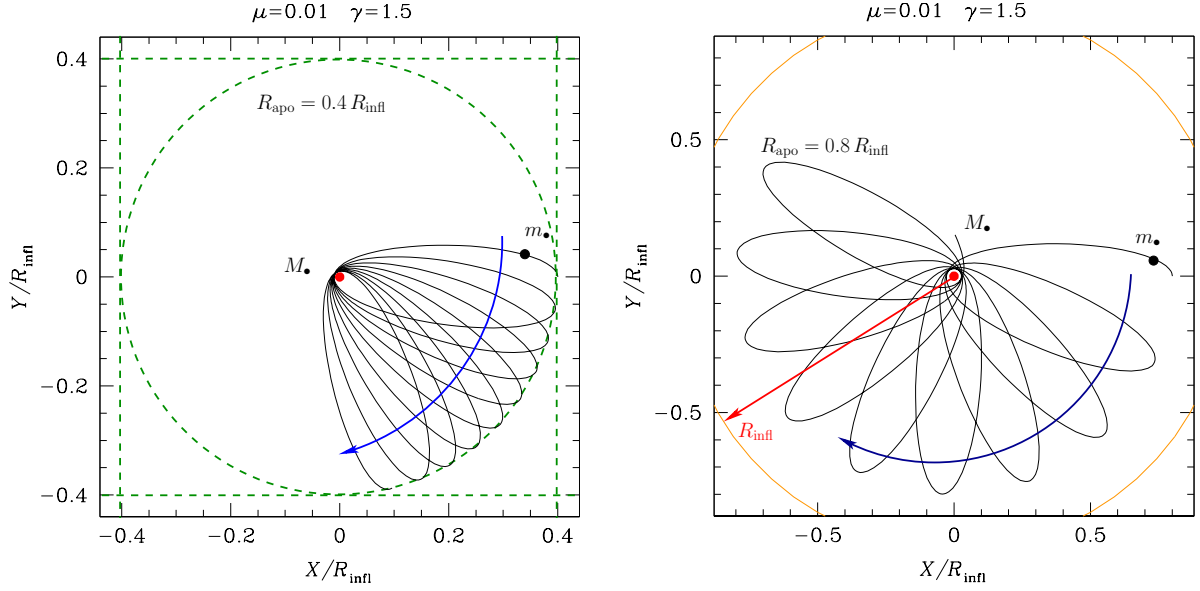


Figure 3.2: Same as figure 3.1 for an apoapsis $R_{\text{apo}} = 0.4, 0.8 R_{\text{infl}}$ and a velocity of the CO of $0.2 V_{\text{circ}}$, with V_{circ} the circular velocity.

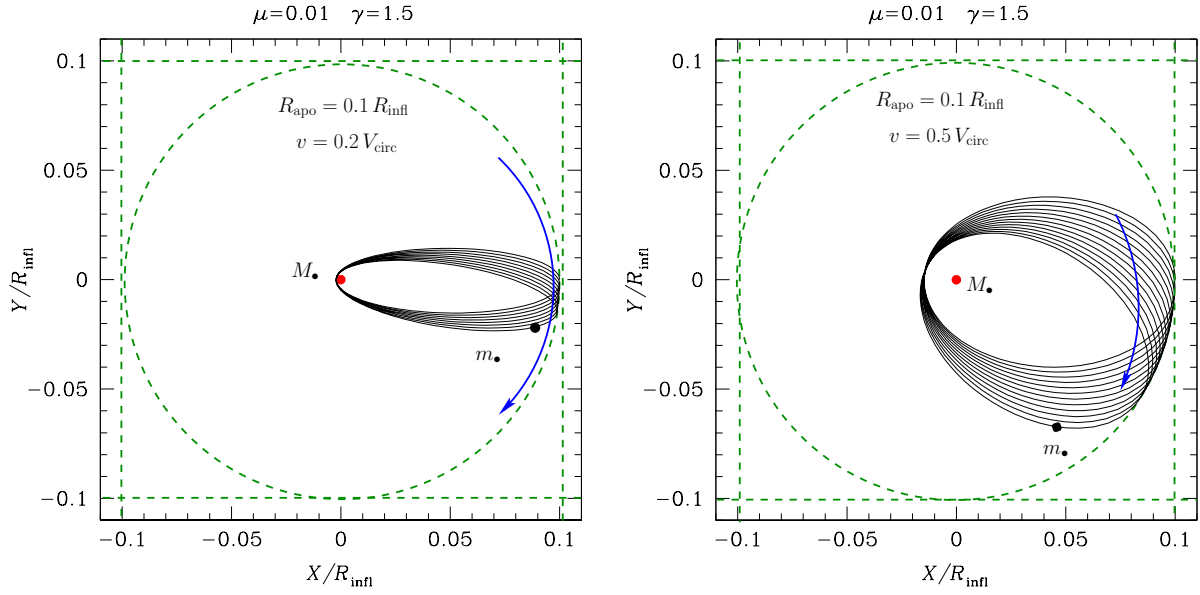


Figure 3.3: Same as figures 3.1 and 3.2 for different values of the apoapsis radius and velocity of the CO.

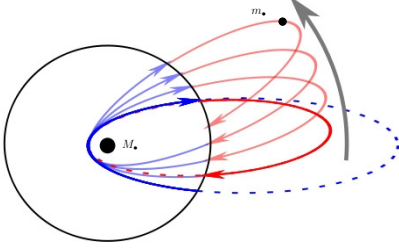


Figure 3.4: In the Newtonian case we have an extended mass distribution, so tha the star feels more mass far away than closer to the centre. When the star traverses the “sphere”, the trajectory abruptly changes and becomes a smaller ellipse. Thus, the object goes back to the centre faster; the orbit precesses in the opposite direction to the orbital one. In the relativistic case the kinetic energy of the star increases its gravitational mass when it's close to the centre: The effective attraction is more efficient and the trajectory is more curved towards the centre.

aside.

We have two different kinds of centrophilic orbits: (i) pyramid or box orbits. These are still regular but a star on such an orbit can reach arbitrarily small distances in its periapsis; (ii) stochastic orbits, which also come arbitrarily close to the centre. The probability for an orbit to get within a distance d from the central MBH, the very centre of your potential, is proportional to d ;

$$N_{\text{pass}}(R_p < d) \propto d \quad (3.3)$$

This is non-intuitive. If you have a target with a mass which you shoot with a projectile at random directions, the probability of coming to a distance d of the target is proportional to d itself and not d^2 (which would have been the case of a total random experiment, without focusing). The reason for this is that our target

is a particular one and influences the projectile through a process called gravitational focusing. The projectile is attracted by the target.

Some to also bear in mind is that all of these simulations are limited by a particular resolution, which is still far from being close to reality, so that we are not in the position of extrapolating these results to the distance where the star will be captured by the MBH and become and EMRI.

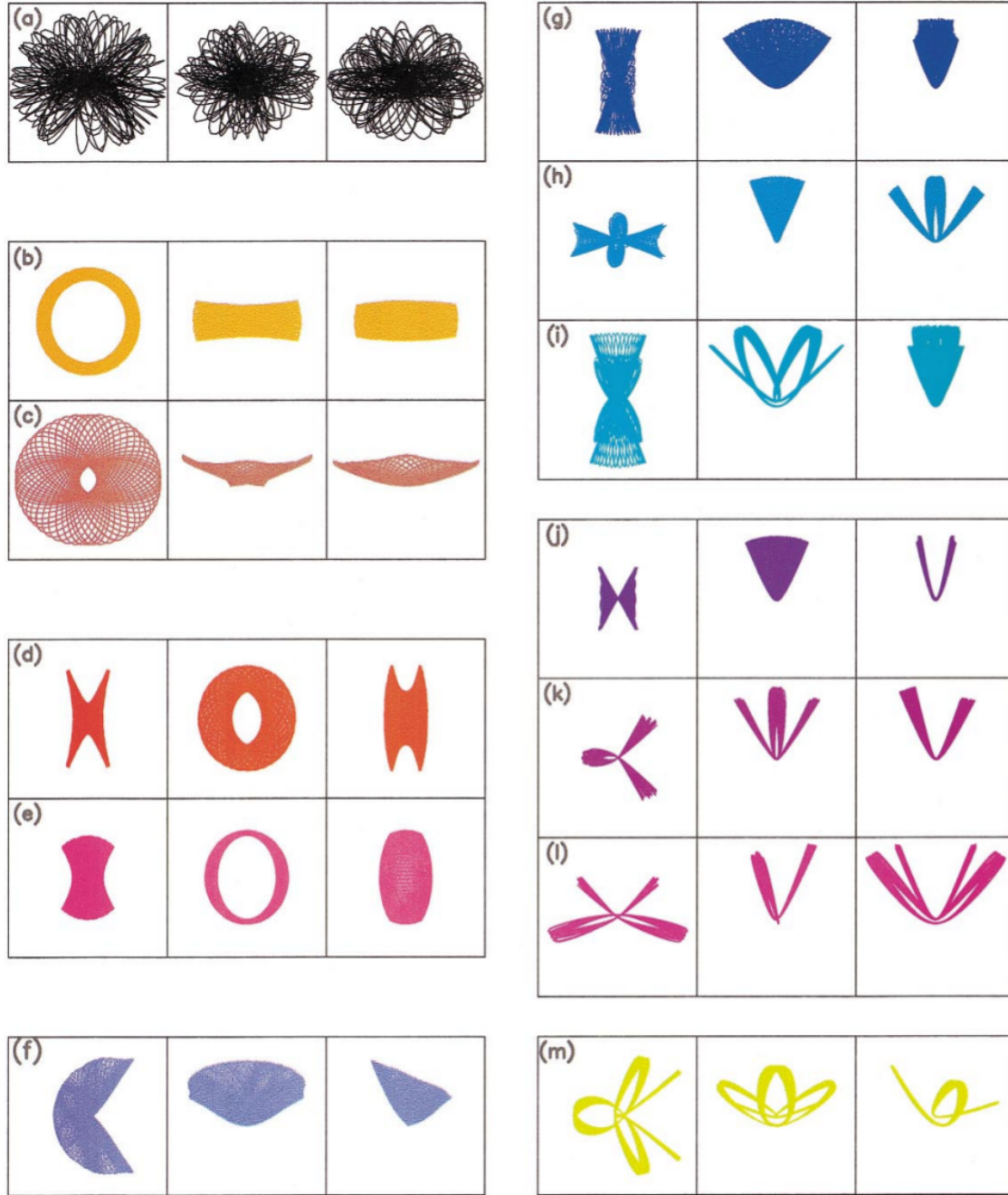


Figure 3.5: From the left to the right and from the top to the bottom, we have stochastic orbits, short-axis tube orbit, saucer orbit, a resonant short-axis tube, inner long-axis tube, long-axis tube, resonant, pyramid, resonant pyramid, resonant pyramid orbit, banana orbit, 2 : 3 : 4 resonant banana, 3 : 4 : 6 resonant banana, and a 6 : 7 : 8 resonant orbit. This figure is figure 1 of Poon and Merritt (2001). We note that the projections of “tube”, centrophilic stellar orbits around a MBH in triaxial nuclei will look aligned in one or another plane depending on the potential.

Chapter 4

Two-body relaxation in galactic nuclei

4.1 Introduction

We are now back to a spherical system world, in which orbits such as in the previous § do not exist. Therefore, as discussed, one needs an additional factor to bring stars close to the MBH. A possibility, as we mentioned earlier, is to have a source of exchange of E and J . We use and abuse the term collisional by any effect not present in a smooth, static potential including what is known in planetary dynamics as secular effects. Among these, standard two-body relaxation excels not due to its relevance of contributing to EMRI sources, but due to the fact that this is the best-studied effect; namely the exchange of E and J between stars due to gravitational interactions.

Another possibility are physical collisions¹. The stars come so close to each other that they collide, they have a hydrodynamic interaction; the outcome depends on a number of factors, but the stars involved in the collision

¹The terminology is somehow and as forewarned misleading; whilst in general we refer to “collisional” to any effect leading to exchange of E and J among stars, here we mean real collisions between two stars. For a nice introduction on the subject and a detailed numerical study, we refer the reader to Freitag and Benz (2002)

could either merge with each other, destroy each other completely or partially. Surprisingly, the impact of these processes for the global evolution of the dynamics of galactic nuclei is negligible (Freitag and Benz, 2002). In most of the cases when these extended stars, such as main-sequence stars (MS) collide, they do not merge due to the very high velocity dispersion, and they will also not be totally destroyed, because for that they would need a nearly head-on collision, so that they have a partial mass-loss and are for our purposes uninteresting. For the kind of objects of our interest in this review, stellar black holes, the probability for them to physically collide or to have a non-Newtonian interaction is negligible.

A third way of altering the J of stars are secular effects. They do nevertheless *not* modify the E . If we assume that the orbits around the MBH are nearly Keplerian, the shape, an ellipse, does not change and the orientation will not change much. If we have another orbit with a different orientation, both orbits will exert a torque among each other. This will change J but not E . A Keplerian orbit can be described with its semi-major axis a and eccentricity e . The a is only connected to E and, for a given a the e is connected to the J . If one changes the

J but not the E , the e will vary but not the a . By decreasing the J , one increases the e .

In this chapter, however, we introduce the fundamentals of relaxation theory, focusing on the aspects that will be more relevant for the main interest of this review. More ahead, in chapter 7, we will address resonant relaxation and other “exotic” (in the sense that they are not part of the traditional two-body relaxation theory) processes. For a comprehensive discussion on two-body relaxation, we recommend the text books Spitzer (1969) and Binney and Tremaine (2008) or, for a shorter but very nice introduction, the article Freitag and Benz (2001).

We will first introduce handy timescales in § 4.2 that will allow us to pinpoint the relevant physical phenomena that reign the process of bringing stars (extended or compact) close to the central MBH. We will then address a particular case of relaxation, in § 4.3, dynamical friction. Later, in § 4.4, we will define more concisely the region of space-phase in which we expect stars to interact with the central MBH. Once we have all of these concepts, we can cope with the problem of how mass segregates in galactic nuclei, in § 5. We will first see in detail the “classical” solution to introduce later a more recent and very important result, the so-called strong mass segregation, in § 7.3

4.2 Two-body relaxation

We introduce in this subsection some useful time-scales to which we will refer often throughout this review; namely the relaxation time, the crossing time and the dynamical time. These three time-scales allow us to delimit our physical system.

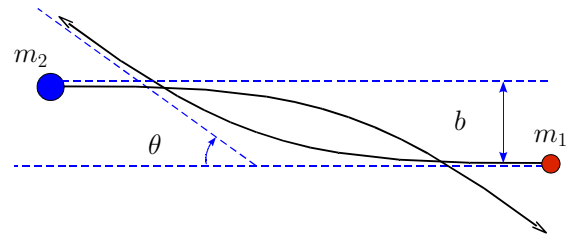


Figure 4.1: Deflection angle θ of a “test” star of mass m_1 with a field star of mass m_2

4.2.1 The relaxation time

Chandrasekhar (1942) defined a time-scale which stems from the 2-body small-angle encounters and gives us a typical time for the evolution of a stellar system.

This relaxation time could be regarded as an analogy of the shock time of the gas dynamics theory, by telling us when a particle (a star) has forgotten its initial conditions or, expressed in another way, when the local thermodynamical equilibrium has been reached. Then we can roughly say that the most general idea is that this is the time over which the star “forgets” its initial orbit due to the series of gravitational tugs caused by the passing-by stars. After a relaxation time the system has lost all information about the initial orbits of all the stars. This means that the encounters alter the star orbit from that one it would have followed if the distribution of matter were smooth. Therefore we can regard the relaxation time as the time interval required for the velocity distribution to reach the Maxwell-Boltzmann form.

Consider two stars of masses m_1 and m_2 deflecting each other such as in figure 4.1. The deflection angle θ is given by the relation

$$\tan \frac{\theta}{2} = \frac{b}{b_0}, \text{ with } b_0 = \frac{G(m_1 + m_2)}{v_{\text{rel}}^2} \quad (4.1)$$

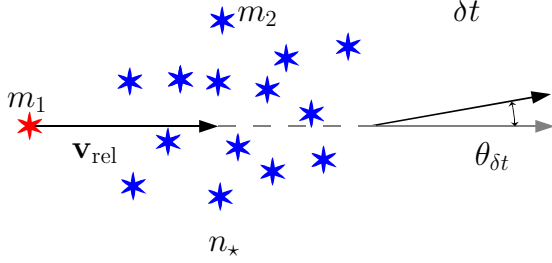


Figure 4.2: Deflection2

If the relative velocity v_{rel} is high, θ is small and the largest the mass, the stronger the deflection. This simple relation expresses the kernel of relaxation. One has to integrate it over all possible parameters to get the relaxation rate. When we do the integration over the impact parameter b whilst keeping v_{rel} and the masses fix, we have the following picture of figure 4.2. The test star encounters a lot of field stars, all of them with the same mass m_2 and relative velocity \mathbf{v}_{rel} . After a time δt , the velocity vector of the test star has slightly changed direction by an angle $\theta_{\delta t}$. On average, $\langle \theta_{\delta t} \rangle = 0$ but

$$\langle \theta_{\delta t}^2 \rangle = \left(\frac{\pi}{2} \right)^2 \frac{\delta t}{\hat{t}_{\text{rlx}}} \quad (4.2)$$

Therefore it is a *diffusion* process; $\langle \theta_{\delta t}^2 \rangle \propto \delta t$. We have introduced the special relaxation time for this situation as

$$\hat{t}_{\text{rlx}} = \frac{\pi}{32 \ln \Lambda G^2 n_* (m_1 + m_2)^2} v_{\text{rel}}^3 \quad (4.3)$$

In this last equation, $\ln \Lambda$, the Coulomb logarithm, has appeared as a result of integrating for all impact parameters. The information encoded in it is how many orders of magnitude of b contribute to the relaxation,

$$\ln \Lambda = \ln \frac{b_{\text{max}}}{b_0} \simeq \ln \frac{P_{\text{orb}}}{b_0/v_{\text{rel}}} \quad (4.4)$$

In this last equation b_0 , which we introduced before, is the effective minimum impact parameter for relaxation. Our main focus is not a detailed review of stellar dynamics. For a detailed description of the Coulomb logarithm, we refer the reader to Binney and Tremaine (2008); Spitzer (1987). Therefore, we will simply comment that, for our purposes, $\ln \Lambda \approx 10 - 15$ always. This is very useful because the exact calculation can be rather arduous and almost an incubus which to our knowledge nobody has attempted to implement in any calculation. Therefore we mention only two special cases for the argument of the logarithm,

$$\ln \Lambda \approx \begin{cases} 0.01 N_* & \text{(a) for self-gravitating stellar cluster} \\ \mathcal{M}_\bullet / m & \text{(b) close to the MBH} \end{cases} \quad (4.5)$$

In case (a) we have a self-gravitating cluster of stars in equilibrium with itself but lacking a central MBH. The argument is proportional to the number of stars in the system. In the situation in which a star is orbiting the MBH, the previous value is formally no valid anymore and one should use the value (b). Nevertheless, in effect this is neglected because the value turns out to be ~ 10 .

We can define a local average value of the relaxation time by integrating over the distribution of relative velocities,

$$\begin{aligned}
 t_{\text{rlx}} &= \frac{0.34}{\ln \Lambda} \frac{\sigma_v^3}{G^2 \langle m \rangle^2 n_\star} \\
 &\simeq 2 \cdot 10^9 \text{ yr} \left(\frac{10^6 \text{ pc}^{-3}}{n_\star} \right) \left(\frac{\sigma_v}{100 \text{ km s}^{-1}} \right)^3 \\
 &\quad \left(\frac{M_\odot}{\langle m \rangle} \right)^2 \quad (4.6)
 \end{aligned}$$

The structure of this equation is basically the same as the previous one, Eq.(4.3). Now we have a velocity dispersion in the numerator and an average mass. If σ_v is large, t_{rlx} will be long, because the deflections are small. Therefore, the closer you get to the MBH, the longer t_{rlx} will be. But on the other hand, t_{rlx} is inversely proportional to the numerical density of stars, n_\star . This generally defeats the former in a galactic nucleus. The density grows faster than σ_v^3 . Thus, t_{rlx} becomes shorter when we approach the MBH. In Eq.(4.6) we have used typical values for a galactic nucleus, so that relaxation should play a role, because $t_{\text{rlx}} \ll 10^{10}$ yrs.

For a typical star in the system, with a mass $m \lesssim \langle m \rangle$, Eq.(4.6) timescale is the time over which the orbital parameters will *completely* change.

4.2.2 Collision time

t_{coll} is defined as the mean time which has passed when the number of stars within a volume $V = \Sigma v_{\text{rel}} \Delta t$ is one (see figure 4.3), where v_{rel} is the relative velocity at infinity of two colliding stars. Computed for an average distance of closest approach $\bar{r}_{\text{min}} = \frac{2}{3} r_\star$, this time is

$$n_\star V(t_{\text{coll}}) = 1 = n_\star \Sigma v_{\text{rel}} t_{\text{coll}}. \quad (4.7)$$

And so,

$$t_{\text{coll}} = \frac{m_\star}{\rho_\star \Sigma \sigma_{\text{rel}}}, \quad (4.8)$$

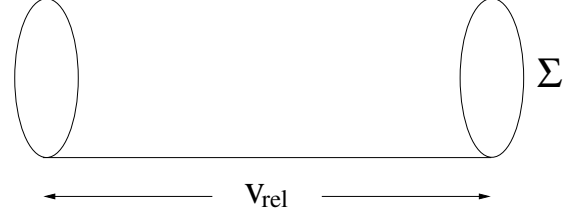


Figure 4.3: Definition of the collision time

with

$$\Sigma = \pi \bar{r}_{\text{min}}^2 \left(1 + \frac{2Gm_\star}{\bar{r}_{\text{min}} \sigma_{\text{rel}}^2} \right); \quad (4.9)$$

$\sigma_{\text{rel}}^2 = 2\sigma_\star^2$ is the stellar velocity dispersion and Σ a collisional cross section with gravitational focusing

4.2.3 The crossing time

As the name suggests, this is the required time for a star to pass through the system, to cross it. Obviously, its value is given by the ratio between space and velocity,

$$t_{\text{cross}} = \frac{R}{v}, \quad (4.10)$$

where R is the radius of the physical system and v the velocity of the star crossing it.

For instance, in a star cluster it would be:

$$t_{\text{cross}} = \frac{r_h}{\sigma_h}; \quad (4.11)$$

where r_h is the radius containing 50 % of the total mass and σ_h is a typical velocity taken at r_h . One denominates it *velocity dispersion* and is introduced by the statistical concept of root mean square (RMS) dispersion; the *variance* σ^2 gives us a measure for the dispersion, or scatter, of the measurements within the statistical

population, which in our case is the star sample,

$$\sigma^2 = \frac{1}{N} \sum_{i=1}^N (x_i - \mu_a)^2.$$

Where x_i are the individual stellar velocities and μ_a is the arithmetic mean,

$$\mu_a \equiv \frac{1}{N} \sum_{i=1}^N x_i.$$

If Virial equilibrium prevails, we have $\sigma_h \approx \sqrt{GM_h/r_h}$, then we get the dynamical time-scale

$$t_{\text{dyn}} \approx \sqrt{\frac{r_h^3}{GM_h}} \approx \frac{1}{\sqrt{G\rho_\star}}, \quad (4.12)$$

where ρ_\star is the mean stellar density.

On the contrary to the gas dynamics, the thermodynamical equilibrium time-scale t_{rlx} in a stellar system is large compared with the crossing time t_{cross} . In a homogeneous, infinite stellar system, we expect in the limit $t \rightarrow \infty$ some kind of stationary state to be established. The decisive feature for such a Virial equilibrium is how quick a perturbation of the system will be smoothed down.

The dynamical time in Virial equilibrium is (cf e.g. Spitzer, 1987):

$$t_{\text{dyn}} \propto \frac{\log(\gamma N)}{N} t_{\text{rlx}} \ll t_{\text{rlx}}. \quad (4.13)$$

If we have perturbations in the system because of the heat conduction, star accretion on the BH, etc. a new Virial equilibrium will be established within a t_{dyn} , which is short. This means that we get again a Virial-type equilibrium in a short time. This situation can be considered not far from a Virial-type equilibrium. We say that the system changes in a quasi-stationary way.

4.3 Dynamical friction

Consider now a star more massive than the average. In this case, relaxation boils down to dynamical friction. The massive intruder will suffer from dynamical friction, which is an effect of all encounters with lighter stars. For this special kind of star, the timescale over which its orbital parameters change is not Eq.(4.6). This star will lose kinetic energy in the following timescale:

$$t_{\text{DF}} \sim \frac{\langle m \rangle}{m} t_{\text{rlx}} \quad (4.14)$$

As we can see, of the object is 10 – 20 times more massive than the average, as the case of a stellar black hole is, this timescale is 20 times shorter than the t_{rlx} .

In figure 4.4 we have an illustration for what DF is. A massive intruder, a stellar black hole, is travelling in a homogenous sea of stars of density ρ and velocity dispersion σ . The velocity vector of the stars are rotated after the deflection and the projected component in the direction of the deflection is shorter. Therefore, the massive object is cumulating just after it a high-density stellar region. The perturber will feel a drag from that region from the conservation of J in the direction of its velocity vector, just as depicted in figure 4.5. The direction does not change to first-order, but the amplitude decreases. The intruder will feel a force given by the Chandrasekhar formula,

$$\vec{a}_{\text{DF}} = -\frac{\vec{v}}{t_{\text{DF}}} - \frac{4\pi \ln \Lambda G^2 \rho M}{v^3} \xi(X) \vec{v} \quad (4.15)$$

In this last equation,

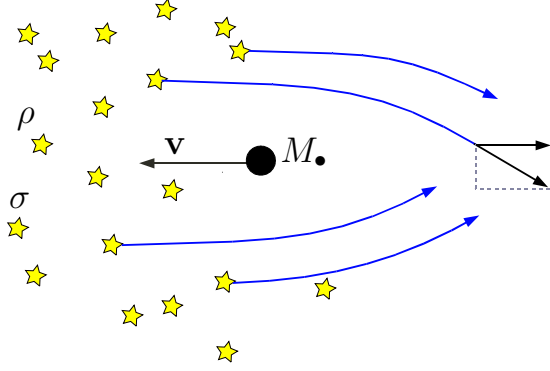


Figure 4.4: In the reference frame of the encounter we depict a massive interloper, a stellar black hole, traversing a sea of lighter stars which are deflected by it. The velocity vector of the stellar black hole is barely modified (at least in direction) by the deflections, because they cancel out on average

$$\xi(X) = \text{erf}(X) - 2\pi^{-1/2} X e^{-X^2} \quad (4.16)$$

$$X = \frac{v}{\sqrt{2}\sigma}$$

The most interesting point is that if we plug into Eq.4.16 the velocity of the perturber which is $v \approx \sigma$, we have that

$$t_{\text{DF}} \sim \frac{m}{M} t_{\text{rlx}} \ll t_{\text{rlx}} \quad (4.17)$$

As we have already mentioned before, galactic nuclei in the range of what a mission like LISA could observe have relaxation times that are shorter than a Hubble time. In figure 4.6, which is an adapted version of the figure to be found in the article of Freitag and Benz (2005), we have a schematic representation of what relaxation times in other observed galaxies could be. Each dot shows the mass of the central MBH or the upper limit to it (the arrows). From

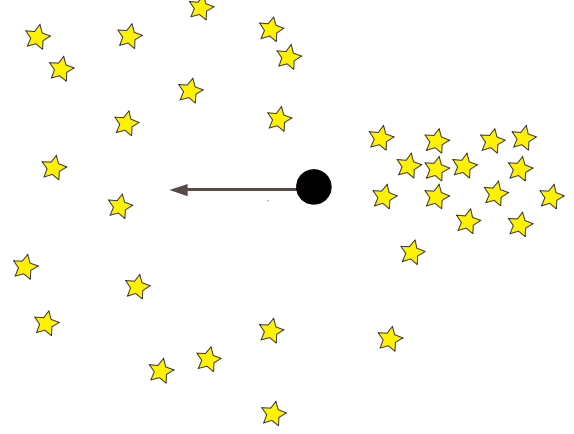


Figure 4.5: The agglomeration of stars right behind the massive perturber creates a region of stellar overdensity that acts on the perturber, slowing it down, braking it.

this mass we can derive what the velocity dispersion would be at 0.1 pc and from observations of the brightness surface profiles we can estimate what the stellar density at that distance would be. In many cases this distance is usually not resolvable, so that one has to extrapolate in order to obtain the density at 0.1 pc, which is what has been done in the figure. The blue, dashed lines correspond to $t_{\text{rlx}}(r = 0.1 \text{ pc})$, the relaxation time at that distance. Any system below the 10^{10} yrs should be relaxed and is, hence, interesting. For the range of frequencies we are interested on, MBHs with masses typically less than a few $10^7 M_{\odot}$ (the region below the red line) we can see only three systems (since M110 is only an upper limit) and M33 possibly lacks an MBH. This low number does not mean that nuclei in the range of frequencies of interest are rare, it simply means that it is hard to observe MBHs in that range of masses. In this regard, a GW mission that could observe MBHs in that region would pro-

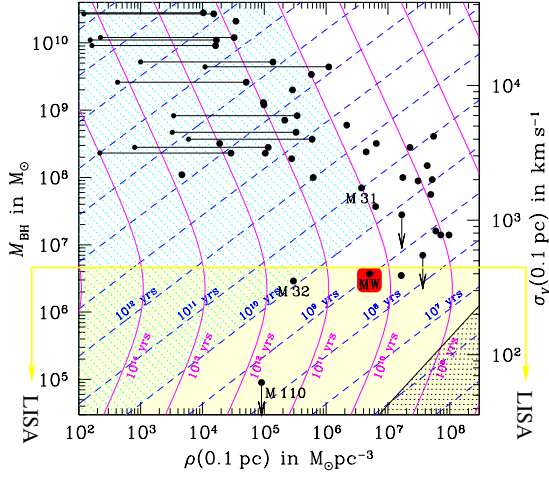


Figure 4.6: Plane of the stellar density at 0.1 pc and the mass of the central MBH (taken from Freitag and Benz, 2005) Relaxation (and collision times) at 0.1 pc from an MBH in the centre of a galactic nucleus.

vide us with very valuable information, since in the electromagnetic domain we are still far from resolving those nuclei.

4.4 The difussion and loss-cone angles

As we have seen, the relaxation time is the required time for $\Delta v_{\perp}^2 / v_{\perp}^2 \simeq 1$ (i.e. the change in the perpendicular velocity component is of the same order as the perpendicular velocity component itself);

$$\begin{aligned} \Delta v_{\perp}^2 &= n_{\text{rlx}} \cdot \delta v_{\perp}^2, \\ \Delta v_{\perp}^2 / v_{\perp}^2 &= 1 = \frac{n_{\text{rlx}} \cdot \delta v_{\perp}^2}{v_{\perp}^2} \end{aligned} \quad (4.18)$$

$$t_{\text{rlx}} = n_{\text{rlx}} \cdot t_{\text{dyn}} = \left(\frac{v_{\perp}^2}{\delta v_{\perp}^2} \right) \cdot t_{\text{dyn}}, \quad (4.19)$$

where n_{rlx} is the numbers of crossings for $\Delta v_{\perp}^2 / v_{\perp}^2 \simeq 1$. This conforms the definition of the relaxation time, $\Delta v_{\perp}^2 / v_{\perp}^2 = t / t_{\text{rlx}}$ (Binney and Tremaine, 1987).

If we consider that θ_D is very small,

$$\begin{aligned} \sin \theta_D &\simeq \frac{\delta v_{\perp}}{v} \simeq \theta_D \\ t_{\text{rlx}} &\simeq \frac{t_{\text{dyn}}}{\theta_D^2} \end{aligned} \quad (4.20)$$

$$\theta_D \simeq \sqrt{\frac{t_{\text{dyn}}}{t_{\text{rlx}}}}. \quad (4.21)$$

We now introduce the loss-cone angle θ_{lc} as an illustrative example. Suppose that the central object with mass M_{\bullet} has an influence radius r_h . To define this radius we say that a star will interact with the central object only when $r \leq r_h$. Then we look for a condition at a place $r > r_h$ for a star to touch or to cross the influence radius of the central object within a crossing time $t_{\text{cross}} = r / \sigma_r$.

As we saw in the text, the condition that defines this angle is the following:

$$\begin{aligned} r_p(E, L) &\leq r_t, \\ \theta &\leq \theta_{\text{lc}}. \end{aligned} \quad (4.22)$$

$$\begin{aligned} \sin \theta &= \frac{v_t}{v}, \text{ with } \theta \ll 1 \\ \theta &\simeq \frac{v_t}{v} = \frac{L/r}{v}. \end{aligned} \quad (4.23)$$

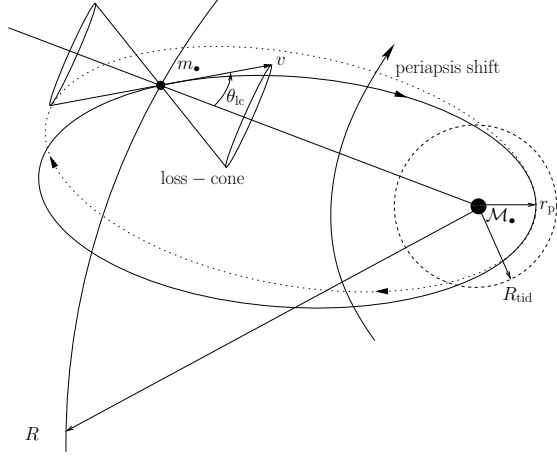


Figure 4.7: Definition of the angle θ_{lc} .

Where $L := r v_t$ is the specific angular momentum.

Now we derive an expression for this angle in terms of the influence radius. Within the region $r \leq r_h$ the star moves under the MBH potential influence, then

$$\begin{aligned} \sigma(r) &\approx \sqrt{\frac{GM_\bullet}{r}} = \sqrt{\frac{GM_\bullet}{R_h}} \sqrt{\frac{R_h}{r}} \\ &= \sigma(R_h) \sqrt{R_h/r} = \sigma_c \sqrt{R_h/r}, \end{aligned} \quad (4.24)$$

since $\sigma_c^2 \equiv GM_\bullet/R_h$. The typical velocity of the orbit is $\langle v^2 \rangle \simeq 3\sigma_c^2$, where the factor three stands for the three directions in the space. Since σ means the one-dimensional dispersion, we have to take into account the dispersion of the velocity in each direction. Then,

$$\langle v \rangle \simeq \sqrt{3}\sigma_c \sqrt{R_h/r}. \quad (4.25)$$

Finally, we obtain the loss-cone angle,

$$\theta_{lc} = \sqrt{\frac{2}{3} \frac{r_t}{r}}. \quad (4.26)$$

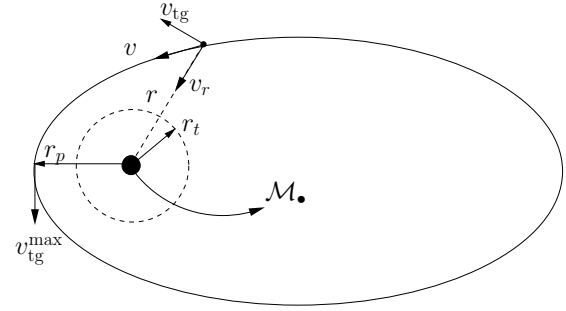


Figure 4.8: Definition of the distance of closest approximation of the star in its orbit to the MBH. In this point the radial component of the velocity of the star cancels and the tangential component is maximum. In the figure " r_p " stands for the periapsis radius and " r_t " for the tidal radius

In the region in which $r \geq r_h$ we can consider that the velocity dispersion is more or less constant from this r_h onwards, $v \approx \sqrt{3}\sigma_c$,

$$\begin{aligned} \theta_{lc} &= \frac{\sqrt{2GM_\bullet r_t}}{\sqrt{3}r\sigma_c}; \\ \sigma_c &= \sqrt{GM_\bullet/r_h}. \end{aligned} \quad (4.27)$$

The angle is

$$\theta_{lc} \approx \frac{1}{r} \sqrt{\frac{2r_t r_h}{3}} \quad (4.28)$$

We derive the loss-cone velocity $v_{lc}(r)$ using angular momentum and energy conservation arguments. We just have to evaluate it at a general radius r and at the tidal radius r_t , where the tangential velocity is maximal and the radial velocity cancels (see figure 4.8).

For a general radius we have that

$$\begin{aligned} E(r) &= \phi(r) - \frac{v_{tg}(r)^2}{2} - \frac{v_r(r)^2}{2} \\ L(r) &= r v_{tg}(r) \end{aligned} \quad (4.29)$$

For the tidal radius:

$$\begin{aligned} E(r_t) &= \phi(r_t) - \frac{v_{tg}(r_t)^2}{2} \\ L(r_t) &= r_t v_{tg}(r_t), \end{aligned} \quad (4.30)$$

from the momentum conservation and the fact that $v_r(r_t) = 0$ we get that:

$$v_{tg}(r_t) = \frac{r}{r_t} v_{tg}(r). \quad (4.31)$$

With energy conservation, and using the last result,

$$\begin{aligned} \phi(r) - \frac{v_{tg}(r)^2}{2} - \frac{v_r(r)^2}{2} &= \\ \phi(r_t) - \frac{r^2}{2r_t^2} v_{tg}(r)^2. \end{aligned} \quad (4.32)$$

Then we get the tangential velocity of the stars in terms of r ; namely, the loss-cone velocity:

$$\begin{aligned} v_{lc}(r) &= \frac{r_t}{\sqrt{r^2 - r_t^2}} \times \\ &\sqrt{2[\phi(r_t) - \phi(r)] + v_r(r)^2}. \end{aligned} \quad (4.33)$$

Therewith, the angular momentum is

$$\begin{aligned} L(r_t) &= r_t v_{tg}(r)|_{\max} = r_t \frac{r}{r_t} v_{tg}(r) = \\ r v_{tg}(r) &= r \frac{r_t}{\sqrt{r^2 - r_t^2}} \sqrt{2\Delta\phi + v_r(r)^2}, \end{aligned} \quad (4.34)$$

where

$$\begin{aligned} \Delta\phi &\equiv \phi(r_t) - \phi(r) = \\ &\frac{GM_\bullet}{r_t} + \phi_\star(r_t) - \frac{GM_\bullet}{r} - \phi_\star(r) \end{aligned} \quad (4.35)$$

If we use the fact that $r \gg r_t$, then

$$\frac{GM_\bullet}{r_t} \gg \left(\frac{GM_\bullet}{r} + \phi_\star(r) \right) = \phi(r) \quad (4.36)$$

Also, since $M_\bullet \gg M_\star(r_t)$,

$$\frac{GM_\bullet}{r_t} \gg \phi_\star(r_t). \quad (4.37)$$

Thus,

$$v_{lc}(r) \approx \frac{r_t}{r} \sqrt{\frac{2GM_\bullet}{r_t}}. \quad (4.38)$$

If we use now the fact that

$$\begin{aligned} \sigma_r(r) &= \sigma_r(r_t) \left(\frac{r}{r_t} \right)^{-1/2} = \\ &\sqrt{\frac{GM_\bullet}{r_t}} \left(\frac{r}{r_t} \right)^{-1/2}, \end{aligned} \quad (4.39)$$

we have that

$$\sqrt{\frac{GM_\bullet}{r_t}} = \sigma_r(r) \left(\frac{r}{r_t} \right)^{-1/2} \quad (4.40)$$

And so, it is in fair approximation

$$v_{lc}(r) \approx \frac{r_t}{r} \sqrt{\frac{2GM_\bullet}{r_t}} \approx \sigma_r(r) \left(\frac{r_t}{r} \right)^{1/2}. \quad (4.41)$$

Chapter 5

“Standard” mass segregation

5.1 Introduction

In order to address the question how many objects do you get a year close enough to the central MBH to be tidally destroyed in the case of an extended star or captured, if a compact object, the zero-th order problem we must solve is how stars distribute in semi-Keplerian systems.

In a system with a spectrum of masses initially distributed equally, the more massive ones have a higher kinetic energy than the lighter ones, simply due to the fact that they have the same velocity dispersion but a higher mass. The heavy stars exchange energy with each other and with the light stars through relaxation. The exchange of energy goes in the direction of equipartition, because the system searches the equilibrium. The heavy stars will lose energy to the light ones. When they do so, since they feel their own potential or the potential well of the MBH, their semi-major axis shrinks and they segregate to the centre of the system. When doing so, their kinetic energy will become higher. The system tries to re-equilibrate itself; the velocity dispersion is larger as it was when the massive stars were at larger distances from the centre. As they approach the MBH, their ki-

netic energy will be higher as compared to the light stars, which slightly extend, they are pushed to the outskirts of the system.

In figure 5.1 we have a density profile which shows us the evolution of a single-mass galactic nucleus with a MBH while letting relaxation play a role (i.e. the simulations were run for at least a T_{rlx}). The initial density profile is depicted in red and shows already a cusp because the authors were using a King model (Freitag et al., 2006b,a), so that it formally diverges at the centre. When we let it evolve, the profile obtains a much higher cusp, the blue curve, reaching later a power-law cusp of $\rho \propto R^{-1.75}$. This cusp is kept as the system continues to evolve and the cluster expands.

This is not intuitive. This phenomenon occurs because at the centre we have a sink, the MBH is removing stars, either through tidal disruptions or EMRIs. The stars removed from the system must have a very negative energy, they are very close to the centre, and stars also physically collide with each other and they are partially or totally destroyed in the process, which also represents a loss of stellar mass in the system. For the rest of the system, this represents actually a *source of heat*. The total energy in the system has increased. We can also envis-

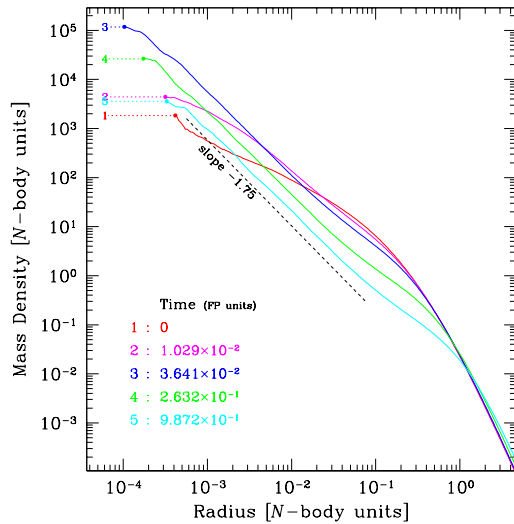


Figure 5.1: Density profile for a galactic nucleus with a single stellar population in different moments of the evolution of the system (from Freitag et al. 2006b) in Fokker Plank units (FP).

age the picture as follows: the stars that will be removed have to give energy to the rest of the stellar system in order to approach the central sink. When they do so, they heat up the system.

In figure 5.2 we have a somehow more realistic situation. In this figure the authors depict the mass density distribution for a system that has different stellar components and not only single-mass stars. After some 10^{10} yrs the total density has not changed much but in the centre, within ~ 0.1 pc, the stellar black holes overwhelmingly defeat the rest of the stellar components. Therefore within a radius of ~ 0.1 pc around an MBH such as the one in our GC, the mass density will be dominated by the stellar black holes. This does not apply to the number density of stellar black holes. They are

less numerous as compared to MS stars, but more massive. The important point here is that we expect to have about $2 \cdot 10^3$ stellar black holes within 0.1 pc, or $2 \cdot 10^4$ within 1 pc of Sgr A^* (Freitag et al., 2006b,a).

Before we further analyse realistic models with a mass spectrum and address the potential implications for EMRI production, we will start from the beginning and step by step. As we mentioned in the foreword, the main goal of this document is to give a self-consistent starting point for newcomers to understand the complexity of the different phenomena associated with EMRIs. Thus, the first kind of systems we will address will contain only one kind of star. As Donald Lynden Bell puts it,

“Only a fool tries to solve a complicated problem when he does not even understand the simplest idealization”.

In this chapter we will be illustrating the different phenomena with numerical simulations published for the first time in this review with the Gas Model. Although the results are not to be taken as if they came from direct-summation N -body simulations with a large number of stars running on GPU clusters, we believe that they are good enough to give the reader an impression of the physics. To win your trust, we also compare to some extent some of the results with direct-summation N -body simulations and show that the two algorithms yield similar results.

5.2 Single-mass clusters

Peebles (1972) was the first one to realise ¹ that

¹We note that eight years ago Gurevich (1964) had

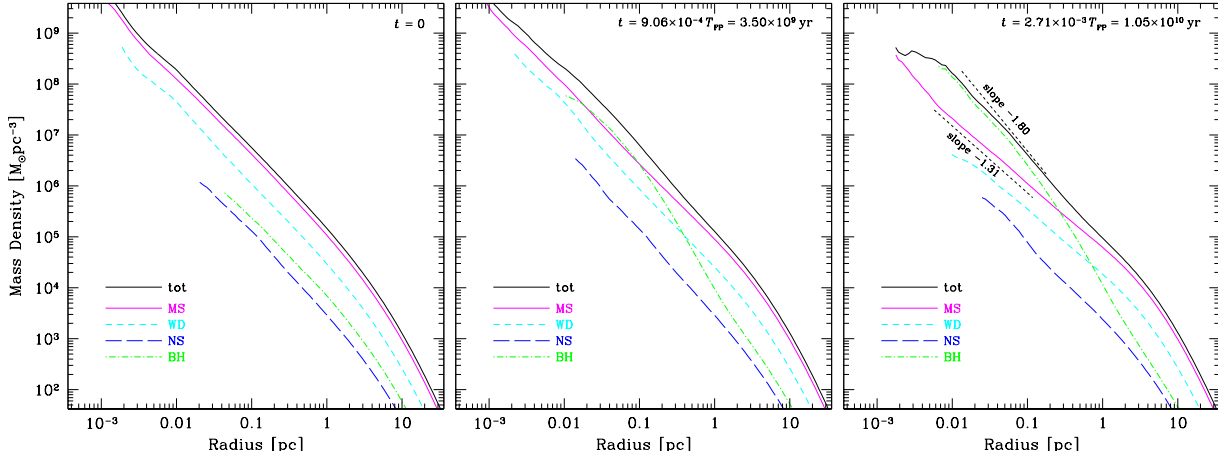


Figure 5.2: Evolution of a multi-mass system corresponding to Sgr A^* . The model, which is taken from Freitag et al. (2006b), their figure 10, contains stellar black holes, with masses between 10 – 30 times larger than MS stars on average. On the left panel we have the initial conditions, at $t = 0$ yr. When we leave the system evolve, the components separate and roughly after a Hubble time we obtain the situation corresponding to the right panel

the statistical thermal equilibrium in a stellar cluster, i.e. the fact that the distribution of energy E in the cluster is $f(E) \propto e^{-E/\sigma^2}$, with σ the velocity dispersion, must be violated when we are close to the MBH, because we have three characteristic radii within which stars are lost for the system. These are the tidal radius, R_t , the “Schwarzschild radius” R_{Schw} (i.e. the capture radius via gravitational loss), and the collisional radius R_{coll} . Peebles found that there could be a steady state with a net inward flux of stars and energy in the stellar system. Nevertheless, well within the influence radius R_h of the MBH but far from R_t , the stars should have nearly-isotropic velocities. Peebles derived a solution in the form of a power-law for a system in which all stars have the

an interesting first idea of this concept: The authors obtained a similar solution for how electrons distribute around a positively charged Coulomb centre.

same mass. The quasi-steady solution takes the form (for an isotropic distribution function) $f(E) \sim E^p$, $\rho(r) \sim r^{-\gamma}$, with $\gamma = 3/2 + p$. Nevertheless, Peebles derived the wrong exponent. A few years later, Bahcall and Wolf (1976) did an exhaustive kinematic treatment for single-mass systems and found that the exponent should be $\gamma = 7/4$ and $p = \gamma - 3/2 = 1/4$. This solution has been corroborated in a number of semi-/analytical approaches, and approximative numerical schemes (see e.g. Shapiro and Marchant, 1978; Marchant and Shapiro, 1979, 1980; Shapiro and Teukolsky, 1985; Freitag and Benz, 2001; Amaro-Seoane et al., 2004a), as well as direct-summation N –body simulations (of which the work of Preto et al., 2004, was the first one).

This is one of the most important phenomena in the production of EMRIs, since the galactic nuclei of interest for us, the ones which are

thought to be harbouring EMRIs in their cores and are in the range of frequencies of interest, are possibly relaxed. These nuclei are relatively small and are likely to have at least gone through a full relaxation time.

5.3 Mass segregation in two mass-component clusters

As we have just seen, the processes that one-component clusters bring about is nowadays relatively well understood and has been plentifully studied by different authors to check for the goodness of their approaches. Nonetheless, the properties of multi-mass systems are only very poorly represented by idealised models in which all stars have a single mass. The processes that one-component clusters bring about is nowadays well understood and has been plentifully studied by different authors to check for the goodness of their approaches. New features of these systems’ behaviour arise when we consider a stellar system in which masses are divided into two groups. Hence, since the idealised situation in which all stars in a stellar cluster have the same mass has arduously examined in the literature, we have morally the right to extend the analysis a little further step. Here we tackle with more realistic configurations in which the stellar system is splitted into various components. The second integer number immediately after one is two and so will we first extend, cautious and wary as we are, our models to two-components star clusters.

Initial mass functions (IMFs) ranging between $\in [0.1, \sim 120] M_{\odot}$ can be approximated to first order by two well-separated mass scales : one with a mass of the order of $\mathcal{O}(1M_{\odot})$ (which could represent main-sequence stars, MS, white

dwarfs, WD, or neutron stars NS) and $\mathcal{O}(10M_{\odot})$ (stellar black holes, SBHs). Depending on how the system taken into consideration is configured will we exclude *dynamical equilibrium* (here it is meant that the system is not stable on dynamical time-scales) or equipartition of different components kinetic energies is not allowed (*thermal equilibrium*).

Spitzer (1969) gave the analysis an initial shove with his study. For some clusters it seemed impossible to find a configuration in which they enjoy dynamical and thermal equilibrium altogether. The heavy component sink into the centre because they cede kinetic energy to the light one when reaching equipartition. The process will carry on until equipartition is fully gained on and the heavy component self-gravity moves out in the core. In the most of the cases, equipartition happens to be impossible, because the subsystem of massive stars will undergo core collapse before equipartition is reached. Anon, a *gravothermal collapse* will happen upon this component and, as a result, a small dense core of heavies is formed (Spitzer, 1969; Lightman and Fall, 1978). This gravothermal contraction is a product of negative heat capacity, a typical property of gravitationally bound systems (Elson et al., 1987).

Disparate authors have addressed the problem of thermal and dynamical equilibrium in such systems, from direct N -body simulations (Portegies Zwart and McMillan, 2000; Khalisi et al., 2007) and Monte Carlo simulations (Watters et al., 2000) to direct integration of the Fokker-Planck equation (Inagaki and Wiyanto, 1984; Kim et al., 1998) or moments of it (Amaro-Seoane et al., 2004a), including Monte Carlo approaches to the numerical integration of this equation (Spitzer and Hart, 1971). For a general and com-

plete overview of the historical evolution of two-stars stellar components, see Watters et al. (2000); Amaro-Seoane et al. (2004a) and references therein.

If we do not have any energy source in the cluster and stars do not collide (physically), the contraction carries on self-similarly indefinitely; in such a case, one says that the system undergoes *core-collapse*. This phenomenon has been observed in a big number of works using different methods (Hénon, 1973; Hénon, 1975; Spitzer and Shull, 1975; Cohn, 1980; Marchant and Shapiro, 1980; Stodołkiewicz, 1982; Takahashi, 1993; Giersz and Heggie, 1994; Takahashi, 1995; Spurzem and Aarseth, 1996; Makino, 1996; Quinlan, 1996; Drukier et al., 1999; Joshi et al., 2000, etc) Core collapse is not just a characteristic of multi-mass systems, but has been also observed in single mass analysis.

Spitzer (1969) gave the analytical criterion to determine whether a two-component system has achieved energy equipartition. According to his analysis, energy equipartition between the light and heavy component exists if the quantity

$$S := \left(\frac{\mathcal{M}_h}{\mathcal{M}_l} \right) \left(\frac{m_h}{m_l} \right)^{3/2} < 0.16. \quad (5.1)$$

Where \mathcal{M}_l and \mathcal{M}_h are the total numbers of light and heavy components, respectively (i.e. the total stellar mass in light stars and heavy stars in the system). More numerical calculations (Watters et al., 2000) have settled this criterion to Λ ,

$$\Lambda := \left(\frac{\mathcal{M}_h}{\mathcal{M}_l} \right) \left(\frac{m_h}{m_l} \right)^{2.4} < 0.16 \quad (5.2)$$

When we modify the ratio $\mathcal{M}_{\max}/\mathcal{M}$, the time required to reach core-collapse is different. In a cluster with, for instance, a broad

Salpeter IMF between $[0.2 M_\odot, 120 M_\odot]$ core-collapse takes place after $\lesssim 0.1 t_{\text{rh}}(0)$, while for a single-mass Plummer model it occurs after $\gtrsim 10 t_{\text{rh}}(0)$ (this specific example was taken from the Monte Carlo-based calculations of Gürkan et al. 2004).

There is an ample evidence for mass-segregation in observed clusters. McCaughrean and Stauffer (1994) Hillenbrand and Hartmann (1998) provided a new deep infrared observations of the Trapezium cluster in Orion that clearly show the mass segregation in the system, with the highest mass stars segregated into the centre of the cluster. To test whether there is evidence for more general mass segregation, they show in figure 5.3 cumulative distributions with radius of stars contained within different mass intervals. They include in the plot four different panels in order to manifest the sensitivity to the limiting radius. They find that, inside 1.0 pc, general mass segregation appears to be established in the cluster, with stars of masses less than 0.3, 0.3-1.0, 1.0-5.0, and greater than 5 M_\odot progressively more centrally concentrated with increasing mass.

At this point, the question looms up whether for very young clusters mass segregation is due to relaxation, like in our models, or rather it reflects the fact that massive stars are formed preferentially towards the centre of the cluster, as some models predict.

Raboud and Mermilliod (1998) study the radial structure of Praesepe and of the very young open cluster NGC 6231. There they find evidence for mass segregation among the cluster members and between binaries and single stars. They put it down to the greater average mass of the multiple systems. In figure 5.4 of Raboud and Mermilliod (1998) again we have

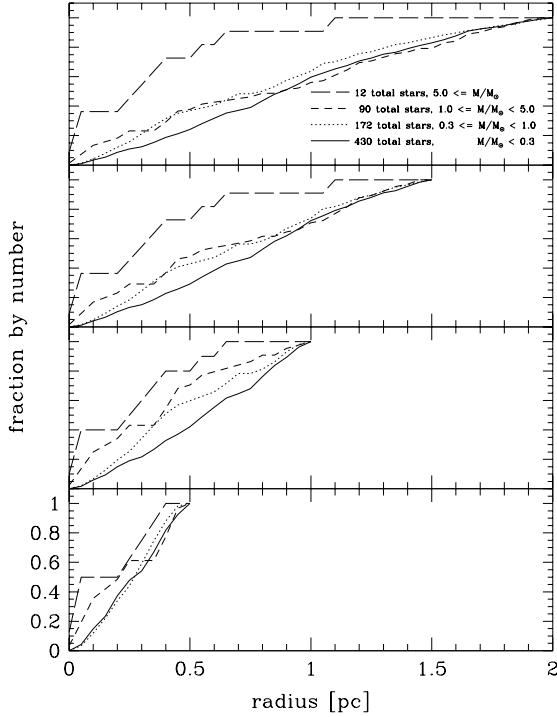


Figure 5.3: In this plot by Hillenbrand and Hartmann (1998) we have a clear-cut evidence for mass-segregation of stars more massive than $5 M_{\odot}$ (long-dashed lines) toward the cluster centre and some evidence for general mass segregation persisting down to $1\text{--}2 M_{\odot}$ in the Orion Nebula cluster. The cumulative radial distributions of source counts over different mass intervals are shown. To clarify the sensitivity of the cumulative plots to the outer radius they have shown here four panels with four different limiting radii

clear evidence for mass segregation in NGC 6231. In the two first panels the mass intervals are set in a different way to those in the bottom.

The two left-hand panels include the 9 bright stars of the cluster Corona, while the right hand two diagrams do not. The manifestation of mass segregation for massive stars (triangles) is clearly nailed down, whilst for stars with masses $\in [5, 20] M_{\odot}$ are spatially well mixed (open squares and crosses); i.e., mass segregation is not yet established over a rather large mass interval. This population is more concentrated than the lower-mass population (here shown with filled squares). They derive from this figure 5.4 that only a dozen, bright, massive, mainly binary stars are well concentrated toward the cluster centre.

It seems therefore interesting to set out for multi-mass models with the two-component ones as a starting point to take care of, since it is well-studied and we have robust observational proofs of this phenomenon. On the other hand, observations do not tell us whether mass segregation is due to relaxation. We now show the results of a set of 10^4 simulations for two-component models that have never been published, using the “Gaseous Model” programme to illustrate this (see § 8). We define two parameters now that describe the physics of the system,

$$\begin{aligned} q &:= \mathcal{M}_h / \mathcal{M}, \\ \mu &:= m_h / m_l \end{aligned} \quad (5.3)$$

In this definition, \mathcal{M} is the total mass of the system, \mathcal{M}_h the total mass in heavies and m_h, l the mass of one heavy (light) star.

If $\zeta \equiv 1 - q$, we have let ζ vary from 10^{-4} to $9.99 \cdot 10^{-1}$. For each ζ value, we let μ vary

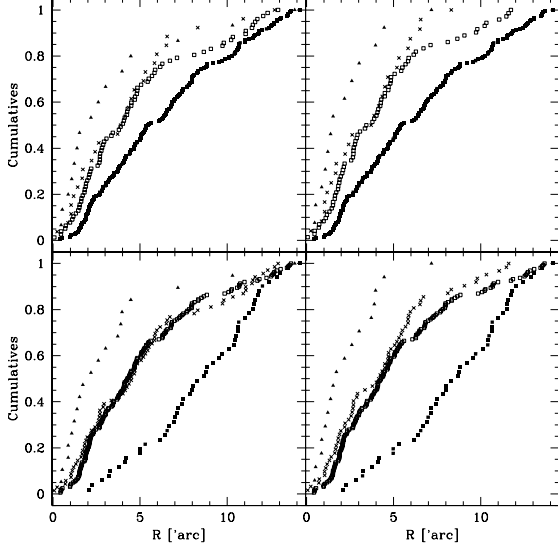


Figure 5.4: Mass segregation in NGC 623 for two mass interval sets. The two left panels include all sample stars, while the right ones do not include the 9 bright stars of the cluster corona. For the two top figures $M < 5 M_{\odot}$ (filled squares), $M \in [5, 10[M_{\odot}$ (open squares), $M \in [10, 20[M_{\odot}$ (crosses) and $M \geq 20 M_{\odot}$ (triangles). For the two bottom figures, $M < 2.5 M_{\odot}$ (filled squares), $M \in [2.5, 6.3[M_{\odot}$ (open squares), $M \in [6.3, 15.8[M_{\odot}$ (crosses) and $M \geq 15.8 M_{\odot}$ (triangles)

between 1.03 and 10^3 .

The values for q are regularly distributed in $\log(\zeta)$. For $\zeta \approx 1$ we have added a series of values in $\log(\zeta - 1)$. The mean particle mass is $1 M_{\odot}$ and the total mass $10^6 M_{\odot}$, but this has not importance for our study, because the physics of the system is ruled by relaxation and therefore the only relevant thing is the relaxation time. If we are using Fokker-Planck or half-relaxation units, we can always extend the physics to any other system containing more particles (if only relaxation is on play). As a

matter of fact, one relates the N -body units to Fokker-Planck units as follows:

$$\mathcal{U}_{\text{FP}} = \mathcal{U}_{\text{NB}} \frac{\mathcal{N}_{\star}}{\ln(\gamma \cdot \mathcal{N}_{\star})} \quad (5.4)$$

Therefore, the relation between FP- and N -body-time units is

$$\mathcal{U}_{\text{FP}|_{\text{time}}} = \mathcal{U}_{\text{NB}|_{\text{time}}} \frac{\mathcal{N}_{\star}}{\ln(\gamma \cdot \mathcal{N}_{\star})} \quad (5.5)$$

In order to be able to compare our results with N -body, this relation is very useful. The mean mass is therefore just a normalisation. What really determines the dynamics of the system are the mass ratios, q and μ .

In figure 5.5 we show the whole (q, μ) -parameter space in a plot where the time at which the core-collapse begins is also included. The green zone corresponds to the quasi single-mass case. In the red zone we have the largest difference between masses and blue is an intermediate case.

In figure 5.6 we show collapse times for clusters models with two mass components normalised to the single-mass core-collapse time $T_{\text{cc}}(\text{s.s.})$ for different values of μ . The initial clusters are Plummer spheres without segregation. The collapse times are displayed as a function of the mass fraction of the heavy component in the cluster. When compared to single-mass component systems, we see that the core-collapse time is accelerated notably for a wide range of the heavy component $\mathcal{M}_{\text{h}} (M_2)$. Even a small number of heavies accelerate the core-collapse time.

It is really interesting to compare the capacity of our approach by comparing the results of this set of simulations to the N -body

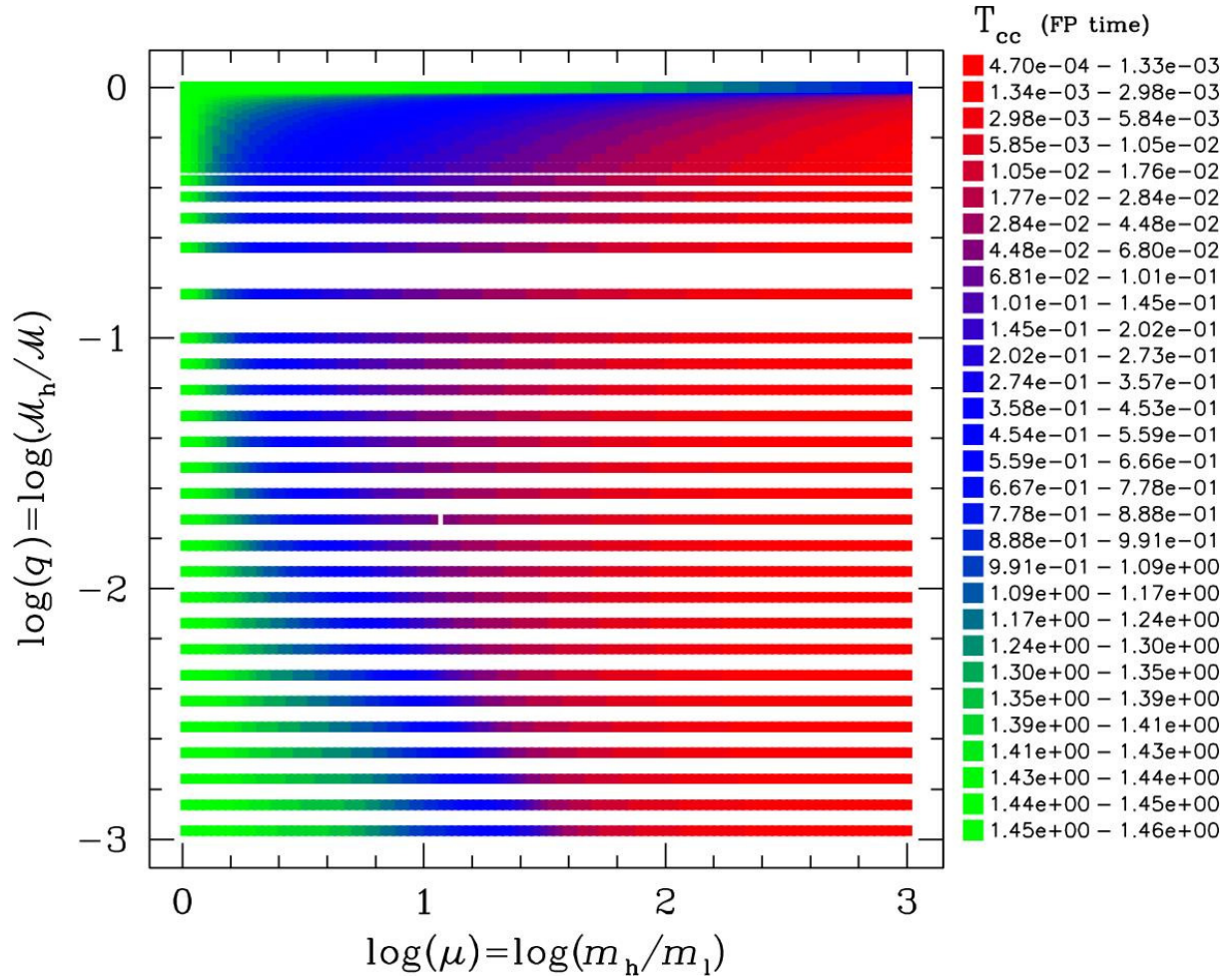


Figure 5.5: Parameter space for the set of 10^4 simulations. Here t_{end} stands for the core collapse time and is expressed in FP units (see text); time at which the simulation ended. q and μ are plotted logarithmically.

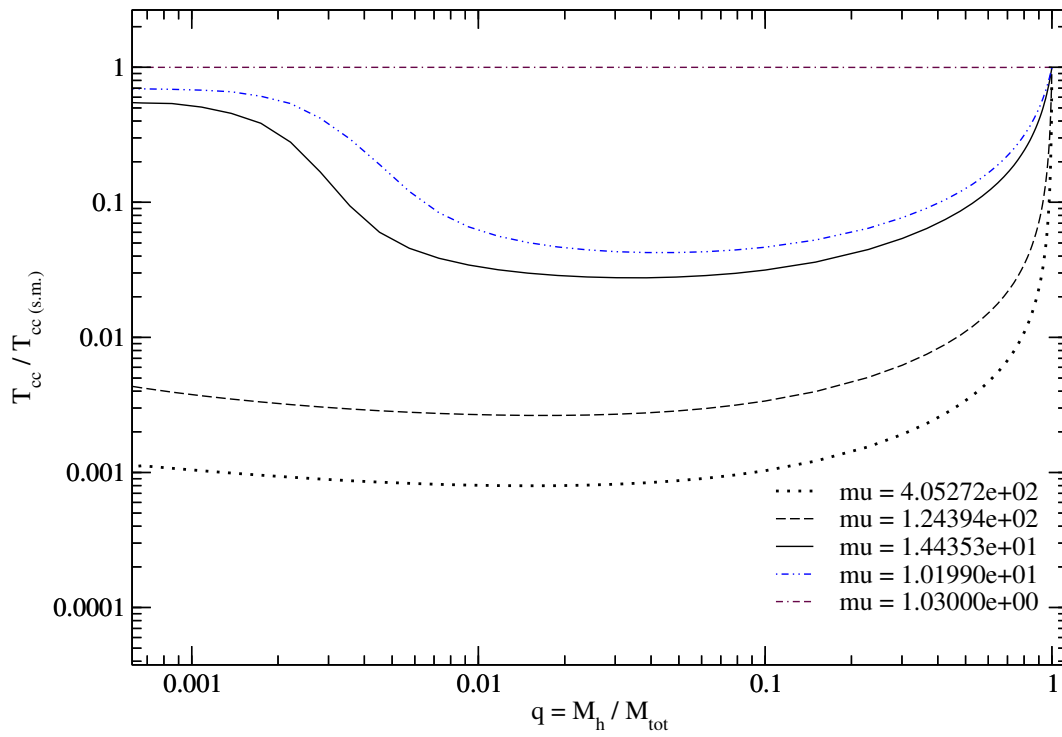


Figure 5.6: Core-collapse time for different values of q and μ

calculations of star clusters with two-mass components performed by Khalisi et al. (2007) with direct-summation techniques. For this aim, we plot the evolution of the average mass in Lagrangian shells of the cluster from the averaged mass in Lagrangian *spheres* containing the following mass percentages [0–1], [2–5], [10–20], [40–50], [75–95] %, among others, to be able to compare with the results of Khalisi et al. (2007). These are the comprised volume between two Lagrangian radii, which contain a fixed mass fraction of the bound stars in the system.

We have calculated the average mass as follows: If $M_r^{(i)}$ is the total mass for the component i comprised at the radius r and $\bar{m}_*^{(i)}$ is the average mass for this component within that radius, we can find out what is the value of $\bar{m}_*^{(i;i+1)}$ (the average mass between $\bar{m}_*^{(i)}$ and $\bar{m}_*^{(i+1)}$) knowing $M_r^{(i)}$, $M_r^{(i+1)}$, $\bar{m}_*^{(i)}$ and $\bar{m}_*^{(i+1)}$. This is schematically shown in figure 5.7. Indeed,

$$\begin{aligned} M_r^{(i+1)} &= N_r^{(i)} \cdot \bar{m}_*^{(i)} + N_r^{(i;i+1)} \cdot \bar{m}_*^{(i;i+1)} \\ &= N_r^{(i+1)} \cdot \bar{m}_*^{(i+1)}. \end{aligned} \quad (5.6)$$

Since

$$N_r^{(i+1)} = N_r^{(i)} + N_r^{(i;i+1)}, \quad (5.7)$$

where

$$N_r^{(i)} = \frac{M_r^{(i)}}{\bar{m}_*^{(i)}} \quad (5.8)$$

we have that, from Eq. (5.6),

$$\bar{m}_*^{(i;i+1)} = \frac{M_r^{(i+1)} - M_r^{(i)}}{\frac{M_r^{(i+1)}}{\bar{m}_*^{(i+1)}} - \frac{M_r^{(i)}}{\bar{m}_*^{(i)}}} \quad (5.9)$$

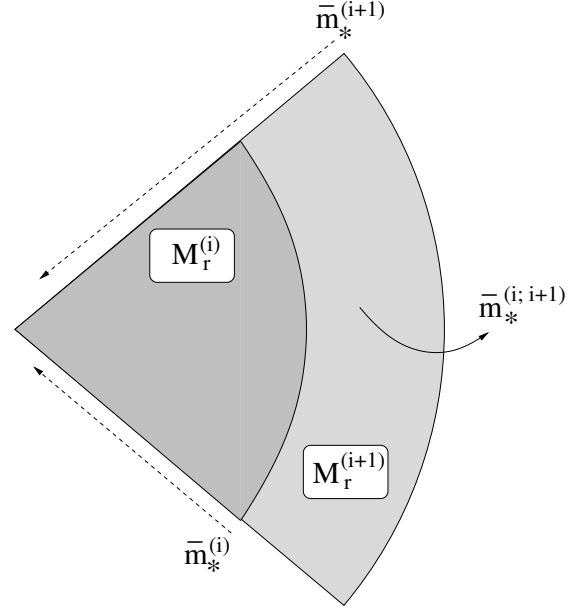


Figure 5.7: Average mass in Lagrangian shells from averaged mass in Lagrangian spheres

μ in Khalisi et al. (2007)	μ in this review
1.25	1.27
1.5	1.56
2	2.06
3	2.92
5	5.09
10	10.2

Table 5.1: Different μ values used in the N -body calculations and in our models for figure 5.8

We show in Figs. (5.8) and (5.9) we show the curves corresponding to the values shown in table 5.1.

We have followed in the curves the evolution of the system until a deep collapse of the system. They show the evolution until the

5.3 Mass segregation in two mass-component clusters

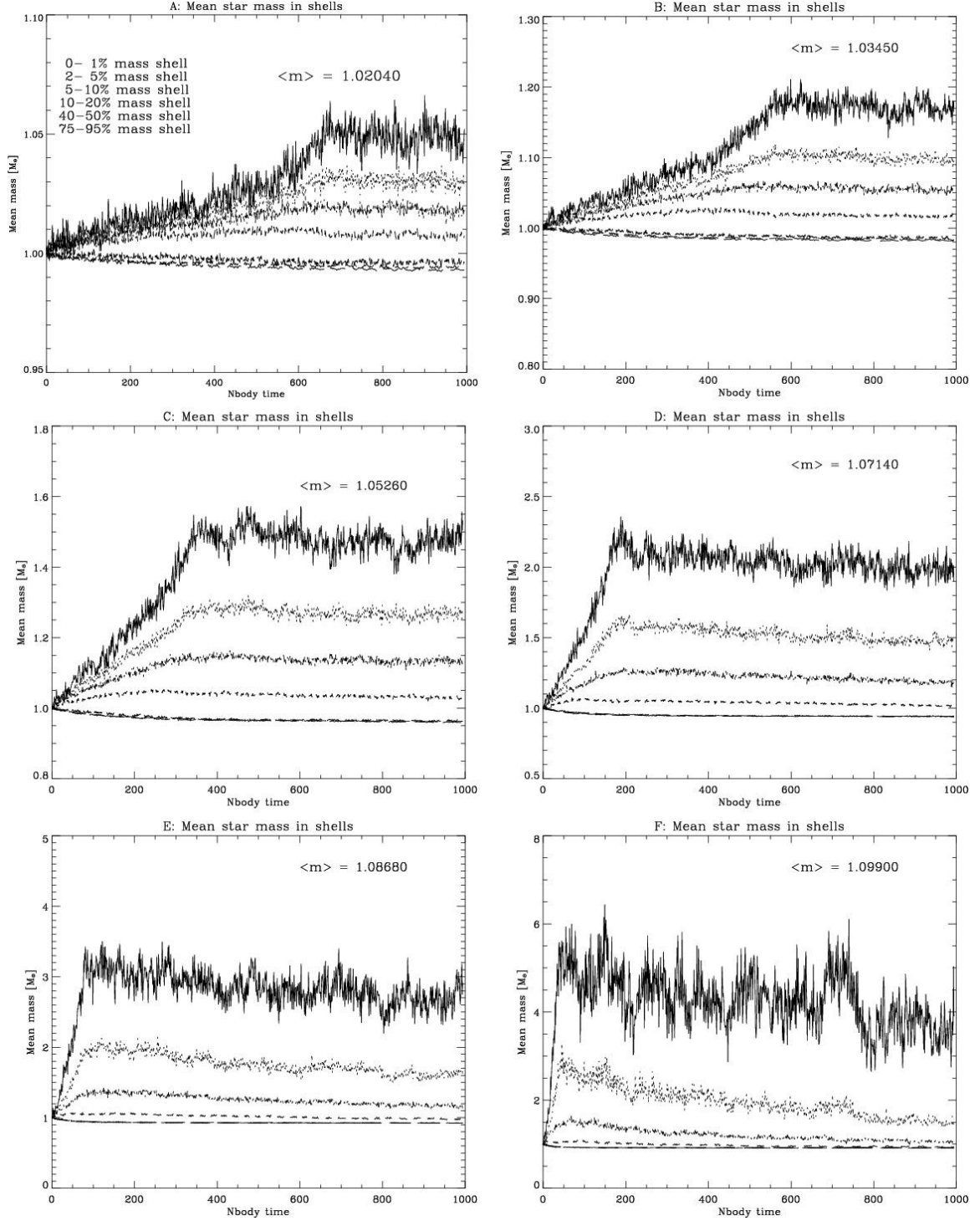


Figure 5.8: Average Lagrangian radii shells for the N -body models of Khalisi et al. (2007) (see text for further explanation)

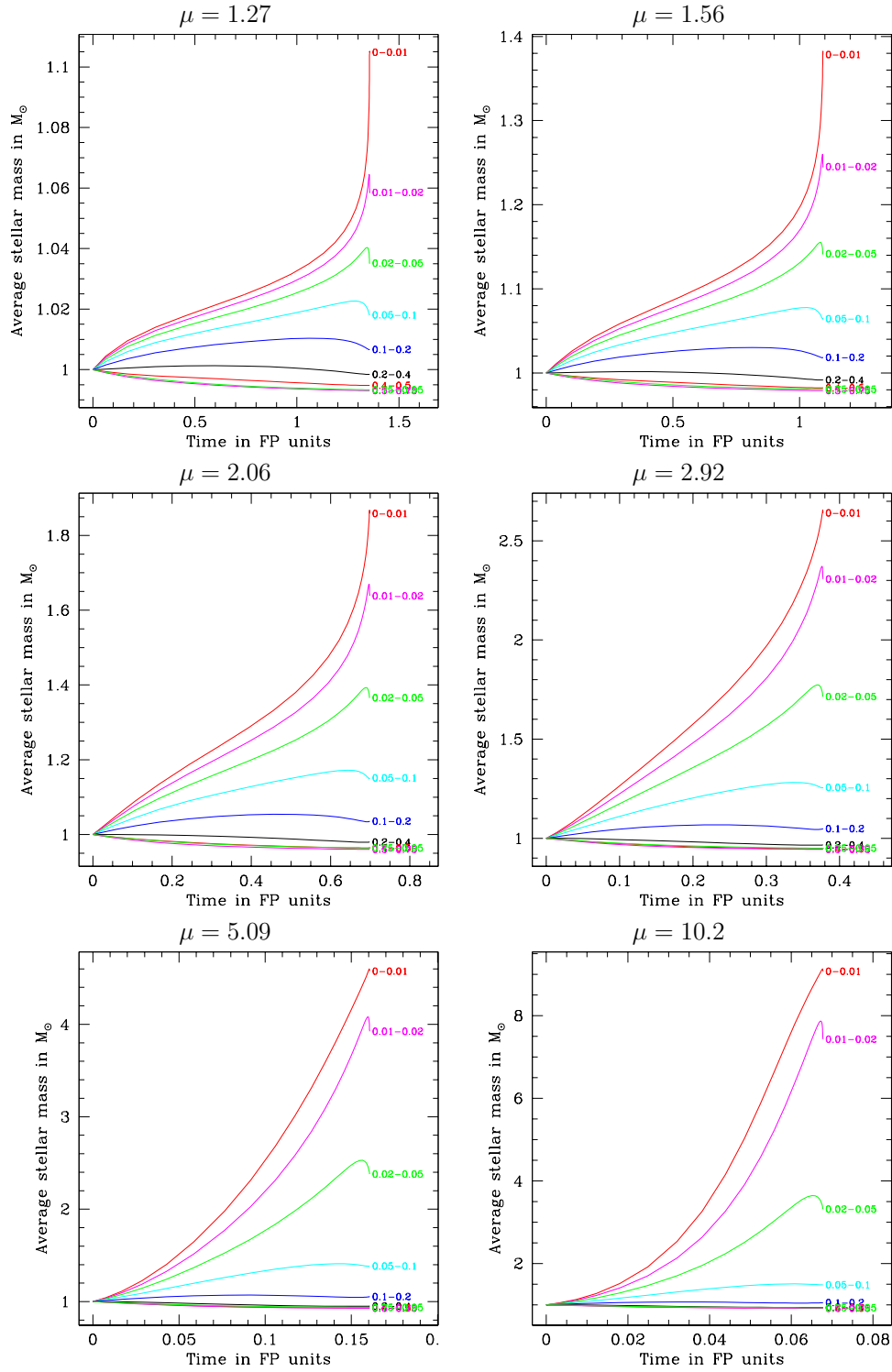


Figure 5.9: Average Lagrangian radii shells for our models, equivalents to those of figure 5.8
STELLAR DYNAMICS IN GALACTIC NUCLEI: EMRIS

most massive component dominates the centre.

In order to compare our plots with those of Khalisi et al. (2007), one should look in his diagrams in the region *during* core contraction. At this point, we can observe in figure 5.8 a self-similarity after core-collapse (Giersz and Heggie, 1996). Binaries are responsible for interrupting core-collapse and driving core re-expansion in the N -body simulations. The flattening in the N -body plots at the moment of core-collapse is due to the binary energy generation. This means that we can only compare the steep rise, but not the saturation.

For instance, in the second plot of the N -body set (second column on the top), we have to look at the point in which the average mass of the N -body system is about 1.20 in the 0 – 1% shell. This establishes the limit until which we can really compare the behaviour as given by both methods. Our simulations yield a very similar evolution until that point. The gaseous model behaves (it clearly shows the tendency) like N -body.

From Eq. (5.5), we get that the conversion factor is the same; namely, for $\gamma = 0.11$, $\ln(\gamma \cdot \mathcal{N}_\star)/\mathcal{N}_\star = 0.0022$. On the other hand, the value of γ is not so well defined and depends on the cluster’s mass spectrum (Hénon, 1975). This means that potentially it is not the same for the different models. For a broader mass spectrum, γ is about 0.01 and, unfortunately, in the case of having a small particle number, it will definitively make an important difference despite the “smoothing” effect of the logarithm, viz $\ln(\gamma \cdot \mathcal{N}_\star)/\mathcal{N}_\star = 0.0013$. Thus, in order to be able to compare the different models, one should consider γ as a free parameter ranging between 0.01 to 0.2 and look

for the best fit for the most of the cases. On the other hand, we must bear in mind that the N -body simulations of Khalisi et al. (2007) do not go in deep core collapse and, so, the moment at which the core radius reaches a minimum is not the same as for our model. To sum up, although we cannot really exactly say until which point we can compare the two methods (the Gas Model and direct-summation simulations), because the core collapse time will be different, the physics of the system is the same in the two cases. This should give the reader a good comprehension of the phenomena in play, as well as a proof that they are independent of the details of the algorithm used.

5.4 Clusters with a broader mass spectrum with no MBH

So as to be able to understand the phenomena that we will describe later, crucial for EMRI formation, it is of relative relevance to understand the physics behind cluster dynamics *without* a central MBH first. This section is by the way also interesting to interpret observations of young stellar clusters extending to a larger number of mass components. Clusters with realistic IMFs equipartition cannot be reached, because the most massive stars build a subsystem in the cluster’s centre as the process of segregation goes on thanks to the kinetic energy transfer to the light mass components until the cluster undergoes core collapse (Spitzer, 1969; Inagaki and Wiyanto, 1984; Inagaki and Saslaw, 1985). Although the case in which the MBH ensconces itself at the centre of the host cluster is more attractive for EMRI production and from a dynamical point of view, one should study, in a first step, more simple models.

In this section we want, thus, to go a step further and evaluate stellar clusters with a broad mass function (MF hereafter). For this, we will be using again the Gas Model, because it is a good compromise between accuracy and integration time for this review.

We study those clusters for which the relaxation time is short enough, because this will lead the most massive stars to the centre of the system due to mass segregation before they have time to leave the main sequence (MS). In this scenario, we can consider as an approximation that stellar evolution plays no role; stars did not have time to start evolving. The configuration is similar to that of Gürkan et al. (2004), but they employ a rather different approach based on a Monte Carlo code, using the ideas of Hénon (1973) that allows one to study various aspects of the stellar dynamics of a dense stellar cluster with or without a central MBH. Our scheme, although being less realistic than MC codes (and direct-summation N -body ones) and unable, in its present version, to account for collision has the advantage, as we will see in the last chapter, of being much faster to run, and providing data that has no numerical noise. It captures the essential features of the physical systems considered in our analysis and is hence an interesting tool for illustrating the different scenarios in this review.

One of the first questions we should do out is up to how many components one should take into consideration when performing our calculations. Since the computational time becomes larger and larger when adding more and more components to the system -even for an approximative scheme such as the Gas Model-, we should first find out what is a realistic number of components in our case. For this end we

performed different computations with different number of stellar components.

For the simulations shown here, the initial cluster models are Plummer models with a Salpeter MF (Salpeter, 1955),

$$\frac{dN_{\star}}{dM_{\star}} \propto M_{\star}^{-\alpha} \quad (5.10)$$

between 0.2 and $120 M_{\odot}$. In this equation $\alpha = 2.35$. There is no initial mass segregation. The discretisation of the mass components follows this recipe:

$$\log(M_{\text{comp}}|_i) = \log(M_{\text{min}}) + \log\left(\frac{M_{\text{max}}}{M_{\text{min}}}\right) \cdot \left(\frac{i}{N_{\text{comp}}+1}\right)^{\delta} \quad (5.11)$$

In this equation δ is the discretisation exponent. If $\delta > 1$ we have more bins at low mass; for $\delta < 1$, we have more bins at high mass. I.e., δ allows one to put more discretised mass components at low masses ($\delta > 1$) or at high masses ($\delta < 1$), $\delta=1$ gives the logarithmical equal spacing. $M_{\text{max, min}}$ are, respectively, the maximum and minimum individual stellar masses for the components. For all simulations that we will present, the number of mass bins has been typically set to 15. We have chosen a Plummer model by default and the stellar clusters have 10^6 stars. The model radius by default is $R_{\text{pl}} = 1$ pc. The default initial mass function is Salpeter.

In figure 5.10 we show the Lagrangian radii for ten different models and look for main dynamical characteristics of the system: the core collapse time and the Lagrangian radii containing 90, 70, 50, 20, 10, 3, 1, 0.3, 0.1, $3 \cdot 10^{-2}$, 10^{-2} , $3 \cdot 10^{-3}$ and 10^{-3} % of the stellar mass. In this plot, N_{comp} stands for the mass spectrum different components number. For $N_{\text{comp}} = 6$

we have performed three simulations varying the δ parameter between 1.0 (equal logarithmic spacing of components), 0.75 (more massive components) and 0.5 (even more). For $N_{\text{comp}} = 12$ we have performed one only simulation (with $\delta = 1$, by default); for the $N_{\text{comp}} = 20$ case we have repeated the same procedure as with six components, the last but one that we have chosen is $N_{\text{comp}} = 20$ and, in this case, we studied two grid resolutions, $N_{\text{sh}} = 200$ (the default value) and 400 grid points, in order to check whether this could influence the results. To finish with, a last simulation with $N_{\text{comp}} = 50$ was performed and included in the analysis. Whilst we can see an important difference between models of 6 and 12 components, we see that the global behaviour from 12 components onwards is very similar. Therefore, unless indicated, we choose 15 components in our study in this section, since a higher number would not contribute anything essential.

To see this in more detail, in figure 5.11 we show the Lagrangian radii for each stellar mass m_i and the corresponding mass fraction f_m for the 25 and 15 components simulations. Again, we cannot see any substantial difference between the 25 and 15 cases.

Taking the last arguments into account, we have done an analysis of mass segregation in multi-mass models with more than two stellar components without BH. In Figs. (5.12) and (5.13), we show in the evolution of a stellar cluster of 15 components (in colours); m is the mass (in M_\odot) of the stars in each component and f_m the corresponding fraction of the total mass. In the upper box we have the density profile, where the solid black line represents the total density; below, we have the average total mass for the system. We show different moments

of the system. At $T = 0$ we have the initial model, which duly shows no mass segregation. As time elapses, at $T = 5.30 \cdot 10^{-2} T_{\text{rh}}(0)$, with $T_{\text{rh}}(0)$ the value of T_{rh} at the beginning of the simulation, we observe how mass segregation has fragmented the initial configuration; the heavy components have sunken into the central regions of the stellar cluster and, thus, risen the mean average mass. The outer parts of the system start losing their heavy stars quickly and, consequently, their density profile retrogresses. This becomes more acute for later times at $T = 6.75 \cdot 10^{-2} T_{\text{rh}}(0)$, as the right plots of figure 5.13 show. In these plots and, more markedly in the right panel of density profile, we can observe a depletion at intermediate radius.

5.5 Core-collapse evolution

Gürkan et al. (2004) shown that for a broad MF –either Salpeter or Kroupa–, mass segregation produces a core-collapse of the system that happens very fast. For clusters of moderate initial concentration, they find that this is in about 10 % of the $T_{\text{rh}}(0)$, the initial half-mass relaxation time (i.e. the half-relaxation time that the cluster had when time started, at $t = 0$). A good and clear illustration of this is figure 5.14 and figure 5.15. In the former one, on the left panel we have the initial configuration of the system. On the right one, we have the cluster at the moment of core-collapse. In the figure, all stars within a slice containing the centre have been depicted. On the other hand, this does not represent a real physical system, because all radii have been magnified (see bottom of each panel). The dashed circles represent spheres containing 1, 3 and 10 % of the total

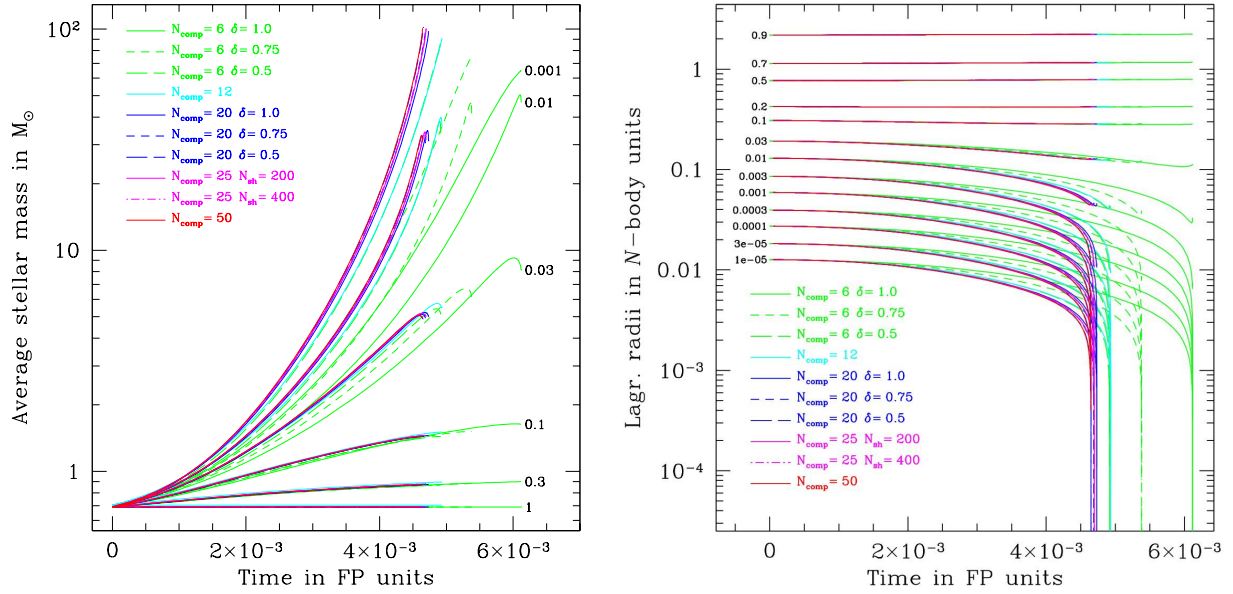


Figure 5.10: Lagrangian radii and average stellar mass for 10 models with different mass spectrum (see text)

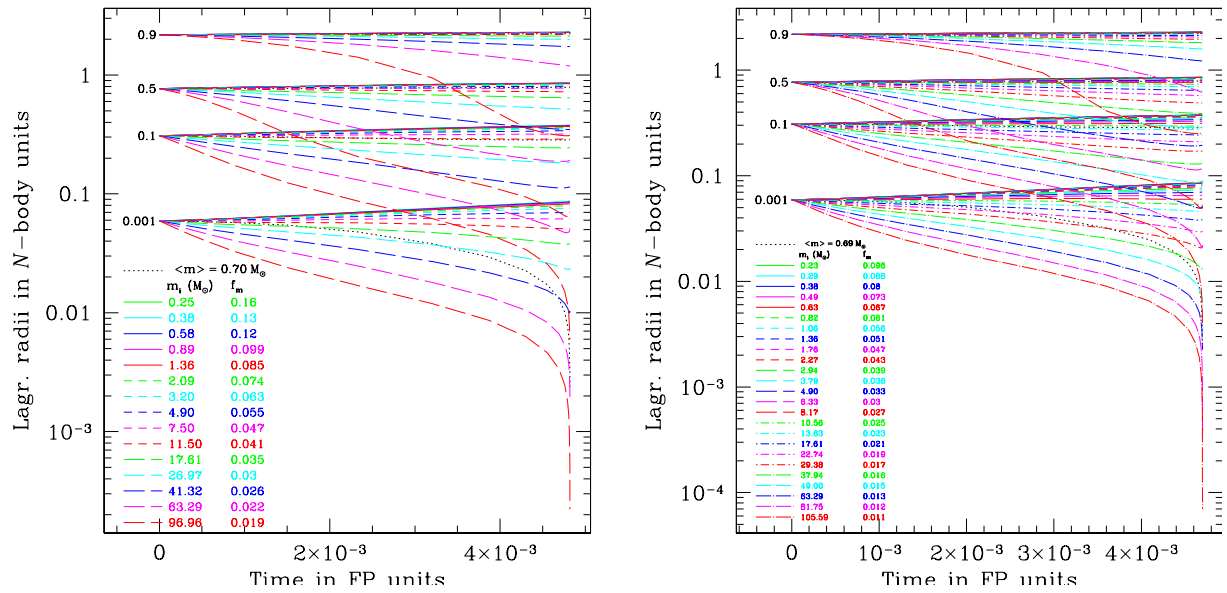


Figure 5.11: Lagrangian radii for each stellar mass m_i for the cases of 25 and 15 mass components

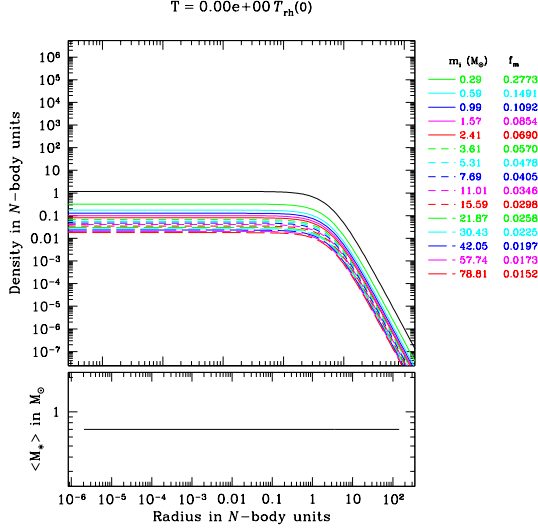


Figure 5.12: Initial density profile for a stellar cluster with 15 components (upper panel) in N -body units and average total stellar mass in M_\odot (lower panel)

cluster mass (from the centre). We can clearly see how the massive, large stars are segregated towards the centre. In figure 5.15, we show the core-collapse evolution of a multi-mass stellar cluster simulated with the gaseous model. As usual, m is the mass (in M_\odot) of the stars in each component and f_m the corresponding fraction of the total mass. On the left panel we display the time evolution of the central density for a model in which we have employed 15 individual mass components. The total density is given by the dotted line. On the right panel we have the evolution of the central velocity dispersions. The dotted black line shows the mass-averaged value

$$\bar{\sigma}^2 = \sqrt{\frac{\sum_{i=1}^{15} m_i \sigma_i^2}{\bar{m}}}, \quad (5.12)$$

and we use N -body units for the y -axes.

One notes that, during core collapse, the central regions of the cluster become completely dominated by the most massive stars. But, contrary to the case of single-mass clusters, the central velocity dispersion *decreases* (see figure 5.15).

5.6 Clusters with a broader mass spectrum with a MBH

The logical next step to the systems studied in previous sections is that of a multi-mass component cluster harbouring a central seed BH that grows due to stellar accretion.

In this final section we extend our analysis to systems for which we use an evolved mass function of an age of about 10 Gyr. We consider a mass spectrum with stellar remnants. We employ a Kroupa IMF (Kroupa et al., 1993; Kroupa, 2001) with M_{zams}^2 from 0.1 to $120 M_\odot$ with the turn-off mass of $1 M_\odot$. We have chosen the following values for the exponent according to the mass interval,

$$\alpha = \begin{cases} 1.3, & 0.008 \leq m_*/M_\odot < 0.5 \\ 2.2, & 0.5 \leq m_*/M_\odot < 1 \\ 2.7, & 1 \leq m_*/M_\odot \leq 120. \end{cases} \quad (5.13)$$

And with the following distribution of components,

²The zero age main sequence (ZAMS) corresponds to the position of stars in the Hertzsprung-Russell diagram where stars begin hydrogen fusion.

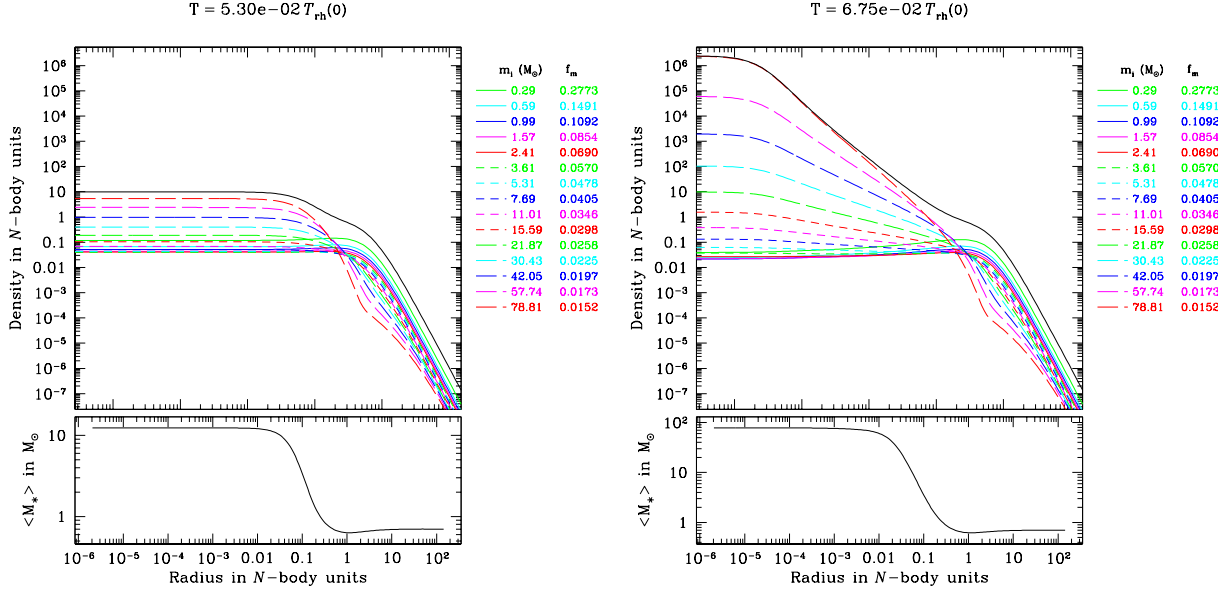


Figure 5.13: Same situation as in figure 5.12 but at later times. See text for explanations

- (i) Main sequence stars of $0.1 - 1 M_{\odot}$ (~ 7 components)
- (ii) White dwarfs of $\sim 0.6 M_{\odot}$ (1 component)
- (iii) Neutron stars of $\sim 1.4 M_{\odot}$ (1 component)
- (iv) Stellar black holes of $\sim 10 M_{\odot}$ (1 component)

The defined IMF evolves and gives us at later times an evolved populations with compact remnants. This means that main sequence stars can transform into white dwarfs, neutron stars or stellar black holes according to their masses. If m_{MS} is the mass of a MS star, we have defined the following mass ranges for the evolution into compact remnants:

- (a) White dwarfs in the range of $1 \leq m_{\text{MS}}/M_{\odot} < 8$
- (b) Neutron stars for masses $8 \leq m_{\text{MS}}/M_{\odot} < 30$
- (c) Stellar black holes for bigger masses, $\geq 30 M_{\odot}$

As we already mentioned, we place at the

centre a seed BH whose initial mass is of $50 M_{\odot}$. The initial model for the cluster is a Plummer sphere with a Plummer radius $R_{\text{pl}} = 1$ pc. The total number of stars in the system is $\mathcal{N}_{\text{cl}} = 10^6$.

The presence of a small fraction of stellar remnants may greatly affect the evolution of the cluster and growth of the BH because they segregate to the centre from which they expel MS stars but, being compact cannot be tidally disrupted. This kind of evolution is shown in Figs. (5.16) and (5.17).

figure 5.16 shows us the time evolution of different Lagrange radii with 0.1, 10, 50, 80 % of the mass of each component. Here the core collapse happens at about $T = 0.18 T_{\text{rh}}(0)$. The henceforth re-opening out is due BH accretion.

In figure 5.17, we plot the density profiles of the system before and after the post-collapse

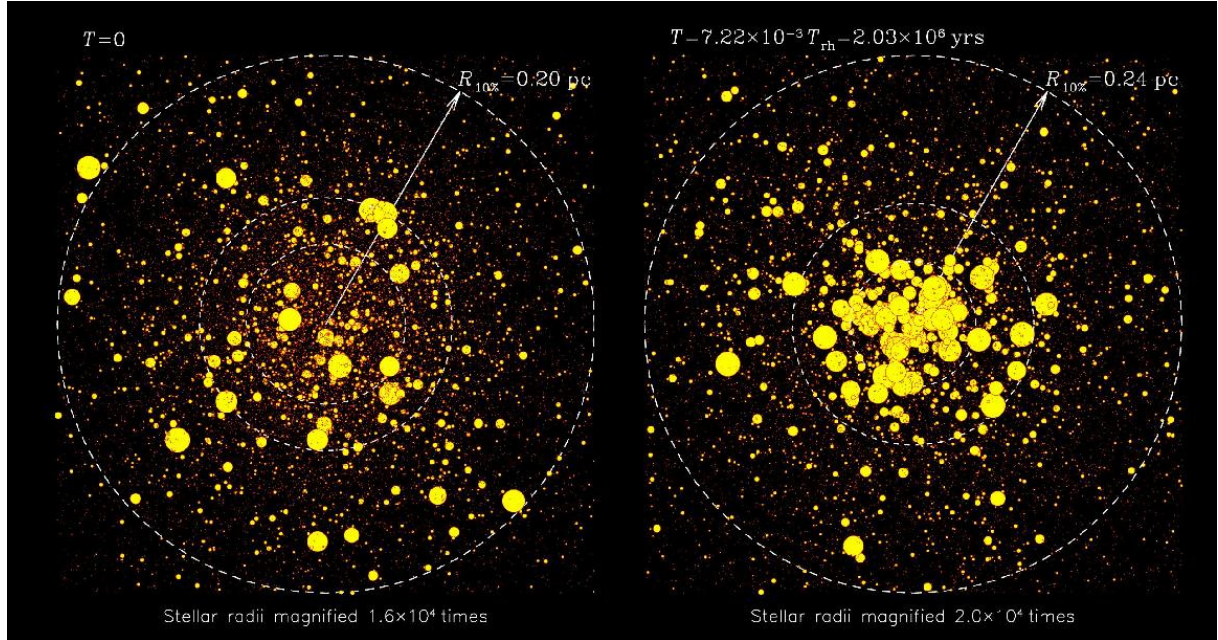


Figure 5.14: Illustration of core-collapse in multi-mass systems treated with a Monte Carlo approach (courtesy of M. Freitag)

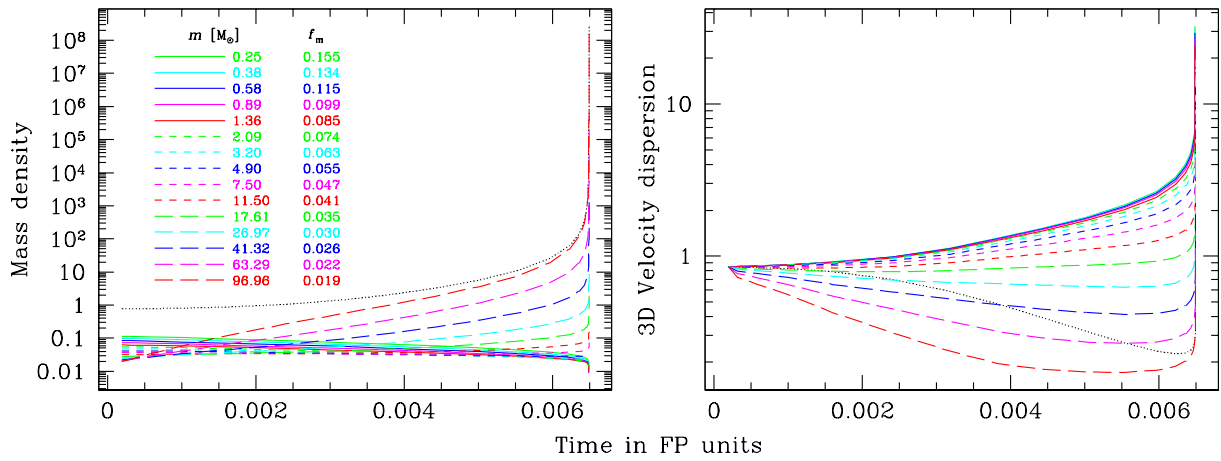


Figure 5.15: Evolution of the central density and 3D-velocity dispersion in a model with 15 components (see text for further explanations)

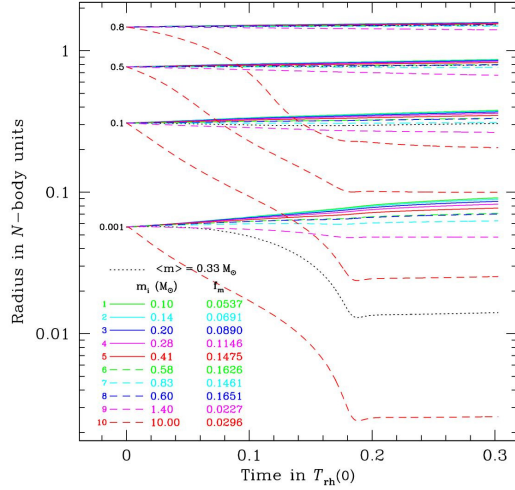


Figure 5.16: Lagrange radii evolution for a 10 components calculation with a seed BH and stellar remnants

phase. We can see that the slope of $\rho \propto R^{-7/4}$ on account of the cusp of stellar BHs that has formed around the central BH. We can see how the different components redistribute in the process, as we mentioned at the beginning of this chapter. We can see how the BH dominates the dynamics at the centre.

We can study how the system evolves from the point of view of the distribution of kinetic energies between the different components of the clusters during the process of mass segregation.

In figure 5.18 we show the evolution of the “temperature” of the system, defined as the mean kinetic energy per star divided by the global mean mass (in order to have a “temperature” expressed in square velocity units). In this plot we show the core collapse situation correspond-

ing to Figs. (5.16) and (5.17): We consider a 10 component cluster with the characteristics explained before. The mean temperature is defined like $\sum n_i \cdot T_i / \sum n_i$, where n_i is the numerical local density for component i . This corresponds to the mean kinetic energy per star. We can see in the plot that it is about the same as the heaviest component in the inner regions, even though one could think that segregation should not have set in in the beginning. This is due to the fact that the moment does not correspond to exactly the initial moment, $T = 0$. On the right, we can already see how the mean central temperature moves back (solid black line) and the most massive component (dashed red line) increases. For later times, the kinetic energies of the different components rise at the inner part of the cluster and the most massive one approaches the sum of all of them. This is even more evident in the last plot, where all components’ temperatures have sunken except for the corresponding to the most massive one. At the exterior zones, the mean temperature is much lower than the most heavy component because the system did not have evolution towards equipartition and, so, the velocity dispersion σ_v of the heavy components is the same that the other’s component velocity dispersion but their kinetic energy is much larger (in terms of mass).

At the current moment we are tackling with these and another configurations, but we have to first resolve the problem of BH growth and grid resolution, because as the BH grows, the grid gets too close to the centre. This problem is being now studied to carry on with new calculations from the cluster re-expansion onwards caused by the BH growth.

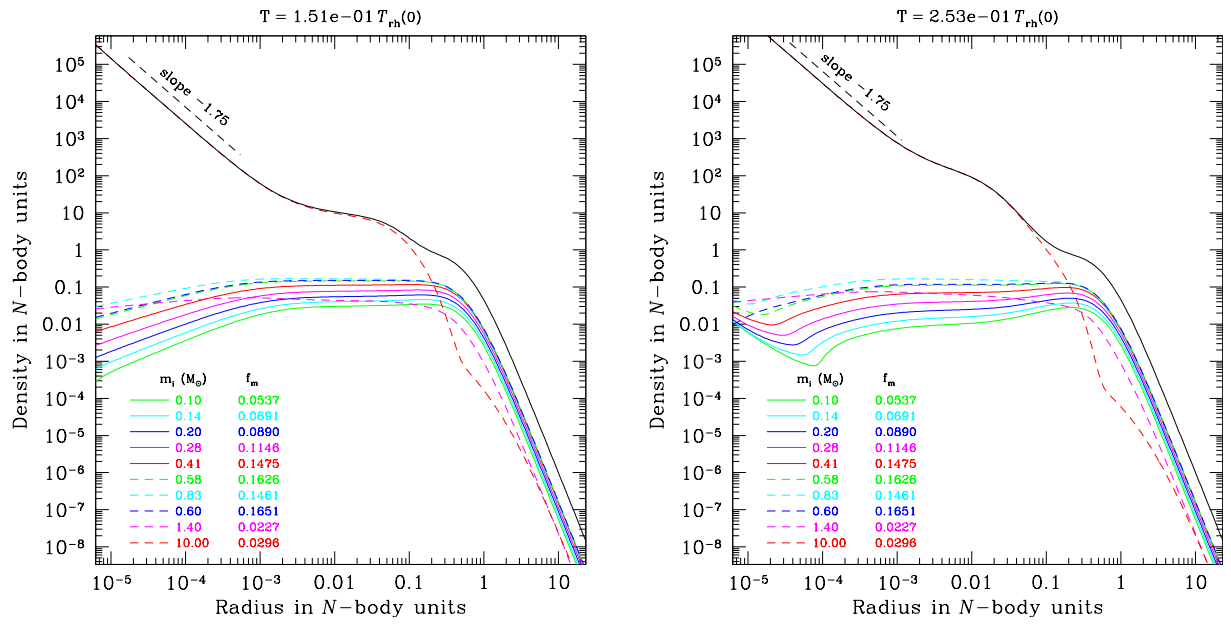


Figure 5.17: Density profiles in a multi-mass system with seed BH before and after core-collapse (see text)

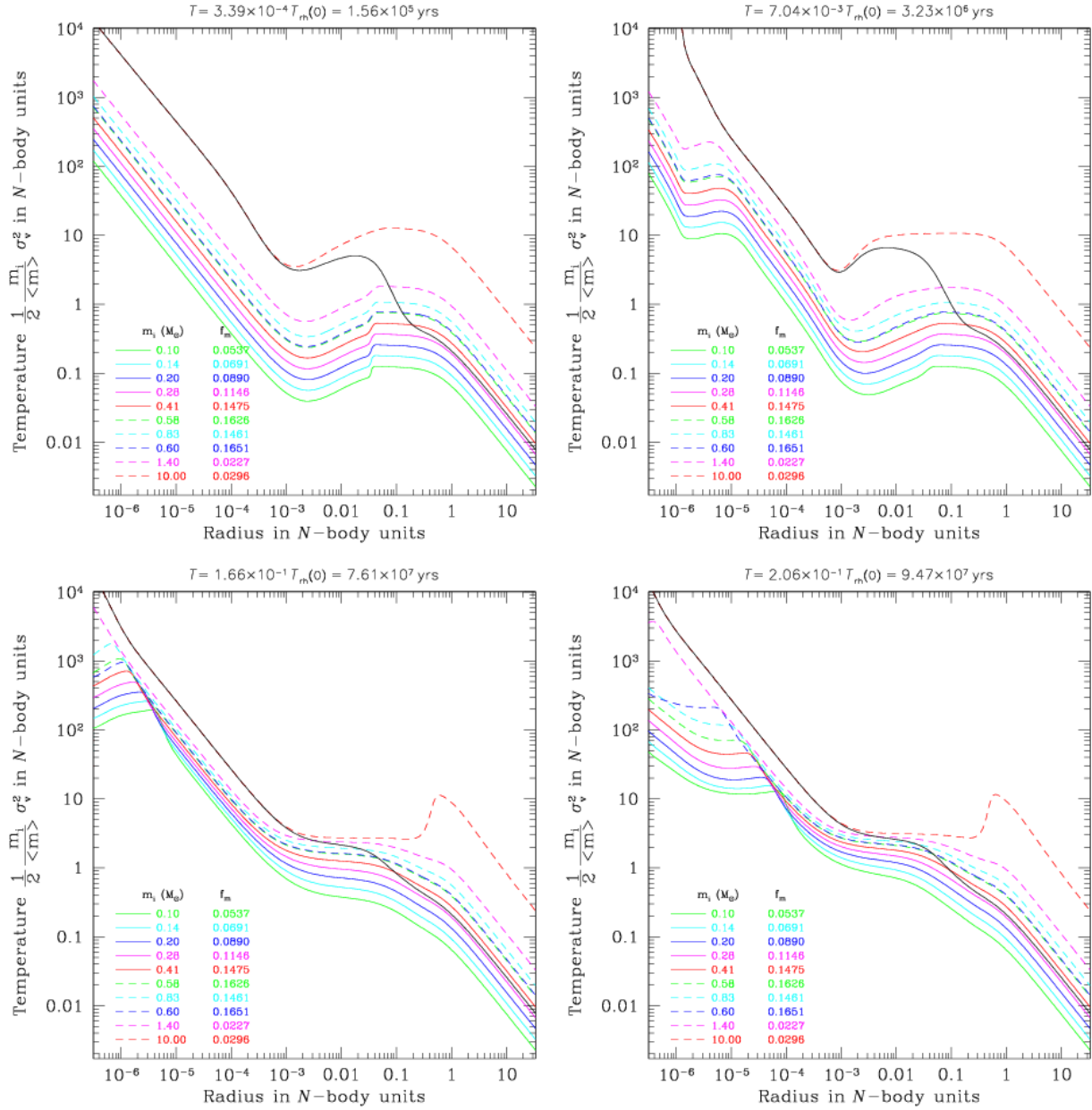


Figure 5.18: Different moments in the evolution of the cluster's temperature for a 10 stellar components system with a seed BH.

Chapter 6

Introduction to EMRIs

After the first chapters we have a good understanding of the fundamentals of two-body relaxation in dense stellar systems, including mass segregation and dynamical friction, which could be roughly described as “relaxation when we have a large mass ratio”. In this chapter we retake the subject of capture of compact objects by a massive black hole. In this chapter we will have a look at the “standard” problem, which we can address within some limitations with the basics of relaxation theory.

6.1 A hidden stellar population in galactic nuclei

The question about the distribution and capture of stellar black holes at the Galactic Centre has been addressed a number of times by different authors, from both a semi- or analytical and numerical standpoint (Sigurdsson and Rees, 1997; Miralda-Escudé and Gould, 2000; Freitag, 2001a, 2003b; Freitag et al., 2006b,a; Hopman and Alexander, 2006a; Amaro-Seoane et al., 2007; Preto and Amaro-Seoane, 2010; Amaro-Seoane and Preto, 2011). Addressing of this problem has direct bearing on a variety of astrophysical questions, including of course in-

spirals of compact objects onto the central MBH, but also on the distribution of X-ray binaries at the Galactic Centre, tidal disruptions of main sequence stars, and the behaviors of “source” stars. Even if we only consider single stellar black holes, the impact they can have on the S-stars is not negligible; a distribution of non-luminous matter around the Galactic Centre would have a clear fingerprint on their orbits. Current data are insufficient to detect such an extended non-luminous cusp which typically would induce a slight Newtonian retrograde precession (Mouawad et al., 2005), so that we will have to wait for future telescopes before we can hope to see such trajectory deflections. Weinberg et al. (2005) estimated that proposed 30 to 100 meter aperture telescopes will allow us to observe about three trajectory deflections per year between any of the monitored “source” stars and a stellar black hole.

The centermost part of the stellar spheroid, the *galactic nucleus*, constitutes an extreme environment for stellar dynamics. With stellar densities higher than $10^6 M_{\odot} \text{pc}^{-3}$, relative velocities in excess of 100 km s^{-1} the nucleus (unlike most of the rest of the galaxy) is the site of a variety of “collisional processes” – both close encounters and actual collisions between

stars, as we have seen in the previous chapters. The central MBH and the surrounding stellar environment interact through various mechanisms: some, like the accretion of gases liberated by stellar evolution or the adiabatic adaptation of stellar orbits as the mass of the MBH increases, are global; others involving the close interaction between a star and the MBH – EMRIs and stellar disruptions – are local in nature. As we have seen in chapter 4.4, to interact closely with the central MBH, stars have to find themselves on “loss-cone” orbits, which are orbits elongated enough to have a very close-in periapsis (Frank and Rees, 1976; Lightman and Shapiro, 1977; Amaro-Seoane and Spurzem, 2001).

The rate of tidal disruptions can be established (semi-)analytically if the phase space distribution of stars around the MBH is known (Magorrian and Tremaine, 1999; Syer and Ulmer, 1999; Wang and Merritt, 2004, for estimates in models of observed nearby nuclei). To account for the complex influence of mass segregation, collisions and the evolution of the nucleus over billions of years, detailed numerical simulations are required, however (David et al., 1987a,b; Murphy et al., 1991; Freitag and Benz, 2002; Baumgardt et al., 2004b; Freitag et al., 2006b; Khalisi et al., 2007; Preto and Amaro-Seoane, 2010; Amaro-Seoane and Preto, 2011).

In the case of a gradual inspiral following the “capture” of a compact object (i.e. an EMRI), the situation becomes even more complex, even in the idealized case of a spherical nucleus with stars all of the same mass. As the star spirals down towards the MBH, it has many opportunities to be deflected back by two-body encounters on to a “safer orbit” (i.e. an orbit which does not lead to gravitational capture

Alexander and Hopman, 2003), hence even the definition of a loss-cone is not straightforward. Once again, the problem is compounded by the effects of mass segregation, general relativity and resonant relaxation, to mention three main complications. As a result, considerable uncertainties are attached to the (semi-)analytical predictions of capture rates and orbital parameters of EMRIs.

Only self-consistent stellar dynamical modeling of galactic nuclei will allow us a better understanding of these questions. Some steps in that direction have been made by (Freitag, 2001b, 2003b,a) with Monte Carlo simulations¹. Later, Freitag et al. (2006b,a) improved upon these results. Yet this study neglected a direct estimation of EMRIs or “direct plunges”, due in part to the fact that, to follow stars on very eccentric orbits, one needs the combined effects of GW emission and relaxation on timescales much shorter than the capabilities of the numerical Monte-Carlo code. Much work remains to confirm these results and improve on them with a more accurate treatment of the physics, to extend them to a larger domain of the parameter space and to more general situations, including non-spherical nuclei.

Classical studies based on approximate stellar dynamics methods that neglect, in particular, the motion of the central MBH and strong 2-body interactions, indicate that, in dense enough cluster, a “seed” BH (in the IMBH mass range) could swallow a significant fraction of the cluster mass, thus becoming an MBH over the span of a few Gyrs (Murphy et al., 1991; Freitag and

¹We do not include here the work of Tal Alexander, Clovis Hopman and collaborators because in this chapter we are limiting the analysis to “standard” two-body theory; i.e. we do not address the effects of resonant relaxation. In the next chapter we study this crucial effect.

Benz, 2002; Amaro-Seoane et al., 2004b). More detailed, higher fidelity N -body simulations of relatively small clusters (Baumgardt et al., 2004a,b) have not confirmed this classical result, calling for a critical re-examination and improvement of approximation techniques, the only ones that can cope with the high particle numbers found in massive clusters such as galactic nuclei. It has also been suggested that some processes, such as the effects of chaotic orbits in a slightly non-spherical potential, may effectively keep the loss-cone orbits populated. In this case disruptions and captures can efficiently feed the central BH and produce the $M - \sigma$ relation (Zhao et al., 2002; Merritt and Poon, 2004b).

Understanding the astrophysical processes within galacto-centric clusters that give rise to EMRI events has significant bearing on LISA's applicability to this science. Accurate predictions of the event rate are important for preparing for LISA data analysis and design — many events lead to source-confusion, which must be dealt with, while a few events necessitate identifying weak sources in the presence of instrumental noise (Amaro-Seoane et al., 2007). More importantly, LISA observations alone cannot decouple the mass distribution of the galactic black hole population from the mass-dependence of the EMRI rate within a single system. If we can improve our understanding of the latter, we improve LISA's utility as a probe of the former. In this chapter we elaborate in detail on the “standard” physics leading to sources of gravitational radiation in the milliHertz regime — i.e. in the bandwidth of a LISA-like detector — originating in two-body relaxation processes.

6.2 Fundamentals of EMRIs

An EMRI consists in the 0-th order approach to the problem, of a binary of two compact objects, a massive black hole (MBH) and a —typically— stellar black hole (SBH) describing a large number of cycles around the MBH as it approaches the last stable orbit (LSO), emitting important, coherent amounts of gravitational waves (GW) at every periapsis passage². After every 2π around the orbit, the semi-major axis decays a fraction proportional to the energy loss. After typically some 10^{4-5} cycles, the small body, the CO, plunges through the horizon of the MBH and the system is lost. The emission of GW finishes. This is what makes this system so attractive. We can regard it as a camera flying around a MBH taking extremely detailed pictures of the space and time around it. With one EMRI we are provided with a set of $\sim 10^{4-5}$ pictures from a binary, and the information contained in them will allow us also to know with an accuracy of no precedent in the history of astronomy about the mass of the system, the inclination, the semi-major axis, the spin, to mention some, and it will as well be an accurate test of the general theory of relativity.

The task seems to be worth doing it; we simply have to analyse a binary which decays slowly in time proportionally $\propto a^4$, where a is the semi-major axis. The work seems to be easy for such a big gain. The only point is that it is not as easy as it seems, because we need to understand how a star can become an EMRI in such a dynamically complex system as a galactic nucleus. Also, the EMRI might to suffer perturbations either from gas or from the stellar

²The systems emits gravitational radiation all the time, but the most important bursts of energy occur at periapsis

system (Kocsis et al., 2011; Amaro-Seoane et al., 2012c).

In figure 6.2 we show what systems missions such as LISA would be most sensitive to. Obviously, this is only an illustration and the data analysis of the signal will be much more complicated in reality but it is just an indication already that if the central MBH has a mass larger than $10^7 M_\odot$, then the signal, even at the last stable orbit (LSO) will have a frequency too low for detecting the system. On the other hand, if it is less massive than $10^4 M_\odot$, the signal will also be quite weak unless the source is very close. This is why one usually assumes that the mass range of MBHs of interest in the search of EMRIs for LISA is between $[10^7, 10^4] M_\odot$ (this picture is shifted towards lighter masses in the NGO/eLISA configuration Amaro-Seoane et al. 2012a,b). Nonetheless, if the MBH is rotating fast, then even if it has a mass larger than $10^7 M_\odot$, the LSO will be closer to the MBH and thus, even at a higher frequency the system should be detectable. This would push to the left the total mass to a few $\sim 10^7 M_\odot$. From the point of view of astrophysics, this range of masses corresponds to low-mass SMBHs. They are not easily detectable and we do not know much about them. There is however an exception to this statement: namely *our* MBH, the one at the centre of our Galaxy, with a mass of $\sim 3 - 4 \times 10^6 M_\odot$. It is sufficiently close to us to be well constrained and it falls well in the LISA range.

In figure 6.1 we have as a function of the total, non-redshifted mass³ of the binary, $M_1 + M_2$, we have the semi-major axis of the binary

³We hope to detect EMRIs up to $z \approx 1 - 2$ the most in the full LISA configuration, and to ≈ 0.7 with the NGO/eLISA, so that for the rest of this work we will simply neglect it.

(assuming that it is circular) and we depict the orbital frequency of the binary. Obviously, for the binary to be in the LISA band, it has to have a frequency of roughly –being generous– between 1 and 10^{-5} Hz. The emission of GW is more efficient as they approach the last stable circular orbit (LSCO), so that LISA will detect the sources when they are close to the LSCO line. The required total mass to observe systems with frequencies between 0.1 Hz and 10^{-4} is of $10^4 - 10^7 M_\odot$. For masses larger than $10^7 M_\odot$ the frequencies even close to the LSCO will be too low, so that their detection will be very difficult. On the other side, for a total mass of less than $10^3 M_\odot$ in principal we could detect them at an early stage but then the amplitude of the GW would be rather low. On the top of that, the existence of such massive black holes is uncertain.

In a spherical potential, at any given time the stars and compact objects in the nucleus simply orbit the MBH with their semi-major axes and eccentricities changing slowly, owing to 2-body relaxation. For an EMRI to occur, in this standard picture, 2-body relaxation has to bring a compact remnant on to an orbit with such a small periapsis distance that dissipation of energy by emission of GWs becomes significant.

If the object is on a very eccentric orbit but one for which the timescale for passage through periapsis, $t_{\text{peri}} \simeq (1 - e)^{3/2} P$, is less than $\sim 10^4$ s, the source will generate bursts of gravitational radiation in the LISA band each time the object passes through periapsis. However, such GW signals consist of bursts which can probably not benefit from coherent signal processing even if they repeat with a periodicity shorter than LISA mission duration. Only if

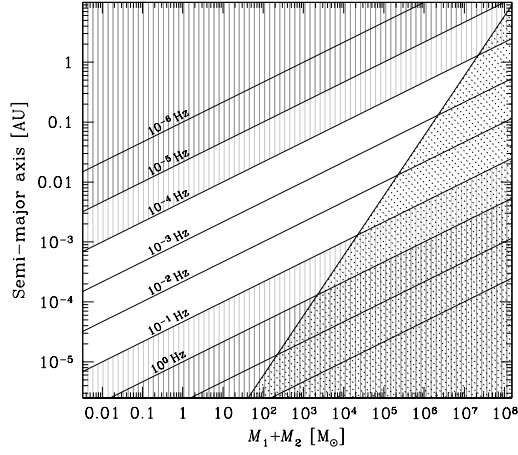


Figure 6.1: Frequency of a binary of total mass $M_1 + M_2$ against their semi-major axis and the corresponding frequencies. The solid, dark straight line delimites the LSCO, so that anything on the right of that line is of no interest for our purposes

they reside at the Milky Way centre is there a non-vanishing probability for LISA to detect such sources Hopman et al. (2007). An extra-galactic source is only likely to be detectable if it radiates continuously in the LISA band. As a rough guide, therefore, a detectable EMRI source must have an orbital frequency higher than about $f_{\text{LISA}} = 10^{-4}$ Hz, corresponding to the condition on the semi-major axis

$$a \lesssim 0.5 \text{ AU} \left(\frac{f_{\text{LISA}}}{10^{-4} \text{ Hz}} \right)^{-2/3} \left(\frac{M_{\bullet}}{10^6 M_{\odot}} \right)^{1/3}. \quad (6.1)$$

As there is no sharp cut-off in the predicted LISA sensitivity curve at 10^{-4} Hz, a strong source might be detectable at a lower frequency.

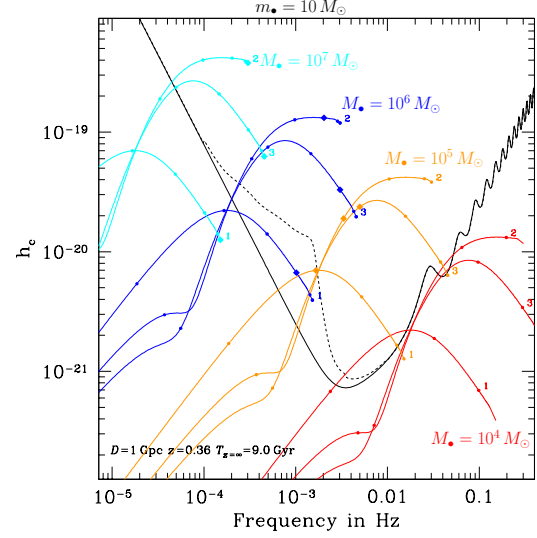


Figure 6.2: LISA's sensitivity window and four EMRI signals. The groups of colour correspond to the 1st, 2nd and 3rd harmonic in the quadrupole approximation for a SBH of $10 M_{\odot}$ inspiralling on to a MBH of mass $10^7 M_{\odot}$ (cyan, left “cascade” of harmonics), $10^6 M_{\odot}$ (blue, second group from the left), $10^5 M_{\odot}$ (orange, third cascade) and $10^4 M_{\odot}$ (red cascade, first from the right). In each case, the distance to the source has been set up to 1 Gpc

Not all objects with an inspiral time by GW emission shorter than a Hubble time will end up as EMRIs. This is because, although relaxation can increase the eccentricity of an object to very high values, it can also perturb the orbit back to a more circular one for which GW emission is completely negligible. Typically, neglecting GW emission, it takes a time of order $t_{\text{rlx}} \ln(1 - e)$ for an orbit to reach a (large) eccentricity e through the effects of 2-body relaxation. However, the periastris distance $R_p = a(1 - e)$ can be significantly altered by relaxation on a timescale $t_{\text{rel,p}} \simeq (1 - e) t_{\text{rlx}}$, so

the condition for a star to become an EMRI is that it moves onto an orbit for which the timescale for orbital decay by GW emission, τ_{GW} (see Eq. 6.11) is sufficiently shorter than $(1 - e) t_{\text{rlx}}$. If the semi-major axis of the orbit is too large, this condition cannot be obeyed unless the star actually finds itself on an unstable, plunging orbit, with $e \geq e_{\text{pl}}(a) \equiv 1 - 4R_{\text{Schw}}/a$ where R_{Schw} is the Schwarzschild radius of the MBH. The very short burst of gravitational radiation emitted during a plunge through the horizon can only be detected if originating from the Galactic centre Hopman et al. (2007). Coherent integration of the GW signal for $> 10^4$ cycles with a frequency in LISA band is required for detection of extragalactic EMRIs. Therefore a central concern in the determination of EMRI rates is to distinguish between plunges and progressive inspirals (Hils and Bender, 1995; Hopman and Alexander, 2005a).

The situation for EMRI production in the standard picture is more complicated than that of tidal disruptions by the MBH (e.g., Rees (1988); Magorrian and Tremaine (1999); Syer and Ulmer (1999); Wang and Merritt (2004)) or GW bursts from stars on very eccentric orbits Rubbo et al. (2006); Hopman et al. (2007) because these processes require a single passage within a well-defined distance R_{enc} from the MBH to be “successful”. In such cases, at any distance from the centre and for any given modulus of the velocity, as mentioned, there exists a “loss cone” inside which the velocity vector of a star has to point for it to pass within R_{enc} of the MBH Frank and Rees (1976); Bahcall and Wolf (1977); Lightman and Shapiro (1977); Amaro-Seoane and Spurzem (2001). In contrast, an EMRI is a progressive process which will only be successful (as a potential source for LISA) if the stellar

object experiences a very large number of successive dissipative close encounters with the MBHs Alexander and Hopman (2003). There is no well-defined loss cone for such a situation.

As described above, a source becomes an EMRI when the orbital period becomes shorter than about 10^4 s. Even at those distances, the evolution of such a tight orbit could in principle be modified by other stars (Amaro-Seoane et al., 2012c), but based on our current knowledge of nuclei it is an extreme situation, because it requires a second star being very close to the EMRI. It is not so unlikely at earlier stages of the inspiral as 2-body relaxation, experienced mostly at apoapsis can easily induce a change in the periapsis distance large enough to either render GW emission completely insignificant or, on the contrary, cause a sudden plunge into the MBH Hils and Bender (1995); Hopman and Alexander (2005a)⁴. The condition for successful inspiral is not that the periapsis distance must be sufficiently small, like for tidal disruptions or GW bursts, but that the timescale for orbit evolution by emission of GWs (see Eq. 6.11) is sufficiently shorter than the timescale over which 2-body relaxation can affect the periapsis distance significantly,

$$\tau_{\text{GW}} < C_{\text{EMRI}} (1 - e) t_{\text{rlx}}. \quad (6.2)$$

What “sufficiently shorter” means is the crux of the problem and is encoded in C_{EMRI} , a “safety” numerical constant that makes this condition sufficient ($C_{\text{EMRI}} < 1$). For a given semi-major axis a , one can define a critical eccentricity $\tilde{e}(a)$ above which GW emission dominates over orbital evolution due to relaxation and a corre-

⁴This is not strictly true, the spin of the MBH might “push out” the LSO and so Schwarzschild plunges are Kerr EMRIs; see Amaro-Seoane et al. (2012d).

sponding time scale

$$\tilde{\tau}(a) \equiv \tau_{\text{GW}}(\tilde{e}, a) \equiv C_{\text{EMRI}}(1 - \tilde{e}) t_{\text{rlx}} \quad (6.3)$$

Plunging orbits have

$$e \geq e_{\text{pl}}(a) \equiv 1 - \frac{4R_{\text{Schw}}}{a}, \quad (6.4)$$

so EMRIs (as opposed to direct plunges) can only happen if $e_{\text{pl}}(a) > \tilde{e}(a)$. This defines a critical semi-major axis which is a typical value for an EMRI at the moment orbital evolution starts being dominated by GW emission,

$$a_{\text{EMRI}} = 5.3 \times 10^{-2} \text{ pc } C_{\text{EMRI}}^{2/3} \times \left(\frac{t_{\text{rlx}}}{10^9 \text{ yr}} \right)^{2/3} \left(\frac{m}{10 M_{\odot}} \right)^{2/3} \left(\frac{M_{\bullet}}{10^6 M_{\odot}} \right)^{-1/3} \quad (6.5)$$

The corresponding eccentricity is given by

$$1 - e_{\text{EMRI}} = 7.2 \times 10^{-6} C_{\text{EMRI}}^{-2/3} \times \left(\frac{t_{\text{rlx}}}{10^9 \text{ yr}} \right)^{-2/3} \times \left(\frac{m}{10 M_{\odot}} \right)^{-2/3} \left(\frac{M_{\bullet}}{10^6 M_{\odot}} \right)^{4/3} \quad (6.6)$$

The situation is represented in figure 6.5 in the semi-major axis, eccentricity plane. We plot schematically the trajectory for a typical EMRI evolving according to the standard scenario (labelled “1-body inspiral” to distinguish it from the binary tidal separation scenario discussed in § 7.4). Initially the values of a and e random walk due to 2-body relaxation. As it

takes of order t_{rlx} to change a by a factor of 2 but only $(1 - e)t_{\text{rlx}}$ to change the value of $1 - e$ (and hence the periapsis), the random walk seems more and more elongated in the horizontal direction, the smaller the value of $1 - e$. It is much more likely for a star to cross over to the plunging or GW-dominated region by acquiring a very high eccentricity than by shrinking a significantly. Typically an EMRI “progenitor” starts with a semi-major axis slightly lower than a_{EMRI} . It takes on average a time of order $\ln(1 - \tilde{e})^{-1} t_{\text{rlx}} \simeq 10 t_{\text{rlx}}$ for relaxation to produce an eccentricity such that GW emission becomes dominant. From that point, the object will follow a path closer and closer to a pure inspiral (approximated by Peters equations Peters 1964). At larger a values, inspirals are practically impossible because GW emission is not significant in comparison to relaxation even on plunge orbits. Unless they first shrink their orbit through 2-body relaxation, these objects will be swallowed by the MBH on a direct plunge. Inspirals starting with $a \ll a_{\text{EMRI}}$ are rare because, for a density cusp $n \propto r^{-\alpha}$ with $\alpha \simeq 1.4 - 1.8$ Baumgardt et al. (2004a,b); Freitag et al. (2006c); Hopman and Alexander (2006c), the number of stars per unit $\log(a)$ is roughly $dN_{\star}/d(\log a) \propto a^{(3-\alpha)}$. Also, as one goes inwards, the value of α is lowered by the progressively larger plunge loss cone (Lightman and Shapiro, 1977; Amaro-Seoane et al., 2004b). In other words, the stellar density is reduced there (in comparison to a pure power law) because to come and populate this region a star has to spend several relaxation times drifting down in energy while avoiding entering the GW-dominated region and inspiraling quickly.

Implementing this basic scenario in various ways (see § 8.7), several authors have es-

estimated the rate at which stellar remnants are captured by the central MBH, with results between $\sim 10^{-6} - 10^{-8} \text{ yr}^{-1}$ for a $10^6 M_\odot$ central black hole Hils and Bender (1995); Sigurdsson and Rees (1997); Ivanov (2002); Hopman and Alexander (2005a). When combined with the uncertainty in the number density of massive black holes with $\mathcal{M}_\bullet < \text{few} \times 10^6 M_\odot$, the net predicted number of detections that LISA spans over three orders of magnitude, from a few to a few thousand events per year.

We note, incidentally, that even in the LISA band (in the final year of inspiral), the eccentricity of the typical EMRI in the standard picture is high enough that a large number of harmonics are likely to contribute to the gravitational waves Freitag (2003b); Barack and Cutler (2004); Hopman and Alexander (2005a). In addition, the orbital plane of the EMRIs is unlikely to be significantly correlated with the spin plane of the MBH. These characteristics are distinct from those in non-standard scenarios (discussed below), leading to optimism that some aspects of the nuclear dynamics could be inferred from just a few events.

The word “capture” is sometimes used to refer to EMRIs, but this is misleading as, in the standard picture, stellar objects are not captured by emission of GWs. They are already bound to the MBH when they are brought into the GW-dominated regime by 2-body relaxation. A star originally unbound to the MBH, with energy $\frac{1}{2}v^2$, will be left bound to it by GW emission if it passes with a periaapsis distance smaller than

$$r_{\text{capt}} \approx 5R_{\text{Schw}} \left(\frac{m}{10 M_\odot} \right)^{2/7} \left(\frac{\mathcal{M}_\bullet}{10^6 M_\odot} \right)^{-2/7} \left(\frac{v}{100 \text{ km/s}} \right)^{-4/7}. \quad (6.7)$$

However, in most cases the star will be left on too wide an orbit. In order to become an EMRI (rather than experience a direct plunge), the semi-major axis has to be smaller than a few 10^{-2} pc (see figure 6.5 and Eq.6.5), requiring a passage within a distance

$$r_{\text{capt, EMRI}} \approx 3R_{\text{Schw}} \left(\frac{m}{10 M_\odot} \right)^{2/7} \left(\frac{\mathcal{M}_\bullet}{10^6 M_\odot} \right)^{-4/7} \left(\frac{a_{\text{capt}}}{0.05 \text{ pc}} \right)^{2/7}. \quad (6.8)$$

Therefore for $\mathcal{M}_\bullet \ll 10^6 M_\odot$ there is a possibility of capturing unbound (or loosely bound) stars directly on to EMRI orbits. To our knowledge, the contribution of this channel to EMRI rates has not been estimated but is probably small because it is present only for the lowest-mass MBHs in the LISA range, although we note that it would be on the “sweet spot” of the new NGO/eLISA configuration (Amaro-Seoane et al., 2012a,b), so that this requires further investigation.

6.3 Orbital evolution due to emission of gravitational waves

Consider a binary with component masses m_1 and m_2 , which thus has total mass $M = m_1 +$

6.3 Orbital evolution due to emission of gravitational waves

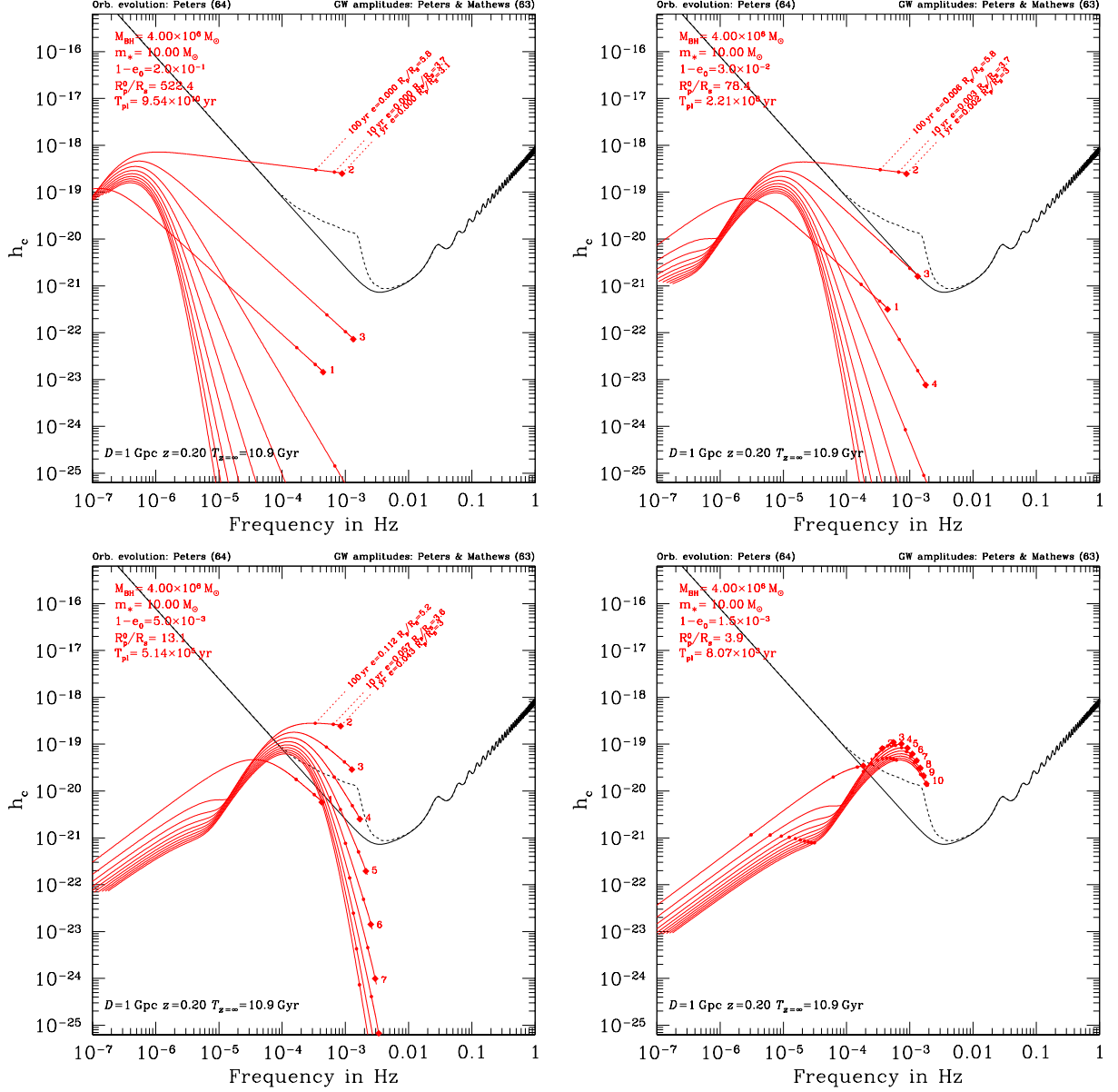


Figure 6.3: Characteristic amplitude of the first harmonics of the quadrupolar gravitational radiation emitted during the inspiral of a stellar-mass BH of $m_* = 10 M_\odot$ (m_* in the plot) into a MBH of mass $M_{\text{BH}} = 4 \times 10^6$ (MBH in the plot). We assume the source is at a distance $D = 1 \text{ Gpc}$. We indicate the noise curve $\sqrt{f} S_h(f)$ for a LISA-like detector (Larson et al., 2000; Larson, 2003), with the Galactic binary white dwarf confusion background in dashed line (Bender and Hils, 1997). Note that the height of the point for the amplitude above the curve does *not* represent the SNR (see text). From the top to the bottom and from left to right, the panels represent a binary which starts at a semi-major axis of 10^{-3} pc and we change the eccentricity, $e = 0.8, 0.97, 0.995, 0.9985$. We show for each panel the ratio R_p^0/R_s , the initial periastris distance over the Schwarzschild radius of the system. For the first three panels we display three moments in the evolution for which the time to coalescence in the is 100, 10 and 1 yr.

m_2 and reduced mass $\mu = m_1 m_2 / M$. Suppose that its semi-major axis is a and eccentricity is e . The Peters equations for gravitational wave emission from a Keplerian orbit Peters (1964) give

$$\left\langle \frac{da}{dt} \right\rangle = -\frac{64}{5} \frac{G^3 \mu M^2}{c^5 a^3 (1-e^2)^{7/2}} \left(1 + \frac{73}{24} e^2 + \frac{37}{96} e^4 \right) \quad (6.9)$$

and

$$\left\langle \frac{de}{dt} \right\rangle = -\frac{304}{15} e \frac{G^3 \mu M^2}{c^5 a^4 (1-e^2)^{5/2}} \left(1 + \frac{121}{304} e^2 \right). \quad (6.10)$$

We note that the Peters formalism does not capture the orbital evolution in the strong-field regime, before plunge. In particular, for EMRIs around a spinning MBH, a slight *increase* in eccentricity might occur in the late evolution Gair and Glampedakis (2006). This does not affect the present discussion. From Eq.6.10, the characteristic time to change the eccentricity is

$$\begin{aligned} \tau_{\text{GW}} &= \frac{e}{|de/dt|} \approx \frac{15}{304} \frac{c^5 a^4 (1-e^2)^{5/2}}{G^3 \mu M^2} \\ &\approx 8 \times 10^{17} \text{ yr} \left(\frac{M_\odot}{\mu} \right) \left(\frac{M_\odot}{M} \right)^2 \\ &\quad \left(\frac{a}{1 \text{ AU}} \right)^4 (1-e^2)^{5/2}. \end{aligned} \quad (6.11)$$

Here we neglect the near-unity factor $(1+121e^2/304)$.

We can rewrite this in terms of gravitational wave frequency. Let us consider in particular

the frequency emitted at periapsis. If the orbit is substantially eccentric, then the orbital frequency at that point will be approximately $\sqrt{2}$ times the circular frequency at that radius (because the speed is $\sqrt{2}$ times greater than a circular orbit). If we designate a maximum gravitational wave frequency f_{max} to be double the frequency at periapsis, then

$$f_{\text{max}} \approx \frac{1}{\pi} \left[\frac{2GM}{(a(1-e))^3} \right]^{1/2}. \quad (6.12)$$

Therefore

$$\begin{aligned} a^4 &= 0.75 \text{ AU}^4 \left(\frac{M}{10^6 M_\odot} \right)^{4/3} \left(\frac{f_{\text{max}}}{10^{-4} \text{ Hz}} \right)^{-8/3} \\ &\quad (1-e)^{-4}, \end{aligned} \quad (6.13)$$

and

$$\begin{aligned} \tau_{\text{GW}} &\approx 6 \times 10^2 \text{ yr} \left(\frac{\mu}{10^3 M_\odot} \right)^{-1} \left(\frac{M}{10^6 M_\odot} \right)^{-2/3} \\ &\quad \left(\frac{f_{\text{max}}}{10^{-4} \text{ Hz}} \right)^{-8/3} (1+e)^{5/2} (1-e)^{-3/2} \\ &\approx 3 \times 10^3 \text{ yr} \left(\frac{\mu}{10^3 M_\odot} \right)^{-1} \left(\frac{M}{10^6 M_\odot} \right)^{-2/3} \\ &\quad \left(\frac{f_{\text{max}}}{10^{-4} \text{ Hz}} \right)^{-8/3} (1-e)^{-3/2} \end{aligned} \quad (6.14)$$

where in the last line we assume a relatively high eccentricity, so that $1+e \approx 2$.

A classic EMRI, with $M = 10^4 - 10^7 M_\odot$ and $\mu = 1 - 10 M_\odot$, could have a significant eccentricity if (as expected in galactic nuclei) the orbits come in from large distances, $a > 10^{-2} \text{ pc}$ with $e \gtrsim 0.9999$. Hopman and Alexander Hopman and Alexander (2005a) made an

estimate of the distribution of eccentricities for one body inspiral and their results showed that it is skewed to high- e values, with a peak of the distribution at $e \sim 0.7$, at an orbital period of 10^4 s. On the other hand, following a binary separation event (and possibly the tidal capture of giant's core), the compact star is deposited on an orbit with semi-major axis of order a few tens to a few hundreds of AU. In this case, the GW-dominated regime is reached with an eccentricity smaller than 0.99 and the orbit should be very close to circular when it has shrunk into LISA band. Such typical orbital evolutions for EMRIs are shown in figure 6.5.

6.4 Decoupling from dynamics into the relativistic regime

In the late stage of the inspiral, a binary may become a detectable source of GWs. The characteristic amplitude of the gravitational radiation from a source emitting at frequency f is

$$h_c = \frac{(2\dot{E}/\dot{f})^{1/2}}{\pi D} \quad (6.15)$$

where D is the distance to the source, \dot{E} is the power emitted and \dot{f} the time derivative of the frequency (Finn and Thorne, 2000). With this definition, the signal-to-noise ratio (SNR) of an event is obtained, assuming ideal signal processing, by the integral⁵

$$(\text{SNR})^2 = \int_{f_1}^{f_2} \frac{h_c^2(f)}{f S_h(f)} d(\ln f) \quad (6.16)$$

⁵This is only meant as a very general illustrative description. We refer the reader to Amaro-Seoane et al. (2007); Babak et al. (2010) for an in-detail introduction to the problem of detection and parameter estimation of EMRIs.

where f_1 and f_2 are the initial and final frequencies of the source during the observation and $S_h(f)$ is the instrumental noise of the detector at frequency f (Phinney, 2002; Barack and Cutler, 2004).

In figure 6.3 we follow the signal emitted by a binary consisting of a Milky Way-lie MBH and a stellar BH during their GW-driven inspiral without taking into account any possible dynamical interaction; i.e. we only allow the system to evolve via gravitational radiation emission. We plot the five lowest harmonics of the quadrupolar emission in a rough approximation (see Peters and Mathews, 1963), only useful for illustrative purposes. In this figure, we assume a distance of 1 Gpc.

For low-eccentric captures only the $n = 2$ harmonic is detectable, during the last few years of inspiral. However, the small residual eccentricity induces a difference in the phase evolution of the $n = 2$ signal compared to a perfect circular inspiral (Amaro-Seoane and Freitag, 2006). If the source is followed from a time τ_{LSO} before merger until merger, the accumulated phase shift is

$$\Delta\psi_e \simeq \left(\frac{e_{10^{-4}\text{Hz}}}{0.05} \right)^2 \left(\frac{\tau_{\text{LSO}}}{1 \text{ yr}} \right)^{17/12} \left(\frac{\mathcal{M}_z}{10^3 M_\odot} \right)^{25/36}, \quad (6.17)$$

where $e_{10^{-4}\text{Hz}}$ is the eccentricity when the $n = 2$ signal has reached a frequency of 10^{-4} Hz and

$$\mathcal{M}_z \equiv (1+z) \frac{(\mathcal{M}_\bullet m_\bullet)^{3/5}}{(\mathcal{M}_\bullet + m_\bullet)^{1/5}} \quad (6.18)$$

is the redshifted chirp mass of the binary (Cutler and Harms, 2006). This means that in prin-

ciple we can easily distinguish between high-eccentricity captures and low-eccentricity captures. The implications of this result will become clear in the next chapters.

We display in figure 6.5 the last stable orbit in the effective Keplerian approximation ($R_p \simeq 4 R_{\text{Schw}}$ for $e \ll 0.1$, see Cutler et al. 1994 with a solid, thick diagonal line. The thin dotted blue lines are contours of constant time left until the final coalescence, T_{GW} in the Peters (1964) approximation. We show the years on the right. The thin diagonal green lines are the inspiral, capture orbits due *only* to the emission of GW. The upper dash-dotted red line shows $\tilde{e}(a)$, defined by $t_e = T_{\text{GW}}$ (Eq. 6.2 with $C_{\text{EMRI}} = 1$) assuming a constant value $t_{\text{rlx}} = 1$ Gyr. The lower dash-dotted red lines depict the same threshold times a factor 10, 100, 1000, 10,000 and 100,000. On the right hand side of these lines the evolution of the binary is driven chiefly by relaxation, GW emission is totally negligible and vice-versa; i.e. on the left hand side the evolution is led by the loss of energy in GWs. An interesting point is the intersection of the first of these red lines (the uppermost one) with the last stable orbit line. This is the transition between the so-called direct plunges and the EMRIs.

The thick, dashed black line shows the tidal disruption radius. Any extended star fording that radius will be torn apart by tidal forces of the MBH, which we assume to have a mass $M_\bullet = 4 \times 10^4 M_\odot$ (*MBH* in the plot). We then depict as an illustration the trajectory of a $10 M_\odot$ stellar BH (m_{bh} in the plot) inspiralling into the MBH. We can separate two kind of sources according to their astrophysical origin; namely low-eccentricity captures, stars captured by tidal binary separation and high-eccentricity captures, stemming from “simple” two-body re-

laxation. The later initially have a of order 100-1000 AU [$5 \times (10^{-4} - 10^{-3})$ pc] and $e = 0.9 - 0.99$ Miller et al. (2005a). The evolution of the eccentricity is a random walk leading after a timescale of about $T_{\text{rlx}} \ln(1 - \tilde{e})^{-1}$ to nearly-circular captures. The latter correspond to stars on capture orbits due to diffusion from large radii or capture by GW emission and have initially have a much larger value of a and hence a higher eccentricity. If a star has a semi-major axis $\gtrsim 5 \times 10^{-2}$ pc, it will not reach small orbital periods, i.e. it will not enter a milliHertz detector such as LISA unless a is reduced considerably, which in the context of “normal” relaxation theory, takes about a t_{rlx} .

A different way of looking at the same picture is by displaying the energy and angular momentum of the system. Working in terms of E and J has advantages that can be important to understanding some very subtle phenomena that possibly play a major role in the process of capturing stars. For this, we now summarise the useful illustration of Tal Alexander, which we reproduce in figure 6.4. To get close to the central MBH the faster way is to relax angular momentum than to relax energy. Let’s assume that we do not have any dissipation mechanism. In the figure we depict the phase-space of the system in terms of E and J and we use the convention that E is defined with a negative sign, so that high positive values of energy mean that the star is very close to the MBH. The red region represents the zone where the star cannot exist, i.e. we are closer to the MBH than the LSCO. The upper right diagonal line expresses the fact that for a value of E you can only have up to some maximum value of J_c , the J of a circular orbit. Our test star, a compact remnant, will suffer gravitational tugs when-

ever it is far away from the E and J edges. These tugs are random and originated by interacting with other stars that happen to have a very close position in phase-space and the scattering rate is very similar in both directions. This means that the time spent in one of the horizontal segments is approximately the same as the time spent in one of the vertical segments in the zig-zag trajectory displayed in the figure.

$$t_J \sim \left(\frac{J}{J_c(E)} \right)^2 t_E \sim t_E \quad (6.19)$$

i.e. the timescale to change J , t_J is approximately the same as the timescale to change E , t_E . This means that if every zig-zag represents a change over a fixed amount of time, say 10^9 yrs, the star will travel approximately the same length in one or the other way. If the star gets close to a very low J , which is statistically probable, then the picture changes: The rate at which the star will change J will be much shorter than at which it changes E . The star moves approximately in phase-space in one dimension, horizontally in the figure. If we wait long enough the star will eventually enter the loss-cone and plunge on to the central MBH “directly”. I.e. the source of GWs is lost after a few periastris passages, a few intense GW bursts and is not as interesting as a gradual, slowly inspiraling source. This picture corresponds to the general scenario that was described already a few decades ago, when people were investigating ways of feeding the MBH (Lightman and Shapiro, 1977; Cohn and Kulsrud, 1978).

However, if we have a dissipation process acting on to the star, which could be energy loss in the form of GWs as well as drag forces

originating in an accretion disc or, obviously also tidal forces created by the central MBH, the picture changes significantly. The process follows the same path and, at some point, the star reaches the region in which it is on a very radial orbit, i.e. where the zig-zag stops and we can approximate the curve by a horizontal line. Nonetheless, in this case, at every periastris passage, the star will emit an intense burst of GW and, thus, shrink its semi-major axis. If this happens “efficiently enough”, i.e. “fast enough” (we will elaborate on this later), the star is more and more bound to the central MBH and drifts away (goes up in the y axis of the figure). The danger of being scattered away from the capture orbit by other stars decreases more and more and the compact object finds itself on a safe inspiraling EMRI orbit. The precise details of the dynamics that lead to this situation determines the distribution of eccentricities that we can expect. The semi-major axis shrinks to the point that the source enters the “Detectable GW” regime (light blue band in the right panel of figure 6.4. As the source advances in that band, the period becomes shorter and shorter and, hence, the power (energy per unit of time) grows larger and larger, so that the gravitational radiation can be measured when it enters the band in frequency of the observatory.

The *statistical* orbital properties of the EMRI in the region where GW is prominent are fully determined by the transition phase between the region dominated by 2-body scattering processes (the right part of the curve) of the random walk in phase-space and the *deterministic* dissipation part of the capture trajectory, i.e. where the energy loss occurs.

As described in Hopman and Alexander (2005b),

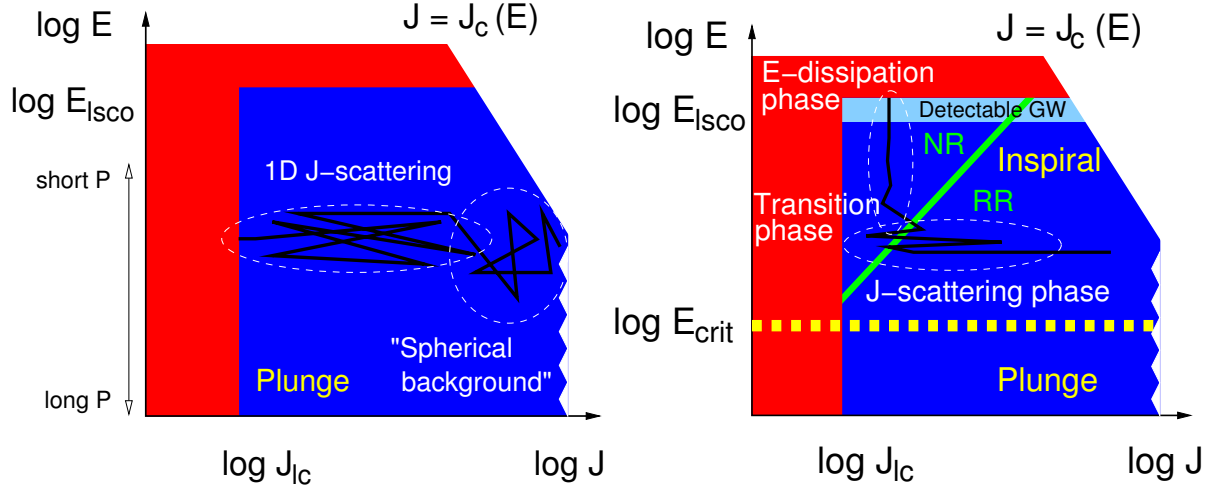


Figure 6.4: Plunge, inspiral and critical energy of an EMRI in phase-space. *Left panel: Direct plunge of a source. Right panel: Adiabatic inspiral of a source subject to dissipation of energy at periapsis and limiting critical energy* (image courtesy of Tal Alexander)

in this statistical treatment there is a critical energy, i.e. a certain distance from the central MBH, of the order $\sim 10^{-2}$ pc, that can be envisaged as the threshold between the two regions. This means that stars with energy below the yellow dashed line of the right panel of figure 6.4 will have “longer horizontal segments”, they will scatter faster in J than in E and then end up as direct plunges. They approach the central MBH in such a radial orbit that they are swallowed after one or, at most, a few intense bursts of GWs. This situation is reverted if the energy of the star is above the line; the star will spiral in adiabatically and it will not be perturbed out of the EMRI trajectory, with a significant amount of GW bursts at periapsis before coalescing with the MBH.

Hence and, again, statistically, at first order, one has to consider only stars whose energy falls within the critical region and we can

ignore all other stars, even if their E and J indicate that they are good candidates to EMRIs. Thus, *the event rate will be determined by the microphysics affecting the innermost volume around the MBH, of radius $\sim 10^{-2}$ pc*. As the reader will surely have guessed by now, the task is non-trivial.

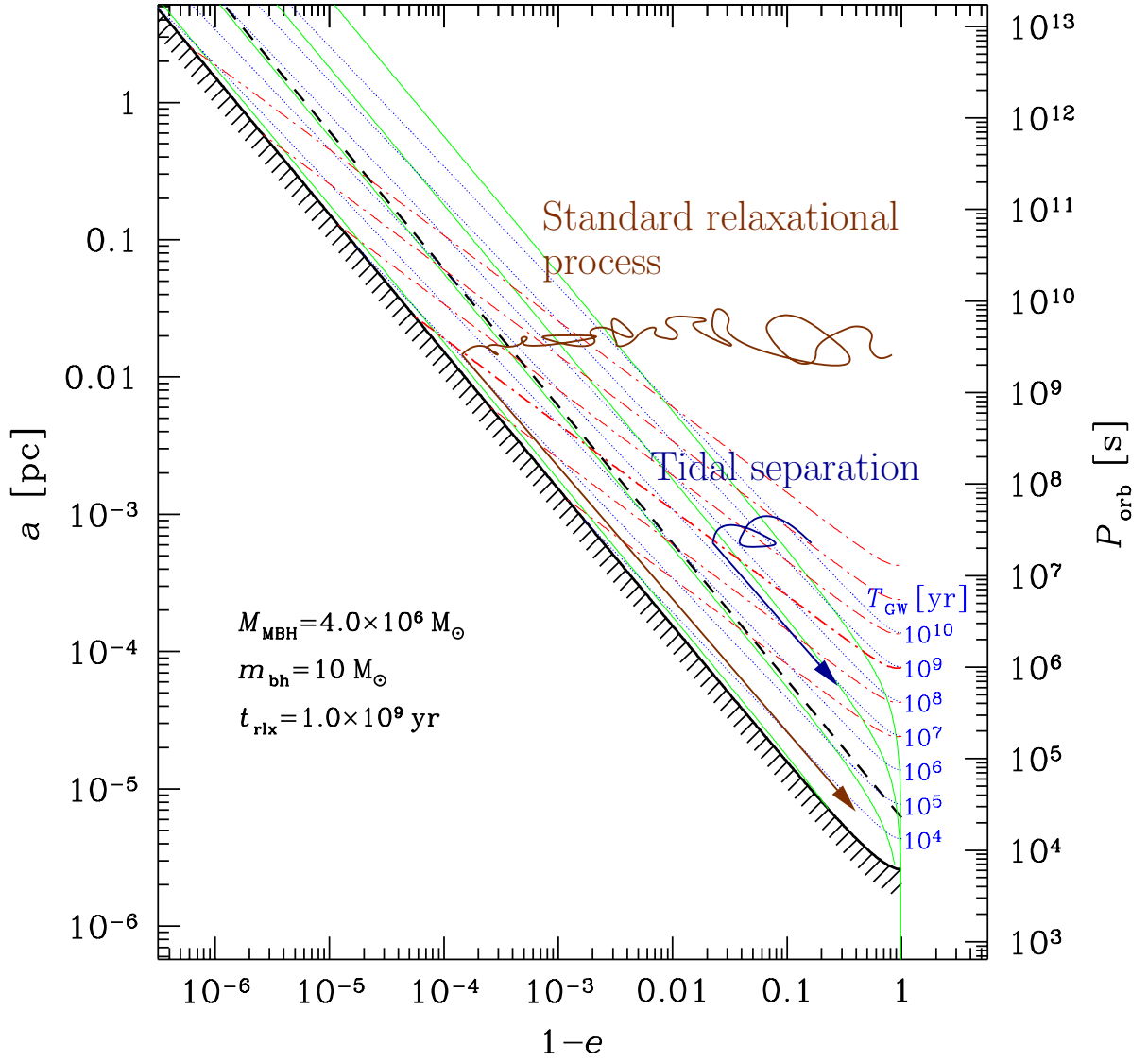


Figure 6.5: Capture trajectories in the $a - (1 - e)$ plane and tidal disruption limit. See text for a detailed explanation of the figure.

Chapter 7

Beyond the standard model of two-body relaxation

7.1 The standard picture

The reader will very surely have realised that the picture is much more complex than plain two-body relaxation. Quoting something that Sterling Colgate said once in Aspen,

“Do you know what the standard (American) model is? : One gallon per flush.”

Although Sterling was not directly referring to our standard model, of course. This means that, illustrating and enlightening as it might be, the standard model we have been describing so far is not exactly correct.

As the interest in a millihertz mission started to grow and develop, astrophysicists started to dedicate more and more time to a problem that, naively, was not very difficult. How do you get a small black hole into a massive black hole in a galactic nucleus? Now, some decades after the very first estimates, we have a much better and clear vision of the main phenomena at play in the process. Well before any space-borne mission is launched, our understanding

of theory related to stellar dynamics has become much broader and new, unexpected effects have emerged.

7.2 Coherent or resonant relaxation

¹In a gravitational potential with a high degree of symmetry as we have discussed previously, a test star will receive gravitational tugs from the rest of the field stars which are not totally arbitrary and hence do not add up in a random walk way, but *coherently*. As we have seen in chapter 3, the potential will prevent stellar orbits from evolving in an erratic way. In a two-body Keplerian system, a SBH will orbit around the MBH in a fixed ellipse. The stellar BH will not feel random gravitational tugs. It evolves coherently as the result of the action of the gravitational potential. When an

¹The reason for the title of this section is that probably the choice of “resonant” for this process is not a good one. Rauch and Tremaine (1996) coined this term thinking of the effect of a resonance between the radial and azimuthal periods in a Keplerian orbit. Tal Alexander has suggested the term *coherent relaxation*.

EMRI approaches the periapsis of its orbit, we can envisage the situation as a pure two-body problem; initially Newtonian but later GR effects must be taken into account as the periapsis grows smaller and smaller. Nonetheless, as the stellar BH goes back to the apoapsis, it will feel the surrounding stellar system, distributed in the shape of a cusp which grows in mass the further away we are from the periapsis. The time spent in the region in which we can regard this as a two-body problem is much shorter than the time in which the stellar BH will feel the rest of the stellar system. This is particularly true for the kind of objects of our interest, since the very high eccentricity implies a large semi-major axis. The time spent on periapsis is negligible as compared with the time spent on apoapsis. In that region, the stellar BH feels the graininess of the potential. The gravitational tugs from other stars will alter its orbit. The mean free path in J -space of that test stellar BH is very large and thus, it has a *fast* random walk. Both the magnitude and direction of J of the stellar blackhole are altered. When the modulus is changed but not the direction, we talk of “escalar” resonant relaxation, and correspondingly when the direction is changed but not the size, “vector” resonant relaxation.

A very radial orbit can become a very eccentric one, so that a compact object initially set on a potential EMRI orbit can be “pushed out” of it. In a more general case, a spherical potential and not only Keplerian, the orbits, as we have described before, are rosettes and averaged over time they are circular anuli. In that case we can change the direction of J but not the modulus. An eccentric orbit will stay eccentric, but any coherence that was there will

be washed out.

In particular, as illustrated in figure 7.1, in the potential of a point mass, orbits are frozen fixed ellipses that exert a continuous torque on the test star. A test star does not feel random kicks from all directions. When we add up the individual contributions coming from all the rest of stars on to the test star, there is a residual, non-negligible torque that will influence its evolution. The mean free path of the star in J space is very large. We will refer to this phenomenon as *scalar* coherent relaxation, because it can change both the magnitude of J and the inclination of the orbital plane of the test star. In this scenario it is a possible way to alter an initially very circular orbit and modify it in such a way that the test star will get very close to the MBH after the torques have acted. I.e. we open a new window for stars to fall into a capture orbit that will lead to an EMRI.

In a more general case, if we have a potential that is simply spherical but not necessarily Keplerian (a point mass), the field stars, the perturbing orbits to the test star, describe rosettes -as we have seen- and averaged over time they can be approximated by a set of anuli that share a centre. From a secular point of view, the masses are smeared over those anuli which create torques that do not change the magnitude of J but they do change the orientation because of reasons of symmetry (Rauch and Tremaine, 1996; Rauch and Ingalls, 1998; Hopman and Alexander, 2006a). Hence a circular test star will keep a negligible eccentricity and it will *not* approach the central MBH. Any coherence that was present in the system will nonetheless be destroyed. We will refer to this as *vectorial* coherent relaxation. From the standpoint of EMRI production, though, this

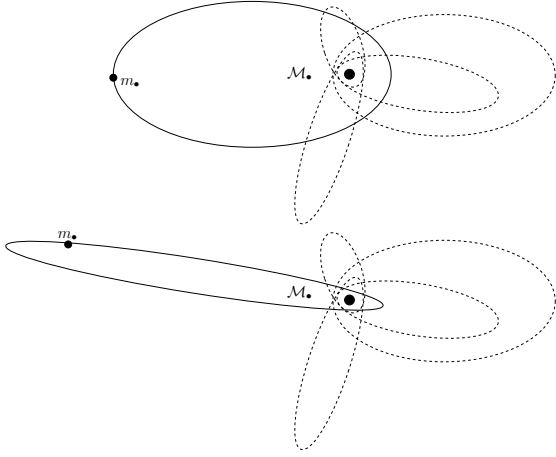


Figure 7.1: If we have a point-like potential, scalar coherent relaxation can modify the size of J and the inclination of the orbital plane of a test star. In dashed lines we depict the perturbing orbits on the test star, $m_•$, whose orbit is displayed as a solid line in two moments of the evolution.

process is not as relevant and we will not further elaborate on it, though it can be very relevant for phenomena related to galactic nuclei as, for instance, warping of accretion discs (Bregman and Alexander, 2009).

However one must note that these illustrations are oversimplifications and depict perfect symmetries that might be affected or even totally cancelled out by other effects such as e.g. the relativistic periastron shift or Newtonian precession. Thus, after a certain time this symmetry is broken and the evolution is again a random walk, one with very large stepsizes. We refer the reader to the review of Tal Alexander for a detailed and excellent description of these processes (Alexander, 2007).

The impact of coherent relaxation on the production of EMRIs is important. While the underlying physics of the process is very ro-

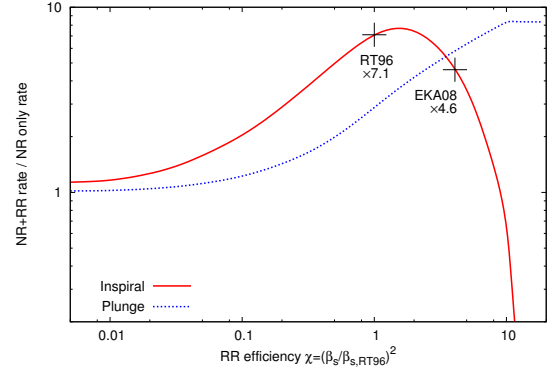


Figure 7.2: EMRI and direct plunges rates by taking into account relaxation and coherent relaxation normalised to the rates that one might expect by the rates that we would obtain neglecting coherent relaxation in function of the coherent relaxation efficiency Ξ . This is figure 6 of Eilon et al. (2009).

bust, it is a rather difficult task to ponderate the efficiency of the different parameters implied in the process. A possible way of evaluating it as Hopman and Alexander (2006a); Eilon et al. (2009) do. In figure 7.2, which is figure 6 of Eilon et al. (2009), we show the rate of EMRIs and plunges in a system in which we take into account both orthodox or regular relaxation and coherent relaxation normalised to what one can expect when only taken into account normal relaxation as function of the Ξ parameter, which gives us the efficiency of coherent relaxation. The units of Ξ are such that the value suggested by Rauch and Tremaine (1996) is unity. We note that the work of these authors was limited to a very low number of particles, but we can consider it as a reference point to refer to. Thus, if coherent relaxation is more efficient than what they found, $\Xi > 1$ and vice-versa, i.e. we approach the regime in which

there is not coherent relaxation. It is very remarkable to see that by choosing the value suggested Rauch and Tremaine (1996) we achieve the maximum of the EMRI rate curve. If the “real” value of Ξ happened to be a factor 10 larger, then we would be drastically dropping the rates and increasing the direct plunges and, of course, also the tidal disruptions event rate, since these occur at larger radii.

At first glimpse everything seems to boil down to calculate the precision of coherent relaxation. One obvious way is to do large-particle number simulations, since the first attempt of Rauch and Tremaine (1996) was really *very* limited and difficult to interpret (they were using less than 100 particles). However, the system we are trying to simulate is much more complicated than what a simplified approach will be able to investigate. From a numerical point of view the complications are big and non-negligible. Nevertheless, there has been an important and impressive advance in this front recently but, before we address it, the results and interpretations, it is probably better to have a look at a very familiar system for us, SgrA*. Hopman and Alexander (2006a) have done this interesting and useful exercise, which is summarised in their figure 6, which we reproduce here in figure 7.3. In this figure, the authors display the relevance of different dynamical components in an attempt to the constraining of the strength of coherent relaxation.

On the vertical axes we have the age of different systems found in the GC as function of the semi-major axis of the stars with the object in SgrA*. On the top of the figure we see a line giving us the timescale for normal relaxation, T_{NR} to use the same nomenclature as the authors and their plot, which is shorter than the

Hubble time but not much shorter. The following two curves from the top give the timescale for scalar coherent relaxation for two cases, the first curve from the top corresponds to a system of $1 M_{\odot}$ stars and $10 M_{\odot}$ stars. At large values the effect is quenched by the presence of an extended mass, i.e. Newtonian precession and at short distances it is periastris shift what decreases its strength. The minima displayed in the figure fence in the potential range of values for the efficiency. The “real” value lies probably somewhere in the middle.

It is nevertheless important to note that the authors did not take into account the effect of a mass spectrum. In this respect, while it is easier to understand the fundamentals of the scenario, the system lacks of an important ingredient in realism that could significantly change the narrative.

On the lower right corner of the figure we have vector coherent relaxation, which is much more efficient with timescales associated shorter than a million of years for a short enough semi-major axis.

In the same figure we display the area from which we believe that EMRIs originate; i.e. within ~ 0.01 pc. These objects are typically compact remnants and, hence, will be accumulated in the left top corner of the figure because they are older than the typical time for relaxation. As we can see, and as shown in the calculations of the authors, they are embedded in the area which is totally dominated by coherent relaxation. This is a very striking result from the standpoint of standard relaxation theory: The dynamics of EMRIs will be dominated by this new “exotic” form of relaxation, coherent relaxation and not by normal (two-body) relaxation.

As we have already explained previously,

there are different populations of stars in the GC that we can observe. One of these are the disc stars, some $\sim 50 - 100$ very massive and young stars observed to be orbiting on discs and almost circularly. The upper limit on the edge is of a few $10^6 M_\odot$ and, thus, the strip in the figure is very narrow. These discs are characterised for having a relatively well-defined and sharp inner cut-off. It is remarkable to note that the cut-off happens to be exactly at the place in the figure where the associated timescale with vectorial coherent relaxation (T_{RR}^V in the plot) crosses the strip, without a fit, as the authors claim. On the left side of the line we have the S-stars, which are *not* on circular orbits, nor aligned with the discs, but randomly orientated. They are sometimes envisaged as the low-mass members of the disc stars. In any case, it is intriguing that these stars lie exactly on the left of the curve, where we expect any disc structure to be destroyed by vectorial coherent relaxation. This would imply that the values derived by Rauch and Tremaine (1996) are very close to the real ones. While it is probably too early to make any strong statement from this fact, it is encouraging to keep us studying and trying to understand normal as well as coherent relaxation in galactic nuclei. Another interpretation of the figure is that we can expect some of the S-stars to have random eccentricities due to the fact that those which are close enough are affected by scalar coherent relaxation. Also, we can in principle explain why late-type giants do not have any particular orientation in their orbits, since they are in that part of the plot.

The numerical simulations of Eilon et al. (2009) show that coherent relaxation can enhance the EMRI rate by a factor of a few over

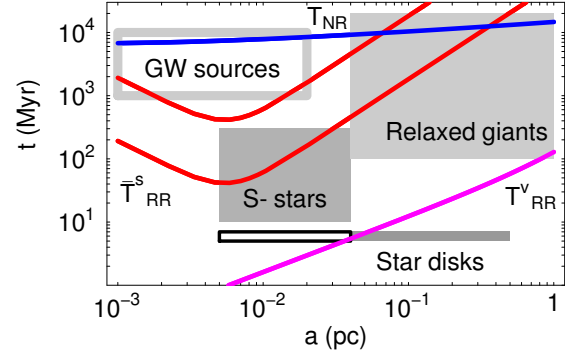


Figure 7.3: Illustration for the different timescales dominating stellar dynamics in the Galactic Centre. This is figure 6 of Hopman and Alexander (2006a).

the rates predicted assuming only slow stochastic two-body relaxation.

7.3 Strong mass segregation

We have seen in chapter 5 that stars with different mass get distributed around a MBH in a galactic nucleus with different density profile. We devoted a significant part of that chapter to study case single-mass, which was firstly correctly described in an analytical way by Bahcall and Wolf (1976). The authors extended the work to stellar systems with two mass components and argued heuristically for a scaling relation that depends on the star's mass ratio only, namely $p_L = m_L/m_H \times p_H$ (Bahcall and Wolf, 1977). They did not give a general result on inner slope of the heavies (the SBHs in our case) and they did not discuss about the dependence of the result on the component's number fractions. Fortunately, Alexander and Hopman (2009) addressed this issue and found that there exist two branches of solutions, parametrised by

$$\Delta \approx \frac{N_H m_H^2}{N_L m_L^2} \frac{4}{3 + m_H/m_L}, \quad (7.1)$$

with capital letters meaning the total stellar mass and low-case letters to individual masses of stars. Δ gives us a measure of the relevance of the SBH self-coupling relative to the other species coupling, the lighter stars in the system, and a main advantage of it is that it depends basically on the mass and number ratios. In this respect, the authors extend elegantly the study of Bahcall and Wolf (1977) to an additional, crucial parameter. For values of $\Delta > 1$ we recover the scaling solutions of Bahcall and Wolf (1977). This is the regime to which Alexander and Hopman (2009) refer to as the “weak branch” of the solution. On the other hand, for $\Delta < 1$, we have a new kind of solution that generalises the Bahcall and Wolf (1977) solution. This is the “strong mass segregation” regime, because the density slopes that one obtains in this case are steeper.

Inspired by their work, Preto and Amaro-Seoane (2010) and Amaro-Seoane and Preto (2011) used direct-summation simulations as a calibration to Fokker-Planck experiments that allowed them to explore this new solution. This is a priori not obvious, since we are in a regime in which scattering is dominated by uncorrelated, 2-body, encounters and dense stellar cusps are robust against ejections. The authors proved that the agreement between both methods is quite good.

The implications of these results are interesting and important for EMRI science, but also particularly timely. This is so because of recent progress in electromagnetic observations of our Galactic Centre. Recently, two independent groups have observed that there seems

to be a deficit of old stars based on number counts of spectroscopically identified, old stars in a sub-parsec region around SgrA* (down to magnitude $K = 15.5$, see Buchholz et al. 2009 and Do et al. 2009). In figure 7.4 we show their main results. The best fits seem to favor slopes $\gamma < 1$ and the possibility of a core with the stellar density decreasing, $\gamma < 0$ is not excluded (Buchholz et al., 2009; Do et al., 2009; Bartko et al., 2010). We would like to note that the detectable stars are essentially giants and they represent only a very small percentage of the underlying population, and the slope of the density profile is still weakly constrained and such a fit is only marginally better than one with $\gamma \sim 1/2$. We think therefore that it is too early to surmise for the inexistence of a segregated cusp.

Nevertheless, Preto and Amaro-Seoane (2010) and Amaro-Seoane and Preto (2011) explored the following situation: How long would take for cusp growth if at some point a central core is carved in the stellar density in a galactic nucleus similar to the Milky Way? They choose as initial condition a model with $\gamma = 1/2$, so that the isotropization time is $\ll t_{\text{rlx}}(r_h)$. The results are shown in figure 7.5.

We can see in the figure that by $t \sim 0.25 t_{\text{rlx}}(r_h)$, cusps with $\gamma_L \sim 1.5$ and $\gamma_H \sim 2$ ($p_L \sim 0.05$ and $p_H \sim 0.5$, where the subscript “L” refers to the light species and “H” to the heavy stars) are *fully developed* (~ 0.02 pc if scaled to a Milky Way-like nucleus). For masses similar to SgrA*, $M_\bullet \lesssim 5 \times 10^6 M_\odot$, this is shorter than a Hubble time. Hence, if indeed a carving event depleted the inner agglomeration of stars around the MBH, as soon as only 6 Gyr later a very steep cusp of SBHs would have had time to re-grow.

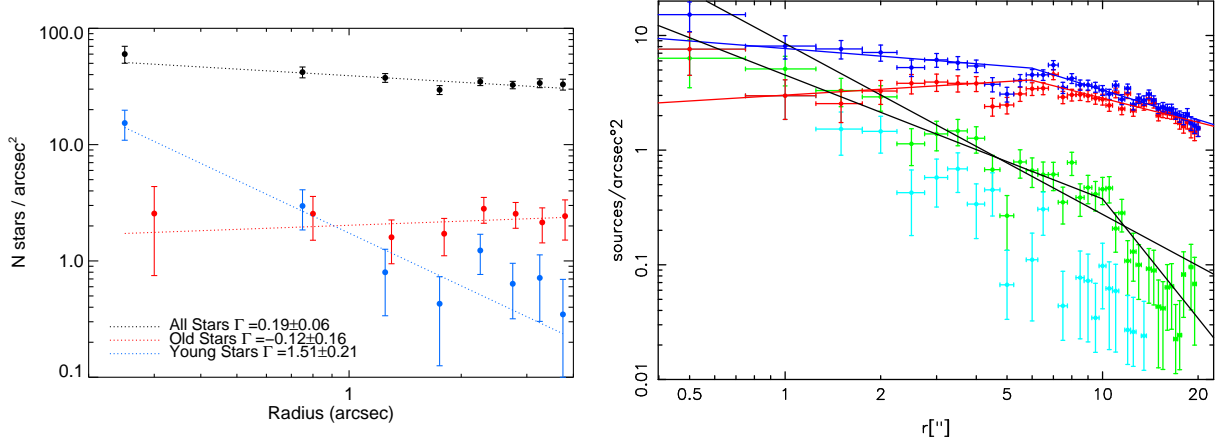


Figure 7.4: Number of sources per arcsec^2 as a function of radius from the Galactic Centre in seconds. These two figures are from Do et al. (2009) (left panel) and Buchholz et al. (2009) (right panel).

We must note that this result is different to what Merritt (2010) finds, but this is probably due to the fact that he only takes into account the effect of dynamical friction from the light stars over the heavy stars, and he neglects the scattering of the heavy stars. In this respect, he is limited in his approach to the early evolution of the system, when the heavy stars only represent a minor perturbation on the light stars. As a matter of fact, very similar results were derived later by Gualandris and Merritt (2012).

The impact on EMRI production is the following: If carved nuclei were common in the range of masses relevant to an observatory like LISA, then we would be cutting down production of old remnants significantly. However, even if our Milky Way *had* a hole in its stellar cusp, LISA EMRI rates peak around $\mathcal{M}_\bullet \sim 4 \times 10^5 - 10^6 M_\odot$ and re-growth times are $\lesssim 1$ Gyr for $\mathcal{M}_\bullet \lesssim 1.2 \times 10^6 M_\odot$, so that we still expect that a substantial fraction of EMRI events will originate from segregated stellar cusps

On the other hand, strong mass segrega-

tion not only “comes to the rescue” in the case of carved nuclei. It helps in the production of EMRIs. Amaro-Seoane and Preto (2011) estimate that thanks to strong mass segregation one might expect EMRI even rates to be $\sim 1-2$ orders of magnitude larger than one would expect if using the Bahcall and Wolf solution.

Their solution for the weak branch is unrealistic, since it predicts a too high event rate because it uses unrealistically high number fractions of SBHs $f_\bullet (\geq 0.05)$. In a more realistic case, when $\Delta \sim 0.03$, ($f_\bullet \sim 10^{-3}$) the Bahcall and Wolf solution would entail a strong suppression of the EMRI rate to –at best – a few tens of events per Gyr.

The new solution of strong mass segregation implies a higher ρ_\bullet well inside the influence radius of the MBH, so that we have a boost in diffusion SBHs close to MBH. When going from number fractions that are based on unrealistic IMF, such as in the work of Bahcall and Wolf (say $\Delta = 3$) to realistic values ($\Delta = 0.030$), the event rate is suppressed by factors of $\sim 100-$

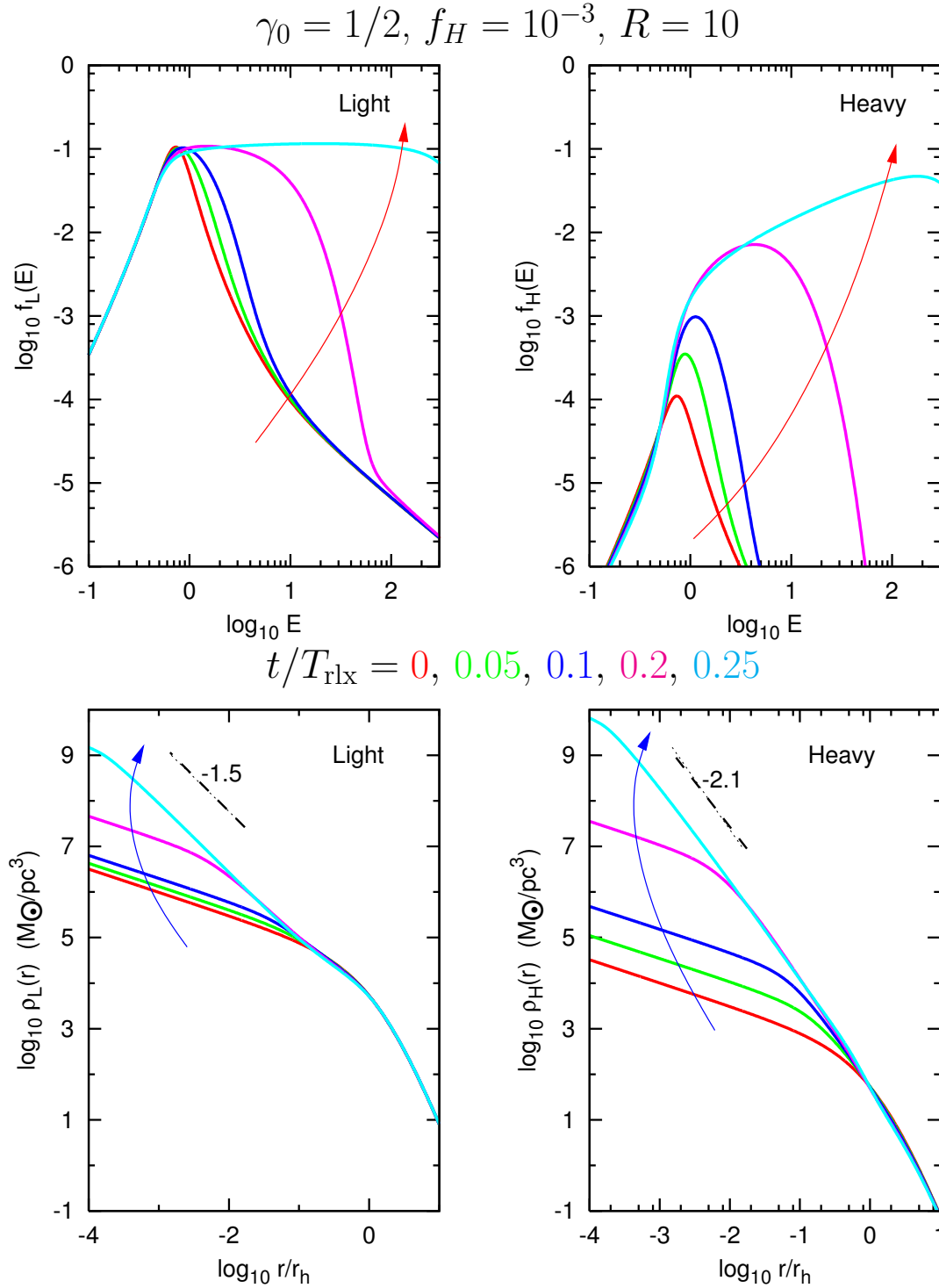


Figure 7.5: Evolution of phase-space $f(E)$ and spatial $\rho(r)$ densities from the simulations of Preto and Amaro-Seoane (2010) using a FP code which is isotropic, orbit-averaged multi-mass in energy space. This is adapted from figure 3 of the authors. They display in different colours different moments in the evolution of the system in units of the relaxation time.

150 if we ignore strong mass segregation. Thanks to this new solution, based on more realistic physics, even for low values of $\Delta = 0.03$, we boost the rates from few tens to a few hundred per Gyr, $\sim 250/\text{Gyr}$ if we consider a mass ratio of 10 between the SBHs and the MS stars and if we take a fractional number for SBHs of $f_{\bullet} = 0.001$.

7.4 Tidal separation of binaries

A process contributing to the creation of EMRIs has its origin in the work of Hills (1988). In his work, Hills describes the possibility of finding escaping stars which originate by this process:

“A close but Newtonian encounter between a tightly bound binary and a million solar mass black hole causes one binary component to become bound to the black hole and the other to be ejected at up to 4000 km/s. The discovery of even one such hypervelocity star coming from the Galactic center would be nearly definitive evidence for a massive black hole. The new companion of the black hole has a high orbital velocity which increases further as its orbit shrinks by tidal dissipation. The gravitational energy released by the orbit shrinkage of such a tidal star can be comparable to its total nuclear energy release.”

His work, about the tidal separation of binaries by an MBH, had not a big impact for some 15 years until the discovery of the so-called “hyper-velocity stars”, stars with a velocity of $> 10^3 \text{ km s}^{-1}$, which had been pre-

dicted in his work. Indeed, several such stars have been discovered in the last years. We refer the reader to the work of Brown et al. (2009) for a discussion of the properties of these stars, as well for references.

While one of the objects is ejected into the stellar system, the other binary member can remain bound to the MBH on a rather tightly orbit. If this star happens to be a compact object, then we would have an EMRI which would be rather “immune” to the problems of EMRIs caused by two-body relaxation. Since the tidal separation happens very close to the MBH, the CO will have a shorter apoapsis (usually only tens of times the periapsis distance) and thus, potential tugs that lead it out of the capture orbit are reduced. This process was described in the work of Miller et al. (2005b). The properties of these EMRIs are very interesting and we describe the process in this section, both from an astrophysical point of view and the observational signature. Moreover, it has been predicted in the work by Hopman (2009) estimates that for a galactic nucleus such as the Galactic Nucleus, the rate at which binaries tidally separate start already far away from the MBH, and is

$$\Gamma_{\text{tid sep}}^{\text{GC}} \sim 7 \times 10^{-7} \left(\frac{f_b^{\text{GC}}}{0.05} \right) \text{ yr}^{-1} \quad (7.2)$$

In this last equation “GC” stands for Galactic Center and f_b is the fraction of stars in binaries. In the work by the same author, in his figure 6, we see that the rate is enhanced when we go to higher energies, because the loss-cone is depleted. Hence, more binaries survive on their trip to the GC. Also, ? make the prediction that the rate might be boosted by an order of magnitude by binaries *not* bound to the MBH. Even

more interestingly, Perets et al. (2007) describe in their paper that the event rate can be enhanced by *orders of magnitude* if one considers the role of massive perturbers, such as giant molecular clouds.

Hence, this mechanism is a very important one in the production of EMRIs and we describe it in some detail in this section.

In figure 7.6 we have a schematic view of the process. A binary which happens to fly by close enough to the central MBH will be tidally separated because the tides acting on the pair overcome the gravity in the binary. One of the stars is captured, in the meaning that it will be bound to the MBH, after losing a bit of energy compared to what it had before and the other companion of the binary will obtain a bit more of energy after the separation, so that it will be ejected with a high velocity, as in a slingshot. It is rather straightforward to make a toy model for the process and get the scalings, which sheds light on the process.

The size of the region where this process will occur, R_{split} , is proportional to the size of the object, the separation of the binary a , the mass of the binary m_{bin} and the mass of the central MBH, \mathcal{M}_\bullet as it was in the case of the tidal disruption of an extended star. Actually we can follow the analogy very closely, only that in that case we have to come closer to the MBH to have the tidal forces overcoming the binding energy of the binary, since $a > R_\star$, with R_\star the radius of the star.

$$R_{\text{split}} \sim a \left(\frac{\mathcal{M}_\bullet}{m_{\text{bin}}} \right)^{1/3} \quad (7.3)$$

The orbital velocity in the binary can be easily computed as follows,

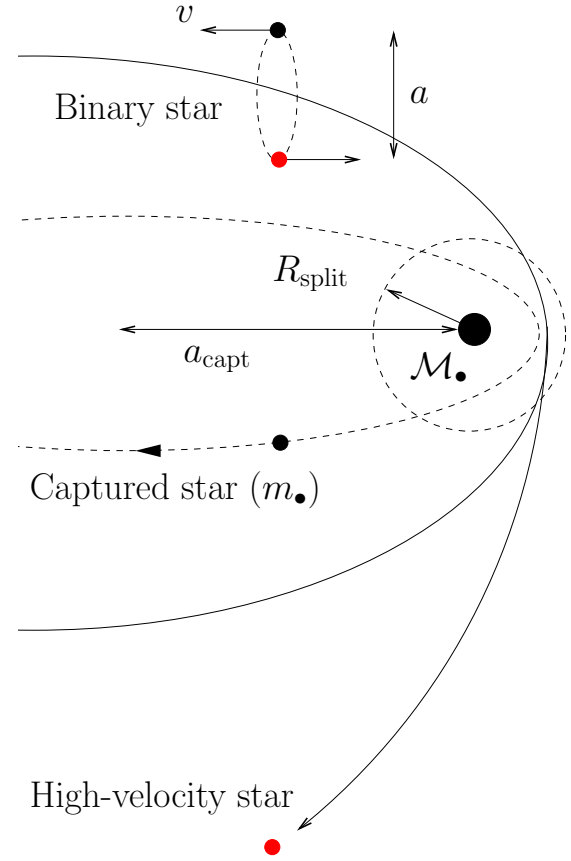


Figure 7.6: Schematic illustration of the process of the tidal separation of a binary by an MBH of mass \mathcal{M}_\bullet . We define R_{split} as the radius within which the tidal forces of the MBH overcome the binding energy of the binary

$$v \sim \sqrt{\frac{G m_{\text{bin}}}{a}} \quad (7.4)$$

We now normalise the last equation to nominal values assuming that it is a hard binary in a galactic nucleus,

$$v \sim 133 \text{ km s}^{-1} \left(\frac{m_{\text{bin}}}{2M_{\odot}} \right)^{1/2} \left(\frac{a}{0.1 \text{ AU}} \right)^{-1/2} \quad (7.5)$$

In figure 7.7 we show a zoom-in of figure 7.6, at the moment in which the binary is at the periapsis of the MBH. We estimate now the ejection velocity. The COM of the binary has a velocity V_{CM} which we can easily calculate by assuming that the encounter is parabolic

$$V_{\text{CM}} \gtrsim \sqrt{\frac{G M_{\bullet}}{R_{\text{split}}}} \sim v \left(\frac{M_{\bullet}}{m_{\text{bin}}} \right)^{1/3} \gg v \quad (7.6)$$

This allows us to estimate the ejection velocity of the slingshot star, because the difference of energy will be

$$\pm \delta E \simeq V_{\text{CM}} \cdot v \geq v^2 \left(\frac{M_{\bullet}}{m_{\text{bin}}} \right)^{1/3} \simeq \frac{v_{\text{eject}}^2}{2} \quad (7.7)$$

Then, we have that

$$v_{\text{eject}} \gtrsim \left(\frac{M_{\bullet}}{m_{\text{bin}}} \right)^{1/6} \quad (7.8)$$

Since we are dealing with a binary, the star of mass m_{\bullet} , which we assume to be a stellar-mass BH, will be slowed down by v , as in Eq.(7.4) and the star of mass m_{\star} , which can be an extended star of a compact object, will be accelerated by the same amount. We now also assume that in that moment the stars do not interact gravitationally with each other and they only “see” the potential created by the MBH. Therefore we have a simple situation with a simplified geometry that allows us to compute the initial orbits of the two companions in the pair at the moment of splitting.

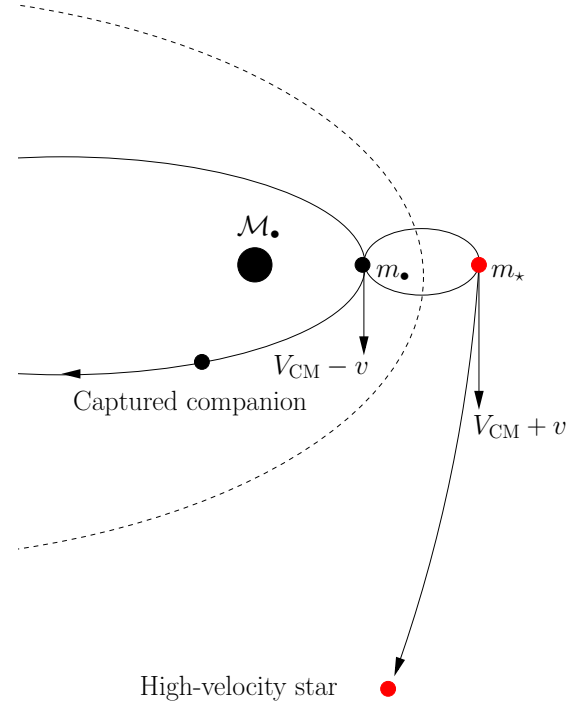


Figure 7.7: Zoom in of figure 7.6 for the splitting of the pair. We assume a parabolic encounter (dashed curve) for the COM of the binary and a mass m_{\bullet} and m_{\star} for the stars.

Hence, the stellar-mass BH is bound to the MBH and the escaping star leaves the system with a high velocity, which is of the order of the velocity in the binary, typically of about $\sim 10 \text{ km s}^{-1}$, multiplied by the same mass ratio as in Eq.(7.3) but to a different power, as we can see in Eq.(7.8).

One very interesting aspect of this particular process to produce capture of compact objects by MBHs is the eccentricity that the orbit has. We can estimate it roughly by computing the semi-major axis of the bound pair after the separation of the initial binary, a_{capt} ,

$$a_{\text{capt}} \approx a \left(\frac{\mathcal{M}_\bullet}{m_{\text{bin}}} \right)^{2/3} \approx 10^4 a \quad (7.9)$$

As we can see in figure 7.6, we can approximate the separation radius R_{split} to the periapsis distance,

$$R_{\text{peri}} = (1 - e_{\text{capt}}) a_{\text{capt}} \approx R_{\text{split}} \sim \left(\frac{\mathcal{M}_\bullet}{m_{\text{bin}}} \right)^{-1/3} \quad (7.10)$$

Hence, we can see that this kind of sources will typically have a capture eccentricity of

$$e_{\text{capt}} = 1 - \left(\frac{\mathcal{M}_\bullet}{m_{\text{bin}}} \right)^{-1/3} \sim 0.98 \quad (7.11)$$

Contrary to “usual” EMRIs, tidally-split MS have a low eccentricity when they reach the bandwidth of the detector (which, for convenience, we will call tidally-split EMRIs, “TSEMRI”). This is because no energy needs to be dissipated in order to have a capture. As a result, capture can occur at much larger radii than is possible in the two-body case, as described by Miller et al. (2005b). For a $10 M_\odot$ object this should be of about $1 - e_{\text{TSEMRI}} \approx 0.99$. On the other hand, we have seen that typical EMRI eccentricities when reaching the LISA bandwidth are $1 - e \approx [10^{-3}, 10^{-7}]$

In order to understand the difference in terms of detectability, we need to introduce some definitions of the geometric model of signal analysis. We treat the waveforms as vectors in a Hilbert space (Helstrom, 1968), which allows us to define the natural scalar product

$$\langle h | s \rangle := 2 \int_0^\infty df \frac{\tilde{h}(f) \tilde{s}^*(f) + \tilde{h}^*(f) \tilde{s}(f)}{S_n(f)}, \quad (7.12)$$

where

$$\tilde{h}(f) = \int_{-\infty}^\infty dt h(t) e^{2\pi i f t} \quad (7.13)$$

is the Fourier transform of the time domain waveform $h(t)$. We have introduced the $S_n(f)$, which is the one-sided noise spectral density of LISA (see e.g. Thorne, 1987; Finn, 1992). One can think of LISA as two orthogonal detectors, so that the signal in each of them is given by $s_i(t) = h_i(t) + n_i(t)$, with $i = 1, 2$ label each detector. We adopt the assumption that the noise $n_i(t)$ is stationary, Gaussian, uncorrelated in each detector and characterized by the noise spectral density $S_n(f)$. Hence, we can define the signal-to-noise ratio in each detector as

$$\rho_i = \frac{\langle h | s_i \rangle}{\sqrt{\langle h | h \rangle}}. \quad (7.14)$$

Therefore, if we consider the waveform of a TSEMRI and compare it with a normal EMRI, we can calculate the mismatch of their expected signal-to-noise ratio for LISA as

$$\mathcal{M} := 1 - \frac{\langle h_{\text{TSEMRI}} | h_{\text{EMRI}} \rangle}{\sqrt{\langle h_{\text{TSEMRI}} | h_{\text{TSEMRI}} \rangle \langle h_{\text{EMRI}} | h_{\text{EMRI}} \rangle}}. \quad (7.15)$$

For a TSEMRI and a normal EMRI starting with exactly the same orbital parameters at the GC and coloured for LISA, we calculate with the LISACode² (Petiteau et al., 2008) that there is a mismatch of 99.9971%. Using the standard definition of signal-to-noise ratio

²<http://www.aei.mpg.de/~petiteau/LISACode>

$$\rho_i = \frac{\langle h | s_i \rangle}{\sqrt{\langle h | h \rangle}}, \quad (7.16)$$

we have that the TSEMRI is calculated to have an average signal-to-noise ratio of $\rho_{\text{TSMI}} \sim 27637$ and the normal EMRI of $\rho_{\text{EMRI}} \sim 18848$, both set to be at a distance of 8.3 kpc.

In figure 7.8 we show the waveforms for an observer at $\theta = 55$ degrees, with origin at the MBH, with a mass of $3 \cdot 10^6 M_\odot$ and z-axis along direction of big black hole spin. The waveforms are from Steve Drasco and have been calculated using the kludge approximation of Gair and Glampedakis (2006).

7.5 The role of the MBH spin

A number of authors have addressed the question of EMRI event rates in a Milky Way-like galaxy. The numbers differ but a common denominator to all estimates is that the number of “direct plunges” is much larger than slowly decaying, “adiabatic” EMRIs. This is so simply because the region of the galaxy from which potential plunges originate contain many more stars than the volume within which we expect EMRIs, as we have seen in chapter 6.

For a long time “plunges” have been considered to be irrelevant for the purposes for which EMRIs are best at. After one intense burst of radiation, the source would be lost along with, obviously, the SBH. Some studies have looked into that, such as the work of Hopman et al. (2007), which is probably the most meticulous one by incorporating a high realism of the physics in that regime. However, the conclusions of the authors are that these sources are not interesting because they could only be detected if they originated in our own Galactic Center.

However, a few years later, Amaro-Seoane et al. (2012d) show that since MBH are likely to be spinning, it is actually very hard for a SBH on a plunge orbit to “hit” the MBH. They show that plunging orbits for spinning MBHs are actually not plunging but EMRI orbits. They prove that since spin allows for stable orbits very near the LSO in the case in which the EMRI is prograde, the contribution of each cycle to the SNR is much bigger than each cycle of an EMRI around a non-spinning MBH. On the other hand, retrograde orbits “push the LSO outwards” and hence, it is easier for a SBH to plunge, and the EMRI is lost. However, this situation is not symmetric, resulting in an effective enhancement of the rates.

The authors also show that vectorial coherent relaxation is not efficient enough to turn a prograde orbit into a retrograde one, which would be fatal for this scenario, once the evolution is dominated by GW loss.

7.6 A barrier for captures

Merritt et al. (2011b) performed direct-summation N -body simulations and found that EMRI event rates are severely suppressed when introducing relativistic precession in the integrations. The precession limits the action of torques from the stellar potential in the orbital angular momenta. Nevertheless, they do find some particles that do cross this barrier, the Schwarzschild barrier, to use their nomenclature. In figure 7.10 we see this scenario. This is from Merritt et al. (2011b), and shows a Newtonian simulation in the left panel. The authors display a and e of the two-body system consisting of one star and the MBH. In the right panel they depict the situation with all the relativistic correction terms

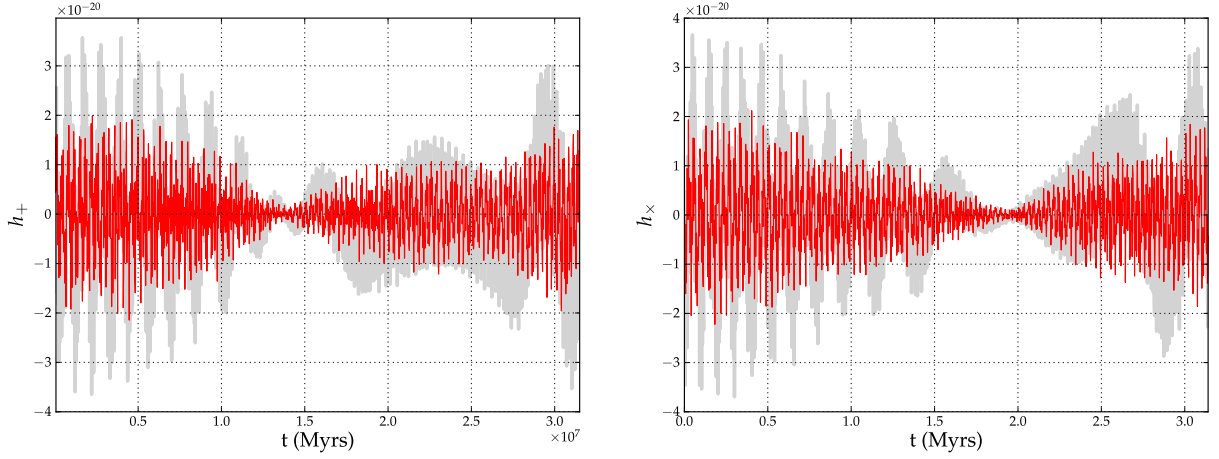


Figure 7.8: Waveforms of a normal EMRI and a TSEMRI (see text) superimposed for a full year of data before the final plunge, which has been defined to happen at a periapsis of $r_{\text{plunge}} \equiv 2 \times r_{\text{ISCO}}$, with r_{ISCO} the radius of the innermost stable circular orbit, which is $\sim 8 M$ in this case. The mass of the central MBH is $3 \times 10^6 M_{\odot}$, the mass of the star $0.53 M_{\odot}$. We have set the spin of the MBH to $a = 0.5 M$ and we neglect the spin of the star.

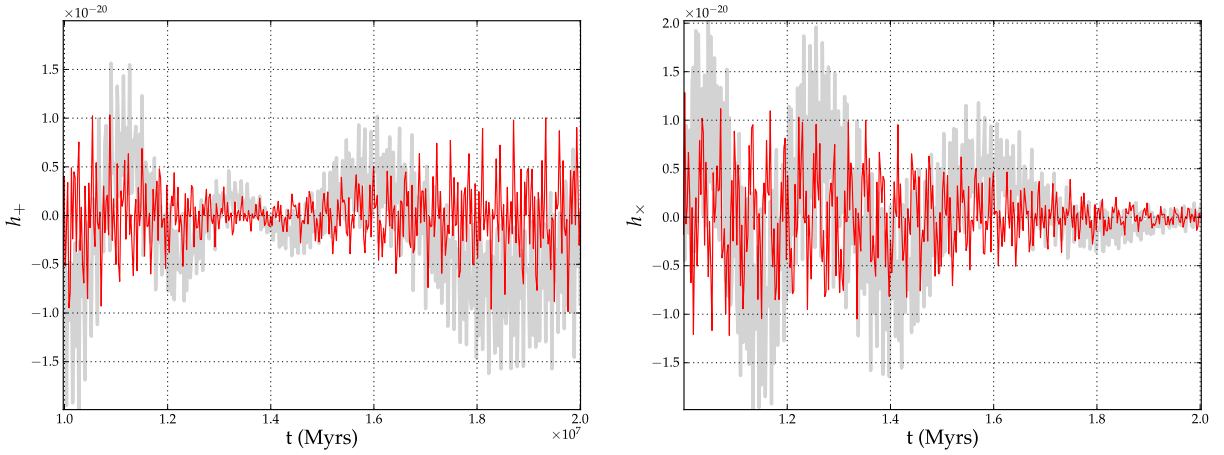


Figure 7.9: Zoom of figure 7.8. For the two figures only one point out of 1600 is used to make the plot lighter. Still, we can see that even in the region of maximum overlap there is a significant difference. In the computation of the mismatch function of Eq.(7.15), however, the full waveform has been used.

“switched on”. a_r and e_r are the 1PN generalisations of the semi-major axis and eccentricity. In the upper panel the red, dotted line corresponds to the barrier, given by their expression:

$$\tilde{a} = C_{\text{SB}} (1 - e^2)^{-1/3} \quad (7.17)$$

where C_{SB} is a constant of order unity. The blue, dash-dotted line corresponds to the GW capture.

This interesting and pioneering scenario would obviously imply a severe suppression of EMRI event rates and deserves a closer analysis.

7.7 Extended stars EMRIs

In this section we review the idea described by Freitag (2003b) that MS stars can be potential sources of GWs in our Galactic Centre. We include this in this chapter because in the whole review our standard’ CO is considered to be a SBH and so, it falls into the category of “not in the standard model”.

Indeed, a MS star can reach close enough distances to the central MBH depending on its average density and stellar structure. For a mass of around $0.07 M_{\odot}$, the density of the MS star is maximum and corresponds to the transition to a sub-stellar object, (Chabrier and Baraffe, 2000). For masses smaller than $0.3 - 0.4 M_{\odot}$, the core is totally convective and can be described with a polytrope of index $n = 3/2$.

Freitag (2001b, 2003b) estimated the number of single MS stars which can become an abundant source of GWs in our GC by inspiralling into the central MBH. In his work, the author estimated with Monte Carlo simulations that there must be one to a few low-mass MS stars sufficiently bound to the GC to be discernible by LISA. In figure 7.11 we show some

of the most relevant results of the investigation. Nevertheless, we note that the assumptions made by the numerical tool are probably biasing the results to an overestimation. These assumptions rely in the nature of the Monte Carlo code.

7.8 The butterfly effect

An interesting effect described in the work of Amaro-Seoane et al. (2012c) is the lack of determinism in an EMRI system if a perturbing star is close enough to the binary formed by the MBH and the SBH. One immediate question that arises is how realistic it is to assume that we can have a second star so close to the EMRI so as to perturb it.

We estimate how likely is to have a star close enough to perturb the EMRI in a measurable way. For this, we take our Galactic Centre as a representative system of the scenario that we want to analyse. If we admit that for SgrA* half of the mass within the orbit of S-2, which has a periaapsis $6 \times 10^{-4} \text{ pc}$ (Ghez et al., 2008; Genzel et al., 2010), is $M_{\text{encl}}/2 = \eta \times M_{\bullet}$, with $\eta \leq 0.040$ and M_{\bullet} the mass of the MBH (Gillessen et al., 2009), i.e. $M_{\text{encl}} = 172,000 M_{\odot}$, and we assume that the stars build a cusp following a power-law of $R^{-\gamma}$, then we can estimate that the mass at radius R is

$$M(R) = \int_0^R 4\pi r^2 \rho(r) dr \propto \int_0^R r^{-\gamma+2} dr \propto R^{3-\gamma} \quad (7.18)$$

for $\gamma < 3$. Hence, the number of stars within a

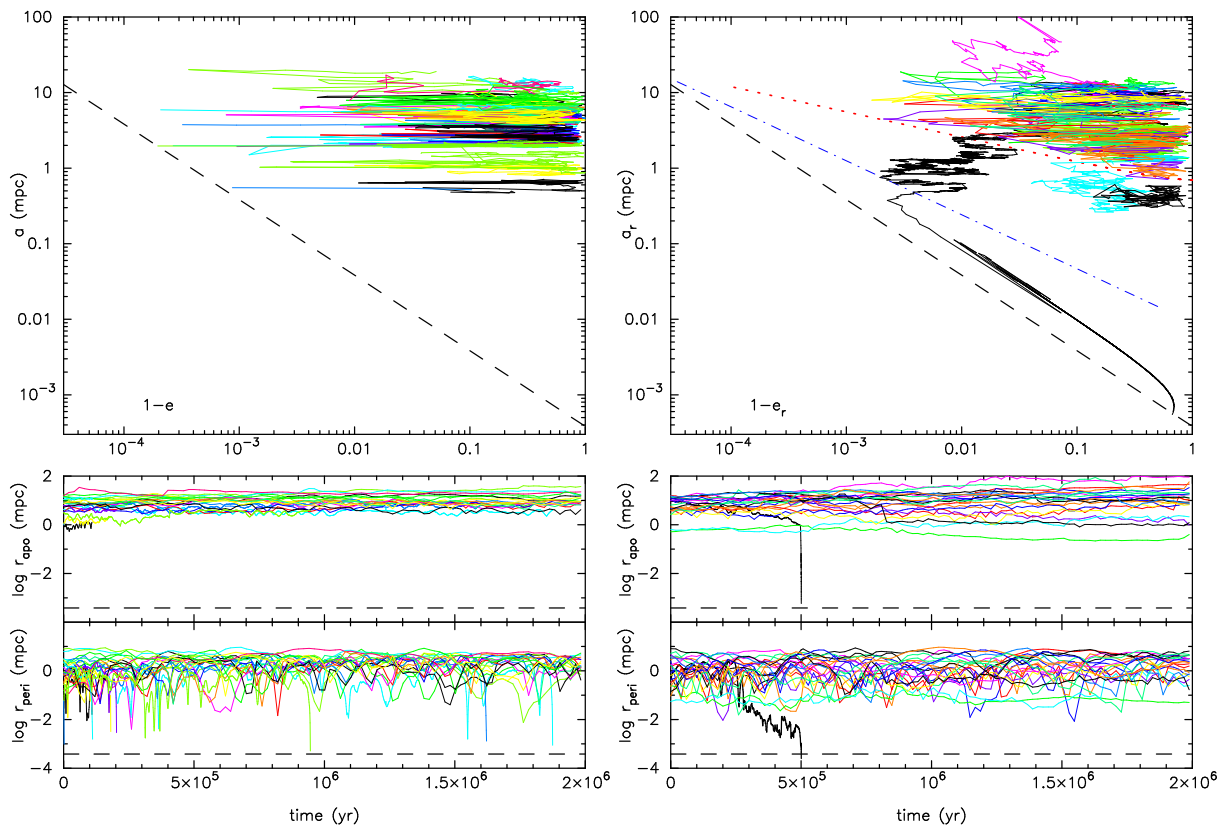


Figure 7.10: The Schwarzschild barrier in the work of Merritt et al. (2011b). In the left panel we have the Newtonian case and in the right the simulations with relativistic corrections. We clearly see the barrier and also a particle crossing it.

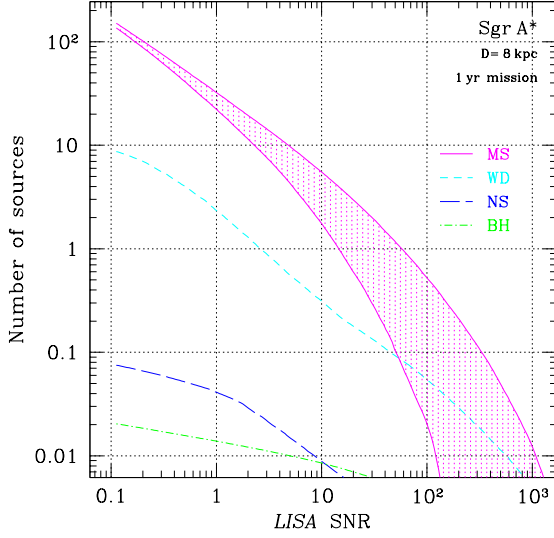


Figure 7.11: Number of sources at the GC depending on their compactness. This figure (taken from Freitag 2003b) displays the number of MSSs, WDs, NSs and SBHs as a function of the SNR in LISA for a one year mission and assuming a distance of 8 kpc.

sphere of radius R is given by

$$N(R) \simeq 8.6 \times 10^4 \left(\frac{R}{6 \times 10^{-4} \text{ pc}} \right)^{3-\gamma} \quad (7.19)$$

And so, the radius within we can expect to find in average a star is

$$R_1 \simeq 6 \times 10^{-4} \text{ pc} \times \left(\frac{1}{8.6 \times 10^4} \right)^{\frac{1}{3-\gamma}} \quad (7.20)$$

We note, however, that the value derived for η is not observational. As a matter of fact, with current limitations in the observations, it is impossible to know whether all mass enclosed by the orbit of S-2 corresponds to the MBH or it contains also an “extended” component. Hence,

in order to obtain η , one has to model the system by admitting that it consists of a punctual source (the MBH) along with a stellar component whose properties are parametrised by following a model, not an observation. In figure 7.12 we show the dependence on γ of R_1 . We can see that $R_1 \simeq 3 \times 10^{-7} \text{ pc}$ for $\gamma = 1.5$ or $7 \times 10^{-8} \text{ pc}$ for $\gamma = 1.75$ (e.g. Amaro-Seoane et al., 2004a; Freitag et al., 2006b; Preto et al., 2004). These distances are of the same order of magnitude than an EMRI which is within the bandwidth of a LISA-like observatory. Even if this argument is based on the concept of a cusp and, hence, difficult to define at such short radii, we note that the work of Freitag et al. (2006b) derive in their Milky Way-like G25 model some $15 M_\odot$ within $3 \times 10^{-4} \text{ pc}$. It is possible that at such distances the mass density is totally dominated by stellar black holes, but the work of Freitag et al. (2006b) does not allow one to resolve them for distances shorter than 0.01 pc. In this case, strong mass segregation would play a crucial role (Alexander and Hopman, 2009; Preto and Amaro-Seoane, 2010; Amaro-Seoane and Preto, 2011), since for the kind of slopes that one can expect in the case the density is dominated by stellar black holes, the “one-star” radius is much shorter.

In figure 7.13 we have the initial setup for the fiducial case in the the work by Amaro-Seoane et al. (2012c). The mass of the MBH is assumed to be $M_\bullet = 10^6 M_\odot$, the initial semi-major axis of the EMRI of $a_{\bullet,i} \simeq 1.45 \times 10^{-6} \text{ pc}$ (i.e. it is well within the band of LISA), the mass of the EMRI is $m_\bullet = 10 M_\odot$ (but they also successfully tested 5 and $1.44 M_\odot$), the mass of the perturbing star is of $m_\star = 10 M_\odot$, the initial semi-major axis of the star $a_{\star,i} \simeq 4.1 \times 10^{-6} \text{ pc}$, and the initial eccentricity $e_{\star,i} =$

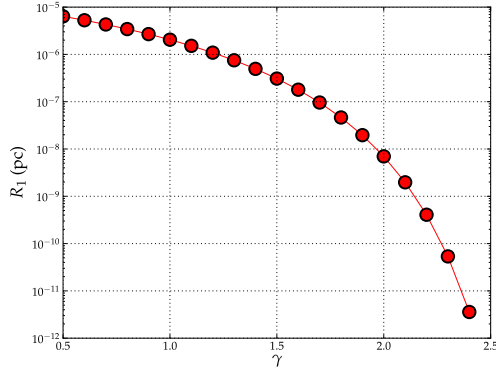


Figure 7.12: Evolution of the one-star radius as a function of the slope as in Eq.(7.20). We can see that for very mild slopes and even a core the distances are within a millihertz gravitational wave detector similar to LISA; i.e. of orbital periods of 10^5 s. In this regime we expect sources of GWs. For instance, an EMRI of $10 M_\odot$ with a MBH of $4 \times 10^6 M_\odot$ has a semi-major axis of about $a_\bullet \approx 8 \times 10^{-4}$ pc and is well within the bandwidth.

0.5 and the inclination is $i_{\bullet,*} = 30^\circ$ at $T = 0$.

The authors find that the interloper introduces an observable modification in the orbit of the EMRI when using a code that uses loss of energy via gravitational radiation at periastris. The interesting result, though, is that when taking into account also the two first-order non-dissipative post-Newtonian contributions, the orbital evolution is not deterministic. We do not know what is the stellar distribution around a MBH at such shorter radii, but if this scenario was possible, then the detection of EMRIs would be much more challenging than thought, because the waveforms developed for detection would be useless. There has also been work about the role of a massive perturber on an EMRI. We refer the reader to the work of Chen et al. (2011); Yunes et al.

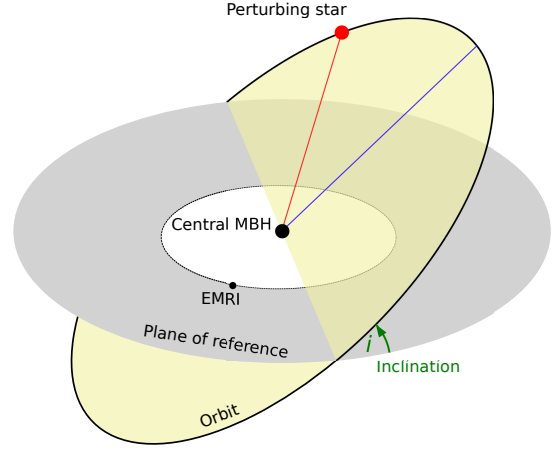


Figure 7.13: Description of the scenario for the butterfly effect of the work by Amaro-Seoane et al. (2012c) (adapted from a figure by Lucas Snyder).

(2011); Seto (2012).

7.9 Role of the gas

Another proposal is related to the presence of massive accretion discs around MBHs. At distances of $\sim 0.1 - 1$ pc from the MBH and at typical accretion rates, these discs can be unstable to star formation Collin and Zahn (1999); Levin and Beloborodov (2003); Goodman (2003); Goodman and Tan (2004); Milosavljević and Loeb (2004); Levin (2003, 2006); Nayakshin (2006). If, as in some calculations, there is a bias towards the production of massive stars in the disc, they could evolve to become black holes, which are then dragged in along with the disc matter. Alternately, massive stars on orbits that cross the disc could be captured and then evolve into black holes Syer et al. (1991); Rauch (1995); Šubr and Karas (1999); Karas and Šubr (2001). Either way,

in the last year of inspiral the holes would be expected to be in nearly circular orbits with orbital planes aligned with the MBH. Rates are highly uncertain as well as the mass of the stellar remnants formed (which could even be IMBHs). However these events would likely have a different signature waveform than those of the other two classes because they should occur on co-rotating, circular orbits lying in the equatorial plane of the spinning MBH if it has gained a significant fraction of its mass by accreting from the disc Bardeen (1970); King et al. (2005); Volonteri et al. (2005). Moreover, there is the exciting possibility that in such a scenario the compact object would open a gap in the disc, which could lead to an optical counterpart to the EMRI event Levin (2006). In any case, perturbations to the SBH are likely to be negligible if accretion on to the hole happens in a low density, radiatively inefficient flow. Such flows are much more common than dense accretion discs, which in principle could yield observable phase shifts during inspiral (Kocsis et al., 2011), at least within the redshift where we expect to be able to observe EMRIs.

Chapter 8

Integration of dense stellar systems and EMRIs

8.1 Introduction

In this chapter we give a summary of the current numerical approaches available for studying stellar dynamics in systems for which relaxation is an important factor¹

As of writing this article only approximate methods using a number of simplifying assumptions have been used to estimate the rates and characteristics of EMRIs. We review these approaches, their accomplishments and limitations. Thanks to the rapid computational power increase and the development of new algorithms, it is most likely that direct N -body techniques will soon be able to robustly confirm or disprove these approximate results and extend them. One of the main issues are the exceptionally long and accurate integrations required to account correctly for secular effects such as coherent relaxation or Kozai oscillations. These requirements, the extreme mass ratio and the typically some 10^3 to integrate pose new challenges to developers of N -body codes.

¹A part of this chapter profits from Amaro-Seoane et al. (2007), though some parts have been significantly expanded and improved.

We can approximately classify the different kinds of techniques employed for studying stellar dynamics according to the dynamical regime(s) they can cope with. In figure 8.1 we have a classification of these techniques. (Semi-)analytical methods are generally sufficient only to study systems which are in dynamical equilibrium and which are not affected by collisional (relaxational) processes. In all other cases, including those of importance for EMRI studies, the complications that arise if we want to extend the analysis to more complex (realistic) situations, force us to resort to numerical techniques.

The N -body codes are the most straightforward approach from a conceptual point of view. In those, one seeks to integrate the orbital motion of N particles interacting gravitationally. It is necessary to distinguish between the *direct* N -body approaches which are extremely accurate but slow and the fast N -body approaches, which are fast but inaccurate and therefore generally deemed inadequate for studying relaxing systems because relaxation is the cumulative effect of *small* perturbations of the overall, smooth, gravitational

potential. Fast N -body codes are usually based on either TREE algorithms (?) or on an FFT (Fast Fourier Transform) convolution to calculate the gravitational potential and force for each particle (?) or on an SCF (self-consistent-field) (?Hernquist and Ostriker, 1992) approach. We will not describe these numerical techniques in this section because they have never been used to study E/IMRIs and the approximations on which they are based make them unsuitable for an accurate study of such systems, since relaxation plays a role of paramount importance. Fast N -body algorithms can only be employed in situations in which relaxation is not relevant or over relatively short dynamical times, such as in studying bulk dynamics of whole galaxies.

On the other hand, if we want to study a system including both collisional effects and dynamical equilibrium, we can employ direct N -body codes or use faster approaches, like the Monte Carlo, Fokker Planck and Gas methods, which we will describe below. The only technique that can cope with all physical inputs is the direct N -body approach, in which we make no strong assumptions other than that gravity is Newtonian gravity (although nowadays post-Newtonian corrections have also been incorporated, see Section 8.9).

If we neglect capture processes driven by tidal effects, the region from where we expect most EMRIs to come from is limited to ~ 0.1 pc around the central MBH. In that zone the potential is totally spherical. Non-spherical structures such as triaxial bulges or stellar discs are common on scales of 100-1000 pc, and the nucleus itself may be non-spherical. For example, it could be rotating, as a result of a merger with another nucleus (Milosavljević and Mer-

		Dynamical equilibrium	
		yes	no
Collisional ($t_{\text{rx}} < \text{age}$)	yes	direct N-body Monte Carlo Fokker Planck / Gas	direct N-body
	no	<i>(semi)analytical:</i> <i>equilibrium models</i> <i>stability analysis...</i>	direct N-body fast N-body: TREE, Grid (FFT), SCF...

Figure 8.1: Methods appropriate to the various realms of stellar dynamics.

rit, 2001) or due to dissipative interactions between the stars and a dense accretion disc (Rauch, 1995). It has been proved that this triaxiality could boost the disruption rates by orders of magnitude (Merritt and Poon, 2004a; Poon and Merritt, 2004b). Whilst assuming sphericity will probably not have any impact on the estimate of capture rates, it is of big relevance for “tidal processes”, since this is the region in which binary tidal separation and the tidal capture of giant cores will happen. For these processes the critical radius is beyond the influence radius of the central MBH and so triaxiality can probably play an important role. Due to insufficient computer power and the limitations of simulation codes galactic nuclei have so far been modelled only as isolated spherical clusters with purely Newtonian gravity (i.e. Murphy et al. (1991); Freitag and Benz (2002)). More realistic situations could only be explored with N -body methods or possibly with hybrid codes (Monte Carlo combined with N -body, for instance).

In figure 8.2 we show a schematic illustration of the current available codes for stellar

Numerical methods for collisional stellar dynamics

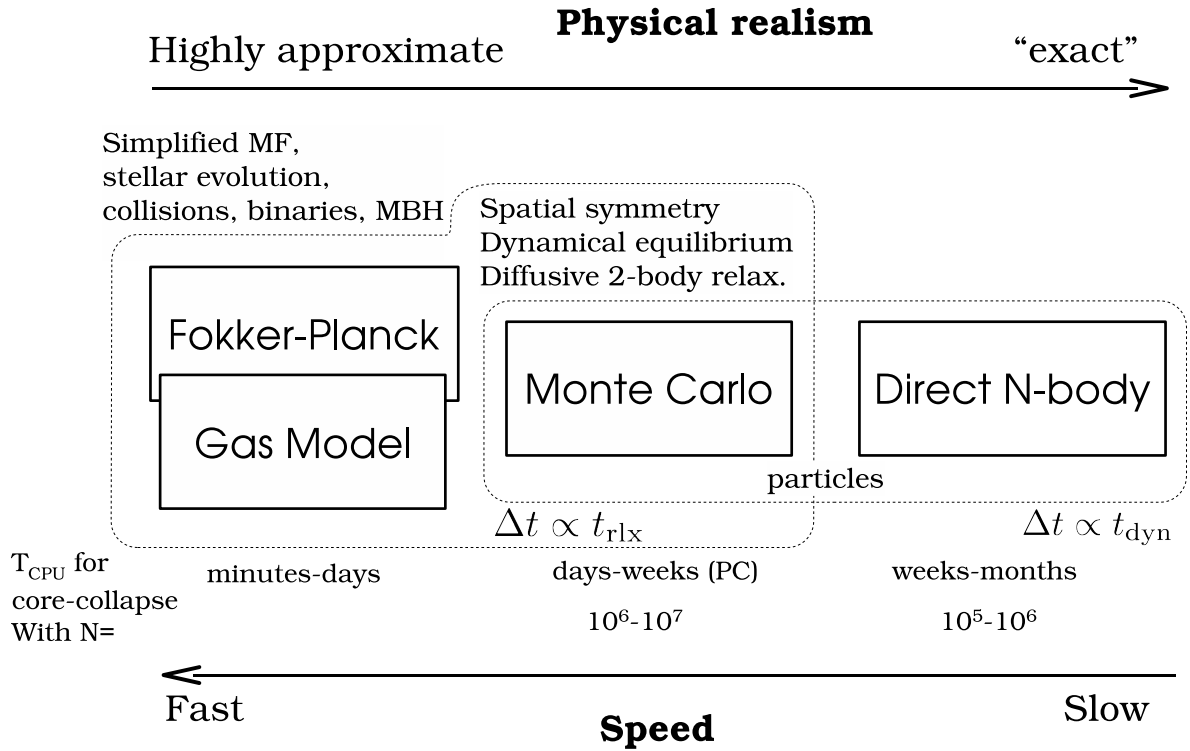


Figure 8.2: The various methods used to study collisional stellar dynamics. In the case of direct N -body the simulations require the use of either special-purpose hardware such as the GRAPEs, Beowulf clusters for the parallel version of Rainer Spurzem or Graphical Computing Units (GPUs). A version of the parallel code N -body6++ ported to GPU architecture is being developed, which will allow us to approach the 10^7 particles limit soon (private communication Rainer Spurzem).

dynamics including relaxation. From the left to the right the *physical realism* of the codes increases while the speed decreases. The two-dimensional numerical direct solutions of the Fokker-Planck equation (Takahashi, 1997, 1996, 1995) probably require the least computational time, but these are followed closely by the gaseous model. The idea behind it is to treat two-body relaxation as a transport process such as in a conducting plasma (Hachisu et al., 1978; Lynden-Bell and Eggleton, 1980). Multi-mass models have been implemented (Louis and Spurzem, 1991; Spurzem, 1992; Giersz and Spurzem, 1994; Spurzem and Takahashi, 1995) and improved for the detailed form of the conductivities by comparing to direct N -body models (described below). The addition of a central accreting MBH and a treatment for loss-cone effects was done by Amaro-Seoane et al. (2004b) (a comprehensive description of the code is in the appendix of the same work) for the single-mass case, and also for a stellar mass spectrum Amaro-Seoane (2004b). The advantage of these two codes are the computational time required to perform a simulation (typically of the order of one minute on a regular PC for a Hubble time) and since they are not particle-based, the resolution can be envisaged as infinite, so that they are not limited by the particle number of the system and there is practically no numerical noise. Nevertheless, although they should be envisaged as powerful tools to make an initial, fast exploration of the parameter space, the results give us *tendencies* of the system, rather than an accurate answer Amaro-Seoane (2004b). Studying the Astrophysical I/EMRI problem requires a meticulous characterisation of the orbital parameters, so that approximate techniques should be regarded as exploratory only (de Freitas Pacheco

et al., 2006).

8.2 Fokker-Planck

Instead of tracking the individual motion of a large number of particles, as in N -body methods, one can attempt to describe a system consisting of a very large number of stars through the *1-particle phase-space distribution function* (DF for short) $f(\vec{x}, \vec{v}, t)$. The best interpretation of f is as a probability density if it is normalised to $1 - \int f(\vec{x}, \vec{v}, t) d^3x d^3v$ is the probability of finding, at time t , any given particle within a volume of phase space $d^3x d^3v$ around the 6-D phase-space point (\vec{x}, \vec{v}) ; the average number of particles in this volume would be $N_* \int f(\vec{x}, \vec{v}, t) d^3x d^3v$. If the particles move in a common smooth potential Φ , the evolution of f is described by the collision-less Boltzmann equation Binney and Tremaine (1987):

$$D_t f \equiv \frac{\partial f}{\partial t} + \vec{v} \cdot \vec{\nabla} f - \vec{\nabla} \Phi \cdot \frac{\partial f}{\partial \vec{v}} = 0. \quad (8.1)$$

Φ is obtained from f and a possible external potential Φ_{ext} (such as produced by a central MBH) from the Poisson equation.

In a real self-gravitating N -particle system the potential cannot be smooth on small scales but has some graininess, i.e., short-term, small-scale fluctuations, $\Phi_{\text{real}} = \Phi + \Delta\Phi_{\text{grainy}}$. Relaxation describes the effects of these fluctuations on f . They arise because a given particle sees the rest of the system as a collection of point masses rather than as a smooth mass distribution. Relaxational effects, also known (somewhat confusingly) as collisional effects, can therefore be seen as particles influencing each other individually as opposed as to collectively. To allow for these effects, a *collision*

term has to be introduced on the right hand side of the Boltzmann equation.

The Fokker-Planck (FP) equation is derived by assuming that relaxation is due to a large number of 2-body gravitational encounters, each of which leads to a small deflection and occurs “locally”, i.e., these affect the velocity of a star without affecting its position. This is the basis for Chandrasekhar’s theory of relaxation (Chandrasekhar, 1960; Binney and Tremaine, 1987; Spitzer, 1987). Under these assumptions, one can write

$$D_t f = - \sum_{i=1}^3 \frac{\partial}{\partial v_i} [f(\vec{x}, \vec{v}) \langle \Delta v_i \rangle] + \frac{1}{2} \sum_{i,j=1}^3 \frac{\partial^2}{\partial v_i \partial v_j} [f(\vec{x}, \vec{v}) \langle \Delta v_i \Delta v_j \rangle], \quad (8.2)$$

where the “diffusion coefficient” $\langle \Delta v_i \rangle$ is the average change in v_i per unit of time due to encounters (see Rosenbluth et al. (1957a); Binney and Tremaine (1987) for a derivation).

From Jeans’ theorem ??, for a spherical system in dynamical equilibrium, the DF f can depend on the phase-space coordinates (\vec{x}, \vec{v}) only through the (specific) orbital binding energy E and angular momentum (in modulus) J ,

$$f(\vec{x}, \vec{v}) = F(E(\vec{x}, \vec{v}), J(\vec{x}, \vec{v})). \quad (8.3)$$

In the vast majority of applications, the Fokker-Planck formalism is applied in the two-dimensional (E, J) -space or, assuming isotropy, the one-dimensional E -space rather than the six-dimensional phase space, through the operation of “orbit averaging” (see Cohn (1979, 1980, 1985); Spitzer (1987) amongst others).

A standard form of the FP equation for an isotropic, spherical system is

$$D_t N(E) \equiv \frac{\partial N}{\partial t} + \frac{\partial N}{\partial E} \frac{dE}{dt} \Big|_{\phi} = - \frac{\partial \mathcal{F}_E}{\partial E} \quad (8.4)$$

where

$$\mathcal{F}_E = m \mathcal{D}_E F - \mathcal{D}_{EE} \frac{\partial F}{\partial E} \quad (8.5)$$

is the flux of particles in the energy space; $dE/dt|_{\phi}$ is the change of energy due to the evolution of the potential ϕ ; $N(E)$ is the density of stars in E -space,

$$N(E) = 16\pi^2 p(E) F(E) \quad (8.6)$$

with $p(E) = \int_0^{r_{\max}} r^2 v dr$. The “flux coefficients” are

$$\mathcal{D}_E = 16\pi^3 \lambda m_f \int_{\phi(0)}^E dE' p(E') F_f(E'), \quad (8.7)$$

$$\mathcal{D}_{EE} = 16\pi^3 \lambda m_f^2 \left[q(E) \int_E^0 dE' F_f(E') + \right. \quad (8.8)$$

$$\left. \int_{\phi(0)}^E dE' q(E') F_f(E') \right], \quad (8.9)$$

where $\lambda \equiv 4\pi G^2 \ln \Lambda$. $q(E) = \frac{1}{3} \int_0^{r_{\max}} r^2 v^3 dr$ is the volume of phase space accessible to particles with energies lower than E , and $p(E) = \partial q / \partial E$ Goodman (1983).

We used an index “f” for “field” to distinguish the mass and DF of the population we follow (“test-stars”) from the “field” objects. This distinction does not apply to a single-component

system but it is easy to generalise to a multi-component situation by summing over components to get the total flux coefficient

$$\mathcal{D}_E = \sum_{l=1}^{N_{\text{comp}}} \mathcal{D}_{E,l}, \quad \mathcal{D}_{EE} = \sum_{l=1}^{N_{\text{comp}}} \mathcal{D}_{EE,l}, \quad (8.10)$$

where the flux coefficient for component l can be written by replacing the subscript “ f ” by “ l ” in Eq. 8.9.

We now explain schematically how the FP equation is implemented numerically to follow the evolution of star clusters. A more detailed description can be found in, e.g., Chernoff and Weinberg (1990). In the most common scheme, pioneered by Cohn (1980), two types of steps are employed alternately, a method known as “operator splitting”.

1. **Diffusion step.** The change in the distribution function F for a discrete time-step Δt is computed by use of the FP equation *assuming the potential ϕ is fixed*, i.e., setting $D_t N = \partial N / \partial t = \partial N / \partial t|_{\text{coll}}$. The FP equation is discretised on an energy grid. The flux coefficients are computed using the DF(s) of the previous step; this makes the equations linear in the values of F on the grid points. The finite-differencing scheme is the implicit Chang and Cooper (1970) algorithm, which is first order in time and energy.
2. **Poisson step.** Now the change of potential resulting from the modification in the DF F is computed and F is modified to account for the term $dE/dt|_{\phi}$, i.e., assuming $D_t N = \partial N / \partial t + \partial N / \partial E dE/dt|_{\phi} = 0$. This can be done implicitly because, as

long as the change in ϕ over Δt is very small, the actions of each orbit are adiabatic invariants. Hence, during the Poisson step, the distribution function, expressed in terms of the actions, does not change. In practice, an iterative scheme is used to compute the modified potential, determined implicitly by the modified DF, through the Poisson equation. The iteration starts with the values of ϕ , ρ , etc. computed before the previous diffusion step.

A variant of the FP equation analogous to Eq. 8.4 can be written which allows for anisotropy by taking into account the dependence of F on J and including a J -flux and corresponding flux coefficients Cohn and Kulsrud (1978); Cohn (1979, 1985); Takahashi (1995, 1996, 1997); Drukier et al. (1999). The expressions for the flux coefficients are significantly longer than in the isotropic case and we do not present them here. However, we note that in galactic nuclei, in contrast to globular clusters, anisotropy plays a key role because of the existence of a loss cone.

The use of the FP approach to determine the distribution of stars around a MBH requires a few modifications. First the (Keplerian) contribution of the MBH to the potential has to be added. Several authors have made use of the FP or similar formalisms to study the dynamics well within the influence radius under the assumption of a fixed potential Bahcall and Wolf (1976, 1977); Lightman and Shapiro (1977); Cohn and Kulsrud (1978); Hopman and Alexander (2006b,c); Merritt et al. (2006b), which is a significant simplification. The static potential included a contribution for the stellar nucleus in the last study Merritt et al. (2006b) but was limited to

a Keplerian MBH potential in the other cases. The presence of the MBH also constitutes a central sink as stars are destroyed or swallowed if they come very close to it. This has to be implemented into FP codes as a boundary condition. Lightman and Shapiro (1977) and Cohn and Kulsrud (1978) have developed detailed (and rather complex) treatments of the loss cone for the anisotropic FP formalism. It can be used in a simplified way in an isotropic FP analysis Bahcall and Wolf (1977) to obtain a good approximation to the distribution of stars around a MBH and of the rates of consumption of stars by the MBH. However, additional analysis is required to determine what fraction of the swallowed stars are EMRIs and what their orbital properties are Hopman and Alexander (2005a, 2006c).

8.3 Moment models

Another way to approximately solve the (collisional) Boltzmann equation is to take velocity moments of it. The moment or order $n = 0$ of the DF is the density, the moments of order $n = 1$ are bulk velocities and $n = 2$ corresponds to (anisotropic) pressures (or velocity dispersions). This is analogous to the derivation of the Jeans equation from the collisionless Boltzmann equation Binney and Tremaine (1987) but the collision term introduces moments of order $n + 1$ in the equations for moments of order n .

In the “gaseous model”, which can be envisaged as a particular case, one assumes spherical symmetry (but not necessarily dynamical equilibrium) and truncates the infinite set of moment equations at $n = 2$. The system is closed with the assumption that energy exchanges

between stars through 2-body relaxation can be approximated by an ad hoc (local) heat conduction prescription Hachisu et al. (1978); Lynden-Bell and Eggleton (1980). This reduces the study of the stellar system to that of a self-gravitating conducting gas sphere. Multi-mass models have been implemented Louis and Spurzem (1991); Spurzem (1992); Giersz and Spurzem (1994); Spurzem and Takahashi (1995) and the detailed forms for the conductivities have been improved by comparing to direct N -body models (described below). The addition of a central accreting MBH and a treatment for loss-cone effects was done by Amaro-Seoane et al. (2004b) for the single-mass case (a comprehensive description of the code is in the appendix of the same work), and by Amaro-Seoane (2004b) for a stellar mass spectrum.

The system is treated as a continuum, which is only adequate for a large number of stars and in well populated regions of the phase space. We consider here spherical symmetry and single-mass stars. We handle relaxation in the Fokker-Planck approximation, i.e. like a diffusive process determined by local conditions. We make also use of the hydrodynamical approximation; that is to say, only local moments of the velocity dispersion are considered, not the full orbital structure. In particular, the effect of the two-body relaxation can be modelled by a local heat flux equation with an appropriately tailored conductivity.

For our description we use polar coordinates, r, θ, ϕ . The vector $\mathbf{v} = (v_i)$, $i = r, \theta, \phi$ denotes the velocity in a local Cartesian coordinate system at the spatial point r, θ, ϕ . For succinctness, we shall employ the notation $u = v_r$, $v = v_\theta$, $w = v_\phi$. The distribution function f , is a function of $r, t, u, v^2 + w^2$ only due to spher-

ical symmetry, and is normalised according to

$$\rho(r, t) = \int f(r, u, v^2 + w^2, t) du dv dw. \quad (8.11)$$

Here $\rho(r, t)$ is the mass density; if m_\star denotes the stellar mass, we get the particle density $n = \rho/m_\star$. The Euler-Lagrange equations of motion corresponding to the Lagrange function

$$\mathcal{L} = \frac{1}{2}(\dot{r}^2 + r^2\dot{\theta}^2 + r^2 \sin^2\theta \dot{\phi}^2) - \Phi(r, t) \quad (8.12)$$

are the following

$$\begin{aligned} \dot{u} &= -\frac{\partial \Phi}{\partial r} + \frac{v^2 + w^2}{r} \\ \dot{v} &= -\frac{uv}{r} + \frac{w^2}{r \tan \theta} \\ \dot{w} &= -\frac{uw}{r} - \frac{vw}{r \tan \theta} \end{aligned} \quad (8.13)$$

And so we get a complete local Fokker-Planck equation,

$$\begin{aligned} \frac{\partial f}{\partial t} + v_r \frac{\partial f}{\partial r} + v_\theta \frac{\partial f}{\partial v_r} + v_\phi \frac{\partial f}{\partial v_\theta} + v_\phi \frac{\partial f}{\partial v_\phi} = \\ \left(\frac{\delta f}{\delta t} \right)_{FP} \end{aligned} \quad (8.14)$$

In our model we do not solve the equation directly; we use a so-called *momenta process*. The momenta of the velocity distribution function f are defined as follows

$$\begin{aligned} \langle i, j, k \rangle := \\ \int_{-\infty}^{+\infty} v_r^i v_\theta^j v_\phi^k f(r, v_r, v_\theta, v_\phi, t) dv_r dv_\theta dv_\phi; \end{aligned} \quad (8.15)$$

We define now the following moments of the velocity distribution function,

$$\langle 0, 0, 0 \rangle := \rho = \int f du dv dw \quad (8.16)$$

$$\langle 1, 0, 0 \rangle := u = \int u f du dv dw \quad (8.17)$$

$$\begin{aligned} \langle 2, 0, 0 \rangle := p_r + \rho u^2 = \\ \int u^2 f du dv dw \end{aligned} \quad (8.18)$$

$$\langle 0, 2, 0 \rangle := p_\theta = \int v^2 f du dv dw \quad (8.19)$$

$$\langle 0, 0, 2 \rangle := p_\phi = \int w^2 f du dv dw \quad (8.20)$$

$$\begin{aligned} \langle 3, 0, 0 \rangle := F_r + 3up_r + u^3 = \\ \int u^3 f du dv dw \end{aligned} \quad (8.21)$$

$$\begin{aligned} \langle 1, 2, 0 \rangle := F_\theta + up_\theta = \\ \int uv^2 f du dv dw \end{aligned} \quad (8.22)$$

$$\begin{aligned} \langle 1, 0, 2 \rangle := F_\phi + up_\phi = \\ \int uw^2 f du dv dw, \end{aligned} \quad (8.23)$$

where ρ is the density of stars, u is the bulk velocity, v_r and v_t are the radial and tangential flux velocities, p_r and p_t are the radial and tangential pressures, F_r is the radial and F_t the tangential kinetic energy flux (Louis and Spurzem, 1991). Note that the definitions of p_i and F_i are such that they are proportional to the random motion of the stars. Due to spherical symmetry, we have $p_\theta = p_\phi =: p_t$ and $F_\theta = F_\phi =: F_t/2$. By $p_r = \rho\sigma_r^2$ and $p_t = \rho\sigma_t^2$ the random velocity dispersions are given, which are closely related to observable properties in stellar clusters.

$F = (F_r + F_t)/2$ is a radial flux of random

kinetic energy. In the notion of gas dynamics it is just an energy flux. Whilst for the θ – and ϕ – components in the set of Eqs. (8.23) are equal in spherical symmetry, for the r and t – quantities this is not true. In stellar clusters the relaxation time is larger than the dynamical time and so any possible difference between p_r and p_t may *survive* many dynamical times. We shall denote such differences anisotropy. Let us define the following velocities of energy transport:

$$\begin{aligned} v_r &= \frac{F_r}{3p_r} + u, \\ v_t &= \frac{F_t}{2p_t} + u. \end{aligned} \quad (8.24)$$

In case of *weak* isotropy ($p_r = p_t$), $2F_r = 3F_t$, and thus $v_r = v_t$, i.e. the (radial) transport velocities of radial and tangential random kinetic energy are equal.

The Fokker-Planck equation (8.14) is multiplied with various powers of the velocity components u , v , w . We get so up to second order a set of moment equations: A mass equation, a continuity equation, an Euler equation (force) and radial and tangential energy equations. The system of equations is closed by a phenomenological heat flux equation for the flux of radial and tangential RMS (*root mean square*) kinetic energy, both in radial direction. The concept is physically similar to that of Lynden-Bell and Eggleton (1980). The set of equations is

$$\begin{aligned} \frac{\partial \rho}{\partial t} + \frac{1}{r^2} \frac{\partial}{\partial r} (r^2 u \rho) &= 0 \\ \frac{\partial u}{\partial t} + u \frac{\partial u}{\partial r} + \frac{GM_r}{r^2} + \frac{1}{\rho} \frac{\partial p_r}{\partial r} + 2 \frac{p_r - p_t}{\rho r} &= 0 \\ \frac{\partial p_r}{\partial t} + \frac{1}{r^2} \frac{\partial}{\partial r} (r^2 u p_r) + 2 p_r \frac{\partial u}{\partial r} + \frac{1}{r^2} \frac{\partial}{\partial r} (r^2 F_r) - \\ \frac{2F_t}{r} &= -\frac{4}{5} \frac{(2p_r - p_t)}{\lambda_A t_{\text{rlx}}} \\ \frac{\partial p_t}{\partial t} + \frac{1}{r^2} \frac{\partial}{\partial r} (r^2 u p_t) + 2 \frac{p_t u}{r} + \frac{1}{2r^2} \frac{\partial}{\partial r} (r^2 F_t) + \\ \frac{F_t}{r} &= \frac{2}{5} \frac{(2p_r - p_t)}{\lambda_A t_{\text{rlx}}}, \end{aligned} \quad (8.25)$$

where λ_A is a numerical constant related to the time-scale of collisional anisotropy decay. The value chosen for it has been discussed in comparison with direct simulations performed with the N –body code (Giersz and Spurzem, 1994). The authors find that $\lambda_A = 0.1$ is the physically realistic value inside the half-mass radius for all cases of N , provided that close encounters and binary activity do not carry out an important role in the system, what is, on the other hand, inherent to systems with a big number of particles, as this is.

With the definition of the mass M_r contained in a sphere of radius r

$$\frac{\partial M_r}{\partial r} = 4\pi r^2 \rho, \quad (8.26)$$

the set of equations is then equivalent to gas-dynamical equations coupled with the equation of Poisson. To close it, we need an independent relation, for moment equations of order n contain moments of order $n + 1$. For this we use the heat conduction closure, a phenomenological approach obtained in an analogous way to gas dynamics. It was used for the first time by Lynden-Bell and Eggleton (1980)

but restricted to isotropy. In this approximation one assumes that heat transport is proportional to the temperature gradient,

$$F = -\kappa \frac{\partial T}{\partial r} = -\Lambda \frac{\partial \sigma^2}{\partial r} \quad (8.27)$$

That is the reason why such models are usually also called *conducting gas sphere models*.

It has been argued that for the classical approach $\Lambda \propto \bar{\lambda}^2/\tau$, one has to choose the Jeans' length $\lambda_J^2 = \sigma^2/(4\pi G\rho)$ and the standard Chandrasekhar local relaxation time $t_{\text{rlx}} \propto \sigma^3/\rho$ (Lynden-Bell and Eggleton, 1980), where $\bar{\lambda}$ is the mean free path and τ the collisional time. In this context we obtain a conductivity $\Lambda \propto \rho/\sigma$. We shall consider this as a working hypothesis. For the anisotropic model we use a mean velocity dispersion $\sigma^2 = (\sigma_r^2 + 2\sigma_t^2)/3$ for the temperature gradient and assume $v_r = v_t$ (Betwieser and Spurzem, 1986). Forasmuch as, the equations we need to close our model are

$$\begin{aligned} v_r - u + \frac{\lambda}{4\pi G\rho t_{\text{rlx}}} \frac{\partial \sigma^2}{\partial r} &= 0 \\ v_r &= v_t. \end{aligned} \quad (8.28)$$

Interaction terms

We now introduce the interaction terms to be added to right hand of the star component equations.

Equation of continuity

We now modify the star continuity equation so as to include the interaction terms (Langbein et al., 1990). The equation

$$\frac{\partial \rho_\star}{\partial t} + \frac{1}{r^2} \frac{\partial}{\partial r} (r^2 \rho_\star u_\star) = 0, \quad (8.29)$$

becomes

$$\begin{aligned} \frac{\partial \rho_\star}{\partial t} + \frac{1}{r^2} \frac{\partial}{\partial r} (r^2 \rho_\star u_\star) &= \\ \left(\frac{\delta \rho_\star}{\delta t} \right)_{\text{coll}} + \left(\frac{\delta \rho_\star}{\delta t} \right)_{\text{lc}}; \end{aligned} \quad (8.30)$$

where the right-hand term reflects the time variation of the star's density due to stars interactions (i.e. due to the calculation of the mean rate of gas production by stars collisions) and loss-cone (stars plunging on to the central object).

If $f(v_{\text{rel}})$ is the stellar distribution of relative velocities, then the mean rate of gas production by stellar collisions is

$$\begin{aligned} \left(\frac{\delta \rho_\star}{\delta t} \right)_{\text{coll}} &= \\ - \int_{|v_{\text{rel}}| > \sigma_{\text{coll}}} \frac{\rho_\star f_c(v_{\text{rel}})}{t_{\text{coll}}} f(v_{\text{rel}}) d^3 v_{\text{rel}} \end{aligned} \quad (8.31)$$

$$\begin{aligned} \left(\frac{\delta \rho_\star}{\delta t} \right)_{\text{coll}} &= \\ - \int_{|v_{\text{rel}}| > \sigma_{\text{coll}}} \frac{\rho_\star f_c(v_{\text{rel}})}{t_{\text{coll}}} f(v_{\text{rel}}) d^3 v_{\text{rel}} \end{aligned} \quad (8.32)$$

In the last expression $f(v_{\text{rel}})$ is a Schwarzschild - Boltzmann distribution,

$$\begin{aligned} f(v_{\text{rel}}) &= \frac{1}{2\pi^{3/2} \sigma_r \sigma_t^2} \cdot \\ \exp \left[-\frac{(v_{\text{rel},r} - u_\star)^2}{4\sigma_r^2} - \frac{v_{\text{rel},t}^2}{2\sigma_t^2} \right] \end{aligned} \quad (8.33)$$

As regards f_c , it is the relative fraction of mass liberated per stellar collision into the gaseous

medium. Under certain assumptions given in the initial work of Spitzer and Saslaw (1966), we can calculate it as an average over all impact parameters resulting in $r_{\min} < 2r_*$ and as a function of the relative velocity at infinity of the two colliding stars, v_{rel} . Langbein et al. (1990) approximate their result by

$$f_c(v_{\text{rel}}) = \begin{cases} \left(1 + q_{\text{coll}} \sqrt{\frac{\sigma_{\text{coll}}}{v_{\text{rel}}}}\right)^{-1} & v_{\text{rel}} > \sigma_{\text{coll}} \\ 0 & v_{\text{rel}} < \sigma_{\text{coll}}, \end{cases} \quad (8.34)$$

with $q_{\text{coll}} = 100$. So, we have that

$$f_c(v_{\text{rel}}) = \begin{cases} 0.01 & \sigma_{\text{coll}} = v_{\text{rel}} \\ 0 & \sigma_{\text{coll}} > v_{\text{rel}}, \end{cases} \quad (8.35)$$

The first interaction term is

$$\left(\frac{\delta \rho_*}{\delta t}\right)_{\text{coll}} = -\rho_* \frac{f_c}{t_{\text{coll}}} \left[1 - \text{erf}\left(\frac{\sigma_{\text{coll}}}{\sqrt{6}\sigma_r}\right)\right] \left[1 - \text{erf}\left(\frac{\sigma_{\text{coll}}}{\sqrt{6}\sigma_t}\right)\right]^2 \quad (8.36)$$

which, for simplification, we re-call like this

$$\left(\frac{\delta \rho_*}{\delta t}\right)_{\text{coll}} \equiv -\rho_* X_{\text{coll}}. \quad (8.37)$$

Since the evolution of the system that we are studying can be regarded as stationary, we introduce for each equation the “logarithmic variables” in order to study the evolution at long-term. In the other hand, if the system happens to have quick changes, we should use the “non-logarithmic” version of the equations. For this reason we will write at the end of each subsection the equation in terms of the logarithmic variables.

In the case of the equation of continuity, we develop it and divide it by ρ_* because we are looking for the logarithm of the stars density, $\partial \ln \rho_*/\partial t = (1/\rho_*)\partial \rho_*/\partial t$. The result is:

$$\frac{\partial \ln \rho_*}{\partial t} + \frac{\partial u_*}{\partial r} + u_* \frac{\partial \ln \rho_*}{\partial r} + \frac{2u_*}{r} = \frac{1}{\rho_*} \left(\frac{\delta \rho_*}{\delta t}\right)_{\text{coll}} + \frac{1}{\rho_*} \left(\frac{\delta \rho_*}{\delta t}\right)_{\text{lc}} \quad (8.38)$$

Momentum balance

The second equation has the following star interaction terms:

$$\frac{\partial u_*}{\partial t} + u_* \frac{\partial u_*}{\partial r} + \frac{GM_r}{r^2} + \frac{1}{\rho_*} \frac{\partial p_r}{\partial r} + 2 \frac{p_r - p_t}{\rho_* r} = \left(\frac{\delta u_*}{\delta t}\right)_{\text{drag}} \quad (8.39)$$

The interaction term is due to the decelerating force at which stars that move inside the gas are subject to.

$$\left(\frac{\delta u_*}{\delta t}\right)_{\text{drag}} = -X_{\text{drag}} \frac{1}{\rho_*} (u_* - u_g) \quad (8.40)$$

where we have introduced the following definition:

$$X_{\text{drag}} \equiv -C_D \frac{\pi r_*^2}{m_*} \rho_* \rho_g \sigma_{\text{tot}}, \quad (8.41)$$

with $\sigma_{\text{tot}}^2 = \sigma_r^2 + \sigma_t^2 + (u_* - u_g)^2$

In the Gas Model we use a logarithmic expression of the equation, so that we multiply Eq. (8.39) by $\rho_* r/p_r$:

$$\frac{\rho_* r}{p_r} \left(\frac{\partial u_*}{\partial t} + u_* \right) + \frac{GM_r}{rp_r} \rho_* + \frac{\partial \ln p_r}{\partial \ln r} + 2 \left(1 - \frac{p_t}{p_r} \right) = -X_{\text{drag}} \frac{r}{p_r} (u_* - u_g) \quad (8.42)$$

Radial energy equation

As regards the last but one equation, the interaction terms are:

$$\begin{aligned} & \frac{\partial p_r}{\partial t} + \frac{1}{r^2} \frac{\partial}{\partial r} (r^2 u_* p_r) + 2p_r \frac{\partial u_*}{\partial r} + \\ & \frac{4}{5} \frac{(2p_r - p_t)}{t_{\text{rlx}}} + \frac{1}{r^2} \frac{\partial}{\partial r} (r^2 F_r) - \frac{2F_t}{r} = \\ & \left(\frac{\delta p_r}{\delta t} \right)_{\text{drag}} + \left(\frac{\delta p_r}{\delta t} \right)_{\text{coll}}, \end{aligned} \quad (8.43)$$

where

$$\begin{aligned} \left(\frac{\delta p_r}{\delta t} \right)_{\text{drag}} &= -2X_{\text{drag}} \sigma_r^2, \\ \left(\frac{\delta p_r}{\delta t} \right)_{\text{coll}} &= -X_{\text{coll}} \rho_* \tilde{\sigma}_r^2 \epsilon. \end{aligned} \quad (8.44)$$

In order to determine ϵ we introduce the ratio k of kinetic energy of the remaining mass after the encounter over its initial value (before the encounter); k is a measure of the inelasticity of the collision: for $k = 1$ we have the minimal inelasticity, just the kinetic energy of the liberated mass fraction is dissipated, while if $k < 1$ a surplus amount of stellar kinetic energy is dissipated during the collision (tidal interactions and excitation of stellar oscillations). If we calculate the energy loss in the stellar system per unit volume as a function of k , we obtain

$$\epsilon = f_c^{-1} [1 - k(1 - f_c)]. \quad (8.45)$$

We divide by p_r so that we get the logarithmic variable version of the equation. We make also the following substitution:

$$\begin{aligned} F_r &= 3p_r v_r \\ F_t &= 2p_t v_t \end{aligned} \quad (8.46)$$

The resulting equation is

$$\begin{aligned} & \frac{\partial \ln p_r}{\partial t} + (u_* + 3v_r) \frac{\partial \ln p_r}{\partial r} \\ & + 3 \left(\frac{\partial u_*}{\partial r} + \frac{\partial v_r}{\partial r} \right) + \\ & \frac{2}{r} \left(u_* + 3v_r - 2v_t \frac{p_t}{p_r} \right) + \frac{4}{5} \frac{2 - p_t/p_r}{t_{\text{rlx}}} = \\ & \frac{1}{p_r} \left(\frac{\delta p_r}{\delta t} \right)_{\text{drag}} + \frac{1}{p_r} \left(\frac{\delta p_r}{\delta t} \right)_{\text{coll}} \end{aligned} \quad (8.47)$$

Tangential energy equation

To conclude the set of equations of the star component with the interaction terms, we have the following equation:

$$\begin{aligned} & \frac{\partial p_t}{\partial t} + \frac{1}{r^2} \frac{\partial}{\partial r} (r^2 u_* p_t) + 2 \frac{p_t u_*}{r} - \\ & \frac{4}{5} \frac{(2p_r - p_t)}{t_{\text{rlx}}} + \frac{1}{r^2} \frac{\partial}{\partial r} (r^2 F_t) + \frac{2F_t}{r} = \\ & \left(\frac{\delta p_t}{\delta t} \right)_{\text{drag}} + \left(\frac{\delta p_t}{\delta t} \right)_{\text{coll}}, \end{aligned} \quad (8.48)$$

where

$$\begin{aligned} \left(\frac{\delta p_t}{\delta t} \right)_{\text{drag}} &= -2X_{\text{drag}} \sigma_t^2 \\ \left(\frac{\delta p_t}{\delta t} \right)_{\text{coll}} &= -X_{\text{coll}} \rho_* \tilde{\sigma}_t^2 \epsilon. \end{aligned} \quad (8.49)$$

We follow the same path like in the last case and so we get the following logarithmic variable equation:

$$\begin{aligned} & \frac{\partial \ln p_t}{\partial t} + (u_\star + 2v_t) \frac{\partial \ln p_t}{\partial r} + \frac{\partial}{\partial r} (u_\star + 2v_t) + \\ & \frac{4}{r} (u_\star + 2v_t) - \frac{4}{5} \frac{2p_r/p_t - 1}{t_{\text{rlx}}} = \\ & \frac{1}{p_t} \left(\frac{\delta p_t}{\delta t} \right)_{\text{drag}} + \frac{1}{p_t} \left(\frac{\delta p_t}{\delta t} \right)_{\text{coll}} \end{aligned}$$

8.4 Solving conducting, self-gravitating gas spheres

In this subsection, we explain briefly how the gaseous model is solved. The algorithm used is a partially implicit Newton-Raphson-Henyey iterative scheme (see Henyey et al., 1959; Kippenhahn and Weigert, 1994, their section 11.2).

Putting aside the bounding conditions, the set of equations to be solved are Eqs. 8.25 to 8.28. In practice, however, the equations are rewritten using the logarithm of all positive quantities as dependant functions. As explained in Giersz and Spurzem (1994), this greatly improves energy conservation. Formally, one may write this system as follows

$$\begin{aligned} & \frac{\partial x^{(i)}}{\partial t} + f^{(i)} \left(\left\{ x^{(j)}, \frac{\partial x^{(j)}}{\partial r} \right\}_{j=1}^{N_{\text{eq}}} \right) = 0 \\ & \text{for } i = 1 \dots 4 \\ & f^{(i)} \left(\left\{ x^{(j)}, \frac{\partial x^{(j)}}{\partial r} \right\}_{j=1}^{N_{\text{eq}}} \right) = 0 \\ & \text{for } i = 5 \dots N_{\text{eq}} \end{aligned} \quad (8.50)$$

where the $x^{(i)}$ are the local quantities defining the state of the cluster, i.e.

$$\begin{aligned} \underline{x} & \equiv \{x^{(1)}, x^{(2)}, \dots, x^{(N_{\text{eq}})}\} \\ & \equiv \{\log \rho, u, \log p_r, \log p_t, \\ & \log M_r, v_r - u, v_t - u\}, \end{aligned} \quad (8.51)$$

with $N_{\text{eq}} = 7$ in the present application.

To be solved numerically, this set of coupled partial differential equations have to be discretised according to time and radius. Let us first consider time stepping. Let Δt be the time step. Assume we know the solution $\underline{x}(t - \Delta t)$ at time $t - \Delta t$ and want to compute $\underline{x}(t)$. For the sake of numerical stability, a partially implicit scheme is used. We adopt the shorthand notations $x^{(i)} \equiv x^{(i)}(t)$ and $y^{(i)} \equiv x^{(i)}(t - \Delta t)$. Time derivation is replaced by finite differences,

$$\frac{\partial x^{(i)}}{\partial t} \rightarrow \Delta t^{-1} (x^{(i)} - y^{(i)}). \quad (8.52)$$

In the terms $f^{(i)}$, we replace the $x^{(j)}$ by $\tilde{x}^{(j)}$ which are values intermediate between $y^{(j)}$ and $x^{(j)}$, $\tilde{x}^{(j)} = \zeta x^{(j)} + (1 - \zeta)y^{(j)}$, with $\zeta = 0.55$ for stability purpose (Giersz and Spurzem, 1994).

Spatial discretisation is done by defining all quantities (at a given time) on a radial mesh, $\{r_1, r_2, \dots, r_{N_r}\}$ with $r_1 = 0$ and $r_{N_r} = r_{\text{max}}$. A staggered mesh is implemented. While values of r , u , v_t , v_r and M_r are defined at the boundaries of the mesh cells, ρ , p_t and p_r are defined at the centre of each cell. When the value of a “boundary” quantity is needed at the centre of a cell, or vice-versa, one does a simple averaging, i.e. $\hat{b}_k = 0.5(b_{k-1} + b_k)$, $\hat{c}_k = 0.5(c_k + c_{k+1})$, if b and c are border- and

centre-defined quantities, and \hat{b}, \hat{c} their centre- and border-interpolations, respectively. For all runs presented here, $N_r = 300$ and the points r_2 to r_{\max} are logarithmically equidistant with $r_{\max} = 10^4$ pc and $r_2 \simeq 1.7 \times 10^{-6}$ pc. Let us adopt the notation $x_k^{(j)}$ for the value of $x^{(j)}$ at position r_k (or \hat{r}_k) and $\Delta r_k \equiv r_k - r_{k-1}$. Then, radial derivatives in the terms $f^{(i)}$ are approximated by finite differences,

$$\frac{\partial x^{(j)}}{\partial r} \rightarrow \frac{\tilde{x}_k^{(j)} - \tilde{x}_{k-1}^{(j)}}{\Delta r_k} \quad (8.53)$$

if the derivative has to be evaluated at a point where x_k is defined (centre or border of a cell), or

$$\frac{\partial x^{(j)}}{\partial r} \rightarrow \frac{\hat{x}_k^{(j)} - \hat{x}_{k-1}^{(j)}}{\Delta r_k} = \frac{\tilde{x}_{k+1}^{(j)} - \tilde{x}_{k-1}^{(j)}}{2\Delta r_k} \quad (8.54)$$

otherwise. As an exception we use upstream differencing in $\partial u / \partial r$ for the second equation in set 8.25, i.e. the difference quotient is displaced by half a mesh point upstream to improve stability.

By making the substitutions for $\partial x^{(j)} / \partial t$ and $\partial x^{(j)} / \partial r$ in the set of differential equations 8.50, one obtains, at each mesh point r_k , a set of N_{eq} non-linear algebraic equations linking the new values to be determined, \underline{x}_{k-1} and \underline{x}_k , to the “old” ones, \underline{y}_{k-1} and \underline{y}_k , which are known,

$$\mathcal{F}_k^{(i)}(\underline{x}_{k-1}, \underline{x}_k | \underline{y}_{k-1}, \underline{y}_k) = 0 \quad (8.55)$$

$$i = 1 \dots N_{\text{eq}}, \quad k = 1 \dots N_r.$$

Note that the structure of the equations is the same at all mesh points, except $k = 1$ and $k = N_r$. In particular, terms $k - 1$ do not appear in $\mathcal{F}_1^{(i)}$. Also, one has to keep in mind

that only the \underline{x}_{k-1} and \underline{x}_k are unknown; the \underline{y}_{k-1} and \underline{y}_k play the role of fixed parameters in these equations (as do the Δr_k). If one defines a $(N_{\text{eq}} \times N_r)$ -dimension vector \mathcal{X}^* whose component $N_{\text{eq}}(k-1) + i$ is $x_k^{(i)}$, one can write the system of $N_{\text{eq}} \times N_r$ equations as $\mathcal{F}^*(\mathcal{X}^*) = 0$, i.e.

$$\mathcal{F}^*(\mathcal{X}^*) \equiv \begin{pmatrix} \mathcal{F}_1^{(1)} \\ \mathcal{F}_1^{(2)} \\ \vdots \\ \mathcal{F}_1^{(N_{\text{eq}})} \\ \mathcal{F}_2^{(1)} \\ \vdots \\ \mathcal{F}_2^{(N_{\text{eq}})} \\ \vdots \\ \mathcal{F}_{N_r}^{(1)} \\ \vdots \\ \mathcal{F}_{N_r}^{(N_{\text{eq}})} \end{pmatrix} = \begin{pmatrix} 0 \\ \vdots \\ 0 \end{pmatrix} \quad (8.56)$$

Where we have defined

$$\mathcal{X}^* \equiv \begin{pmatrix} x_1^{(1)} \\ x_1^{(2)} \\ \vdots \\ x_1^{(N_{\text{eq}})} \\ x_2^{(1)} \\ \vdots \\ x_2^{(N_{\text{eq}})} \\ \vdots \\ x_{N_r}^{(1)} \\ \vdots \\ x_{N_r}^{(N_{\text{eq}})} \end{pmatrix}. \quad (8.57)$$

The system is solved iteratively using Newton-Raphson scheme. If $\mathcal{X}^*_{[m]}$ is the approxima-

tion to the solution of Eq. 8.56 after iteration m , with $\mathcal{F}^*_{[m]} \equiv \mathcal{F}^*(\mathcal{X}^*_{[m]}) \neq 0$, the solution is refined through the relation

$$\mathcal{X}^*_{[m+1]} = \mathcal{X}^*_{[m]} - \left(\frac{\partial \mathcal{F}^*}{\partial \mathcal{X}^*} \right)^{-1} \mathcal{F}^*_{[m]} \quad (8.58)$$

where $(\partial \mathcal{F}^* / \partial \mathcal{X}^*)^{-1}$ is the inverse of the matrix of derivatives. The latter, of dimension $(N_{\text{eq}} N_r) \times (N_{\text{eq}} N_r)$, has the following structure

$$\frac{\partial \mathcal{F}^*}{\partial \mathcal{X}^*} = \begin{pmatrix} \blacksquare & \square_+ & & & \\ \square_- & \blacksquare & \square_+ & & \\ & \square_- & \blacksquare & \square_+ & \\ & & \ddots & \ddots & \\ & & \square_{-k} & \blacksquare_k & \square_{+k} \\ & & & \ddots & \ddots \\ & & & \square_- & \blacksquare & \square_+ \\ & & & & \square_- & \blacksquare \end{pmatrix}. \quad (8.59)$$

In this diagram, each square is a $N_{\text{eq}} \times N_{\text{eq}}$ sub-matrix. For $2 \leq k \leq N_r - 1$, lines $N_{\text{eq}}k - 6$ to $N_{\text{eq}}k$ of $\partial \mathcal{F}^* / \partial \mathcal{X}^*$ are composed of a group of 3 such $N_{\text{eq}} \times N_{\text{eq}}$ matrices, \square_{-k} , \blacksquare_k , \square_{+k} that span columns $N_{\text{eq}}k - 13$ to $N_{\text{eq}}k + N_{\text{eq}}$, while the rest is composed of zeros,

$$\blacksquare_k = \begin{pmatrix} \frac{\partial \mathcal{F}_k^{(1)}}{\partial x_k^{(1)}} & \frac{\partial \mathcal{F}_k^{(1)}}{\partial x_k^{(2)}} & \cdots & \frac{\partial \mathcal{F}_k^{(1)}}{\partial x_k^{(N_{\text{eq}})}} \\ \vdots & \vdots & & \vdots \\ \frac{\partial \mathcal{F}_k^{(N_{\text{eq}})}}{\partial x_k^{(1)}} & \frac{\partial \mathcal{F}_k^{(N_{\text{eq}})}}{\partial x_k^{(2)}} & \cdots & \frac{\partial \mathcal{F}_k^{(N_{\text{eq}})}}{\partial x_k^{(N_{\text{eq}})}} \end{pmatrix}$$

$$\square_{\pm k} = \begin{pmatrix} \frac{\partial \mathcal{F}_k^{(1)}}{\partial x_{k\pm 1}^{(1)}} & \frac{\partial \mathcal{F}_k^{(1)}}{\partial x_{k\pm 1}^{(2)}} & \cdots & \frac{\partial \mathcal{F}_k^{(1)}}{\partial x_{k\pm 1}^{(N_{\text{eq}})}} \\ \vdots & \vdots & & \vdots \\ \frac{\partial \mathcal{F}_k^{(N_{\text{eq}})}}{\partial x_{k\pm 1}^{(1)}} & \frac{\partial \mathcal{F}_k^{(N_{\text{eq}})}}{\partial x_{k\pm 1}^{(2)}} & \cdots & \frac{\partial \mathcal{F}_k^{(N_{\text{eq}})}}{\partial x_{k\pm 1}^{(N_{\text{eq}})}} \end{pmatrix}. \quad (8.60)$$

We can see this more explicitly in the two big matrix expressions of $\partial \mathcal{F}^* / \partial \mathcal{X}^*$, given ahead, in Eqs.(??).

The Heyney method is a way to take advantage of the special structure of matrix $\partial \mathcal{F}^* / \partial \mathcal{X}^*$ to solve system (8.58) efficiently, with a number of operation scaling like $\mathcal{O}(N_r)$ rather than $\mathcal{O}(N_r^3)$ as would be the case if one uses a general-purpose matrix inversion scheme². Setting $\mathcal{B}^* \equiv -\mathcal{F}^*_{[m]}$ and $\mathcal{W}^* \equiv \mathcal{X}^*_{[m+1]} - \mathcal{X}^*_{[m]}$, Eq. (8.58) is equivalent to

$$\left(\frac{\partial \mathcal{F}^*}{\partial \mathcal{X}^*} \right) \mathcal{W}^* = \mathcal{B}^* \quad (8.63)$$

with \mathcal{W}^* the unknown vector. We further decompose vectors \mathcal{W}^* and \mathcal{B}^* into N_{eq} -dimensional sub-vectors, each one representing the values at a given mesh points,

$$\mathcal{W}^* = \begin{pmatrix} \mathcal{W}_1 \\ \mathcal{W}_2 \\ \vdots \\ \mathcal{W}_k \\ \vdots \\ \mathcal{W}_{N_r} \end{pmatrix}. \quad (8.64)$$

²Memory usage is also reduced, scaling like $\mathcal{O}(N_r)$ rather than $\mathcal{O}(N_r^2)$.

$$\frac{\partial \mathcal{F}^*}{\partial \mathcal{X}^*} = \begin{pmatrix} \frac{\partial \mathcal{F}_1^1}{\partial x_1^1} & \dots & \frac{\partial \mathcal{F}_1^1}{\partial x_1^{N_{\text{eq}}}} & \frac{\partial \mathcal{F}_1^1}{\partial x_2^1} & \dots & \frac{\partial \mathcal{F}_1^1}{\partial x_2^{N_{\text{eq}}}} & 0 & \dots & 0 \\ \vdots & & & & & \vdots & \vdots & & \vdots \\ \frac{\partial \mathcal{F}_1^{N_{\text{eq}}}}{\partial x_1^1} & \dots & \frac{\partial \mathcal{F}_1^{N_{\text{eq}}}}{\partial x_1^{N_{\text{eq}}}} & \frac{\partial \mathcal{F}_1^{N_{\text{eq}}}}{\partial x_2^1} & \dots & \frac{\partial \mathcal{F}_1^{N_{\text{eq}}}}{\partial x_2^{N_{\text{eq}}}} & 0 & \dots & 0 \\ \frac{\partial \mathcal{F}_2^1}{\partial x_1^1} & \dots & \frac{\partial \mathcal{F}_2^1}{\partial x_1^{N_{\text{eq}}}} & \frac{\partial \mathcal{F}_2^1}{\partial x_2^1} & \dots & \frac{\partial \mathcal{F}_2^1}{\partial x_2^{N_{\text{eq}}}} & \frac{\partial \mathcal{F}_2^1}{\partial x_3^1} & \dots & \frac{\partial \mathcal{F}_2^1}{\partial x_3^{N_{\text{eq}}}} & 0 & \dots & 0 \\ \vdots & & & & & & \vdots & & \vdots & \vdots & & \vdots \\ \frac{\partial \mathcal{F}_2^{N_{\text{eq}}}}{\partial x_1^1} & \dots & \frac{\partial \mathcal{F}_2^{N_{\text{eq}}}}{\partial x_1^{N_{\text{eq}}}} & \frac{\partial \mathcal{F}_2^{N_{\text{eq}}}}{\partial x_2^1} & \dots & \frac{\partial \mathcal{F}_2^{N_{\text{eq}}}}{\partial x_2^{N_{\text{eq}}}} & \frac{\partial \mathcal{F}_2^{N_{\text{eq}}}}{\partial x_3^1} & \dots & \frac{\partial \mathcal{F}_2^{N_{\text{eq}}}}{\partial x_3^{N_{\text{eq}}}} & 0 & \dots & 0 \\ \dots & \dots & \dots & \dots & \dots & \dots & \dots & \dots & \dots & \dots & \dots & \dots \\ 0 & \dots & \dots & \dots & \dots & 0 & \frac{\partial \mathcal{F}_{N_r}^1}{\partial x_{N_r-1}^1} & \dots & \frac{\partial \mathcal{F}_{N_r}^1}{\partial x_{N_r-1}^{N_{\text{eq}}}} & \frac{\partial \mathcal{F}_{N_r}^1}{\partial x_{N_r}^1} & \dots & \frac{\partial \mathcal{F}_{N_r}^1}{\partial x_{N_r}^{N_{\text{eq}}}} \\ \vdots & & & & & \vdots & \vdots & & \vdots & \vdots & & \vdots \\ 0 & \dots & \dots & \dots & \dots & 0 & \frac{\partial \mathcal{F}_{N_r}^{N_{\text{eq}}}}{\partial x_{N_r-1}^1} & \dots & \frac{\partial \mathcal{F}_{N_r}^{N_{\text{eq}}}}{\partial x_{N_r-1}^{N_{\text{eq}}}} & \frac{\partial \mathcal{F}_{N_r}^{N_{\text{eq}}}}{\partial x_{N_r}^1} & \dots & \frac{\partial \mathcal{F}_{N_r}^{N_{\text{eq}}}}{\partial x_{N_r}^{N_{\text{eq}}}} \end{pmatrix} \quad (8.61)$$

$$\frac{\partial \mathcal{F}^*}{\partial \mathcal{X}^*} = \begin{pmatrix} \begin{array}{cc} \boxed{\text{diagonal}} & \boxed{\text{diagonal}} \\ \boxed{\text{diagonal}} & \boxed{\text{diagonal}} \end{array} & & & & \\ & \begin{array}{ccc} \boxed{\text{diagonal}} & \boxed{\text{diagonal}} & \boxed{\text{diagonal}} \end{array} & & & \\ & & \begin{array}{ccc} \boxed{\text{diagonal}} & \boxed{\text{diagonal}} & \boxed{\text{diagonal}} \end{array} & & & \\ & & & \begin{array}{ccc} \boxed{\text{diagonal}} & \boxed{\text{diagonal}} & \boxed{\text{diagonal}} \end{array} & & \\ & & & & \ddots & \ddots & \ddots \\ & & & & & \begin{array}{ccc} \boxed{\text{diagonal}} & \boxed{\text{diagonal}} & \boxed{\text{diagonal}} \end{array} \\ & & & & & & \begin{array}{cc} \boxed{\text{diagonal}} & \boxed{\text{diagonal}} \end{array} \end{pmatrix} \quad (8.62)$$

Then, the system (8.64) can be written as a set of coupled N_{eq} -dimensional vector equations,

$$\begin{aligned} \blacksquare_1 \mathcal{W}_1 + \square_{+1} \mathcal{W}_2 &= \mathcal{B}_1 \\ \square_{-k} \mathcal{W}_{k-1} + \blacksquare_k \mathcal{W}_k + \square_{+k} \mathcal{W}_{k+1} &= \mathcal{B}_k \\ \square_{-N_r} \mathcal{W}_{N_r-1} + \blacksquare_{N_r} \mathcal{W}_{N_r} &= \mathcal{B}_{N_r}. \end{aligned} \quad (8.65)$$

The algorithm operates in two passes. First, going from $k = 1$ to N_r , one defines recursively a sequence of N_{eq} -vectors \mathcal{V}_k and $(N_{\text{eq}} \times N_{\text{eq}})$ -matrices \mathfrak{M}_k through

$$\begin{aligned} \mathcal{V}_1 &= (\blacksquare_1)^{-1} \mathcal{B}_1 \\ \mathfrak{M}_1 &= (\blacksquare_1)^{-1} \square_{+1} \\ \mathcal{V}_k &= (\blacksquare_k - \square_{-k} \mathfrak{M}_{k-1})^{-1} (\mathcal{B}_k - \square_{-k} \mathcal{V}_{k-1}) \\ \mathfrak{M}_k &= (\blacksquare_k - \square_{-k} \mathfrak{M}_{k-1})^{-1} \square_{+k}, \quad 2 \leq k \leq N_r. \end{aligned} \quad (8.66)$$

\mathfrak{M}_{N_r} is not defined. In the second pass, the values of the unknown \mathcal{V}_k are computed, climbing back from $k = N_r$ to 1, with

$$\begin{aligned} \mathcal{W}_{N_r} &= \mathcal{V}_{N_r} \\ \mathcal{W}_k &= \mathcal{V}_k - \mathfrak{M}_k \mathcal{W}_{k+1}, \quad 1 \leq k \leq N_r - 1. \end{aligned} \quad (8.67)$$

Note that, with this algorithm, only $(N_{\text{eq}} \times N_{\text{eq}})$ matrices have to be inverted. We use Gauss elimination for this purpose because this venerable technique proves to be robust enough to properly deal with the kind of badly conditioned matrices that often appear in this application.

The initial model for the Newton-Raphson algorithm is given by the structure of the cluster at the previous time, $\mathcal{X}_{[0]}^*(t) = \mathcal{X}^*(t - \Delta t)$. One iterates until the following convergence criteria are met. Let us set $\delta x_k^{(i)} \equiv x_k^{(i)}|_{[m+1]} - x_k^{(i)}|_{[m]}$. Then, the condition for logarithmic

quantities is

$$\max_{i=1 \dots N_{\text{eq}}} \frac{1}{N_r} \sum_{k=1 \dots N_r} \left(\delta x_k^{(i)} \right)^2 < \varepsilon_1, \quad (8.68)$$

with $\varepsilon_1 = 10^{-6}$. For velocities $(u, v_r - u, v_t - u)$, one checks

$$\max_{i=1 \dots N_{\text{eq}}} \frac{1}{N_r} \sum_{k=1 \dots N_r} \left(\frac{\delta x_k^{(i)}}{x_k^{(i)} + \varepsilon_1 w_k} \right)^2 < \varepsilon_2, \quad (8.69)$$

with $\varepsilon_2 = 10^{-3}$ and $w_k = r_k (4\pi G \rho_k)^{1/2}$. Generally, two iterations are sufficient to reach convergence.

8.5 The local approximation

There are two alternative ways of further simplification for FP or moment models. One is the orbit average, which uses that any distribution function, being a steady state solution of the collisionless Boltzmann equation, can be expressed as a function of the constants of motion of an individual particle (Jeans' theorem). For the sake of simplicity, it is assumed that all orbits in the system are regular, as it is the case for example in a spherically symmetric potential; thus the distribution function f now only depends on maximally three independent integrals of motion (strong Jeans' theorem). Let us transform the Fokker-Planck equation to a new set of variables, which comprise the constants of motion instead of the velocities v_i . Since in a spherically symmetric system the distribution only depends on energy and the modulus of the angular momentum vector J , the number of independent coordinates in this example can be reduced from six to two, and all terms in the transformed equation (8) containing derivatives to other variables than E and J

vanish (in particular those containing derivatives to the spatial coordinates x_i). Integrating the remaining parts of the Fokker-Planck equation over the spatial coordinates is called orbit averaging, because in our present example (a spherical system) it would be an integration over accessible coordinate space for given E and J (which is a spherical shell between $r_{\min}(E, J)$ and $r_{\max}(E, J)$, the minimum and maximum radius for stars with energy E and angular momentum J). Such volume integration is, since f does not depend any more on x_i carried over to the diffusion coefficients D , which become orbit-averaged diffusion coefficients.

Orbit-averaged Fokker-Planck models treat very well the diffusion of orbits according to the changes of their constants of motion, taking into account the potential and the orbital structure of the system in a self-consistent way. However, they are not free of any problems or approximations. They require checks and tests, for example by comparisons with other methods, like the one described in the following. We treat relaxation like the addition of a big non-correlated number of two-body encounters. Close encounters are rare and thus we suppose that each encounter produces a very small deflection angle. Thence, relaxation can be regarded as a diffusion process³.

A typical two-body encounter in a large stellar system takes place in a volume whose linear dimensions are small compared to other typical radii of the system (total system dimension, or scaling radii of changes in density or velocity dispersion). Consequently, it is assumed

³Anyhow, it has been argued that rare deflections with a large angle may play a important role in the vicinity of a BH (Lin and Tremaine, 1980).

that an encounter only changes the velocity, not the position of a particle. Thenceforth, encounters do not produce any changes $\Delta \mathbf{x}$, so all related terms in the Fokker-Planck equation vanish. However, the local approximation goes even further and assumes that the entire cumulative effect of all encounters on a test particle can approximately be calculated as if the particle were surrounded by a very big homogeneous system with the local distribution function (density, velocity dispersions) everywhere. We are left with a Fokker-Planck equation containing only derivatives with respect to the velocity variables, but still depending on the spatial coordinates (a local Fokker-Planck equation).

In practical astrophysical applications, the diffusion coefficients occurring in the Fokker-Planck equation are not directly calculated, containing the probability Ψ for a velocity change $\Delta \mathbf{v}$ from an initial velocity \mathbf{v} . Since $D(\Delta v_i)$, and $D(\Delta v_i \Delta v_j)$ are of the dimension velocity (change) per time unit, and squared velocity (change) per time unit, respectively, one calculates such velocity changes in a more direct way, considering a test star moving in a homogeneous sea of field stars. Let the test star have a velocity \mathbf{v} and consider an encounter with a field star of velocity \mathbf{v}_f . The result of the encounter (i.e. velocity changes Δv_i of the test star) is completely determined by the impact parameter p and the relative velocity at infinity $v_{\text{rel}} = |\mathbf{v} - \mathbf{v}_f|$; thus by an integration of the type

$$\langle \Delta \dot{v}_i \rangle_p = 2\pi \int (\Delta v_i) v_{\text{rel}} n_f p dp, \quad (8.70)$$

the rate of change of the test star velocity due to encounters with v_{rel} , in field of stars with particle density n_f , averaged over all relevant

impact parameters is computed. The integration is normally carried out from p_0 (impact parameter for 90° deflection) until R , which is some maximum linear dimension of the system under consideration. Such integration generates in subsequent equations the Coulomb logarithm $\ln \Lambda$; as we have seen previously, it can be well approximated by $\ln(0.11N)$, where N is the total particle number. The diffusion coefficient finally is

$$D(\Delta v_i) = \int \langle \Delta \dot{v}_i \rangle_p f(\mathbf{v}_f) d^3 \mathbf{v}_f, \quad (8.71)$$

where $f(\mathbf{v}_f)$ is the velocity distribution of the field stars. In an equal mass system, $f(\mathbf{v}_f)$ should be equal to the distribution function of the test stars occurring in the Fokker-Planck equation for self-consistency. In case of a multi-mass system, however, $f(\mathbf{v}_f)$ could be different from the test-star distribution, if the diffusion coefficient arising from encounters between two different species of stars is to be calculated. The diffusion coefficients are (for an exact procedure see Binney and Tremaine 2008):

$$\begin{aligned} D(\Delta v_i) &= 4\pi G^2 m_f \ln \Lambda \frac{\partial}{\partial v_i} h(\mathbf{v}) \\ D(\Delta v_i v_j) &= 4\pi G^2 m_f \ln \Lambda \frac{\partial^2}{\partial v_i \partial v_j} g(\mathbf{v}) \end{aligned} \quad (8.72)$$

with the Rosenbluth potentials Rosenbluth et al. (1957b)

$$\begin{aligned} h(\mathbf{v}) &= (m + m_f) \int \frac{f(\mathbf{v}_f)}{|\mathbf{v} - \mathbf{v}_f|} d^3 \mathbf{v}_f \\ g(\mathbf{v}) &= m_f \int f(\mathbf{v}_f) |\mathbf{v} - \mathbf{v}_f| d^3 \mathbf{v}_f. \end{aligned} \quad (8.73)$$

With these results we can finally write down the local Fokker-Planck equation in its standard form for the Cartesian coordinate system of the v_i :

$$\begin{aligned} \left(\frac{\delta f}{\delta t} \right)_{\text{enc}} &= -4\pi G^2 m_f \ln \Lambda \\ &\left[\sum_{i=1}^3 \frac{\partial}{\partial v_i} \left(f(\mathbf{v}) \frac{\partial h}{\partial v_i} \right) \right. \\ &\left. + \frac{1}{2} \sum_{i,j=1}^3 \frac{\partial^2}{\partial v_i \partial v_j} \left(f(\mathbf{v}) \frac{\partial^2 g}{\partial v_i \partial v_j} \right) \right] \end{aligned} \quad (8.74)$$

Note that in Rosenbluth et al. (1957b) the above equation is given in a covariant notation, which allows for a straightforward transformation into other curvilinear coordinate systems.

Before going ahead the question is raised, why such approximation can be reasonable, regarding the long-range gravitational force, and the impossibility to shield gravitational forces as in the case of Coulomb forces in a plasma by opposite charges. The key is that logarithmic intervals in impact parameter p contribute equally to the mean square velocity change of a test particle, provided $p \gg p_0$ (see e.g. Spitzer 1987, chapter 2.1). Imagine that on one hand side the lower limit of impact parameters (p_0 , the 90° deflection angle impact parameter) is small compared to the mean interparticle distance d . Let on the other hand side D be a typical radius connected with a change in density or velocity dispersions (e.g. the scale height in a disc of a galaxy), and R be the maximum total dimension of the system. Just to be specific let us assume $D = 100d$, and $R = 100D$. In that case the volume of the spherical shell with radius between D and R is 10^6 times larger than the volume of the shell defined by the radii d

and D . Nevertheless the contribution of both shells to diffusion coefficients or the relaxation time is approximately equal. This is a heuristic illustration why the local approximation is not so bad; the reason is with other words that there are a lot more encounters with particles in the outer, larger shell, but the effect is exactly compensated by the larger deflection angle for encounters happening with particles from the inner shell. If we are in the core or in the plane of a galactic disc the density would fall off further out, so the actual error will be smaller than outlined in the above example. By the same reasoning one can see, however, that the local approximation for a particle in a low-density region, which suffers from relaxation by a nearby density concentration, is prone to failure.

These rough handy examples should illustrate that under certain conditions the local approximation is not a priori bad. On the other hand, it is obvious from our above arguments, that if we are interested in relaxation effects on particles in a low-density environment, whose orbit occasionally passes distant, high-density regions, the local approximation could be completely wrong. One might think here for example of stars on radially elongated orbits in the halo of globular clusters or of stars, globular clusters, or other objects as massive black holes, on spherical orbits in the galactic halo, passing the galactic disc. In these situations an orbit-averaged treatment seems much more appropriate.

8.6 Hénon Monte-Carlo codes

The Monte-Carlo (MC) numerical scheme is intermediate in realism and numerical efficiency between Fokker-Planck or moment/gas approaches,

which are very fast but based on a significantly idealised description of the stellar system, and direct N -body codes, which treat (Newtonian) gravity in an essentially assumption-free way but are extremely demanding in terms of computing time. The MC scheme was first introduced by Hénon to follow the relaxational evolution of globular clusters Hénon (1971b,a); Hénon (1973); Hénon (1975). To our knowledge there exist three independent codes in active development and use which are based on Hénon's ideas. The first is the one written by M. Giersz (see Giersz 2006), which implements many of the developments first introduced by Stodółkiewicz Stodółkiewicz (1982, 1986). Second is the code written by K. Joshi Joshi et al. (2000, 2001) and greatly improved and extended by A. Gürkan and J. Fregeau (see for instance Fregeau et al. (2003); Gürkan et al. (2004); Fregeau et al. (2005); Gürkan et al. (2006)). These codes have been applied to the study of globular and young clusters. Finally, M. Freitag developed an MC code specifically aimed at the study of galactic nuclei containing a central MBH Freitag and Benz (2001, 2002); Freitag et al. (2006c). The description of the method given here is based on this particular implementation.

The MC technique assumes that the cluster is spherically symmetric and represents it as a set of particles, each of which may be considered as a homogeneous spherical shell of stars sharing the same orbital and stellar properties. The number of particles may be lower than the number of stars in the simulated cluster but the number of stars per particle has to be the same for each particle. Another important assumption is that the system is always in dynamical equilibrium so that orbital time scales need not be resolved and the natural time-step is a

fraction of the relaxation (or collision) time. Instead of being determined by integration of its orbit, the position of a particle (i.e., the radius R of the shell) is picked up at random, with a probability density for R that reflects the time spent at that radius: $dP/dR \propto 1/V_r(R)$ where V_r is the radial velocity. The Freitag scheme adopts time steps that are some small fraction f of the local relaxation (or collision) time: $\delta t(R) \simeq f_{\delta t} (t_{\text{rlx}}^{-1} + t_{\text{coll}}^{-1})^{-1}$. Consequently the central parts of the cluster, where evolution is faster, are updated much more frequently than the outer parts. At each step, a pair of neighbouring particles is selected randomly with probability $P_{\text{selec}} \propto 1/\delta t(R)$. This ensures that a particle stays for an *average* time $\delta t(R)$ at R before being updated.

Relaxation is treated as a diffusive process, using the classical Chandrasekhar theory on which FP codes are also based. The long-term effects on orbits of the departure of the gravitational field from a smooth stationary potential are assumed to arise from a large number of uncorrelated, small angle, hyperbolic 2-body encounters. If a star of mass M_1 travels with relative velocity v_{rel} through a homogeneous field of stars of mass M_2 with number density n for a time δt , then in the centre-of-mass reference frame, its trajectory will be deflected by an angle $\theta_{\delta t}$ with average values

$$\begin{aligned} \langle \theta_{\delta t} \rangle &= 0 \quad \text{and} \\ \langle \theta_{\delta t}^2 \rangle &= 8\pi \ln \Lambda G^2 n (M_1 + M_2)^2 \delta t, \quad (8.75) \end{aligned}$$

where G is the gravitational constant and $\ln \Lambda \simeq 10 - 15$ is the Coulomb logarithm. In the MC code, at each step, the velocities of the particles of the selected pair are modified as if by a hyperbolic encounter with deflection angle $\theta_{\text{eff}} =$

$\sqrt{\langle \theta_{\delta t}^2 \rangle}$. The particles are then put at random positions on the slightly modified orbits. As a given particle will be selected many times, at various positions on its orbit, the MC scheme will integrate the effect of relaxation over the particle's orbit and over all possible field particles. Proper averaging is ensured if the time steps are sufficiently short for the orbit to be modified significantly only after a large number of effective encounters. The energy is trivially conserved to machine accuracy in such a scheme because the same deflection angle θ_{eff} is applied to both particles in an interacting pair. Only the direction of the relative velocity vector is changed by θ_{eff} .

Using a binary tree structure which allows quick determination and updating of the potential created by the particles, the self gravity of the stellar cluster is included accurately. This potential is not completely smooth because the particles are infinitesimally thin spherical shells whose radii change discontinuously. Test computations have been used to verify that the additional, unwanted, relaxation is negligible provided the number of particles is larger than a few tens of thousands.

Although Hénon's method is based on the assumption that all departures from the smooth potential can be treated as 2-body small angle scatterings, it is flexible enough to incorporate more realism. The dynamical effect of binaries (i.e., the dominant 3- and 4-body processes), which may be important in the evolution of globular clusters, has been included in various MC codes through the use of approximate analytical cross-sections Stodołkiewicz (1986); Giersz and Spurzem (2000); Rasio et al. (2001). Recently, Fregeau Fregeau et al. (2005); Gürkan et al. (2006) has introduced a much more realis-

tic treatment of binaries by on-the-fly, explicit integrations of the 3- or 4-body interactions, a brute force approach that is necessary to deal with the full diversity of unequal-mass binary interactions. This approach was pioneered by Giersz and Spurzem Giersz and Spurzem (2003) in a hybrid code where binaries are followed as MC particles while single stars are treated as a gaseous component.

The few 2-body encounters that lead to large angle ($> \pi/10$, say) deflections are usually neglected. In globular clusters, these “kicks” have a negligible imprint on the overall dynamics Hénon (1975); Goodman (1983) but it has been suggested that they lead to a high ejection rate from the density cusp around a central (I)MBH Lin and Tremaine (1980). Kicks can be introduced in the MC code, where they are treated in a way similar to collisions, with a cross section $\pi b_{l.a.}^2$, where $b_{l.a.} = f_{l.a.} G(M_1 + M_2) v_{rel}^{-2}$. $f_{l.a.}$ is a numerical factor to distinguish between kicks and “normal” small angle scatterings (impact parameter $> b_{l.a.}$). However, simulations seem to indicate that such kicks have little influence on the evolution of a stellar cusp around a MBH (Freitag et al., 2006c).

The MC code is much faster than a direct N -body integration: a simulation of a Milky-Way-type galactic nucleus represented by 10^7 particles requires between a few days and a few weeks of computation on a single CPU. Furthermore, with the proper scaling with the number of stars, the number of stars represented is independent of the number of particles. A high particle number is obviously desirable for robust statistics, particularly when it comes to rare events such as star-MBH interactions. In contrast, because they treat gravitational (Newtonian) interactions on an elementary level, with-

out relying on any theory about their collective and/or long-term effects, the results of direct N -body codes can generally be applied only to systems with a number of stars equal to the number of particles used.

8.7 Applications of Monte-Carlo and Fokker-Planck simulations to the EMRI problem

MC and FP codes are only appropriate for studying how collisional effects (principally relaxation) affect spherical systems in dynamical equilibrium. These assumptions are probably valid within the radius of influence of MBHs with masses in the LISA range. Indeed, assuming naively that the Sgr A* cluster at the centre of our Galaxy is typical (as far as the total stellar mass and density is concerned) and that one can scale to other galactic nuclei using the $M - \sigma$ relation in the form $\sigma = \sigma_{MW} (\mathcal{M}_\bullet / 3.6 \times 10^6 M_\odot)^{1/\beta}$ with $\beta \approx 4 - 5$ Ferrarese and Merritt (2000); Tremaine et al. (2002), one can estimate the relaxation time at the radius of influence to be $t_{rlx}(R_{infl}) \approx 25 \times 10^9 \text{ yr} (\mathcal{M}_\bullet / 3.6 \times 10^6 M_\odot)^{(2-3/\beta)}$.

Although observations suggest a large spread amongst the values of the relaxation time at the influence radius of MBHs with similar mass (see, e.g., figure 4 of Merritt et al. (2006b)), most galactic nuclei hosting MBHs less massive than a few $10^6 M_\odot$ are probably relaxed and amenable to MC or FP treatment. Even if the age of the system is significantly smaller than its relaxation time, such approaches are valid as long as the nucleus is in dynamical equilibrium, with a smooth, spherical distribution of matter. In such conditions, relaxational processes are still controlling the EMRI rate, no matter how long

the relaxation time is, but one cannot assume a steady-state rate of diffusion of stars onto orbits with small periapsis, as is often done in FP codes (see the discussion in Milosavljević and Merritt (2003), in the different context of the evolution of binary MBHs).

The Hénon-type MC scheme has been used by Freitag and collaborators to determine the structure of galactic nuclei Freitag (2000); Freitag and Benz (2002); Freitag et al. (2006c). Predictions for the distribution of stars around a MBH have also been obtained by solving some form of the Fokker-Planck equation Bahcall and Wolf (1977); Murphy et al. (1991); Hopman and Alexander (2006b,c); Merritt et al. (2006b) or using the gaseous model Amaro-Seoane (2004b); Amaro-Seoane et al. (2004b). These methods have proved useful to determine how relaxation, collisions, large-angle scatterings, MBH growth, etc., shape the distribution of stars around the MBH, which is an obvious prerequisite for the determination of the rate and characteristics of EMRIs. Of particular importance is the inward segregation of stellar BHs as they lose energy to lighter objects. This effect, combined with the fact that stellar BHs produce GWs with higher amplitude than lower-mass stars, explains why they are expected to dominate the EMRI detection rate Sigurdsson and Rees (1997); Hopman and Alexander (2006c). An advantage of the MC approach is that it can easily and realistically include a continuous stellar mass spectrum and extra physical ingredients. However, the first point might not be critical here as MC results suggest that, for models where all the stars were born ~ 10 Gyr ago, the pattern of mass segregation can be well approximated by a population of two components only, one representing the stellar BHs and the other repre-

senting all other (lighter) objects Freitag et al. (2006c). Furthermore, the uncertainties are certainly dominated by our lack of knowledge about where and when stellar formation takes place in galactic nuclei, what the masses of the stars which form might be, and what type of compact remnants they become.

The most recent FP results concerning mass segregation were obtained under the assumptions of a fixed potential and an isotropic velocity dispersion, with the effects of (standard or resonant) relaxation being averaged over J at a given energy. The MC code includes the self-gravity of the cluster so the simulated region can extend past the radius of influence, allowing a more natural outer boundary condition. We note that one has to impose a steeper density drop-off at large radii than what is observed to limit the number of particles to a reasonable value while keeping a good resolution in the region of influence. The MC code naturally allows anisotropy and implicitly follows relaxation in both E and J . Anisotropic FP codes for spherical self-gravitating systems exist Takahashi (1996, 1997); Drukier et al. (1999) but, to our knowledge, none are currently in use that also include a central MBH. Unique amongst all stellar dynamical codes based on the Chandrasekhar theory of relaxation is FOPAX, a FP code which assumes axial rather than spherical symmetry, thus permitting the study of clusters and nuclei with significant global rotation (see Fiestas et al. (2006) and references therein) and which has been adapted to include a central MBH Fiestas (2006).

Determining the EMRI rates and characteristics is a harder challenge for statistical stellar dynamics codes because these events are intrinsically rare and critically sensitive to rather

fine details of the stellar dynamics around a MBH. As we explained previously, the main difficulty, in comparison with, for example, tidal disruptions, is that EMRIs are not “one-passage” events but must be gradual. The first estimate of EMRI rates was performed by Hils and Bender (1995). Assuming a static cusp profile, they followed the evolution of the orbits of test-particles subject to GW emission (Equations 6.9 and 6.10) and 2-body relaxation introduced by random perturbations of the energy and angular momentum according to pre-computed “diffusion coefficients”. Hopman & Alexander (2005a) have used a refined version of this “single-particle Monte-Carlo method”, as well as the Fokker-Planck equation, to make a more detailed analysis. It was found that no more than $\sim 10\%$ of the compact objects swallowed by the MBH are EMRIs, while the rest are direct plunges.

Determination of EMRI rates and characteristics were also attempted with Freitag’s MC code Freitag (2001b, 2003b,a). Despite its present limitations, this approach might serve to inspire future, more accurate, computations and is therefore worth describing in some detail. The MC code does not include GW emission explicitly (or any other relativistic effects). At the end of the step in which two particles have experienced an encounter (to simulate 2-body relaxation), each particle is tested for entry into the “radiation-dominated” regime, defined by Eq. 6.2 (with $C_{\text{EMRI}} = 1$). A complication arises because the time step δt used in the MC code is a fraction $f_{\delta t} = 10^{-3} - 10^{-2}$ of the local relaxation time $t_{\text{rlx}}(R)$, which is generally much larger than the critical timescale defined by the equality $\tau_{\text{GW}}(e, a) = C_{\text{EMRI}} (1-e)t_{\text{rlx}}$. In other words, the effective diffusion angle θ_{eff} is gen-

erally much larger than the opening angle of the “radiation cone”, $\tilde{\theta} \equiv (1 - \tilde{e})^{1/2}$. So that the entry of the particle into the radiation cone (corresponding to a possible EMRI) is not missed, it is assumed that, over δt , the energy of a given particle does not change. Hence, each time it comes back to a given distance from the centre, its velocity vector has the same modulus but relaxation makes its direction execute a random walk with an individual step per orbital period of $\theta_{\text{orb}} = \theta_{\text{eff}}(P_{\text{orb}}/\delta t)^{1/2}$. Entry into the unstable or radiation cone is tested at each of these sub-steps. If the particle is found on a plunge or radiation-dominated orbit, it is immediately removed from the simulation and its mass is added to the MBH.

Unfortunately, in addition to this approximate way of treating relaxation on small time scales, there are a few reasons why the results of these simulations may be only indicative. One is the way t_{rlx} is estimated, using the coefficient in front of δt in Eq. 8.75, i.e., an estimate based on the neighbouring particle. Even if it is correct on average, this estimate is affected by a very high level of statistical noise and its value can be far too long in some cases (e.g., when the relative velocity between the particles in the pair is much larger than the local velocity dispersion). This could lead one to conclude erroneously that a star has reached the radiation-dominated regime and will become an EMRI. To improve on this one could base the t_{rlx} estimate on more than one point on the orbit and on more than one “field-particle” (the number of stars within a distance of 10^{-2} pc of Sgr A* is probably larger than 1000, so t_{rlx} is a well-defined quantity even at such small scales). Another limitation is that GW emission is not included in the orbital evolution, which

forces one to assume an abrupt transition when $\tau_{\text{GW}} = (1 - e)t_{\text{rlx}}$. Hopman & Alexander (2005a) have also shown that a value of C_{EMRI} as small as 10^{-3} might be required to be sure the EMRI will be successful. Furthermore, the MC simulations carried out so far suffer from relatively poor resolution, with each particle having the statistical weight of a few tens of stars. To improve this one would need to limit the simulation to a smaller volume (such as the influence region) or develop a parallel implementation of the MC code to use $\sim 10^8$ particles. Finally, these MC simulations did not include resonant relaxation, an effect which can increase the EMRI rate by of order 10 or completely suppress it, depending on its strength (Hopman and Alexander, 2006b).

8.8 Future of statistical stellar-dynamical simulations for EMRIs

Despite recent progress, a full understanding of the stellar dynamical processes leading to EMRIs and a robust prediction for their rate and characteristics (eccentricities, stellar types and masses etc.) are still lacking. The key points to address include:

1. Interplay between relaxation and GW emission in the orbital evolution of EMRI “precursors”.
2. Importance of resonant relaxation.
3. Dynamics of binaries in a galactic nucleus.
4. Effects of non-sphericity in the potential.

We now suggest how new or updated statistical stellar-dynamics methods can contribute to clarify these points.

A self-gravitating, multi-mass, anisotropic Fokker-Planck Murphy et al. (1991) code, including a detailed treatment of the loss-cone Cohn and Kulsrud (1978) and with additional terms to include GW-emission and resonant relaxation Ivanov (2002); Hopman and Alexander (2005a, 2006b) could provide EMRI (and direct-plunge) rates while accounting for mass segregation at all scales, from the vicinity of the MBH to well beyond the radius of influence, thus including the whole volume where relaxational effects might play a role. Contrary to FP codes the gaseous approach does not operate in (E, J) phase-space where each point correspond to a well-defined orbit, but in direct space (i.e., the radial coordinate R) at each point of which only statistical quantities (velocity dispersions) are used to represent approximately the kinematics of all orbits crossing this position. Therefore the treatment of loss-cone effects can only be done in a much more approximate way Amaro-Seoane (2004b); Amaro-Seoane et al. (2004b), making it probably unsuitable for determining EMRI rates. The FP codes evolve distribution functions, therefore relying on the assumption that any “interesting” element of phase-space always contains a significant number of stars. It is not clear how to apply them to or interpret their results for situations such as EMRIs, corresponding to rare events where small-number effects might be important. They require that the stellar population be discretised into a set of “components” sharing the same properties (E, J , stellar mass and age, etc.) and can therefore not treat accurately a continuous mass function, a mixed-age

population, or binaries.

Monte-Carlo codes are based on a more direct star-by-star (or particle-by-particle) approach making it much easier to consider realistically complex stellar populations and to follow in detail the evolution of individual orbits. Although single-particle MC computations lack self-consistency, the only application of an Hénon-type code to EMRIs suffered from a few shortcomings connected with insufficient resolution in time or particle number. However there are different avenues for useful MC work:

- **Monte-Carlo simulations of binary dynamics.** The evolution of binaries in a galactic nucleus is still a virtually unexplored territory whose study is made urgent both by the possibility of forming EMRIs (and hyper-velocity stars) through binary separation and by the observation of X-ray binaries around Sgr A* Muno et al. (2005b,a). Binary stars can be included in a very realistic way into Hénon-type MC codes, using explicit few-body integrations to treat interactions between a binary and another single or binary star Giersz and Spurzem (2003); Fregeau et al. (2005) or between a binary and the central MBH.
- **Keplerian Monte-Carlo.** Barring tidal processes such as binary separation or the capture of the core of a giant, the rate of EMRIs is determined by the stellar dynamics well within the influence radius of the MBH. To follow the dynamics in this region with both accuracy and computational efficiency, the development of a specialised MC code is planned. The potential will be the simple Keplerian con-

tribution of the MBH with no account for self gravity of the stellar cluster besides relaxation. It is expected that, in such an external potential, one does not need to conserve energy exactly as for a self-gravitating cluster. Therefore, each particle (representing just one star) can have its own time step, adapted to its orbit. The effects of GW emission can be taken into account explicitly and the dynamics in or close to the “radiative” cone can be followed on appropriately short timescales.

- **Non-spherical hybrid code.** Departure from the assumption of sphericity may be important for two non-standard EMRI channels. The first is the one involving a dense accretion disc. In this case, the potential might still be essentially spherical but dissipative interactions with the disc might cause a flattening of the distribution of stars and a significant rate of equatorial circular EMRI events. The second situation is the contribution of binary tidal separations which (unlike standard EMRIs) can be increased significantly by replenishing the loss cone outside the sphere of influence. At the present time FOPAX is the only statistical stellar-dynamics code which does not rely on the assumption of spherical symmetry. It is, however, limited to axially symmetric systems and a particle-based method would be more suitable for the inclusion of star-disc interaction effects or binaries. Following a suggestion already made by Hénon (Hénon, 1971a), a collision-less N -body code could be used as a “backbone” orbit integrator and complemented by the

pairwise treatment of relaxation of the Monte-Carlo method. S. Sigurdsson has applied a similar idea to the study of globular clusters by combining the self-consistent field N -body algorithm with FP terms for 2-body relaxation Johnston et al. (1999).

Some possibly important aspects of the dynamics cannot be treated directly by statistical methods. Important examples are resonant relaxation or the possible effects of the motion of the MBH (Merritt et al. (2006a) and references therein). These processes require direct N -body simulations for their study before they can be introduced in an approximate way into FP or MC codes.

8.9 Direct-summation N -body codes

We finish by considering the direct N -body approach (Aarseth, 1999, 2003; Portegies Zwart et al., 2001). This is the most expensive method because it involves integrating all gravitational forces for all particles at every time step, without making any a priori assumptions about the system. The N -body codes use the improved Hermite integration scheme as described in (Aarseth, 1999, 2003), which requires computation of not only the accelerations but also their time derivatives. Since these approaches integrate Newton's equations directly, all Newtonian gravitational effects are included naturally. More relevant for this subject is that the family of the direct N -body codes of Aarseth also includes versions in which both *KS regularisation* and *chain regularisation* are employed, so that when particles are tightly bound or their separation becomes too small during a hyperbolic

encounter, the system is regularised (as described first in Kustaanheimo and Stiefel (1965); Aarseth (2003)) to prevent dangerous small individual time steps. This means that we can accurately follow and resolve individual orbits in the system. Other schemes which make use of a softening in the gravitational forces (i.e. $1/(r^2 + \epsilon^2)$ instead of $1/r^2$, where ϵ is the softening parameter) cannot be employed because ϵ can induce unacceptable errors in the calculations. The N -body codes scale as N_*^2 , or $\Delta t \propto t_{\text{dyn}}$, which means that even with special-purpose hardware, a simulation can take of the order of weeks if not months. This hardware is the GRAPE (short for GRAVity PipE), a family of hardware which acts as a Newtonian force accelerator. For instance, a GRAPE-6A PCI card has a peak performance of 130 Gflop, roughly equivalent to 100 single PCs (Fukushige et al., 2005). It is possible to parallelise basic versions of the direct N -body codes (without including regularisation schemes) on clusters of PCs, each equipped with one GRAPE-6A PCI card. This leads to efficiencies greater than 50% and speeds in excess of 2 TFlops and thus the possibility of simulating up to $N_* = 2 \cdot 10^6$ stars (Harfst et al., 2006). Nevertheless, when we consider the situation relevant to an EMRI, in which mass ratios are large and we need to follow thousands of orbits, the Hermite integrator is not suitable and problems show up even in the Newtonian regime. Aarseth et al. Aarseth (2006, 2003) summarise different methods developed to cope with large systems with one or more massive bodies. The problem becomes even more difficult when including relativistic corrections to the forces when the stellar black hole approaches the central MBH, because extremely small time-scales are involved in the integra-

tion. Progress is being made in this direction with a developed time-transformed leapfrog method (Mikkola and Aarseth, 2002) (for a description of the leapfrog integrator see (Mikkola and Merritt, 2006)) and the even more promising wheel-spoke regularisation, which was developed to handle situations in which a very massive object is surrounded by strongly bound particles, precisely the situation for EMRIs (Zare, 1974; Aarseth, 2003). Additionally, one must include post-Newtonian corrections in the direct N -body code because secular effects such as Kozai or resonant relaxation may be smoothed out significantly by relativistic precession and thus have an impact on the number of captures (see Merritt et al., 2011a, e.g.).

There already exist versions of direct N -body that include relativistic corrections at 1PN, 2PN (periapsis shifts) and 2.5PN (energy loss in the form of gravitational wave emission). The pioneer work was done in Kupi et al. (2006). The authors included perturbations in the *KS regularisation* scheme, so that the forces (actually the accelerations) were modified by

$$F = \underbrace{F_0}_{\text{Newtonian}} + \underbrace{c^{-2}F_2}_{\text{1PN}} + \underbrace{c^{-4}F_4}_{\text{2PN}} + \underbrace{c^{-5}F_5}_{\text{2.5PN}} + \mathcal{O}(c^{-6}) \quad (8.76)$$

periapsis shift GW

Note that the perturbations do not need to be small compared to the two-body force (Mikkola, 1997). The method will be applicable even when the relativistic terms become comparable to the Newtonian term provided the KS time step is duly adjusted. The desired frame is the centre-of-mass frame, which is equivalent to the centre-of-mass Hamiltonian in the ADM (Arnowit, Deser and Misner) formalism Blanchet and Iyer (2003). The relative accelerations then

have the form

$$\frac{dv^i}{dt} = -\frac{m}{r^2} \left[(1 + \mathcal{A}) n^i + \mathcal{B} v^i \right] + \mathcal{O} \left(\frac{1}{c^7} \right), \quad (8.77)$$

(Blanchet and Iyer, 2003) where the relative separation of the binary components is $x^i = y_1^i - y_2^i$, $r = |\mathbf{x}|$ and $n^i = x^i/r$; \mathcal{A} and \mathcal{B} are given by the expressions (3.10a) and (3.10b) of Blanchet and Iyer (2003). Whilst the gauge choice was not a problem for the system studied in (Kupi et al., 2006), since they were interested in the global dynamical evolution, for the EMRI problem the centre-of-mass frame (located at the origin of the coordinates) must be employed. The integration cannot be extended to velocities higher than $\sim 0.3c$, because at these velocities the post-Newtonian formalism can no longer be applied accurately. This means that we cannot reach the final coalescence of the stellar BH with the MBH, but nonetheless the parameter space that can be explored is unprecedented in scope. We note that it will not be possible to include in N-body codes all the PN corrections that are required for accurate modelling of the phase evolution of the EMRI during the last few years before plunge. However, the N-body codes are not required in that regime, since the system is then decoupled from the rest of the stellar cluster.

8.10 List of public available codes and URLs

1. Direct-summation N -body codes

- Sverre Aarseth family of N -body, including post-Newtonian treatment

<http://www.ast.cam.ac.uk/~sverre/web/pages/nbody.htm>

- Starlab

<http://www.sns.ias.edu/~starlab/>

- fewbody

<http://www.astro.northwestern.edu/~fregeau/code.html>

Note: There exists a version of fewbody including relativistic corrections which can be requested to Pau.Amaro-Seoane@aei.mpg.de

2. The gaseous anisotropic “spedi” code

<http://www.ari.uni-heidelberg.de/gaseous-model/>

3. The Monte Carlo code M_c MESSY**2

<http://www.aei.mpg.de/~pau/MESSY/index.html>

Chapter 9

A note on the use of the Ancient Greek word *barathron* to refer to a black hole

In the literature related to the main subject of this review I have now and again found the expression *peribathron* to refer to the concept of *periapsis*. Some authors use it in the case in which one has a black hole instead of a simple star (for which we have *periastron*). In this last section I will try to convince the reader (from the Latin *cum vincere*, i.e. win with her or him the truth) that this is not correct. Nevertheless, if one has an uncontrollable urge to be pedantic, I would instead recommend the term *apo-* or *peribarathron*. In the next lines I explain why.

From the Dictionnaire grec français, A. Bailly. Ed. Hachette, édition n°44, p. 347 we can find that

βάραθρον, -ου; τό I trou profond, d'où: 1 abîme, gouffre, ARSTT. Probl. 26, 28; part. à Athènes, barathre, gouffre où l'on précipitait les condamnés (cf. à Sparte καιάδας, DT. 7, 133; PLAT. Gorg. 516 e; AR. Nub. 1450 // 2 fig. ruine, perte, DÈM. 101, 1; d'où cause de ruine ou de perte, "un vrai gouffre", en parl. d'une femme, THÉOPH. (ATH. 587 f) // II ornement de femme, AR. fr. 309, 8 // III c. βάραθρον HDT. I. c. v. ce mot (R. *gwera-/ gwre/o¹, cf. ἔβρων, lat. uoro, etc.).

In p. 340, we have the definition of βάθρον

βάθρον, -ου; τό surface servant de fondement, d'où: 1 base HDT. 1, 183; part. piédestal d'une statue, HDT. 5, 85; ESCH. Pers. 811; XÉN. Eq. 1, 1 // 2 degré, marche, HDT. 7, 23; SOPH. O. C. 1591; part. degré d'échelle, échelon, EUR. Ph. 1179; HDN. 4, 2, 9; fig. κινδύνου βάραθρον, EUR. Cycl. 352, les approches (litt. les degrés d'un danger) // 3 banc, siège SOPH.

¹Unfortunately I was unable to reproduce the Indo-European root with the appropriate diacritical marks, due to limitations of typography, so I have approximated it.

O. R. 142; O. C. 101; PLAT. Prot. 315 c; DÉM. 313, 12, etc.; βάθρον (Δίκμς) SOPH. Ant. 854, le trône (de la Justice)// 4 en gén. fondement solide, d'où sol (d'une maison, SOPH. Aj. 860; d'un pays, SOPH. Aj. 135; Phil. 1000); ou fondations, assises (de la terre, SOPH. O. C. 1662; d'une ville, EUR. Suppl. 1198); fig. fondement, support, PD. O. 13, 6; ἐν βάθροις εἶναι EUR. Tr. 47, être ferme sur de solides fondements; ἐκ βάθρον DH. 8, 1; LUC. de fond en comble (βαίνω -θρον; βαθρός)

The Greek-English Lexicon, Liddell-Scott, gives similar definitions. The short version can be consulted at the website of the Perseus Project.

The *barathron* (as it has been transliterated e.g. by García Gual in the *Odyssey*, is described as an abyss, the pit of Tartarus, even though the name itself has never been employed exclusively – there is no “*Barathron*” par excellence. Here are the oldest references to it in the Homeric texts (reproduced below). By the way in the Epic and in the Ionic dialect of Herodotus, one finds not βάραθρον, but the dialect variety βέρεθρον, as Bailly indicates.

Iliad 8, 14 (Zeus very angry)

“Hear me,” said he, “gods and goddesses, that I may speak even as I am minded. Let none of you neither goddess nor god try to cross me, but obey me every one of you that I may bring this matter to an end. If I see anyone acting apart and helping either Trojans or Danaans, he shall be beaten inordinately ere he come back again to Olympus; or I will hurl him down into dark Tartarus far into the **deepest pit** under the earth, where the gates are iron and the floor bronze, as far beneath Hades as heaven is high above the earth, that you may learn how much the mightiest I am among you.”

Odyssey 12, 94 (Spanish, by García Gual)

La otra ruta se abre entre dos promontorios. La cima de uno de ellos se clava en el cielo anchuroso(...) Tenebrosa caverna se abre a mitad de su altura orientada a las sombras de ocaso y del Érebo (...) Ni el más hábil arquero podría desde el fondo del barco con su flecha alcanzar la oscuridad de la cueva en que Escila vive haciendo sentir desde allí sus terribles aullidos (...) La mitad de su cuerpo se esconde en la cóncava gruta; las cabezas, empero, por fuera del **báratro** horrible van mirando hacia el pie de la escarpa y exploran su presa (...)

Regarding this dialect variation (βέρεθρον), we should note that it has been attested in a shorter or contracted form through syncope: βέθρον. This is what may lead to the mistake of using “*bathron*” instead of the correct form “*barathron*”. No dictionary mentions a potential form βάθρον with the appropriate meaning, which might have existed under the same rule as βέθρον, i.e. as syncope form of the Attic variant βάραθρον.

Chantraine, in his book *La formation des noms en grec ancien*, states that *barathron* is a word with religious meaning. This should have been formed from an Indo-European root meaning “to devour” plus the suffix *-thron* (*-θρον*), which expresses an instrument, tool or place, much like the suffixes *-tron* and *-terion*. Its meaning is therefore something akin to “place of devouring”, “instrument or means of devouring”, “tool of devouring”. English “devour” comes through French from the Latin form *voro*, from the same Indo-European root.

Bathron, on the other hand, seems to be formed from the same root as the verb *βαίνω*, which expresses the action of walking, lean the feet on the floor or in general to do any kind of movement on the floor. To this root one must add the same suffix of before and, so, we have a “place, tool or instrument to lean on”.

In conclusion, I maintain the words “*bathron*” and “*barathron*” are nearly antonyms. “*Barathron*” expresses what one needs to express in the context of a black hole; “*bathron*” can be envisaged as the opposite. What’s more, and what’s worse, in modern Greek, a “*bathron*” is a cesspit. In that case we would then be talking in terms of “*peribathroom*” (the credit for this brilliant remark goes to my wife Sabine Pendl).

The *Barathron* was in ancient Greece a cliff in Athens, below which lay an inaccessible or invisible place, where criminals were thrown to their deaths. This is attested in the works of Aristophanes, Plato and Herodotus (7,133), and compiled by Bailly. It is not clear whether this *Barathron* was a common name or a proper noun, namely a specific cliff. One should look in the “*Clouds*” of Aristophanes.

According to Bailly, a cliff similar to the *Barathron* of Athens existed with the name “*kaiadas*”. So we can choose: *peribarathron* or *perikaiadas*.

Nevertheless, I would suggest something different. If you do not fancy *periapsis* or *apoapsis*, you could always make up a new word based on a modern language, such as English. In that case I would advocate for the very nice term my friend Dave J. Vanecek coined in an e-mail exchange: “*periholion*”, from the English word “hole”. I include here an excerpt from the e-mail:

```
Date: Sat, 11 Jun 2011 17:28:06 -0400
From: Dave J. Vanecek
To: Pau Amaro-Seoane
Subject: Re: gnuplot
```

```
Yeah, that's going to be relativistic, orbital period of 1.x days! Must
be really screaming at "periholion".
```

Acknowledgements

I would like to thank Sabine Pendl for her extraordinary support at the Rote Insel during the long preparation of this work and also for coping with my spastic and even spasmodic changes of mood as the article randomly either progressed or retrogressed. It is a pleasure for me to show my most sincere gratitude to Francine Leeuwijn and Marc Dewi Freitag. The many discussions and unaccountable number of hours I spent with them devoted to the topic of stellar dynamics contributed enormously to the writing up of this review. More importantly, they “also” contributed enormously to my *human* formation during my freshman years of PhD student. I am also thankful to Tal Alexander, Steve Drasco, Cole Miller, Rainer Spurzem, Rainer Schödel, Simos Konstantinidis, and Miguel Preto, both for discussions and their friendship (and waveforms, in the case of Steve). Talking of that, I must thank Paloma Marí Mus for a long one and her help on doing the little research that led to the note presented in the last chapter. I show gratitude to Prof. Lau, Prof. Liu, and Rainer for visits to the AMSS, the National Astronomical Observatories of China, the Chinese Academy of Sciences and the Kavli Institute for Astronomy and Astrophysics in Beijing, where part of this work was completed. This work has been supported by the Transregio 7 “Gravitational Wave Astronomy” financed by the Deutsche Forschungsgemeinschaft DFG (German Research Foundation).

Chapter 10

Bibliography

Bibliography

- Aarseth, S. J. (1999). From NBODY1 to NBODY6: The Growth of an Industry. *The Publications of the Astronomical Society of the Pacific*, 111:1333–1346.
- Aarseth, S. J. (2003). *Gravitational N-Body Simulations*. ISBN 0521432723. Cambridge, UK: Cambridge University Press, November 2003.
- Aarseth, S. J. (2006). N-Body Codes. *Modelling Dense Stellar Systems, 26th meeting of the IAU, Joint Discussion 14, 22-23 August 2006, Prague, Czech Republic, JD14, #1*, 14.
- Alexander, T. (2007). Stellar Relaxation Processes Near the Galactic Massive Black Hole. *ArXiv e-prints*.
- Alexander, T. and Hopman, C. (2003). Orbital inspiral into a massive black hole in a galactic center. *ApJ Lett.*, 590:29–32.
- Alexander, T. and Hopman, C. (2009). Strong mass segregation around a massive black hole. *ApJ*, 697:1861–1869.
- Amaro-Seoane, P. (2004a). *Dynamics of dense gas-star systems. Black holes and their precursors*. PhD thesis, PhD Thesis, Combined Faculties for the Natural Sciences and for Mathematics of the University of Heidelberg, Germany. VII + 174 pp. (2004), <http://www.ub.uni-heidelberg.de/archiv/4826>.
- Amaro-Seoane, P. (2004b). *Dynamics of dense gas-star systems. Black holes and their precursors*. PhD thesis, Heidelberg University.
- Amaro-Seoane, P., Aoudia, S., Babak, S., Binétruy, P., Berti, E., Bohé, A., Caprini, C., Colpi, M., Cornish, N. J., Danzmann, K., Dufaux, J.-F., Gair, J., Jennrich, O., Jetzer, P., Klein, A., Lang, R. N., Lobo, A., Littenberg, T., McWilliams, S. T., Nelemans, G., Petiteau, A., Porter, E. K., Schutz, B. F., Sesana, A., Stebbins, R., Sumner, T., Vallisneri, M., Vitale, S., Volonteri, M., and Ward, H. (2012a). eLISA: Astrophysics and cosmology in the millihertz regime. *ArXiv e-prints*.
- Amaro-Seoane, P., Aoudia, S., Babak, S., Binétruy, P., Berti, E., Bohe, A., Caprini, C., Colpi, M., Cornish, N. J., Danzmann, K., Dufaux, J.-F., Gair, J., Jennrich, O., Jetzer, P., Klein, A., Lang, R. N., Lobo, A., Littenberg, T., McWilliams, S. T., Nelemans, G., Petiteau, A., Porter, E. K., Schutz, B. F., Sesana, A., Stebbins, R., Sumner, T., Vallisneri, M., Vitale, S., Volonteri, M., and Ward, H. (2012b). Low-frequency gravitational-wave science with eLISA/NGO. *ArXiv e-prints*.
- Amaro-Seoane, P., Barranco, J., Bernal, A., and Rezzolla, L. (2010). Constraining scalar fields with stellar kinematics and collisional dark matter. *Journal of Cosmology and Astroparticle Physics*, 11:2–+.

BIBLIOGRAPHY

- Amaro-Seoane, P., Brem, P., Cuadra, J., and Armitage, P. J. (2012c). The Butterfly Effect in the Extreme-mass Ratio Inspiral Problem. *ApJ Lett.*, 744:L20.
- Amaro-Seoane, P. and Freitag, M. (2006). Intermediate-Mass Black Holes in Colliding Clusters: Implications for Lower Frequency Gravitational-Wave Astronomy. *ApJ Lett.*, 653:L53–L56.
- Amaro-Seoane, P., Freitag, M., and Spurzem, R. (2004a). Accretion of stars on to a massive black hole: A realistic diffusion model and numerical studies. *MNRAS*.
- Amaro-Seoane, P., Freitag, M., and Spurzem, R. (2004b). Accretion of stars on to a massive black hole: a realistic diffusion model and numerical studies. *MNRAS*, 352:655–672.
- Amaro-Seoane, P., Gair, J. R., Freitag, M., Miller, M. C., Mandel, I., Cutler, C. J., and Babak, S. (2007). TOPICAL REVIEW: Intermediate and extreme mass-ratio inspirals. Astrophysics, science applications and detection using LISA. *Classical and Quantum Gravity*, 24:113–+.
- Amaro-Seoane, P. and Preto, M. (2011). The impact of realistic models of mass segregation on the event rate of extreme-mass ratio inspirals and cusp re-growth. *Classical and Quantum Gravity*, 28(9):094017–+.
- Amaro-Seoane, P., Sopuerta, C. F., and Freitag, M. (2012d). *ArXiv e-prints*.
- Amaro-Seoane, P. and Spurzem, R. (2001). The loss-cone problem in dense nuclei. *MNRAS*, 327:995–1003.
- Arons, J., Kulsrud, R. M., and Ostriker, J. P. (1975). A multiple pulsar model for quasi-stellar objects and active galactic nuclei. *apj*, 198:687–705.
- Babak, S., Baker, J. G., Benacquista, M. J., Cornish, N. J., Larson, S. L., Mandel, I., McWilliams, S. T., Petiteau, A., Porter, E. K., Robinson, E. L., Vallisneri, M., Vecchio, A., Data Challenge Task Force, t. M. L., Adams, M., Arnaud, K. A., Blaut, A., Bridges, M., Cohen, M., Cutler, C., Feroz, F., Gair, J. R., Graff, P., Hobson, M., Shapiro Key, J., Królak, A., Lasenby, A., Prix, R., Shang, Y., Trias, M., Veitch, J., Whelan, J. T., and participants, t. C. . (2010). The Mock LISA Data Challenges: from challenge 3 to challenge 4. *Classical and Quantum Gravity*, 27(8):084009–+.
- Bahcall, J. N. and Wolf, R. A. (1976). Star distribution around a massive black hole in a globular cluster. *ApJ*, 209:214–232.
- Bahcall, J. N. and Wolf, R. A. (1977). The star distribution around a massive black hole in a globular cluster. II unequal star masses. *ApJ*, 216:883–907.
- Barack, L. and Cutler, C. (2004). LISA capture sources: Approximate waveforms, signal-to-noise ratios, and parameter estimation accuracy. *Physical Review D*, 69(8):082005–+.
- Bardeen, J. M. (1970). Kerr Metric Black Holes. *Nat*, 226:64–65.
- Bartko, H., Martins, F., Trippe, S., Fritz, T. K., Genzel, R., Ott, T., Eisenhauer, F., Gillessen, S., Paumard, T., Alexander, T., Dodds-Eden, K., Gerhard, O., Levin, Y., Mascetti, L., Nayakshin, S., Perets, H. B., Perrin, G., Pfuhl, O., Reid, M. J., Rouan, D., Zilka, M., and

- Sternberg, A. (2010). An Extremely Top-Heavy Initial Mass Function in the Galactic Center Stellar Disks. *ApJ*, 708:834–840.
- Baumgardt, H., Makino, J., and Ebisuzaki, T. (2004a). Massive Black Holes in Star Clusters. I. Equal-Mass Clusters. *ApJ*, 613:1133–1142.
- Baumgardt, H., Makino, J., and Ebisuzaki, T. (2004b). Massive Black Holes in Star Clusters. II. Realistic Cluster Models. *ApJ*, 613:1143–1156.
- Begelman, M. C. (2010). Evolution of super-massive stars as a pathway to black hole formation. *MNRAS*, 402:673–681.
- Bender, P. L., Armitage, P. J., Begelman, M. C., and Perna, R. (2005). Massive Black Hole Formation and Growth. *White Paper submitted to the NASA SEU Roadmap Committee*.
- Bender, P. L. and Hils, D. (1997). Confusion noise level due to galactic and extragalactic binaries. *Classical and Quantum Gravity*, 14:1439–1444.
- Bettwieser, E. and Spurzem, R. (1986). Anisotropy in stellar dynamics. 161:102–112.
- Binney, J. and Tremaine, S. (1987). *Galactic Dynamics*. Princeton University Press.
- Binney, J. and Tremaine, S. (2008). *Galactic Dynamics: Second Edition*. Princeton University Press.
- Blanchet, L. and Iyer, B. R. (2003). Third post-Newtonian dynamics of compact binaries: equations of motion in the centre-of-mass frame. *Classical and Quantum Gravity*, 20:755–776.
- Bregman, M. and Alexander, T. (2009). Accretion Disk Warping by Resonant Relaxation: The Case of Maser Disk NGC 4258. *ApJ Lett.*, 700:L192–L195.
- Brown, W. R., Geller, M. J., Kenyon, S. J., and Bromley, B. C. (2009). The Anisotropic Spatial Distribution of Hypervelocity Stars. *ApJ Lett.*, 690:L69–L71.
- Buchholz, R. M., Schödel, R., and Eckart, A. (2009). Composition of the galactic center star cluster. Population analysis from adaptive optics narrow band spectral energy distributions. *A&A*, 499:483–501.
- Chabrier, G. and Baraffe, I. (2000). Theory of low-mass stars and substellar objects. *ARA&A*, 38:337–377.
- Chandrasekhar, S. (1942). Principles of stellar dynamics. *Physical Sciences Data*.
- Chandrasekhar, S. (1960). *Principles of stellar dynamics*. New York: Dover, 1960, Enlarged ed.
- Chang, J. S. and Cooper, G. (1970). A practical difference scheme for fokker-planck equations. *J. Comp. Phys.*, 6:1–16.
- Chen, X., Sesana, A., Madau, P., and Liu, F. K. (2011). Tidal Stellar Disruptions by Massive Black Hole Pairs. II. Decaying Binaries. *ApJ*, 729:13–+.
- Chernoff, D. F. and Weinberg, M. D. (1990). Evolution of globular clusters in the galaxy. *ApJ*, 351:121–156.
- Cohn, H. (1979). Numerical integration of the fokker-planck equation and the evolution of star clusters. *ApJ*, 234:1036–1053.

BIBLIOGRAPHY

- Cohn, H. (1980). Late core collapse in star clusters and the gravothermal instability. *ApJ*, 242:765–771.
- Cohn, H. (1985). Direct Fokker-Planck calculations. In *IAU Symp. 113: Dynamics of Star Clusters*, pages 161–177.
- Cohn, H. and Kulsrud, R. M. (1978). The stellar distribution around a black hole - numerical integration of the fokker-planck equation. *ApJ*, 226:1087–1108.
- Collin, S. and Zahn, J. P. (1999). Accretion disks and star formation. In Terzian, Y., Khachikian, E., and Weedman, D., editors, *IAU Symp. 194: Activity in Galaxies and Related Phenomena*, volume 194, page 246.
- Crowder, J. and Cornish, N. J. (2005). Beyond LISA: Exploring future gravitational wave missions. *Physical Review D*, 72(8):083005–+.
- Cutler, C. and Harms, J. (2006). Big Bang Observer and the neutron-star-binary subtraction problem. *Phys. Rev. D*, 73(4):042001.
- Cutler, C., Kennefick, D., and Poisson, E. (1994). Gravitational radiation reaction for bound motion around a Schwarzschild black hole. *Ph. Rev. D*, 50:3816–3835.
- Danzmann, K. (2000). LISA Mission Overview. *Advances in Space Research*, 25:1129–1136.
- David, L. P., Durisen, R. H., and Cohn, H. N. (1987a). The evolution of active galactic nuclei. I - models without stellar evolution. *ApJ*, 313:556–575.
- David, L. P., Durisen, R. H., and Cohn, H. N. (1987b). The evolution of active galactic nuclei. II - models with stellar evolution. *ApJ*, 316:505–516.
- de Freitas Pacheco, J. A., Filloux, C., and Regimbau, T. (2006). Capture rates of compact objects by supermassive black holes. *Phys. Rev. D*, 74(2):023001–+.
- Do, T., Ghez, A. M., Morris, M. R., Lu, J. R., Matthews, K., Yelda, S., and Larkin, J. (2009). High Angular Resolution Integral-Field Spectroscopy of the Galaxy’s Nuclear Cluster: A Missing Stellar Cusp? *ApJ*, 703:1323–1337.
- Drukier, G. A., Cohn, H. N., Lugger, P. M., and Yong, H. (1999). Anisotropic fokker-planck models for the evolution of globular star clusters: The core-halo connection. *ApJ*, 518:233–245.
- Eilon, E., Kupi, G., and Alexander, T. (2009). The Efficiency of Resonant Relaxation Around a Massive Black Hole. *ApJ*, 698:641–647.
- Eisenhauer, F., Genzel, R., Alexander, T., Abuter, R., Paumard, T., Ott, T., Gilbert, A., Gillessen, S., Horrobin, M., Trippe, S., Bonnet, H., Dumas, C., Hubin, N., Kaufer, A., Kissler-Patig, M., Monnet, G., Ströbele, S., Szeifert, T., Eckart, A., Schödel, R., and Zucker, S. (2005). SINFONI in the Galactic Center: Young Stars and Infrared Flares in the Central Light-Month. *ApJ*, 628:246–259.
- Eisenhauer, F., Perrin, G., Brandner, W., Straubmeier, C., Richichi, A., Gillessen, S., Berger, J. P., Hippler, S., Eckart, A., Schöller, M., Rabien, S., Cassaing, F., Lenzen, R., Thiel, M., Clénet, Y., Ramos, J. R., Kellner, S., Fédou, P., Baumeister, H., Hofmann, R., Gendron, E., Boehm, A., Bartko, H., Haubois, X., Klein, R., Dodds-Eden, K., Houairi, K., Hormuth, F., Gräter, A., Jocou, L., Naranjo, V., Genzel, R., Kervella, P.,

- Henning, T., Hamaus, N., Lacour, S., Neumann, U., Haug, M., Malbet, F., Laun, W., Kolmeder, J., Paumard, T., Rohloff, R.-R., Pfuhl, O., Perraut, K., Ziegler, J., Rouan, D., and Rousset, G. (2008). GRAVITY: getting to the event horizon of Sgr A*. In *Society of Photo-Optical Instrumentation Engineers (SPIE) Conference Series*, volume 7013 of *Society of Photo-Optical Instrumentation Engineers (SPIE) Conference Series*.
- Elson, R., Hut, P., and Inagaki, S. (1987). Dynamical evolution of globular clusters. *araa*, 25:565–601.
- Erwin, P., Graham, A. W., and Caon, N. (2004). The Correlation between Supermassive Black Hole Mass and the Structure of Ellipticals and Bulges. In L. C. Ho, editor, *Coevolution of Black Holes and Galaxies*.
- Ferrarese, L. and Ford, H. (2005). Supermassive Black Holes in Galactic Nuclei: Past, Present and Future Research.
- Ferrarese, L. and Merritt, D. (2000). A fundamental relation between supermassive black holes and their host galaxies. *ApJ Lett.*, 539:9–12.
- Ferrarese, L., Pogge, R. W., Peterson, B. M., Merritt, D., Wandel, A., and Joseph, C. L. (2001). Supermassive Black Holes in Active Galactic Nuclei. I. The Consistency of Black Hole Masses in Quiescent and Active Galaxies. *ApJ Lett.*, 555:79–82.
- Fiestas, J. (2006). *Dynamical evolution of rotating globular clusters with embedded black holes*. PhD thesis, Heidelberg University.
- Fiestas, J., Spurzem, R., and Kim, E. (2006). 2D Fokker-Planck models of rotating clusters. *MNRAS*, 373:677–686.
- Finn, L. S. (1992). Detection, measurement, and gravitational radiation. *prd*, 46:5236–5249.
- Finn, L. S. and Thorne, K. S. (2000). Gravitational waves from a compact star in a circular, inspiral orbit, in the equatorial plane of a massive, spinning black hole, as observed by lisa. *Phys. Rev. D*, 62:124021.
- Frank, J., King, A., and Raine, D. J. (2002). *Accretion Power in Astrophysics: Third Edition*. Accretion Power in Astrophysics: Third Edition, by Juhan Frank, Andrew King, and Derek J. Raine. Cambridge University Press, 2002, 398 pp.
- Frank, J. and Rees, M. J. (1976). Effects of massive central black holes on dense stellar systems. *MNRAS*, 176:633–647.
- Fregeau, J. M., Gürkan, M. A., Joshi, K. J., and Rasio, F. A. (2003). Monte Carlo Simulations of Globular Cluster Evolution. III. Primordial Binary Interactions. *ApJ*, 593:772–787.
- Fregeau, J. M., Gürkan, M. A., and Rasio, F. A. (2005). Star Cluster Evolution with Primordial Binaries. submitted to *ApJ*, preprint astro-ph/0512032.
- Freitag, M. (2000). *Collisional stellar dynamics in galactic nuclei hosting a massive black hole*. PhD thesis, Université de Genève.
- Freitag, M. (2001a). Monte Carlo cluster simulations to determine the rate of compact star inspiralling to a central galactic black hole. *Classical and Quantum Gravity*, 18:4033–4038.

BIBLIOGRAPHY

- Freitag, M. (2001b). Monte Carlo cluster simulations to determine the rate of compact star inspiralling to a central galactic black hole. *Classical and Quantum Gravity*, 18:4033–4038.
- Freitag, M. (2003a). Captures of stars by a massive black hole: Investigations in numerical stellar dynamics. In Centrella, J. M., editor, *The Astrophysics of Gravitational Wave Sources*, volume 686 of *AIP Conference Proceedings*, pages 109–112. American Institute of Physics.
- Freitag, M. (2003b). Gravitational Waves from Stars Orbiting the Sagittarius A* Black Hole. *ApJ Lett.*, 583:L21–L24.
- Freitag, M., Amaro-Seoane, P., and Kalogera, V. (2006a). Models of mass segregation at the Galactic Centre. *Journal of Physics Conference Series*, 54:252–258.
- Freitag, M., Amaro-Seoane, P., and Kalogera, V. (2006b). Stellar Remnants in Galactic Nuclei: Mass Segregation. *ApJ*, 649:91–117.
- Freitag, M., Amaro-Seoane, P., and Kalogera, V. (2006c). Stellar Remnants in Galactic Nuclei: Mass Segregation. *ApJ*, 649:91–117.
- Freitag, M. and Benz, W. (2001). A new monte carlo code for star cluster simulations: I. relaxation. *A&A*, 375:711–738.
- Freitag, M. and Benz, W. (2002). A new monte carlo code for star cluster simulations: II. central black hole and stellar collisions. *A&A*, 394:345–374.
- Freitag, M. and Benz, W. (2005). A comprehensive set of simulations of high-velocity collisions between main-sequence stars. *MNRAS*, 358:1133–1158.
- Fukushige, T., Makino, J., and Kawai, A. (2005). GRAPE-6A: A Single-Card GRAPE-6 for Parallel PC-GRAPE Cluster Systems. *PASJ*, 57:1009–1021.
- Gürkan, M. A., Freitag, M., and Rasio, F. A. (2004). Formation of Massive Black Holes in Dense Star Clusters. I. Mass Segregation and Core Collapse. *ApJ*, 604:632–652.
- Gair, J. R. and Glampedakis, K. (2006). Improved approximate inspirals of test bodies into Kerr black holes. *Ph. Rev. D*, 73(6):064037.
- Gebhardt, K., Lauer, T. R., Kormendy, J., Pinkney, J., Bower, G., Green, R., Gull, T., Hutchings, J. B., Kaiser, M. E., Nelson, C. H., Richstone, D., and Weistrop, D. (2001). M33: A galaxy with no supermassive black hole. *AJ*, 122:2469–2476.
- Gebhardt, K., Rich, R. M., and Ho, L. C. (2002). A $20000 M_{\odot}$ Black Hole in the Stellar Cluster G1. *ApJ Lett.*, 578:41–45.
- Genzel, R., Eisenhauer, F., and Gillessen, S. (2010). The Galactic Center massive black hole and nuclear star cluster. *Reviews of Modern Physics*, 82:3121–3195.
- Gerssen, J., van der Marel, R. P., Gebhardt, K., Guhathakurta, P., Peterson, R. C., and Pryor, C. (2002). Hubble Space Telescope Evidence for an Intermediate-Mass Black Hole in the Globular Cluster M15. II. Kinematic Analysis and Dynamical Modeling. *AJ*, 124:3270–3288.

- Gezari, S., Halpern, J. P., Komossa, S., Grupe, D., and Leighly, K. M. (2003). Follow-Up Hubble Space Telescope/Space Telescope Imaging Spectroscopy of Three Candidate Tidal Disruption Events. *ApJ*, 592:42–51.
- Gezari, S., Heckman, T., Cenko, S. B., Eracleous, M., Forster, K., Gonçalves, T. S., Martin, D. C., Morrissey, P., Neff, S. G., Seibert, M., Schiminovich, D., and Wyder, T. K. (2009). Luminous Thermal Flares from Quiescent Supermassive Black Holes. *ApJ*, 698:1367–1379.
- Ghez, A. M., Duchêne, G., Matthews, K., Hornstein, S. D., Tanner, A., Larkin, J., Morris, M., Becklin, E. E., Salim, S., Kremenek, T., Thompson, D., Soifer, B. T., Neugebauer, G., and McLean, I. (2003). The First Measurement of Spectral Lines in a Short-Period Star Bound to the Galaxy's Central Black Hole: A Paradox of Youth. *ApJ Lett.*, 586:L127–L131.
- Ghez, A. M., Salim, S., Hornstein, S. D., Tanner, A., Lu, J. R., Morris, M., Becklin, E. E., and Duchêne, G. (2005a). Stellar Orbits around the Galactic Center Black Hole. In Ghez et al. (2005b), pages 744–757.
- Ghez, A. M., Salim, S., Hornstein, S. D., Tanner, A., Lu, J. R., Morris, M., Becklin, E. E., and Duchêne, G. (2005b). Stellar Orbits around the Galactic Center Black Hole. *ApJ*, 620:744–757.
- Ghez, A. M., Salim, S., Weinberg, N. N., Lu, J. R., Do, T., Dunn, J. K., Matthews, K., Morris, M. R., Yelda, S., Becklin, E. E., Kremenek, T., Milosavljevic, M., and Naiman, J. (2008). Measuring Distance and Properties of the Milky Way's Central Supermassive Black Hole with Stellar Orbits. *ApJ*, 689:1044–1062.
- Giersz, M. (2006). Monte Carlo simulations of star clusters - III. A million-body star cluster. *MNRAS*, 371:484–494.
- Giersz, M. and Heggie, D. C. (1994). Statistics of n -body simulations - part two - equal masses after core collapse. *MNRAS*, 270:298.
- Giersz, M. and Heggie, D. C. (1996). Statistics of n -body simulations - III. unequal masses. *MNRAS*, 279:1037–1056.
- Giersz, M. and Spurzem, R. (1994). Comparing direct n -body integration with anisotropic gaseous models of star clusters. *MNRAS*, 269:241.
- Giersz, M. and Spurzem, R. (2000). A stochastic monte carlo approach to model real star cluster evolution - II. self-consistent models and primordial binaries. *MNRAS*, 317:581.
- Giersz, M. and Spurzem, R. (2003). A stochastic Monte Carlo approach to modelling real star cluster evolution - III. Direct integration of three- and four-body interactions. *MNRAS*, 343:781–795.
- Gillessen, S., Eisenhauer, F., Trippe, S., Alexander, T., Genzel, R., Martins, F., and Ott, T. (2009). Monitoring Stellar Orbits Around the Massive Black Hole in the Galactic Center. *ApJ*, 692:1075–1109.
- Gillessen, S., Perrin, G., Brandner, W., Straubmeier, C., Eisenhauer, F., Rabien, S., Eckart, A., Lena, P., Genzel, R., Paumard, T., and Hippler, S. (2006). GRAVITY: the adaptive-optics-assisted two-object beam combiner instrument for the VLTI. In *Society of Photo-Optical Instrumentation Engineers*

BIBLIOGRAPHY

- (SPIE) Conference Series, volume 6268 of *Society of Photo-Optical Instrumentation Engineers (SPIE) Conference Series*.
- Ginzburg, V. and Ozernoy, L. M. (1964). *Sov. Phys. JETP*, 20:489.
- Gong, X., Xu, S., Bai, S., Cao, Z., Chen, G., Chen, Y., He, X., Heinzl, G., Lau, Y.-K., Liu, C., Luo, J., Luo, Z., Pulido Patón, A., Rüdiger, A., Shao, M., Spurzem, R., Wang, Y., Xu, P., Yeh, H.-C., Yuan, Y., and Zhou, Z. (2011). A scientific case study of an advanced LISA mission. *Classical and Quantum Gravity*, 28(9):094012–+.
- Goodman, J. (1983). Core collapse with strong encounters. *ApJ*, 270:700–710.
- Goodman, J. (2003). Self-gravity and quasi-stellar object discs. *MNRAS*, 339:937–948.
- Goodman, J. and Tan, J. C. (2004). Supermassive Stars in Quasar Disks. *ApJ*, 608:108–118.
- Gualandris, A. and Merritt, D. (2012). Long-term Evolution of Massive Black Hole Binaries. IV. Mergers of Galaxies with Collisionally Relaxed Nuclei. *ApJ*, 744:74.
- Gurevich, A. (1964). Instability of the disturbed zone in the vicinity of a charged body in plasma. *Geomag. Aeronom.*, 4:247–255.
- Gürkan, M. A., Fregeau, J. M., and Rasio, F. A. (2006). Massive Black Hole Binaries from Collisional Runaways. *ApJ Lett.*, 640:L39–L42.
- Hachisu, I., Nakada, Y., Nomoto, K., and Sugimoto, D. (1978). Post-collapse evolution of a gaseous cluster model. *Prog. Theor. Phys.* 60, 393, 393:60.
- Hara, T. (1978). Evolution of a super-massive star in a dense stellar system. *Progress of Th. Phys.*, 60:711–723.
- Harfst, S., Gualandris, A., Merritt, D., Spurzem, R., Portegies Zwart, S., and Berczik, P. (2006). Performance Analysis of Direct N-Body Algorithms on Special-Purpose Supercomputers. *ArXiv Astrophysics e-prints*.
- Häring, N. and Rix, H.-W. (2004). On the black hole massbulge mass relation. *ApJ Lett.*, 604:L89–L92.
- Helstrom, C. W. (1968). *Statistical Theory of Signal Detection*.
- Hénon, M. (1971a). The monte carlo method. *Ap&SS*, 14:151–167.
- Hénon, M. (1971b). Monte carlo models of star clusters. *Ap&SS*, 13:284–299.
- Hénon, M. (1973). Collisional dynamics of spherical stellar systems. In Martinet, L. and Mayor, M., editors, *Dynamical structure and evolution of stellar systems, Lectures of the 3rd Advanced Course of the Swiss Society for Astronomy and Astrophysics (SSAA)*, pages 183–260.
- Hénon, M. (1975). Two recent developments concerning the monte carlo method. In Hayli, A., editor, *IAU Symp. 69: Dynamics of Stellar Systems*, page 133.
- Heney, L. G., Wilets, L., Böhm, K. H., Lelequier, R., and Levee, R. D. (1959). A Method for Atomic Computation of Stellar Evolution. *ApJ*, 129:628.
- Hernquist, L. and Ostriker, J. P. (1992). A self-consistent field method for galactic dynamics. *ApJ*, 386:375–397.

- Herrnstein, J. R., Moran, J. M., Greenhill, L. J., Diamond, P. J., Inoue, M., Nakai, N., Miyoshi, M., Henkel, C., and Riess, A. (1999). A geometric distance to the galaxy ngc 4258 from orbital motions in a nuclear gas disk. *Nat*, 400:539–541.
- Hillenbrand, L. A. and Hartmann, L. W. (1998). A Preliminary Study of the Orion Nebula Cluster Structure and Dynamics. *ApJ*, 492:540–+.
- Hills, J. G. (1975). Possible power source of Seyfert galaxies and QSOs. *Nat*, 254:295–298.
- Hills, J. G. (1988). Hyper-velocity and tidal stars from binaries disrupted by a massive galactic black hole. *Nat*, 331:687–689.
- Hils, D. and Bender, P. L. (1995). Gradual approach to coalescence for compact stars orbiting massive black holes. *ApJ Lett.*, 445:7–10.
- Hopman, C. and Alexander, T. (2005a). The Orbital Statistics of Stellar Inspiral and Relaxation near a Massive Black Hole: Characterizing Gravitational Wave Sources. *ApJ*, 629:362–372.
- Hopman, C. and Alexander, T. (2005b). The Orbital Statistics of Stellar Inspiral and Relaxation near a Massive Black Hole: Characterizing Gravitational Wave Sources. *ApJ*, 629:362–372.
- Hopman, C. and Alexander, T. (2006a). Resonant Relaxation near a Massive Black Hole: The Stellar Distribution and Gravitational Wave Sources. *ApJ*, 645:1152–1163.
- Hopman, C. and Alexander, T. (2006b). Resonant Relaxation near a Massive Black Hole: The Stellar Distribution and Gravitational Wave Sources. *ApJ*, 645:1152–1163.
- Hopman, C. and Alexander, T. (2006c). The Effect of Mass Segregation on Gravitational Wave Sources near Massive Black Holes. *ApJ Lett.*, 645:L133–L136.
- Hopman, C., Freitag, M., and Larson, S. L. (2007). Gravitational wave bursts from the Galactic massive black hole. *MNRAS*, 378:129–136.
- Hopman, C. (2009). Binary Dynamics Near a Massive Black Hole. *ApJ*, 700:1933–1951.
- Inagaki, S. and Saslaw, W. C. (1985). Equipartition in multicomponent gravitational systems. *ApJ*, 292:339–347.
- Inagaki, S. and Wiyanto, P. (1984). On equipartition of kinetic energies in two-component star clusters. *PASJ*, 36:391–402.
- Ivanov, P. B. (2002). On the formation rate of close binaries consisting of a super-massive black hole and a white dwarf. *MNRAS*, 336:373–381.
- Johnston, K. V., Sigurdsson, S., and Hernquist, L. (1999). Measuring mass-loss rates from Galactic satellites. *MNRAS*, 302:771–789.
- Joshi, K. J., Nave, C. P., and Rasio, F. A. (2001). Monte carlo simulations of globular cluster evolution. II. mass spectra, stellar evolution, and lifetimes in the galaxy. *ApJ*, 550:691–702.
- Joshi, K. J., Rasio, F. A., and Portegies Zwart, S. (2000). Monte carlo simulations of globular cluster evolution. i. method and test calculations. *ApJ*, 540:969–982.

BIBLIOGRAPHY

- Karas, V. and Šubr, L. (2001). Orbital decay of satellites crossing an accretion disc. *A&A*, 376:686–696.
- Khalisi, E., Amaro-Seoane, P., and Spurzem, R. (2007). A comprehensive NBODY study of mass segregation in star clusters: energy equipartition and escape. *MNRAS*.
- Kim, S. S., Lee, H. M., and Goodman, J. (1998). Two-Component Fokker-Planck Models for the Evolution of Isolated Globular Clusters. *ApJ*, 495:786–+.
- King, A. R., Lubow, S. H., Ogilvie, G. I., and Pringle, J. E. (2005). Aligning spinning black holes and accretion discs. *MNRAS*, 363:49–56.
- Kippenhahn, R. and Weigert, A. (1994). *Stellar Structure and Evolution*. Springer-Verlag Berlin Heidelberg.
- Kocsis, B., Yunes, N., and Loeb, A. (2011). Observable signatures of extreme mass-ratio inspiral black hole binaries embedded in thin accretion disks. *Phys. Rev. D*, 84(2):024032–+.
- Komossa, S. (2002). X-Ray Evidence for SMBHs in Non-Active Galaxies: Detection of X-Ray Flare Events, Interpreted as Tidal Disruptions of Stars by SMBHs. In *Lighthouses of the Universe: The Most Luminous Celestial Objects and Their Use for Cosmology Proceedings of the MPA/ESO*, page 436.
- Komossa, S., Halpern, J., Schartel, N., Hasinger, G., Santos-Lleo, M., and Predehl, P. (2004). A Huge Drop in the X-Ray Luminosity of the Nonactive Galaxy RX J1242.6-1119A, and the First Postflare Spectrum: Testing the Tidal Disruption Scenario. *ApJ Lett.*, 603:L17–L20.
- Kong, A. K. H., Heinke, C. O., Di Stefano, R., Barmby, P., Lewin, W. H. G., and Primini, F. A. (2009). X-Ray Localization of the Intermediate-Mass Black Hole in the Globular Cluster G1 with Chandra. *ArXiv e-prints*.
- Kormendy, J. (2003). The Stellar-Dynamical Search for Supermassive Black Holes in Galactic Nuclei. In Ho, L., editor, *Coevolution of Black Holes and Galaxies*, *Carnegie Observatories, Pasadena*. astro-ph/0306353.
- Kormendy, J. (2004). The Stellar-Dynamical Search for Supermassive Black Holes in Galactic Nuclei. In Ho, L., editor, *Coevolution of Black Holes and Galaxies, from the Carnegie Observatories Centennial Symposia*, page 1. Cambridge University Press.
- Krolik, J. H. (1999). *Active galactic nuclei: from the central black hole to the galactic environment*. Princeton University Press.
- Kroupa, P. (2001). On the variation of the initial mass function. *MNRAS*, 322:231–246.
- Kroupa, P., Tout, C. A., and Gilmore, G. (1993). The distribution of low-mass stars in the Galactic disc. *MNRAS*, 262:545–587.
- Kupi, G., Amaro-Seoane, P., and Spurzem, R. (2006). Dynamics of compact object clusters: a post-Newtonian study. *MNRAS*, pages L77+.
- Kustaanheimo, P. E. and Stiefel, E. L. (1965). Perturbation theory of Kepler motion based on spinor regularization. *J. Reine Angew. Math.*
- Langbein, T., Fricke, K. J., Spurzem, R., and Yorke, H. W. (1990). Interactions between stars and gas in galactic nuclei. 227:333–341.

- Larson, S. L. (2003). Online sensitivity curve generator. <http://www.srl.caltech.edu/shane/sensitivity/>.
- Larson, S. L., Hiscock, W. A., and Hellings, R. W. (2000). Sensitivity curves for space-borne gravitational wave interferometers. *Physical Review D*, 62:062001.
- Lauer, T. R., Faber, S. M., Ajhar, E. A., Grillmair, C. J., and Scowen, P. A. (1998). M32 +/- 1. *AJ*, 116:2263–2286.
- Levin, Y. (2003). Formation of massive stars and black holes in self-gravitating AGN discs, and gravitational waves in LISA band. *astro-ph/0307084*.
- Levin, Y. (2006). Starbursts near supermassive black holes: young stars in the Galactic Center, and gravitational waves in LISA band. preprint, *astro-ph/0603583*.
- Levin, Y. and Beloborodov, A. M. (2003). Stellar Disk in the Galactic Center: A Remnant of a Dense Accretion Disk? *ApJ Lett.*, 590:L33–L36.
- Lightman, A. P. and Fall, S. M. (1978). An approximate theory for the core collapse of two-component gravitating systems. *ApJ*, 221:567–579.
- Lightman, A. P. and Shapiro, S. L. (1977). The distribution and consumption rate of stars around a massive, collapsed object. *ApJ*, 211:244–262.
- Lin, D. N. C. and Tremaine, S. (1980). A reinvestigation of the standard model for the dynamics of a massive black hole in a globular cluster. *ApJ*, 242:789–798.
- Louis, P. D. and Spurzem, R. (1991). Anisotropic gaseous models for the evolution of star clusters. *MNRAS*, 251:408–426.
- Lynden-Bell, D. (1967). Statistical mechanics of violent relaxation in stellar systems. *MNRAS*, 136:101.
- Lynden-Bell, D. (1969). Galactic Nuclei as Collapsed Old Quasars. *nat*, 223:690–+.
- Lynden-Bell, D. and Eggleton, P. P. (1980). On the consequences of the gravothermal catastrophe. *MNRAS*, 191:483–498.
- Lynden-Bell, D. and Rees, M. J. (1971). On quasars, dust and the galactic centre. *MNRAS*, 152:461–+.
- Magorrian, J. and Tremaine, S. (1999). Rates of tidal disruption of stars by massive central black holes. *MNRAS*, 309:447–460.
- Makino, J. (1996). Postcollapse evolution of globular clusters. *ApJ*, 471:796.
- Marchant, A. B. and Shapiro, S. L. (1979). Star clusters containing massive, central black holes. II - self-consistent potentials. *ApJ*, 234:317–328.
- Marchant, A. B. and Shapiro, S. L. (1980). Star clusters containing massive, central black holes. III - evolution calculations. *ApJ*, 239:685–704.
- McCaughrean, M. J. and Stauffer, J. R. (1994). High resolution near-infrared imaging of the trapezium: A stellar census. *AJ*, 108:1382–1397.

BIBLIOGRAPHY

- McCray, R. (1979). *Spherical accretion onto supermassive black holes*, pages 227–239. Active galactic nuclei. (A79-50785 22-90) Cambridge, Cambridge University Press, 1979, p. 227-239. NSF-supported research.
- Merritt, D. (2006). Dynamics of galaxy cores and supermassive black holes. *Reports on Progress in Physics*, 69:2513–2579.
- Merritt, D. (2010). The Distribution of Stars and Stellar Remnants at the Galactic Center. *ApJ*, 718:739–761.
- Merritt, D., Alexander, T., Mikkola, S., and Will, C. (2011a). Stellar Dynamics of Extreme-Mass-Ratio Inspirals. *ArXiv e-prints*.
- Merritt, D., Alexander, T., Mikkola, S., and Will, C. M. (2011b). Stellar dynamics of extreme-mass-ratio inspirals. *Ph. Rev. D*, 84(4):044024.
- Merritt, D., Berczik, P., and Laun, F. (2006a). Brownian Motion of Black Holes in Dense Nuclei. preprint, astro-ph/0408029.
- Merritt, D., Ferrarese, L., and Joseph, C. L. (2001). No Supermassive Black Hole in M33? *Science*, 293:1116–1119.
- Merritt, D., Harfst, S., and Bertone, G. (2006b). Collisionally Regenerated Dark Matter Structures in Galactic Nuclei. *ArXiv Astrophysics e-prints*.
- Merritt, D. and Poon, M. Y. (2004a). Chaotic Loss Cones and Black Hole Fueling. *ApJ*, 606:788–798.
- Merritt, D. and Poon, M. Y. (2004b). Chaotic Loss Cones and Black Hole Fueling. *ApJ*, 606:788–798.
- Merritt, D. and Vasiliev, E. (2011). Orbits Around Black Holes in Triaxial Nuclei. *ApJ*, 726:61.
- Michell, J. (1784). O the Means of Discovering the Distance, Magnitude, &c. of the Fixed Stars, in Consequence of the Diminution of the Velocity of Their Light, in Case Such a Diminution Should be Found to Take Place in any of Them, and Such Other Data Should be Procured from Observations, as Would be Farther Necessary for That Purpose. by the Rev. John Michell, B. D. F. R. S. I a Letter to Henry Cavendish, Esq. F. R. S. and a. S. *Royal Society of London Philosophical Transactions Series I*, 74:35–57.
- Mikkola, S. (1997). Numerical Treatment of Small Stellar Systems with Binaries. *Celestial Mechanics and Dynamical Astronomy*, 68:87–104.
- Mikkola, S. and Aarseth, S. (2002). A Time-Transformed Leapfrog Scheme. *Celestial Mechanics and Dynamical Astronomy*, 84:343–354.
- Mikkola, S. and Merritt, D. (2006). Algorithmic regularization with velocity-dependent forces. *MNRAS*, 372:219–223.
- Miller, M. C. and Colbert, E. J. M. (2004). Intermediate-Mass Black Holes. *International Journal of Modern Physics D*, 13:1–64.
- Miller, M. C., Freitag, M., Hamilton, D. P., and Lauburg, V. M. (2005a). Binary Encounters with Supermassive Black Holes: Zero-Eccentricity LISA Events. *ApJ Lett.*, 631:L117–L120.

- Miller, M. C., Freitag, M., Hamilton, D. P., and Lauburg, V. M. (2005b). Binary Encounters with Supermassive Black Holes: Zero-Eccentricity LISA Events. *ApJ Lett.*, 631:L117–L120.
- Milosavljević, M. and Merritt, D. (2003). Long-Term Evolution of Massive Black Hole Binaries. *ApJ*, 596:860–878.
- Milosavljević, M. and Loeb, A. (2004). The Link between Warm Molecular Disks in Maser Nuclei and Star Formation near the Black Hole at the Galactic Center. *ApJ Lett.*, 604:L45–L48.
- Milosavljević, M. and Merrit (2001). Formation of Galactic Nuclei. *ApJ*, 563:34–62.
- Miralda-Escudé, J. and Gould, A. (2000). A cluster of black holes at the galactic center. *ApJ*, 545:847–853.
- Miyoshi, M., Moran, J., Herrnstein, J., Greenhill, L., Nakai, N., Diamond, P., and Inoue, M. (1995). Evidence for a black-hole from high rotation velocities in a sub-parsec region of ngc4258. *Nat.*, 373:127.
- Moran, J. M., Greenhill, L. J., and Herrnstein, J. R. (1999). Observational Evidence for Massive Black Holes in the Centers of Active Galaxies. *Journal of Astrophysics and Astronomy*, 20:165.
- Mouawad, N., Eckart, A., Pfalzner, S., Schödel, R., Moutaka, J., and Spurzem, R. (2005). Weighing the cusp at the Galactic Centre. *Astronomische Nachrichten*, 326:83–95.
- Muno, M. P., Lu, J. R., Baganoff, F. K., Brandt, W. N., Garmire, G. P., Ghez, A. M., Hornstein, S. D., and Morris, M. R. (2005a). A Remarkable Low-Mass X-Ray Binary within 0.1 Parsecs of the Galactic Center. *ApJ*, 633:228–239.
- Muno, M. P., Pfahl, E., Baganoff, F. K., Brandt, W. N., Ghez, A., Lu, J., and Morris, M. R. (2005b). An Overabundance of Transient X-Ray Binaries within 1 Parsec of the Galactic Center. *ApJ Lett.*, 622:L113–L116.
- Murphy, B. W., Cohn, H. N., and Durisen, R. H. (1991). Dynamical and luminosity evolution of active galactic nuclei - models with a mass spectrum. *ApJ*, 370:60–77.
- Nayakshin, S. (2006). Massive stars in subparsec rings around galactic centres. *MNRAS*, 372:143–150.
- Ostriker, J. P. (2000). Collisional Dark Matter and the Origin of Massive Black Holes. *Physical Review Letters*, 84:5258–5260.
- Peebles, P. J. E. (1972). Star distribution near a collapsed object. *ApJ*, 178:371–376.
- Perets, H. B., Hopman, C., and Alexander, T. (2007). Massive Perturber-driven Interactions between Stars and a Massive Black Hole. *ApJ*, 656:709–720.
- Perley, R. A., Dreher, J. W., and Cowan, J. J. (1984). The jet and filaments in Cygnus A. *ApJ Lett.*, 285:L35–L38.
- Peters, P. C. (1964). Gravitational Radiation and the Motion of Two Point Masses. *Physical Review*, 136:1224–1232.
- Peters, P. C. and Mathews, J. (1963). Gravitational Radiation from Point Masses in a Keplerian Orbit. *Physical Review*, 131:435–440.

BIBLIOGRAPHY

- Petiteau, A., Auger, G., Halloin, H., Jeannin, O., Plagnol, E., Pireaux, S., Regimbau, T., and Vinet, J. (2008). LISACode: A scientific simulator of LISA. *Physical Review D*, 77(2):023002-+.
- Phinney, E. S. (2002). LISA Science Requirements. available on-line at www.its.caltech.edu/~esp/lisa/LISTwg1.req-pr.pdf.
- Pian, E., Urry, C. M., Treves, A., Maraschi, L., Penton, S., Shull, J. M., Pesce, J. E., Grandi, P., Kii, T., Kollgaard, R. I., Madejski, G., Marshall, H. L., Wamsteker, W., Celotti, A., Courvoisier, T. J.-L., Falomo, R., Fink, H. H., George, I. M., and Ghisellini, G. (1997). Multiwavelength Monitoring of the BL Lacertae Object PKS 2155-304 in 1994 May. II. The IUE Campaign. *ApJ*, 486:784.
- Pinkney, J., Gebhardt, K., Bender, R., Bower, G., Dressler, A., Faber, S. M., Filippenko, A. V., Green, R., Ho, L. C., Kormendy, J., Lauer, T. R., Magorrian, J., Richstone, D., and Tremaine, S. (2003). Kinematics of 10 Early-Type Galaxies from Hubble Space Telescope and Ground-based Spectroscopy. *ApJ*, 596:903-929.
- Poon, M. Y. and Merritt, D. (2001). Orbital Structure of Triaxial Black Hole Nuclei. *ApJ*, 549:192-204.
- Poon, M. Y. and Merritt, D. (2004a). A Self-Consistent Study of Triaxial Black Hole Nuclei. *ApJ*, 606:774-787.
- Poon, M. Y. and Merritt, D. (2004b). A Self-Consistent Study of Triaxial Black Hole Nuclei. *ApJ*, 606:774-787.
- Portegies Zwart, S. F., Baumgardt, H., McMillan, S. L. W., Makino, J., Hut, P., and Ebisuzaki, T. (2006). The Ecology of Star Clusters and Intermediate-Mass Black Holes in the Galactic Bulge. *ApJ*, 641:319-326.
- Portegies Zwart, S. F. and McMillan, S. L. W. (2000). Black Hole Mergers in the Universe. *ApJ Lett.*, 528:L17-L20.
- Portegies Zwart, S. F., McMillan, S. L. W., Hut, P., and Makino, J. (2001). Star cluster ecology - IV. Dissection of an open star cluster: photometry. *MNRAS*, 321:199-226.
- Preto, M. and Amaro-Seoane, P. (2010). On Strong Mass Segregation Around a Massive Black Hole: Implications for Lower-Frequency Gravitational-Wave Astrophysics. *ApJ Lett.*, 708:L42-L46.
- Preto, M., Merritt, D., and Spurzem, R. (2004). N-Body Growth of a Bahcall-Wolf Cusp around a Black Hole. *ApJ Lett.*, 613:L109-112.
- Quinlan, G. D. (1996). The time-scale for core collapse in spherical star clusters. *New Astronomy*, 1:255-270.
- Quinlan, G. D. and Shapiro, S. L. (1990). The dynamical evolution of dense star clusters in galactic nuclei. *ApJ*, 356:483-500.
- Raboud, D. and Mermilliod, J.-C. (1998). Evolution of mass segregation in open clusters: some observational evidences. 333:897-909.
- Rasio, F. A., Fregeau, J. M., and Joshi, K. J. (2001). Binaries and Globular Cluster Dynamics. In *The influence of binaries on stellar population studies, Astrophysics and space*

- science library (ASSL)*, Vol. 264., page 387. Kluwer Academic Publishers.
- Rauch, K. P. (1995). Dynamical evolution of star clusters around a rotating black hole with an accretion disc. *MNRAS*, 275:628–640.
- Rauch, K. P. and Ingalls, B. (1998). Resonant tidal disruption in galactic nuclei. *MNRAS*, 299:1231–1241.
- Rauch, K. P. and Tremaine, S. (1996). Resonant relaxation in stellar systems. *New Astronomy*, 1:149–170.
- Rees, M. J. (1984). "black hole models for active galactic nuclei". *ARA&A*, 22:471–506.
- Rees, M. J. (1988). Tidal disruption of stars by black holes of 10 to the 6th-10 to the 8th solar masses in nearby galaxies. *Nat*, 333:523–528.
- Rees, M. J. (1990). 'dead quasars' in nearby galaxies? *Science*, 247:817–823.
- Renzini, A., Greggio, L., di Serego-Alighieri, S., Cappellari, M., Burstein, D., and Bertola, F. (1995). An ultraviolet flare at the centre of the elliptical galaxy ngc4552. *Nat*, 378:39.
- Rosenbluth, M. N., MacDonald, W. M., and Judd, D. L. (1957a). Fokker-Planck Equation for an Inverse-Square Force. *Physical Review*, 107:1–6.
- Rosenbluth, M. N., MacDonald, W. M., and Judd, D. L. (1957b). Fokker-Planck Equation for an Inverse-Square Force. *Physical Review*, 107:1–6.
- Rubbo, L. J., Holley-Bockelmann, K., and Finn, L. S. (2006). Event Rate for Extreme Mass Ratio Burst Signals in the Laser Interferometer Space Antenna Band. *ApJ Lett.*, 649:L25–L28.
- Salpeter, E. E. (1955). The luminosity function and stellar evolution. *ApJ*, 121:161.
- Schödel, R., Ott, T., Genzel, R., Hofmann, R., Lehnert, M., Eckart, A., Mouawad, N., Alexander, T., Reid, M. J., Lenzen, R., Hartung, M., Lacombe, F., Rouan, D., Gendron, E., Rousset, G., Lagrange, A.-M., Brandner, W., Ageorges, N., Lidman, C., Moorwood, A. F. M., Spyromilio, J., Hubin, N., and Menten, K. M. (2002). A star in a 15.2-year orbit around the supermassive black hole at the centre of the Milky Way. *Nat*, 419:694–696.
- Schaffer, S. (1979). John Mitchell and Black Holes. *Journal for the History of Astronomy*, 10:42–+.
- Schödel, R., Ott, T., Genzel, R., Eckart, A., Mouawad, N., and Alexander, T. (2003). Stellar Dynamics in the Central Arcsecond of Our Galaxy. *ApJ*, 596:1015–1034.
- Seto, N. (2012). Relativistic resonant relations between massive black hole binary and extreme mass ratio inspiral. *Ph. Rev. D*, 85(6):064037.
- Shapiro, S. L. and Marchant, A. B. (1978). Star clusters containing massive, central black holes - monte carlo simulations in two-dimensional phase space. *ApJ*, 225:603–624.
- Shapiro, S. L. and Teukolsky, S. A. (1979). Gravitational collapse of supermassive stars to black holes - Numerical solution of the Einstein equations. *ApJ Lett.*, 234:L177–L181.

BIBLIOGRAPHY

- Shapiro, S. L. and Teukolsky, S. A. (1985). The collapse of dense star clusters to supermassive black holes - the origin of quasars and agns. *ApJ Lett.*, 292:41–44.
- Sigurdsson, S. and Rees, M. J. (1997). Capture of stellar mass compact objects by massive black holes in galactic cusps. *MNRAS*, 284:318–326.
- Softan, A. (1982). Masses of quasars. *MNRAS*, 200:115–122.
- Spitzer, L., J. and Saslaw, W. C. (1966). On the evolution of galactic nuclei. *ApJ*, 143:400.
- Spitzer, L. (1987). *Dynamical evolution of globular clusters*. Princeton, NJ, Princeton University Press, 1987, 191 p.
- Spitzer, L. and Shull, J. M. (1975). Random gravitational encounters and the evolution of spherical systems. VI - plummer's model. *ApJ*, 200:339–342.
- Spitzer, L. J. (1969). Equipartition and the formation of compact nuclei in spherical stellar systems. *ApJ Lett.*, 158:139.
- Spitzer, L. J. and Hart, M. H. (1971). Random gravitational encounters and the evolution of spherical systems. II. models. *ApJ*, 166:483.
- Spurzem, R. (1992). Evolution of stars and gas in galactic nuclei. In *Reviews of Modern Astronomy*, volume 5, pages 161–173.
- Spurzem, R. and Aarseth, S. J. (1996). Direct collisional simulation of 100000 particles past core collapse. *MNRAS*, 282:19.
- Spurzem, R. and Takahashi, K. (1995). Comparison between fokker-planck and gaseous models of star clusters in the multi-mass case revisited. *MNRAS*, 272:772–784.
- Stodółkiewicz, J. S. (1982). Dynamical evolution of globular clusters. i. *Acta Astron.*, 32:63–91.
- Stodółkiewicz, J. S. (1986). Dynamical evolution of globular clusters. II - binaries method. *Acta Astron.*, 36:19–41.
- Syer, D., Clarke, C. J., and Rees, M. J. (1991). Star-disc interactions near a massive black hole. *MNRAS*, 250:505–512.
- Syer, D. and Ulmer, A. (1999). Tidal disruption rates of stars in observed galaxies. *MNRAS*, 306:35–42.
- Takahashi, K. (1993). A new powerful method for solving the orbit-averaged fokker-planck equation regarding stellar dynamics. *PASJ*, 45:233–242.
- Takahashi, K. (1995). Fokker-planck models of star clusters with anisotropic velocity distributions i. pre-collapse evolution. *PASJ*, 47:561–573.
- Takahashi, K. (1996). Fokker-planck models of star clusters with anisotropic velocity distributions II. post-collapse evolution. *PASJ*, 48:691–700.
- Takahashi, K. (1997). Fokker-planck models of star clusters with anisotropic velocity distributions III. multi-mass clusters. *PASJ*, 49:547–560.
- Terlevich, R. (1989). Active galactic nuclei without black-holes. In *Evolutionary Phenomena in Galaxies*, pages 149–158.
- Thorne, K. S. (1987). *Gravitational radiation.*, pages 330–458.

- Tremaine, S., Gebhardt, K., Bender, R., Bower, G., Dressler, A., Faber, S. M., Filippenko, A. V., Green, R., Grillmair, C., Ho, L. C., Kormendy, J., Lauer, T. R., Magorrian, J., Pinkney, J., and Richstone, D. (2002). The Slope of the Black Hole Mass versus Velocity Dispersion Correlation. *ApJ*, 574:740–753.
- Šubr, L. and Karas, V. (1999). An orbiter crossing an accretion disc. *A&A*, 352:452–458.
- Volonteri, M., Madau, P., Quataert, E., and Rees, M. J. (2005). The Distribution and Cosmic Evolution of Massive Black Hole Spins. *ApJ*, 620:69–77.
- Wang, J. and Merritt, D. (2004). Revised Rates of Stellar Disruption in Galactic Nuclei. *ApJ*, 600:149–161.
- Watters, W. A., Joshi, K. J., and Rasio, F. A. (2000). Thermal and dynamical equilibrium in two-component star clusters. *ApJ*, 539:331–341.
- Weinberg, N. N., Milosavljević, M., and Ghez, A. M. (2005). Stellar Dynamics at the Galactic Center with an Extremely Large Telescope. *ApJ*, 622:878–891.
- Yu, Q. and Tremaine, S. (2002). Observational constraints on growth of massive black holes. *MNRAS*, 335:965–976.
- Yunes, N., Miller, M. C., and Thornburg, J. (2011). Effect of massive perturbers on extreme mass-ratio inspiral waveforms. *Ph. Rev. D*, 83(4):044030.
- Zare, K. (1974). A regularization of multiple encounters in gravitational n-body problems. *Celestial Mechanics*, 10:207–215.
- Zhao, H.-S., Haehnelt, M. G., and Rees, M. J. (2002). Feeding black holes at galactic centres by capture from isothermal cusps. *New Astronomy*, 7:385–394.